LINEAR AND NONLINEAR OPTICAL PULSE CHARACTERISATION

Andrew Finch

A Thesis Submitted for the Degree of PhD
at the
University of St Andrews

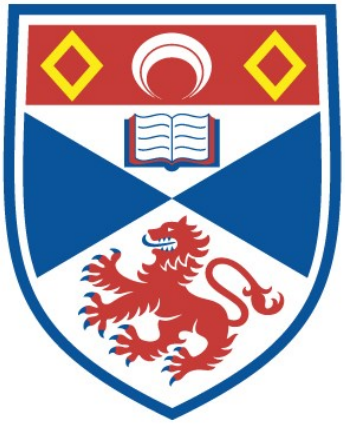

1989

LINEAR AND NONLINEAR OPTICAL PULSE CHARACTERISATION

A thesis submitted for the degree of Doctor of Philosophy to

the University of St. Andrews

by

Andrew Finch, B.A., M.Sc.

March 1989

1974

DECLARATIONS

I, Andrew Finch, hereby certify that this thesis has been composed by myself, that it is a record of my own work, and that it has not been accepted in partial or complete fulfilment of any other degree of professional qualification. I was admitted to the Faculty of Science of the University of St.Andrews under Ordinance general No 12 on October, 1984 and as a candidate for the degree of Ph.D on October, 1985.

In submitting this thesis to the University of St.Andrews I understand that I am giving permission for it to be made available for use in accordance with the regulations of the University Library for the time being in force, subject to any copyright vested in the work not being affected thereby. I also understand that the title and abstract will be published, and that a copy of the work may be made and supplied to any bona fide library or research worker.

A.Finch

March 1989

I hereby certify that the candidate has fulfilled the conditions of the Resolution and Regulations appropriate to the Degree of Ph.D.

W.Sibbett

Research Supervisor

March 1989

ABSTRACT

Developmental work on the generation and measurement of ultrashort pulses has been performed. A colliding pulse, passively mode-locked (CPM) ring dye laser has been investigated by spectral analysis and the nonlinear technique of second harmonic generation autocorrelation. Two systems for the intracavity compensation of group velocity dispersion (GVD) have been experimentally compared in the CPM laser. Initially one scheme, utilising Gires-Tournois interferometers, has achieved pulse durations of 64 fs. A second technique employing a four-prism sequence within the cavity gave typical pulse durations of ~40 fs and focussing adjustments within the jets achieved durations as short as 19 fs for the first time. A realtime interferometric autocorrelator was constructed and detailed theoretical work has been performed to model the resultant fringe resolved autocorrelations as a function of pulseshape and frequency chirp. Spectral and autocorrelation analysis of the CPM laser led to the inference that the laser pulse intensity profiles were distinctly asymmetric. The main sources of frequency chirp within the laser cavity were assessed in order to find possible explanations for this type of laser behaviour.

The linear pulse measurement technique employing synchroscan streak cameras was also critically assessed in terms of the available temporal resolutions as a function of phase noise in the RF deflection signal. Two streak tube designs, the Photochron II and the Photochron IV, have been experimentally compared employing the CPM laser as a test pulse source. Optimisation of the synchronisation circuitry has allowed the notable achievement of a temporal resolution of 0.93ps for the Photochron IV streak camera. A computer-interfaced readout system incorporating a charge coupled device (CCD) sensor has been developed which allows the recording of synchroscan streak events with a digitisation accuracy up to 12 bits. Preliminary experimentation was also performed to investigate the feasibility of incorporating a electron sensitive CCD structure within the envelope of the streak camera. It is intended that such a streak camera will be incorporated

in a spaceborne laser ranging system and a theoretical assessment of the expected instrument performance has been performed.

The above investigations have direct relevance to other types of ultrashort pulse sources and their application in optical communications, time-resolved spectroscopy and ultrafast electrooptic sampling.

Dedicated to my mother,

Will, Jackie and Dave.

Frontispiece (overleaf): Photograph of the colliding pulse, mode-locked ring dye laser.

CONTENTS

INTRODUCTION

Over recent years the need for improvement in the measurement and characterisation of ultrashort pulses has become of prime importance. Refinement of mode-locked lasers has led to the direct generation of sub-30fs duration pulses in the visible spectral region [1] and pulse durations of ~200fs in the near-infrared range [2,3]. Additional extracavity amplification and temporal compression has produced pulse durations as short as 6fs at 630nm [4] and 9fs at 800-840nm [5]. Consequently it is vital that pulse monitoring systems can exhibit the temporal resolutions required to characterise such lasers and to further allow time-resolved analysis of the excitation processes these ultrashort pulse sources may induce.

The object of this thesis is to report on the work carried out during a PhD project into the development and improvement of two separate and distinct techniques of pulse characterisation: (i) a linear technique employing electron-optical streak cameras, and (ii) the nonlinear technique of second harmonic generation (SHG) autocorrelation. The available resolution of each technique differs at present by several orders of magnitude – in the case of the streak camera pulse durations of ~1ps are measurable, whereas SHG autocorrelation can provide temporal characterisations in the femtosecond regime. The systems described here were developed around a colliding-pulse, passively mode-locked (CPM) CW ring dye laser incorporating Rhodamine 6G as the gain and DODCI as the passive medium. Initial results will concern the laser operated without any form of cavity dispersion compensation and later results are presented with a 4-prism dispersion compensation system included. The CPM laser output is monitored in realtime by the SHG correlation technique and provides excellent "quasi-delta function" test pulses for the streak camera which, as stated above, cannot resolve the tens of femtosecond duration pulses that the laser produces. Not that this implies the streak camera is of no use as a diagnostic of the laser performance. It has proved invaluable in the assessment of the stability of the laser pulse train and indeed the radical improvement of the laser performance both temporally

(the notable reduction of pulse durations from ~80 fs to <20 fs) and in terms of phase and amplitude stability was assisted in part by streak camera studies.

The thesis is presented with an initial introductory chapter, two main sections, a final general conclusion and relevant appendices. In the Chapter 1 the CPM laser is introduced including an historical overview of passive mode-locking techniques. The theories developed to explain the underlying physical processes leading to ultrashort pulse generation [6,7] are also presented. The importance of compensation of the group velocity dispersion (GVD) from cavity optics is discussed and how by incorporation of suitable compensating elements pulse duration can be reduced. Following this the main part of this thesis is divided into two sections.

Section I is devoted to streak cameras, the development of novel electronic methods for driving them in repetitive or "synchroscan" mode and the design and implementation of charge coupled device (CCD) streak camera readout systems for laboratory and spaceborne applications. Including an historical overview of streak camera design, details of the factors which limit streak tube performance and the computational techniques employed in their design are dealt with in Chapter 2. Two particular streak tube designs are introduced, namely the Photochron II [8] and Photochron IV [9] and when tested in synchroscan mode the experimental observations are presented in Chapters 3 and 4 respectively. Within this experimentation the importance of laser stability is demonstrated and a theoretical analysis of the effects of phase noise in the drive signal on achievable temporal resolution is presented. Chapters 5 and 6 are concerned with the development and performance evaluation of CCD readout systems for streak cameras; the latter chapter including the assessment of the performance of an electron-sensitive CCD device incorporated within the vacuum envelope of a circular scan streak tube (CSST). It is intended that such streak cameras will form an integral component of a spaceborne laser ranging system [10] and this technique is outlined in Appendix A. An analysis of the sensitivity requirements of the CCD device is given in a conference reprint [11] which is included in Appendix B.

Section II is concerned with SHG correlation pulse measurement techniques, the development of a realtime interferometric autocorrelator [12] and the theoretical analysis of

autocorrelation functions as an aid to determining pulseshape and chirp content. In Chapter 7 numerical techniques employed to calculate expected autocorrelation functions for pulses of differing intensity profiles and containing various types of frequency chirp are described. The pertinent design aspects of a realtime interferometric correlator are discussed in Chapter 8 where details are included for a system employed in the characterisation of the CPM dye laser. In Chapter 9 the CPM laser itself is examined although some of its properties will have been referred to in preceding chapters. Here the performance characteristics of the CPM laser developed at St. Andrews are detailed for two schemes of GVD compensation using Gires-Tournois Interferometers (GTI's) [13] and a four-prism sequence [14]. The frequency chirping processes inside the absorber jet are investigated and the frequency sweep across the laser pulse under various operating conditions is calculated [15]. Temporal and spectral data are presented which suggests that the pulses emanating from this particular laser have an asymmetrical intensity profile.

Finally in the concluding Chapter 10 the research project is summarised and future avenues of development suggested for the CPM laser, the SHG autocorrelator and the synchroscan streak camera.

REFERENCES

1 J.A Valdmanis, R.L Fork, and J.P Gordon, Opt. Lett. **10** 131 (1985).

2 N.Langford, R.S.Grant, W.Sibbett, and K.Smith, CLEO '88 Tech. Dig. 7, THJ2 326, (1988).

3 P.Kean, X.Zhu, D.W.Crust, R.S.Grant, N.Langford and W.Sibbett, Opt. Lett. **14** 39 (1989).

4 R.L.Fork, C.H.Brito-Cruz, P.C.Becker, and C.V.Shank, Opt. Lett. **12** 483 (1987).

5 P.C.Becker, H.L.Fragnito, R.L.Fork, F.A.Beisser, and C.V.Shank, Proc. IQEC'88, Post-deadline paper PD-15, 36 (1988).

6 G.H.C.New, Rep. Prog. Phys. **46** 877 (1983).

7 O.E.Martinez, R.L.Fork and J.P.Gordon, J.Opt. Soc. Am B **2** 753 (1985).

[8] P.R.Bird, D.J.Bradley and W.Sibbett, Proc. XIth ICHSP 112 (1974).

[9] W.Sibbett, H.Nui, and M.R. Baggs, Rev. Sci. Instr. **53** 758 (1982).

[10] H.Lutz, W.Krause and G.Barthel, *Space 2000* Amer. Inst. of Aeronautics and Astronautics, New York, p.236 (1983).

[11] A.Finch, W.Sibbett, W.E.Sleat, C.Claeys, I.Debusschere and W.Krause, Proc. Conf.on Solid State imagers and their applications, SPIE **591** 31 (1985).

[12] J.C.Diels, J.J.Fontaine, I.C.McMichael and F.Simoni, Appl. Optics **24** 1270 (1985).

[13] P.M.W.French, G.F.Chen and W.Sibbett, Opt. Comm. **57** 263 (1986).

[14] R.L.Fork, O.E.Martinez and J.P.Gordon, Opt. Lett. **9** 150 (1984).

[15] R.S.Miranda, G.R.Jacobovitz, C.H.Brito Cruz and A.F.Sarpara, Opt. Lett. **11** 224 (1986).

CHAPTER 1: ULTRASHORT PULSE GENERATION – THE COLLIDING PULSE MODE-LOCKED DYE LASER

1.0 INTRODUCTION

The colliding-pulse passively mode-locked (CPM) CW ring dye laser has proved to be an excellent ultrashort pulse source for the development and refinement of the pulse measurement techniques discussed in the following two sections. The purpose of this chapter is to describe the general operating principles of the CPM laser and its historical development. An outline is given of the principles of mode-locking with particular reference to the case of passive mode-locking and this theory is then expanded to incorporate the role of intracavity group velocity dispersion (GVD) and self-phase modulation (SPM).

1.1 THE DYE LASING MEDIUM

The gain medium usually employed in CPM lasers is an organic dye molecule dissolved in a suitable solvent (eg. ethylene glycol). Such molecules contain large numbers of conjugated carbon bonds which produce a set of delocalised π-electrons free to move along the molecule's length. Effectively the electrons can be seen to be confined along the molecule chain and a set of energy levels are generated characteristic of the eigenstates of a one-dimensional potential well. An electron if excited can reside in an upper level with spin antiparallel (singlet) or parallel (triplet) to the singlet ground state. The singlet-singlet transition is short lived (fluorescence lifetime ~1ns) and consequently is a useful lasing transition whereas the slower spin forbidden triplet-singlet phosphorescence transition of order several μs can be a problematic bottleneck. Superimposed on the fine structure are a set of vibrational and rotational splittings giving the overall energy diagram represented in figure 1.1 which applies to the Rhodamine 6G dye molecule. From the diagram it can be seen that the dye molecule is a 4-level lasing system. Pump excitation raises the molecule into some level in the vibrational manifold which is followed by a fast non-radiative decay to the lowest S_1 state. Then either a fast (lasing) transition can occur into the S_0 manifold

followed by thermalisation to the ground state or a slower (~10 ns) spin forbidden transition occurs to the triplet level leading to a loss in lasing efficiency. Additionally since the T_1–T_2 transition overlaps with the fluorescence spectrum there exist other transition paths which contibute to loss.

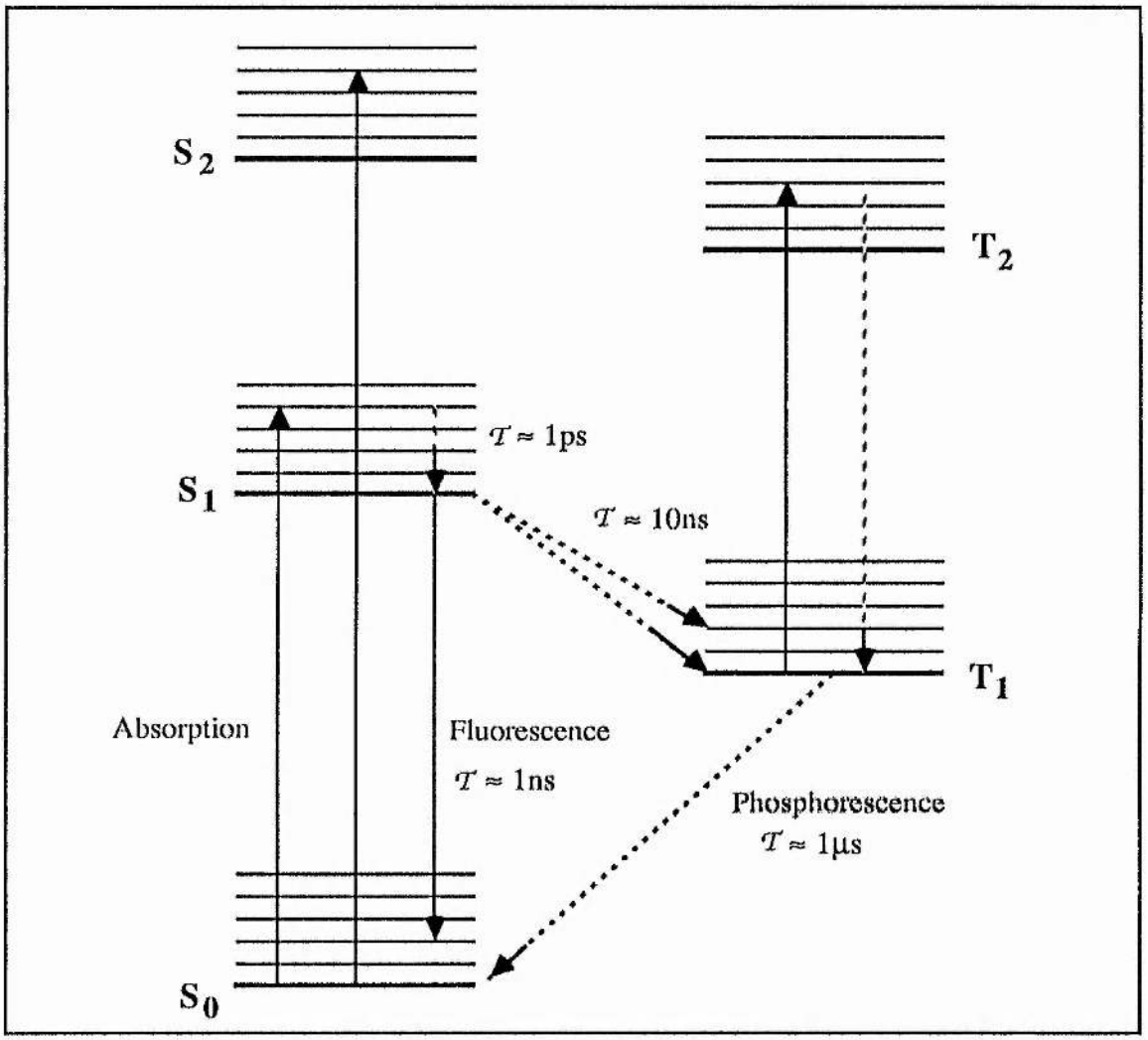

Figure 1.1 Energy level diagram of a typical dye molecule showing radiative (solid lines) and non-radiative (broken lines) transitions.

The vibrational and rotational splitting in the molecular energy levels allow pumping and fluorescence across a wide range of wavelengths. Even though the dye medium is homogeneously broadened, spatial hole burning is sufficient for lasing modes to be simultaneously supported across a wide bandwidth in standing-wave cavities and consequently dyes make excellent lasing media for ultrashort pulse sources.

1.2 PRINCIPLES OF MODE-LOCKING

The phase-locking of the longitudinal modes of a laser cavity leads to the confinement of a photon flux within the cavity into a small spatial region or, alternatively, it may be viewed as the maintenance of the photon energy to within a single short time period fluctuation. To explain how mode-locking is brought about we must first look at the spectral characteristics of the radiation inside a laser cavity (detailed treatments of this are also presented elsewhere [1,2,3,4]).

The radiation field inside a laser cavity of length, L and mirror radius, R, with no spectral tuning elements will consist of a series of cavity modes with frequencies v defined by:

$$v = \partial v\left[q + \frac{1}{\pi}(1+m+n)\cos^{-1}(1-\frac{L}{R})\right] \qquad \text{–eq(1.1)}$$

where $\partial v = c/2L = T_{cav}^{-1}$ the cavity round-trip time.

Ignoring the second term for the moment the above expression represents the allowed frequencies that the cavity can sustain such that a electric field node exists at each mirror surface (ie there is an integer number, q of half-wavelengths inside the cavity - although this not exactly true since there is an axial phase delay at the cavity focus). The integers, m and n characterise the higher frequency transverse modes of the cavity for a given axial mode, defined by the integer q. For the confocal case, (1–L/R)=0 and all transverse modes are degenerate with the fundamental TEM_{00} axial modes and for this reason this cavity configuration is often used for scanning Fabry-Perot interferometers. The following discussion is confined to axial mode-locking although treatments exist for the special case of transverse mode-locking [2] they are not relevant in the case of the CPM laser.

The instantaneous cavity field, E(t) will be the sum of the axial modes and can be represented in complex form by the Fourier series:

$$E(t) = \sum_n E_n \exp(i w_n t)$$

$$= \sum_n E_n \exp(i\{(w_o + nw)t + \varnothing_n)\} \qquad \text{–eq(1.2)}$$

where $w = 2\pi\partial v$ and w_o is an arbitrarily chosen centre reference frequency. E_n and $\varnothing_n$ specify the amplitude and phase of the spectral components of the laser radiation.

Analogous to a mathematical treatment of phase noise (given in §4.4), if there is no fixed phase relationship between the axial modes, equation 1.2 represents the vector sum of a set of uncorrelatated oscillators and the resulting temporal evolution of the electric field will be chaotic. In this particular case the random intensity variations in V(t) arise because of random interference between modes rather than intensity fluctuations of individual modes.

If a definite phase relationship is imposed on the discrete spectral components then the resultant field will vary periodically with time and the laser is said to be *mode-locked* although this term is usually reserved for the particular case when $\emptyset_n$ is a linear function of n ie) $\emptyset_n = \emptyset_o + \alpha n$. The simplest case of mode-locking is when $\emptyset_n$ is made zero in which case equation 1.2 becomes for N oscillating modes:

$$E(t) = \sum_{-(N-1)/2}^{(N-1)/2} E_n \, e^{i(\omega_o + n\omega)t} \qquad \text{–eq(1.3)}$$

Assuming for simplicity that all axial modes have equal amplitudes ($E_n = 1$), the average laser output becomes [1,3]:

$$P(t) \propto \frac{\sin^2(N\omega t/2)}{\sin^2(\omega t)} \qquad \text{–eq(1.4)}$$

The mathematical anlaysis is almost identical to the description of the spatial intensity distribution of light diffracted by a grating except here we have a temporal analogue. From the above expression we can see that the power is emitted as a pulse-train of period $2\pi / \omega = T_{cav}$ and the individual pulse widths Δt are related to the number of oscillating modes by $\Delta t = T_{cav} / N$. Hence the larger the mode-locked bandwidth the shorter the pulse duration that is produced.

There are a variety of methods available by which mode-locking can be achieved and these can be separated into two distinct types, namely *active* and *passive* mode-locking.

1.3 ACTIVE MODE-LOCKING

In this method a periodic modulation in loss, gain or phase is applied to the radiation in the laser cavity at the cavity round-trip frequency or a harmonic by means of an acousto-optic or electro-optic device. Viewed in the time domain, a pulse propagating inside the cavity passing through the modulator at the peak of its transmission will experience the

maximum gain and so the laser will tend to pulsed operation. Alternatively in the frequency domain the applied modulation can be seen as generating amplitude sidebands on each of the existing longitudinal modes. When the modulating frequency is tuned to the cavity frequency these side-bands overlap with adjacent modes, effectively coupling the various axial oscillators and thereby achieving mode-locking. One might wonder how this can occur in an homogeneously broadened medium but it should be remembered that the typically broad gain bandwidth is relatively flat near line centre and consequently many modes can compete and exist at the onset of the mode-locking process. Typical durations are 10-100ps limited by the gain bandwidth of the lasing media (and hence the maximum number of modes that can be coupled) and the quality of the active mode-locking mechanism and power levels required (thermal effects in the modulating element, etc).

Shorter pulse durations can be achieved from lasers pumped by actively mode-locked lasers when their cavity lengths are matched to that of the source [5,6,7]. Typically ten-fold compression in duration is available by such *synchronous-pumping* techniques although in some cases femtosecond pulse have been produced by suitably dispersion-compensated cavity configurations (cf reference [8] where 29fs has been reported). Employing more exotic synchronously-pumped configurations, with coupled cavity feedback systems which inject chirped pulses back into a master colour centre cavity, ultrashort pulse durations of around 100fs have recently been generated [9]. Such so-called *soliton* lasers – perhaps more generally *coupled-cavity mode-locked* (CCM) lasers is a better nomenclature – show excellent stability, comparable to passive mode-locked sources.

1.4 PASSIVE MODE-LOCKING

This simple technique in general produces the shortest pulses. The mode-locking mechanism relies on the presence inside the cavity of an absorber that saturates at the power levels attained during lasing action. The absorber can be treated as a two-level system. For low intensities the medium absorbs the incident flux creating an excited state population. Further increase in the flux intensity causes the stimulated emission of the upper population until at a certain intensity the stimulated absorption rate is equal to the

stimulated emission rate and the medium is effectively transparent or bleached. In this situation large intensity fluctuations will experience less loss than lower intensity variations and the absorber acts to filter out a single family of fluctuations or a 'noise burst' from the random summation of the uncorrelated oscillating axial mode ensemble. In effect the absorber operates as an optical shutter which switches at the repetition frequency of the cavity. Because the pulse propagating in the cavity acts to open and close this the absorber switch itself, this mechanism is termed passive mode-locking.

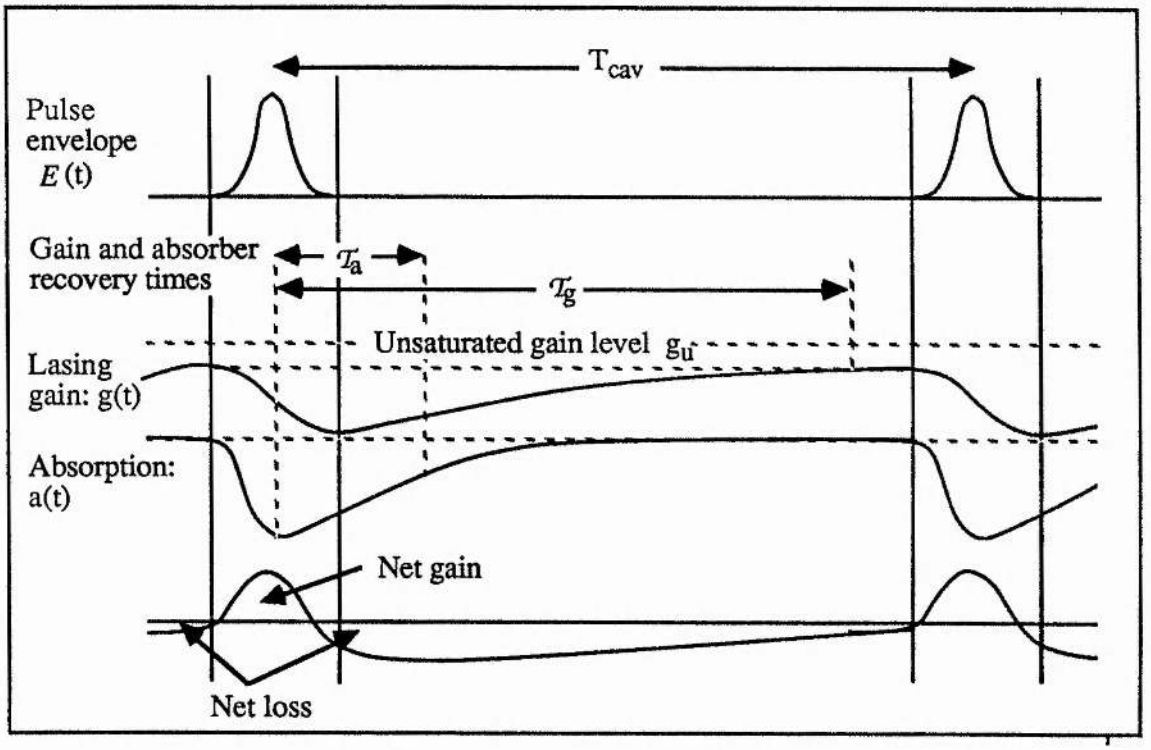

Figure 1.2 Schematic diagram showing action of gain and absorber saturation

Since in general the spectral bandwidths of passively modelocked pulses are of the order several nanometers and consequently a very large number of axial modes are phase-locked ($N \approx 10^4$), the passive mode-locking mechanism can be readily explained in the temporal domain. Earlier theoretical analyses have been made by various authors including New [1] and Haus [10,11] to explain the pulse forming kinetics of the absorber and gain media in the laser. Figure 1.2 (adapted from reference [1]) shows the net gain presented to the selected noise burst as a function of time; indicated on the diagram is the relative recovery of the absorber and gain medium (a(t) and g(t) respectively). In basic terms the

absorber, having preferentially selected a family of intensity fluctuations, will sharpen the leading edge of this noise burst and during its passage through the amplifying medium the trailing edge of the initial 'pulse' is also steepened due to gain saturation. The regime where this net pulse compression effect can occur is dependent on a critical interplay of relative small signal gain and absorption cross-section, but passive mode-locking can be achieved for a relatively wide range of absorber recovery times, τ_a (up to nanoseconds) as long as the gain medium can be effectively depleted by the central, peak intensity region of the pulse. This usually requires that the gain recovery time, τ_g is the of same order as T_{cav}. After a few hundred cavity round-trips the initial noise burst is compressed and shaped into a discrete optical pulse, the ultimate pulse duration being determined by chirp processes inside the nonlinear gain and absorber and their interaction with intracavity group velocity dispersion (see §1.6).

Using a simple rate equation approach New [1,12] determined the necessary conditions for pulse compression to occur. These mode-locking criteria stipulate that the saturation parameter (s –parameter), the ratio of the adsorber and gain cross-sections, should satisfy the condition:

$$s = \frac{\sigma_a}{\sigma_g} > 1 + \frac{\Gamma}{g_u} \qquad \text{–eq(1.4)}$$

where Γ is the cavity loss per round-trip and g_u the unsaturated absorption coefficient, and secondly the gain recovery time should be longer than that of the absorber, that is:

$$\frac{\tau_a}{\tau_g} < 1. \qquad \text{–eq(1.5)}$$

The first condition specifies that the absorber cross-section should significantly exceed the gain cross-section, in other words the absorber medium should saturate more rapidly than the amplifying medium. These conditions are in general valid for most practical mode-locked lasers where the time variation of the laser pulse is slow compared to the dephasing time, T_2 in the saturable absorber – in effect the absorption process can be treated as a simple homogeneous transition and hence simple rate equations apply. For pulses with duration comparable or shorter than T_2 (≈20fs for DODCI [13]) then more complex analyses are required [14]. In a series of papers by H.A.Haus [10,11,4] a formulation

describing CW mode-locking was developed which looked for steady state solutions of a differential equation descibing the temporal evolution of the pulse envelope E(t):

$$\frac{1}{w_o^2}\frac{d^2E}{dt^2} - \left[\frac{\partial_1}{w_o} + \partial T\right]\frac{dE}{dt} + \{g(t) + a(t) - \Gamma\}E(t) = 0 \qquad \text{–eq(1.6)}$$

where: ∂_1 represents any linear dispersion in the cavity and ∂T denotes a small time delay imposed on the pulse due to time varying effects in gain and absorber. One such formal self consistent solution to this basic cavity equation is the hyperbolic secant function as described in Section II:

$$E(t) = E_o \text{ sech } (\frac{t}{\tau_p}) \qquad \text{–eq(1.7)}$$

The solution does not immediately yield unique values of pulsewidth, τ_p but rather generates a set of interrelated algebraic equations defining τ_p, peak intensity $|E_o|^2$ and ∂T in terms of the cavity parameters. Investigation of the various conditions necessary to generate $sech^2$ pulse intensity profiles from initial noise fluctuations lead to a defined regime of laser parameters which can only be met in a limited set of laser arrangements. Indeed experimental fitting of autocorrelation functions for durations of around 100 fs give reasonable agreement to the above envelope function. However, when mode-locked pulses have durations of less than ~100 fs higher-order dispersion and self-phase modulation must be included in equation 1.6 and self-consistent envelope functions will not necessarily be of $sech^2$ form or even symmetrical. This is discussed further in Chapter 9.

1.5 THE CPM DYE LASER – AN HISTORICAL OVERVIEW

Passive mode-locking in dyes was first observed in 1968 by Schmidt and Schafer [15] following a period of intensive research of passively mode-locked Nd:glass lasers. With the advent of the continuous wave dye laser first demonstrated by Peterson [16] in 1971 there then followed a number of developments in the field of mode-locking. This work is summarised in Table 1.1 and culminates in the invention of the CPM laser by Fork and coworkers in 1981 [17] who reported pulse durations of less than 100fs for the first time. A similar system was developed at Imperial college in 1982 [18] and rebuilt in St. Andrews in 1986 (figure 1.3). The advantage of this CPM ring laser configuration is that it utlilises the

Table 1.1 Historical summary of passive modelocking in dye lasers

Year	*Researchers*	*Key development*
	Flashlamp pumped mode-locked dye lasers	
1968	Schmidt & Schafer [15]	Flash-lamp pumped passive modelocking; gain medium: Rh6G; absorber: DODCI.
1969	Bradley & O'Neill [19]	As above and Rh6G/ rhodamine B combination; intracavity grating to tune wavelength and hence optimise *s*–parameter. End contacting of absorber dye cell to cavity mirror achieved pulsewidths of 6ps.
1971	Arthurs et al. [20]	Tunable pulses (602-625nm) Rh6G / DODCI.
1972	" [21]	Tunable pulses (584-702nm) Rh6G / Rh B / Cresyl violet.
1973	" [22]	Extensive streak camera studies demonstrating build-up of mode-locking; measurement of $\tau_a \approx 300$ps for DODCI and examination of the role the photoisomer.
1977 – 1982	Lill et al.[23], Wyatt[24] Mialocq & Goujon [25], Sibbett & Taylor [26]	Extension of flash-lamp pumped mode-locking into the blue using various Coumarin dyes (460 – 590 nm); pulse durations 3 – 10 ps.
	CW mode-locked dye lasers	
1972	Ippen & Shank [27]	CW operation of Rh6G / DODCI laser. Peak powers 100W; $\Delta t \sim 1.5$ ps. Measured by SHG autocorrelation.
	O'Neill [28]	$\Delta t \sim 4$ ps measured with streak camera.
1973	Letouzey & Sari [29]	Use of dye jets rather than dye cells.
1974	Scavennec et al. [30]	Single dye jet operation (Rh6G / DODCI mixture).
	Shank & Ippen [31]	As above with additional acousto-optic cavity dumper; achieved kW peak powers and $\Delta t < 1$ps.
1975	Shank & Ippen [32]	Reverted to double jet configuration; malachite green absorber. Observation of chirped pulses. Extracavity compression with grating pair yielded 300 fs pulses.
1976	Ruddock & Bradley [33]	Direct production of 400 fs pulses.
1978	Diels et al. [34]	Removal of tuning prism in cavity and replacement with a multi-layer dielectric reflector gave $\Delta t \sim 200$ fs.
1981	Fork et al. [17]	Operation of CPM ring dye laser; first optical pulses <100fs

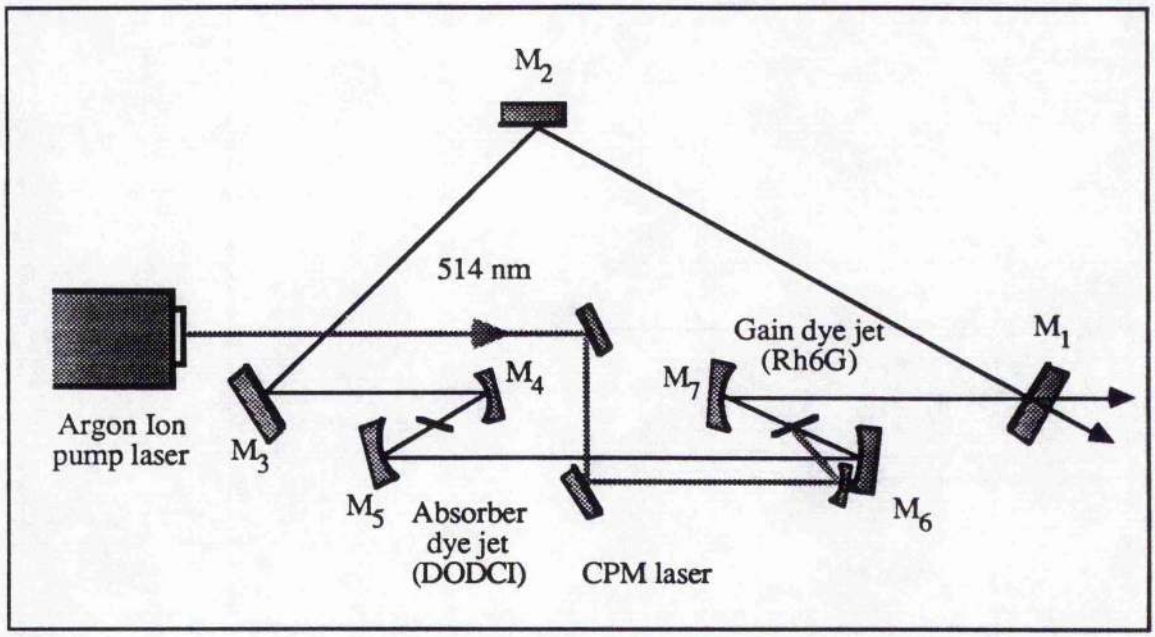

Figure 1.3 Schematic of colliding pulse ring dye laser

coherent interaction of two optical pulses to more effectively saturate the absorber dye. As the pulses collide in the absorber jet coherent interference sets up a standing wave which creates a periodic absorption–grating throughout the medium. At the antinodes of this standing wave the intensity is highest and the absorber is completely saturated with minimum loss. Similarly at the nodes of the electric field loss is minimised since, although the absorber is unsaturated, the field is a minimum. The net effect of the collision process is to reduce the saturation energy of the absorber by a factor of ~1.5 compared to single-pulse propagation. In the above mode-locked configuration two pulses counter-propagate around a three metre cavity perimeter (ie T_{cav} = 10 ns). The dye jets are separated by one-quarter of the cavity perimeter to maximise the gain recovery time between pulse transits and hence each pulse is initially incident upon a fully recovered gain medium. Consequently on arrival at the absorber jet the two pulses supply twice as much energy to saturate the medium compared to single-pulse operation and the *s* –parameter is increased by a factor of 2-3 depending on the absorber jet thickness.

It should be noted that enhancement of mode-locking by pulse collision is not a new idea as can be seen by referencing early work by Bradley [19] where improvement in mode-locking performance was observed by the positioning of absorber dye cells close to or in contact with the end mirror of linear flashlamp pumped cavities. The important difference

in the CPM case is that two different pulses collide with each other. Detailed analyses made by Stix et al [35] have suggested that the resultant absorption grating acts to synchronise the two pulses and mode-locking is further enhanced by energy transfer processes.

Table 1.2 Sources of frequency chirp in CPM dye laser

(E_p= pulse energy; E_{sat}= saturation energy of dye medium)

Source of frequency chirp	Sign of self-phase modulation induced	GVD compensation
Absorber saturation (λ>line centre)	Ep/Esat large: +SPM (blue shift at leading edge of pulse) Ep/Esat small: – SPM (across centre of pulse)	± + GVD
Gain saturation (λ>line centre)	Ep/Esat large: – SPM (red shift at leading edge of pulse) Ep/Esat small: + SPM (across centre of pulse)	± – GVD
Optical Kerr effect (in dye solvent)	+ SPM (across centre of pulse)	– GVD

1.6 DISPERSION COMPENSATION IN THE CPM LASER

By using the colliding pulse technique it was possible to readily generate pulses around 100fs. Because of the large spectral bandwidths associated with ultrashort pulses it was soon realised, however, that in order to optimise CPM laser performance it was vital to have some control of intracavity group velocity dispersion, Ø" [13]. Moreover, since peak intensities in the absorber would typically reach tens of gigawatts/cm^2 nonlinear self-phase-modulation effects due to the optical Kerr effect in the dye solvent and absorber saturation must be taken into consideration [36]. In Table 1.2 the sources of frequency chirp in the CPM dye laser are summarised together the sign of the resulting SPM. The mathematical formalism representing these sources of frequency chirp is dealt with in Section II. Obviously if the pulses have any degree of wavelength variation across their temporal profile then interaction with intracavity GVD will drastically effect the pulseshape, pulse duration and laser stability. Silvestri et al [37] performed a detailed investigation of the

contributing factors to the dispersion in the laser cavity and showed that the mirror GVD (typical values ~ $\pm 300 fs^2$) was the dominant source. Various optical systems have been proposed which can act to control and compensate the cavity GVD; these include Gires-Tournois interferometers [38,39], angle tuning of mirrors [40], and a sequence of Brewster-angled prisms [41,42]. The relative merits of each will be discussed in turn.

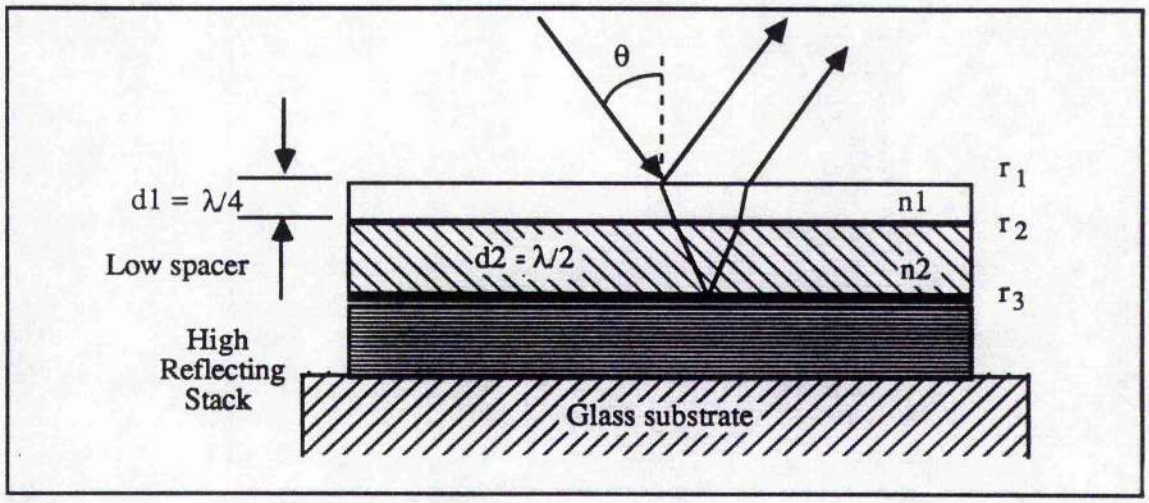

Figure 1.4 Schematic of a typical Gires-tournois structure.

1.6.1 GIRES-TOURNOIS INTERFEROMETERS

Figure 1.4 shows a shematical representation of a Gires-Tournois interferometer (GTI) structure. This cavity element consists of a highly reflecting surface (dielectric stack or metallic coating) and a spacer layer with usually a secondary protective cover layer on top thus generating a "half-silvered" etalon. The phase changes at each surface and their wavelength dependence allow the GTI to introduce varying degrees of GVD as a function of spacer layer thickness and incident angle. It is often assumed that the dispersive contribution, Ø" of this structure can be calculated using basic formulae in which case [38]:

$$\text{Ø}'' = \frac{d^2\text{Ø}}{dw^2} = \frac{2T_2^2(1-r^2)r \sin wT_2}{(1+r^2-2r\cos wT_2)^2} \qquad \text{–eq(1.8)}$$

where the system is treated as a single layer of reflectivity, r in contact with a single fully reflecting layer with a spacer layer of physical thickness d_1 (yielding a pathlength difference $T_2=2d_2n\cos\theta/c$). It is more realistic, however, to extend the treatment to accommodate the top cover layer to yield the complex reflection coefficient [43]:

$$r = \frac{r_1 + r_2 e^{-iT_1} + r_3 e^{-i(T_1+T_2)} + r_1r_2r_3 e^{-iT_2}}{1 + r_1r_2 e^{-iT_1} + r_1r_3 e^{-i(T_1+T_2)} + r_2r_3 e^{-iT_2}} \quad \text{–eq(1.9)}$$

Representing this as $\mathbf{r} = r \exp(i\emptyset)$ the phase argument can be extracted to give:

$$\emptyset = \eta - \xi$$

with:
$$\tan \xi = \frac{r_2 \sin T_1 + r_3 \sin(T_1+T_2) + r_1r_2r_3 \sin T_2}{r_1 + r_2 \cos T_1 + r_3 \cos(T_1+T_2) + r_1r_2r_3 \cos T_2}$$

and
$$\tan \eta = \frac{r_1r_2 \sin T_1 + r_1r_3 \sin(T_1+T_2) + r_2r_3 \sin T_2}{1 + r_1r_2 \cos T_1 + r_1r_3 \cos(T_1+T_2) + r_2r_3 \cos T_2} \quad \text{–eq(1.10).}$$

Double differentiation of $\emptyset$ with respect to angular frequency gives the dispersion of the system. Unfortunately, for the structure shown in figure 1.4 the dispersion has a strong wavelength dependence and it can change quite dramatically across the bandwidth of an ultrashort pulse [44]. Figure 1.5 shows this variation for the typical wavelengths encountered in the DODCI / Rh6G passively mode-locked laser. Moreover, the above calculation takes no acount of the dispersive contribution from the high reflectivity multi-layer stack, if present.

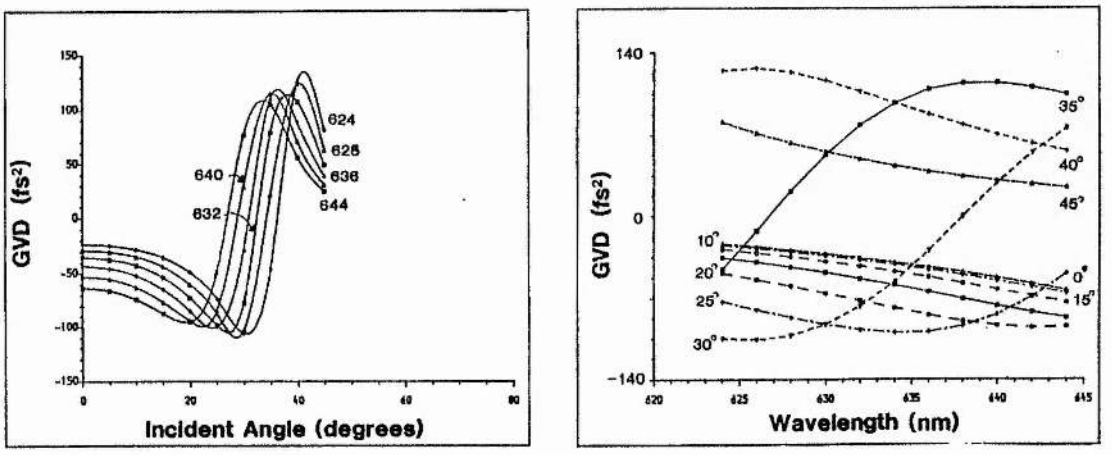

Figure 1.5 Variation in GVD contribution by a GTI component as a function of angle and wavelength.

The basic requirements for control of GVD by an intracavity optical component are; (i) low insertion loss, (ii) the ability to vary its linear dispersion contribution from negative to positive values, and (iii) equal dispersion contribution across the spectral bandwidth of the pulse. Thin film interferometers that have previously been reported [39,45] have had a structure similar to that shown in figure 1.4 where a spacer layer is deposited on top of a high reflectivity stack. Examination of the GVD contribution of the GTI across a 20 nm bandwidth shows that the structure is far from ideal as a means for controlling linear dispersion because large amounts of cubic and higher-order terms appear between the turning points of the GVD curve. It can only provide linear dispersion within a rather restricted angular regime and for this reason use of GTI's for GVD compensation is fairly limited. Experimental studies of GTI's will be discussed in Chapter 9.

1.6.2 ANGLE TUNING OF MIRRORS

Once the dispersive contribution of cavity mirrors was recognised it is possible by careful mirror design and angle tuning to effect dispersion control and thus optimise laser performance. Practical difficulties arise as cavity realignment is required each time the dispersion is changed and this can be tedious in day-to-day operation. Nevertheless Yamashita et al [40] have demonstrated 45 fs pulses with a CPM laser employing no other cavity components apart from their specially designed mirrors. Similarly French has achieved 50 fs using the cavity depicted in figure 1.3 and angle tuning the apex mirrors. This technique makes use of the property that a mirror designed for reflectivity over a certain bandwidth and at a particular angle will introduce negative GVD if operated at angles larger than its specification and positive GVD for smaller angles. The calculation of the mirror dispersive contribution requires complex matrix analysis of the multilayer structure and although the lasing system is simple it is far from flexible.

1.6.3 DISPERSION COMPENSATION USING PRISM PAIRS

The use of prisms for dispersion control inside the mode-locked laser was first reported as early as 1983 by Diels and Dietel [46] who employed a single prism and collimating mirror in their cavity configuration. They argued that such a system allowed control of the

positive dispersion in the cavity. Soon after coworkers Fork and Gordon demonstrated that the cavity system had additional negative GVD due to angular refraction [47]. The proposition that angular refraction at a glass interface gave negative GVD was recognised also by Silvestri et al [48] but use of prism pairs was first proposed and demonstrated by Fork et al in 1984 [41,42]. Their configuration is shown in figure 1.6 where each prism is

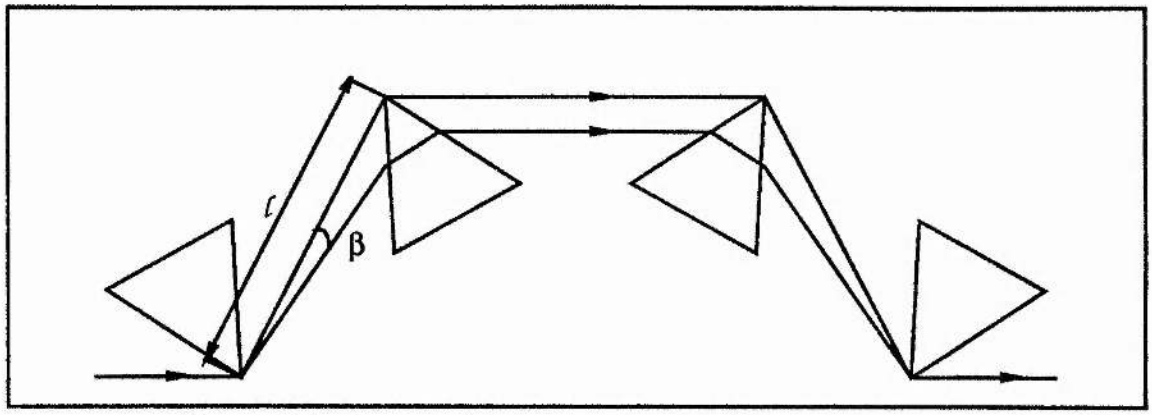

Figure 1.6 Four prism sequence used to introduce negative GVD

operated at minimum deviation and apex angles are set so that incident angles are at Brewster's angle to minimise loss. The obvious advantage of this system is that the incident and transmitted beams are colinear and thus it is ideal for introducing negative GVD into existing laser systems. The dispersion contribution of the prism system ignoring any additional material path length is given by [41]:

$$\varnothing'' = \frac{2\lambda^3 \ell}{\pi c^2}\left\{\left[\frac{d^2n}{d\lambda^2} + \left(2n - \frac{1}{n^3}\right)\left(\frac{dn}{d\lambda}\right)^2\right]\sin\beta - 2\left(\frac{dn}{d\lambda}\right)^2\cos\beta\right\} \quad \text{-eq(1.11)}$$

Providing that $d^2n/d\lambda^2$ is not excessively large compared with $(dn/d\lambda)^2$ and since β is of the same order as the angular deviation of the incident ray bundle (therefore $\sin\beta << \cos\beta$), the prism arrangement will give negative dispersion. This negative GVD is offset in practice by the positive GVD contribution of the glass material through which the beam must traverse and consequently the system can provide positive or negative GVD depending on the material path length through the prisms. Taking the lower transit path to lie at twice the beam diameter (in this case $\ell \sin\beta \approx 2$mm) below the prism apex and incorporating typical values at 630 nm for quartz the various derivatives yield the dispersive relation:

$$\emptyset'' = 457.8 - 3.31\ \ell\ \text{fs}^2 \qquad \text{-eq(1.12)}$$

where ℓ is measured in mm. The above equation implies that setting a prism separation of 250 mm will give a negative GVD sufficient to compensate for 6.6 mm of glass. The inherently low insertion loss and the dispersive tunability of this prism sequence – dispersion being controlled by the simple translation of a single prism without effecting cavity alignment – makes this configuration ideal for inclusion in both ring and linear laser cavities. Also, the higher order dispersion contributions are relatively small and thus the dispersive contribution is mainly linear across large bandwidths.

1.7 Summary

The pertinent theory and historical background of the CPM dye laser has been presented. For control of cavity GVD the prism sequence has shown to be far superior to Gires-Tournois interferometers and mirror angle tuning techniques. Indeed using such a system Valdmanis and Fork have achieved 27 fs duration in a six mirror CPM cavity [42]. This purpose of this chapter was intended to be an introduction to the CPM laser which was utilised as a ultrashort pulse source in the development of streak camera and SHG autocorrelation pulse measurement techniques which are discussed in the following sections. In Chapter 9 I will return to the above discussion within the context of the parameterisation and optimisation of the experimental CPM laser.

REFERENCES

1 G.H.C.New, Rep. Prog. Phys. **46** 877 (1983).

2 P.W.Smith, M.A.Duguay and E.P.Ippen, Prog. Quant. Electron. **3** 107 (1974).

3 A.Yariv in *Optical Electronics* : publ. Holt, Rinehart and Winston - New York (1985).

4 A.E.Siegman in *Lasers* : publ. University Science Book - California (1986).

5 B.H.Soffer and J.W.Linn, J.Appl. Phys. **39** 5859 (1968).

6 W.H.Glen, M.J.Breiza and A.J.Demaria, Appl. Phys. Lett. **12** 54 (1968).

7 M.C.Adams, D.J.Bradley, W.Sibbett and J.R.Taylor, Phil. Trans. R. Soc. Lond. **A298** 217 (1980).

[8] M.Nakazawa, H.Kubota and K.Kurokawa in *Ultrafast Phenomena VI* : Springer series in Chem. Phys **48** 24 (1988).

[9] P.N.Kean, X.Zhu, D.W.Crust, R.S.Grant, N.Langford and W.Sibbett, Opt. Lett. **14** 39 (1989).

[10] H.A.Haus, J.Appl. Phys. **46** 3049 (1975).

[11] H.A.Haus, IEEE J. Quant. Electron. **QE-11** 736 (1976).

[12] G.H.C.New, IEEE J. Quant. Electron. **QE-10** 115 (1974).

[13] R.S.Miranda, G.R.Jacobovitz, C.H.Brito Cruz and A.F.Sarpara, Opt. Lett. **11** 224 (1986).

[14] W.Rudolph and B.Wilhelmi, Appl. Phys. B **35** 37 (1984).

[15] W.Schmidt and F.P.Schafer, Phys. Lett. **26A** 558 (1974).

[16] O.G.Peterson, S.A.Tuccio and B.B.Snavely, Appl. Phys. Lett. **17** 245 (1970).

[17] R.L.Fork, BI.Greene and C.V.Shank, Appl. Phys. Lett. **38** 671 (1981).

[18] P.M.W.French, Phd thesis - Imperial College, London (1986).

[19] D.J.Bradley, A.J.F.Durrant, F.O'Neill and B.Sutherland, Phys. Lett. **30A** 535 (1969).

[20] E.G.Arthurs, D.J.Bradley and A.G.Roddie, Appl. Phys. Lett. **19** 480 (1971).

[21] E.G.Arthurs, D.J.Bradley and A.G.Roddie, Appl. Phys. Lett. **20** 125 (1972).

[22] E.G.Arthurs, D.J.Bradley and A.G.Roddie, Appl. Phys. Lett. **22** 88 (1973).

[23] E.Lill, S.Scheider and F.Dorr, Opt. Comm. **20** 223 (1977).

[24] R.Wyatt, Opt. Comm. **38** 64 (1980).

[25] J.C.Mialocq and P.Goujou, Opt. Comm. **24** 255 (1978).

[26] W.Sibbett and J.R.Taylor, Opt. Comm. **43** 50 (1982).

[27] E.P.Ippen, C.V.Shank and A.Dienes, Appl. Phys. Lett. **21** 348 (1972).

[28] F.O'Neill, Opt. Comm. **6** 360 (1972).

[29] J.P.Letouzey and S.O.Sari, Appl. Phys. Lett. **23** 311 (1973).

[30] A.Scavennec and N.S.Nahman, IEEE J.Quant. Electron. **QE-10** 95 (1974).

[31] C.V.Shank and E.P.Ippen, Appl. Phys. Lett. **24** 373 (1974).

[32] C.V.Shank and E.P.Ippen, Appl. Phys. Lett. **26** 62 (1975).

[33] I.S.Ruddock and D.J.Bradley, Appl. Phys. Lett. **29** 296 (1976).

[34] J.C.Diels, E.Von Stryland and G.Benedict, Opt. Comm. **25** 93 (1978).

[35] M.S.Stix and E.P.Ippen, IEEE J.Quantum Electron. **QE-19** 520 (1983).

[36] O.E.Martinez, R.L.Fork and J.P.Gordon, Opt. Lett. **9** 156 (1984).

[37] S.de Silvestri, P.Laporta and O.Svelto, **QE-20** 533 (1984).

[38] P.M.W.French, G.F.Chen and W.Sibbett, Opt. Comm. **57** 263 (1986).

[39] J.Kuhl and J.Heppner, Appl. Phys. Lett. **47** 453 (1985).

[40] M.Yamashita, S.Kaga, K.Torizuka and T.Sato in *Ultrafast Phenomena VI* : Springer series in Chem. Phys. **48** 37 (1988).

[41] R.L.Fork, O.E.Martinez and J.P.Gordon, Opt. Lett. **9** 150 (1984).

[42] A.Valdmanis and R.L.Fork, IEEE J.Quant. Electron. **QE-22** 112 (1986).

[43] O.S.Heavens in *Optical properties of solid thin films* : Butterworths Scientific Publ. - London (1955).

[44] A.Finch, E.Williams and W.Sibbett, Tech. Dig. XVI Int. Quant. Electron. Conf. (IQEC'88) paper MP16 92 (1988).

[45] D.Kuhlke, T.Bonkhofer and D.Von Der Linde, Opt. Comm. **59** 208 (1986).

[46] W.Dietel, J.J.Fontaine and J.C.Diels, Opt. Lett. **8** 4 (1983).

[47] J.P.Gordon and R.L.Fork, Opt. Lett. **9** 153 (1984).

[48] S. de. Silvestri (Private communication).

SECTION I

LINEAR PULSE MEASUREMENT

– STREAK CAMERAS –

CHAPTER 2: STREAK CAMERA DESIGN, CONSTRUCTION AND OPERATION

2.0 INTRODUCTION

With the ready availability of subpicosecond, indeed femtosecond light pulses, there is a vital need for the development of linear monitoring instruments to accommodate the ultrashort optical pulse regime if such laser sources are to be fully understood and exploited. Photodiode technology employing III-V and II-VI semiconductors has now extended linear electronic diagnostics into the sub-10 picosecond region [1] – the measured results of the latter reference were in fact generated on the CPM laser discussed in this thesis. However, since there is as yet no commercially available oscilloscope with sufficient sampling speed or bandwidth to display the output from such devices, they are not useable directly as linear monitors of ultrashort events; relying more on the rather circuitous methods of Fourier harmonic analysis [1], electro-optical sampling [2] or cross-correlation techniques [3,4].

Ultrahigh speed cameras, on the other hand, based on the principles of electron optical image tubes, have consistently been at the forefront of linear optical pulse measurement applications. Recent years have seen the limiting temporal resolution, T_r of these cameras improve by over an order of magnitude to the present state of the art of < 300 fs [5]. They have been shown to offer high sensitivity and can provide temporal and spectral information over time windows of hundreds of picoseconds - as a consequence these instruments are the mainstay of the developing field of *ultrafast chronoscopy* [6].

In the following chapters the important design criteria of these streak tubes are described in respect of their modes of operation and the limitations on their performance. The final chapters of this section are devoted to the development of solid-state readout systems for these cameras (both an external format and an internal system incorporated within the tube envelope) and is referenced to a specific spaceborne laser ranging application.

2.1 IMAGE TUBE DESIGN AND OPERATION

2.1.1 CONSTRUCTION

There is a wide variety of picosecond image tube designs currently available but all operate on the same basic principle. Figure 2.1 illustrates the two modes of operation of these instruments namely that of streak mode and framing mode. Figure 2.1a demonstrates the operation of a streak camera which records ultrashort events in time and one spatial direction (along the length of the input slit), while figure 2.1b demonstrates the application of a framing camera [7] which can record one or more *snapshots* of very short duration events (~100ps) with two spatial dimensions.

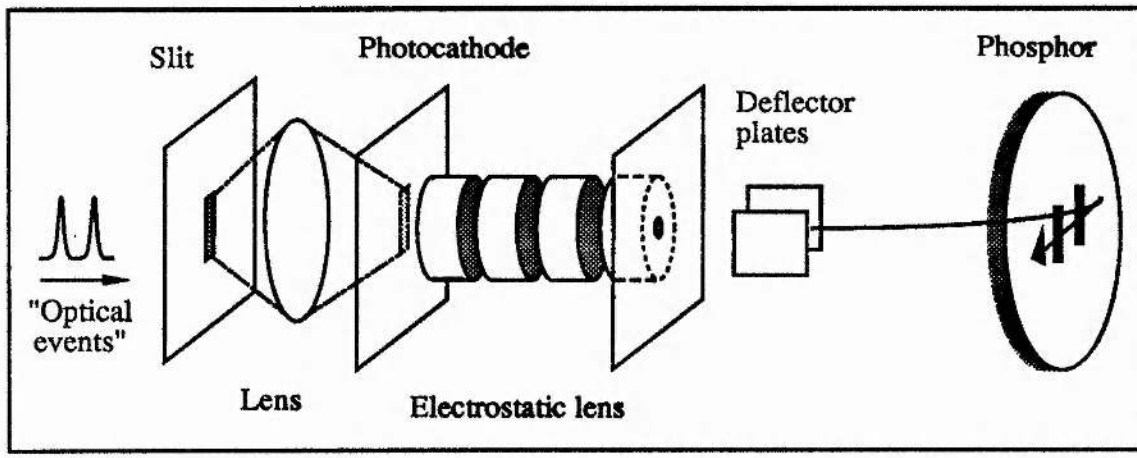

Figure 2.1a: Schematic of a Streak Camera

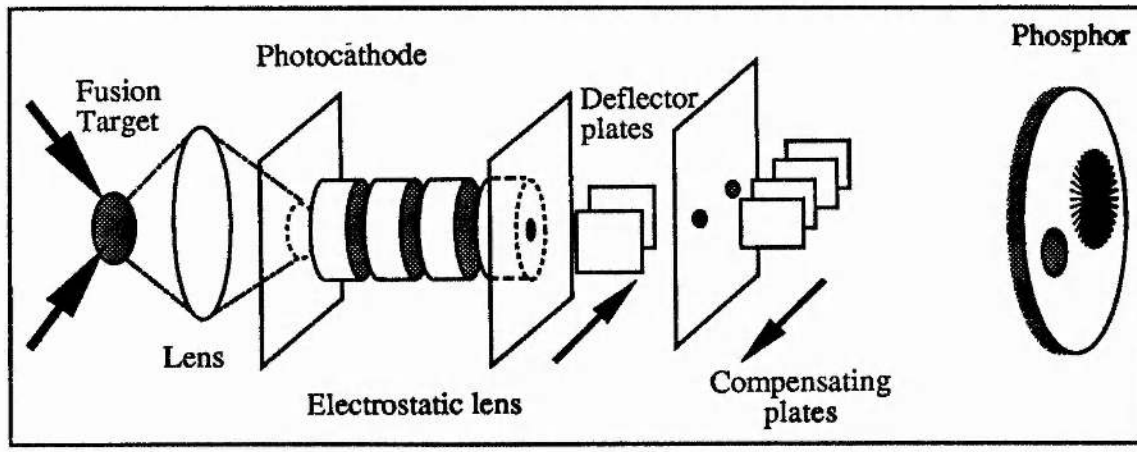

Figure 2.1b: Schematic of a Framing Camera

Both types of tube consist of a photocathode (with a spectral response tailored to the operating wavelengths of the mode-locked lasers or ultrashort events that are to be

analysed), a electrostatic lensing section, a deflection region in which deflector plates of differing design and number are enclosed, a drift region and finally an image recording section which sometimes includes a proximity focused microchannel plate (MCP) intensifier in front of a phosphor if high detection sensitivity is required. The outer tube envelope is constructed from glass or ceramic with Nilo flanges sectioning the different tube regions. High vacuum is imperative for avoiding internal discharge, so-called multipactor discharge [8] during dynamic operation and maintenance of photocathode life.

2.1.2 DYNAMIC OPERATION OF IMAGE TUBES

The mechanism whereby a streak camera works is basically quite straightforward (complicated theoretical analyses are, however, necessary to describe the details of the streaking process). Light incident at an input slit is focused onto the photocathode causing the liberation of photoelectrons which are accelerated down the tube. The electrostatic lens arrangement modulates the electron momenta such that all electron trajectories see an equal time of flight (an analogy with Fermat's Principle which will be discussed later) and are imaged under static operation at the phosphor screen where the image information is converted back to optical data. The electron-optical image tube is designed to have good lensing characteristics in static mode with high spatial resolution and minimal distortion of image information.

In streak mode as the electrons pass through the deflector plates a voltage ramp is applied which deflects or streaks the electrons along a direction perpendicular to the input slit length. If we imagine a short optical event, ie) an optical pulse incident on the camera, then this will generate at the photocathode a distribution of electrons whose number density along the axis of the tube is linearly proportional to the intensity distribution across the optical pulse. On streaking at the deflection plates the electron distribution is mapped out spatially on the phosphor, in other words one spatial axis of the image tube has been converted into a temporal axis. The light emanating from the phosphor will be linearly proportional to the incident electron number density and consequently recording the intensity of light across the phosphor as a function of distance thus provides a linear record

of the input light pulse intensity distribution. Spatial information along the length of the slit is maintained thereby allowing the measurement of one dimensional events (eg. the spectral fluorescence decay from a dye molecule after excitation from an ultrashort light pulse [9]).

For framing cameras a second set (or sets) of deflector plates is present in the deflection region to which the same voltage ramp is applied but of the opposite polarity to that generated on the the first pair of plates. This acts to compensate for the streaking effect from the primary deflectors and effectively freeze the image presented at the photocathode. This provides two-dimensional information with a frame time determined by ramp speeds and aperture sizes in front of the secondary compensating plates. The design and operation of framing cameras is offering wide interest in the monitoring of events such as the examination of deuterium-tritium target spheres during laser induced fusion [10], but a full treatment of this area of research is beyond the scope of this section which is devoted purely to the use of streak cameras.

2.1.3 SINGLE-SHOT OPERATION

As mentioned above the streak image is produced by a ramp voltage applied to the deflection plates. When a single ramp voltage is applied the tube is said to be operating in single-shot mode whereby single events are temporally isolated on the phosphor. Employing intensifier stages either internally or externally allows discrimination of light pulses of energies in the picojoule regime. Such operation ensures that the tube offers its optimum temporal resolution as current densities inside the tube are limited (see §2.2). The voltage ramps that are required to be applied are of several kilovolts switched in a few nanoseconds thereby generating near light speed writing speeds at the phosphor. For picosecond or better temporal resolutions the time window at the phophor screen can be less than 200ps and consequently any jitter between deflection ramp and streaked event will cause the streaked image position to vary from shot-to-shot. Avoidance of jitter precludes many ramp generating sources, avalanche transistor chains [11] (jitter ~ 100ps) or optical switching of GaAs Auston switches [12] holding off D.C. kilovolt potentials (jitter as low

as ±2ps [13]) being the most suitable. The latter voltage ramp source has the disadvantage that it requires high energy optical pulses of 10-100 μJ for effective low jitter switching.

2.1.4 SYNCHROSCAN OPERATION

Although single-shot streak operation has many applications in the field of pulsed mode-locked lasers diagnostics and associated picosecond pulsed experiments, with the advent of CW mode-locked laser sources and their application to time-domain spectroscopy, this mode of streaking is not the most appropriate. Thus to exploit the repetitive nature of the pulse trains obtained from CW mode-locked sources an alternative streak mode was developed [14] which was termed *synchroscan* streak operation. In this mode the single fast voltage ramp is replaced by a repetitive linear deflection waveform. Usually in practice this drive waveform is a high frequency (eg 200 MHz) sinusoid where advantage is taken of the fact that the central sixth of one period of the sinusoid is linear to within 5% (see figure 2.2).

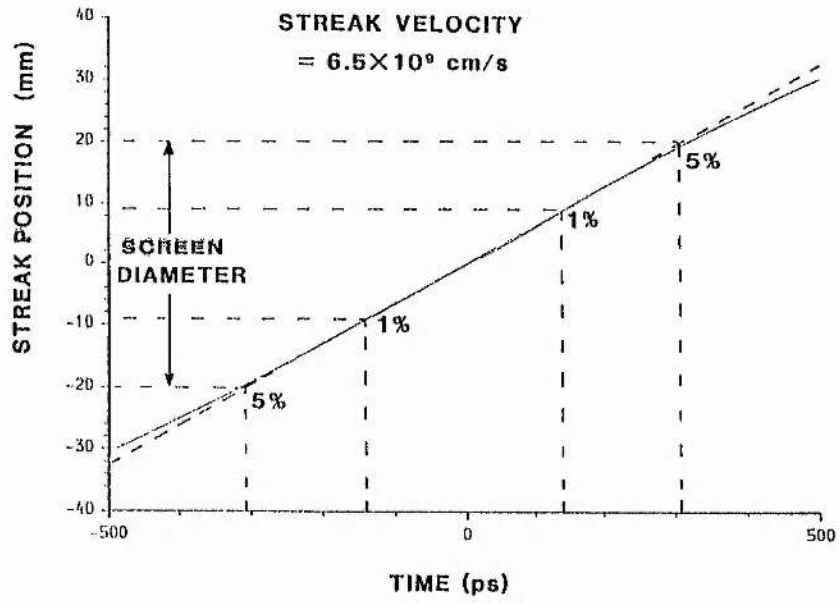

Figure 2.2 Linearity curve of a 200 MHz sinusoid

The frequency of the waveform is chosen to be identical or an exact harmonic of that of the repetitive laser initiated photoluminescent event being monitored (see figure 2.3). By this means a large number of streak images are overwritten on the phosphor screen providing effective signal gain.

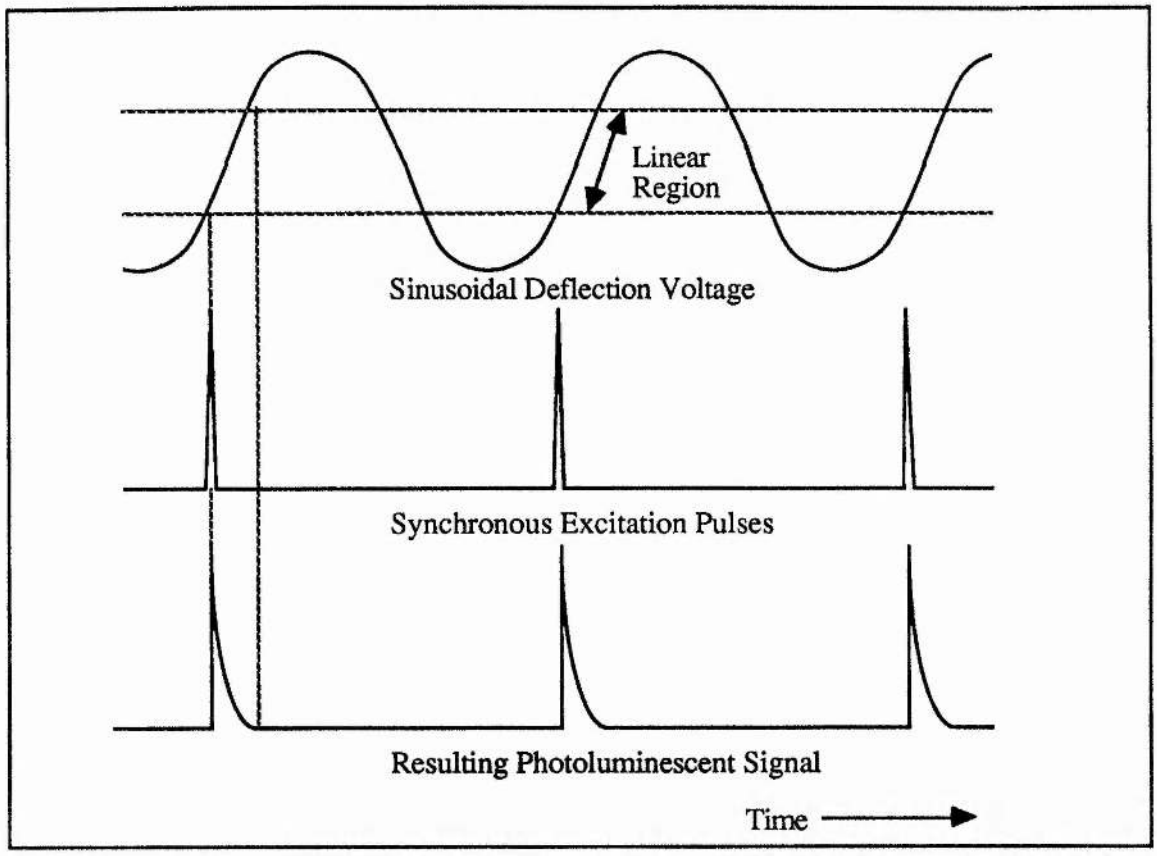

Figure 2.3 Synchroscan operation

Synchroscan operation has several immediate advantages including: (i) compatibility with repetitive pulse sources such as all CW mode-locked lasers, (ii) inherent signal gain and thus no requirement, in most cases, for image intensification, (iii) signal averaging and as a consequence large signal-to-noise, high sensitivity and dynamic range, (iv) low photocurrent values and therefore optimal camera resolution, and (v) effective realtime monitoring of repetitive events which are conveniently readout by one- or two-dimensional optical multichannel analysers which can be either photoelectronic or photoconductive based.

The prerequisite of low jitter between the sinusoidal deflection signal and the optical events being monitored is further compounded by the need for low jitter in the pulse train itself. However with recently enhanced low phase noise CW pulse sources operating at various wavelengths picosecond resolution is now readily attainable. Several methods have been developed for synchroscan deflection voltage generation, two of which are discussed and experimentally compared in Chapters 3 and 4.

2.2 STREAK TUBES

2.2.1 PERFORMANCE CRITERIA AND DEFINITIONS

The criteria used to describe the performance of streak cameras are based upon a number of specific parameters. The property most often measured is the *temporal impulse response*, $\mathcal{T}_r$ ie) the temporal resolution (FWHM) obtained at the phosphor of the streak tube when an infinitely short optical pulse is incident. Physically this represents the minimum duration of temporal event (FWHM) that could be resolved at the phosphor. One basic tube property that the temporal resolution depends upon is the *static resolution* of the camera (often quoted in line pairs per millimetre –lp/mm) which effectively defines the minimium spatial (and therefore temporal) extent of the streak, Δs that can be displayed on the phosphor. Conversely the *dynamic spatial resolution* is a measure of the detail that can be resolved perpendicular to the streak direction ie) the amount of resolvable spectral information, say, that can be displayed during streak operation. Parameters which define the degradation of imaging or temporal performance include *spatial distortion* which defines the variation in magnification (image to object height ratio) as a function of position in the image and *temporal distortion* which describes the variation of the mean time of flight of the electron pulse from the photocathode to the phosphor as a function of object position. This latter property manifests itself most clearly with a so-called dynamic slit curvature in the streaked image (see figure 2.4).

Streak direction

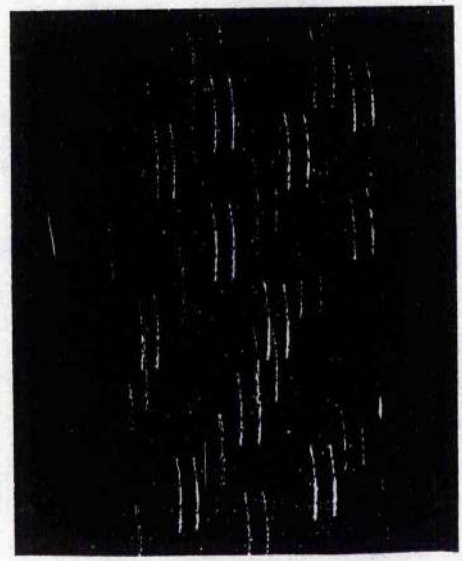

Figure 2.4 Example of dynamic slit curvature

An important performance criterion for a streak tube defining its usefulness is its *dynamic range* which describes the useful input intensity range before deterioration in temporal resolution becomes too large. There are several definitions, a reasonable one being the ratio of the peak pulse intensity for which the measured temporal width is 20% greater than the actual width of the incident pulse to background or the noise intensity level of the recording medium. One origin of this limitation to temporal performance is the space charge effect [15] whereby the close proximity of electrons as they travel in the streak tube yield appreciable Coulomb repulsive interactions which tend to spatially broaden the charge packet and thus temporally broaden the streaked image. A second cause has been ascribed to the degradation of spatial resolution due to microlensing effects occurring at the photocathode [16]. During intense irradiation the large localised photocurrent drawn from the photocathode leads to a surface potential peturbation and a defocussing effect of the tube elctrostatic lens and subsequent loss in temporal resolution. This effect can be offset by the provision of adequate intensification, thereby keeping photocurrents low, and the manufacture of low resistivity (10 Ω/square) photocathodes so that any voltage perturbations are minimised.

2.2.2 FUNDAMENTAL LIMITATIONS

For operation in the visible spectrum with pulses containing central optical carriers of ~10^3 THz the absolute fundamental limit on τ_r is around 10 fs [17] and is dictated by the ultimate photocathode response time. Although streak camera designs presently exist with calculated resolutions of less than 100 fs [18], measured performances are significantly poorer than this ultimate figure. There are several valid physical and practical reasons why this is so but the main factor governing achievable resolution is the nature of photoelectron emission from a photocathode. A minimum energy, the work function, ϕ of the photocathode material, is required to liberate electrons from the photocathode into the external vacuum. Consequently for incident light with photon energy, $h\nu < \phi$ no photoelectrons can be emitted leading to a long-wavelength cutoff, λ_c given by: $\lambda_c = hc/\phi$. For $h\nu > \phi$ the emitted electrons are not monoenergetic due to the electron-hole generation

mechanism and scattering processes in the lattice [19]. This distribution of initial energies between zero and $h\nu - \phi$ naturally gives a distribution of times of flight for the electrons from photocathode to phosphor independent to the incident optical pulse, this is generally referred to as the transit-time dispersion. It is this photoelectron energy distribution (typically ~ 600 meV for multi-alkali photocathodes) which in practice will define the fundamental limiting temporal resolution of all streak tubes.

This problem can be reduced by increasing the electric field close to the photocathode to a high value (>20kV cm^{-1}) thereby accelerating the photoelectrons to high energies over a very short period and making insignificant their initial energies [20]. For a cathode field E_{pc} the transit time spread, Δt_d of an image tube is commonly expressed as [20]:

$$\Delta t_d = \frac{m}{e}\frac{\Delta u}{E_{pc}} \qquad \text{–eq(2.1)}$$

where m and e are the electronic mass and charge respectively and Δu is the half width of the initial electron velocity distribution. This expression although valid for tubes exhibiting resolutions of several picoseconds is not an adequate description for $\tau_r < 1ps$ [21]. In practical systems a large value of E_{pc} is achieved by the insertion of a fine mesh in close proximity (~1-2 mm) to the cathode and which is held at a high positive voltage with respect to it [20]. The maximum value of this electric field near the photocathode is usually limited by the maximum voltage the cathode or mesh surfaces can hold off before field emission occurs and is dependent on surface quality. The improvement in temporal performance is offset slightly by the obvious loss in signal electrons (~50%) and the reduction in image quality due to microlensing by the mesh apertures.

A second factor which ultimately limits the achievable temporal resolution is the finite time taken for the electrons to leave the photocathode. This delay will depend on the initial electron energy, the cathode thickness, composition and structure. There is no firm evidence for the extent of a distribution in emission times and opinions differ as to the importance and degree of this effect, but an analysis by Bulygin [22] by modelling a typical S1 type silver–ceasium-oxygen cathode put a limiting figure for τ_r at ~50 fs due to emission time distribution. Experimental evidence [20,31] showing the dependency of τ_r on

cathode field E_{pc} indicates that emission time distributions limit performance only very marginally and to much less than a picosecond.

Naturally the imaging quality of the tube has important effects on dynamic performance; all spatial aberrations of the electrostatic lensing system (spherical aberration, astigmatism, microlensing, coma, etc) translate into temporal aberrations during streaking. For a given resolution the minimum spatial width, Δs and streak speed, v_s define the optimum temporal resolution achievable, often denoted the *technical limiting resolution,* Δt_s and is given by:

$$\Delta t_s = \frac{\Delta s}{v_s} \qquad \text{–eq(2.2)}$$

Consequently to a good approximation for picosecond responses the overall *instrumental temporal resolution,* $\mathcal{T}_r$ is given by:

$$\mathcal{T}_r = \sqrt{(\Delta t_s)^2 + (\Delta t_d)^2 + (\Delta t_p)^2} \qquad \text{–eq(2.3)}$$

where Δt_p is the optical pulse duration.

Finally dynamic operation in itself can have an effect on image quality. The simple effect of fringe fields near the edges of deflectors can limit the available time windows on the screen and radio frequency (RF) coupling into electron optics and mesh voltages can have a very considerable effects on available temporal resolution as will be shown later.

2.3 Tube Designs – A Brief Historical Overview

A comprehensive historical review of streak camera design and comparative performance has been made by Jones [21]. The transformation of an optical image into an electron analogue and then back into light at a different wavelength was first proposed in 1930 by Farnsworth [23] and later Holst [24]. In 1949 Courtney-Pratt achieved nanosecond temporal resolutions by externally scanning the electron beam of an image converter tube [25]. Indeed initial streak tubes were simply modified image tubes and as a consequence their temporal performance was severely limited. The first purpose designed streak tubes were developed by Butslov et al and designated the name PIM-3 and PIM-4 [26]. In the early 60's Walters et al developed a similar design to the PIM series which was later manufactured by EEV and called the P856 [27]. These tubes had limiting temporal

resolutions of approximately 20-50 ps due to the low value of E_{pc} the photocathode field (~600 Vcm^{-1}). A radical breakthrough was achieved when the P856 was modified in 1971 to include a fine mesh close to the photocathode and held at a high positive voltage so yielding the P855 [20]. The reduction of transit time spread by increasing the value of E_{pc} to 3.3 kV cm^{-1} saw τ_T reduced initially to 6.3 ps [20] and then 4 ps [28] after further modifications, enhancements of deflection electronics and an increase in mesh voltage. At the same time by applying 20ns high voltage pulses to the shutter grid of an RCA streak tube Schelev et al obtained 10 ps temporal resolutions [29]. Minor redesign of P855 eventually resulted in the first of the Photochron series image tubes (Photochron I) for which a demonstrated temporal resolution of ~2 ps was reported [30]. The dynamic spatial resolutions of all these tubes were relatively poor at a few lp mm^{-1}.

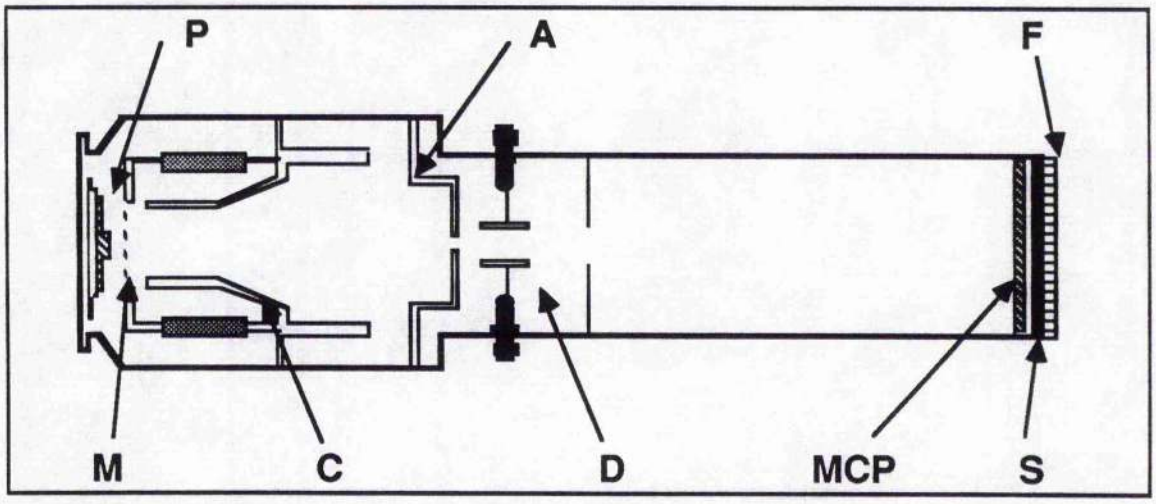

Figure 2.5: Schematic of the Photochron IIA streak tube: P = Photocathode, M = Mesh, A = Anode, C = Cone, D = Deflectors, MCP = Microchannel Plate, F = Fibre-optic faceplate, S = Phosphor Screen.

In 1974 the Photochron II image tube (shown schematically in figure 2.5) was introduced with redesigned electron optics to allow a reduced cathode – mesh spacing (0.5 mm) and weakened mesh-cone electron lens [31]. Significant improvement in static spatial resolution was seen (attaining 18 lp mm^{-1} at the phosphor screen) and dynamic performance was correspondingly enhanced to achieve measured single-shot temporal resolutions for the first time of less than 1ps [32], results being limited by deflection systems rather than by the tube.

The Photochron I, II have been widely used as laboratory diagnostics manufactured commercially by Instrument Technology Ltd (ITL) and the English Electric Valve company (EEV). The Photochron II is still in current use in streak camera systems built by Hadlands Photonics and has proved a highly successful design. Other streak tubes have also had success; there are some good designs manufactured by other workers (such as Hamamatsu) but detailed discussion of these designs is outwith the scope of this thesis which is primarily concerned with the optimisation of Photochron streak tube designs.

All of the above designs evolved by primarily empirical processes, adaptations of ordinary image tubes to allow streaking and then several modifications to improve performance as the relevant limiting factors to temporal resolution became better understood. The modifications were for the most part decided upon by optical analogues, intuition and 'demountable' experimental studies. It would be true to say that the first streak tube to be designed from basic principles was the Emichron I (Jones, Sibbett, Bradley - 1975 [21]) followed by the Photochron III [21] and the Photochron IV (Baggs, Niu and Sibbett [33]) which is shown in figure 2.6. The Photochron III and IV, which were designed extensively with the aid of well-established computer program suites, were radically different in their lensing system from any of their forerunners. Notable achievements made with the optimised Photochron IV design include a single-shot resolution of 0.8ps [34,14] and 0.9ps for synchroscan operation (see Chapter 4).

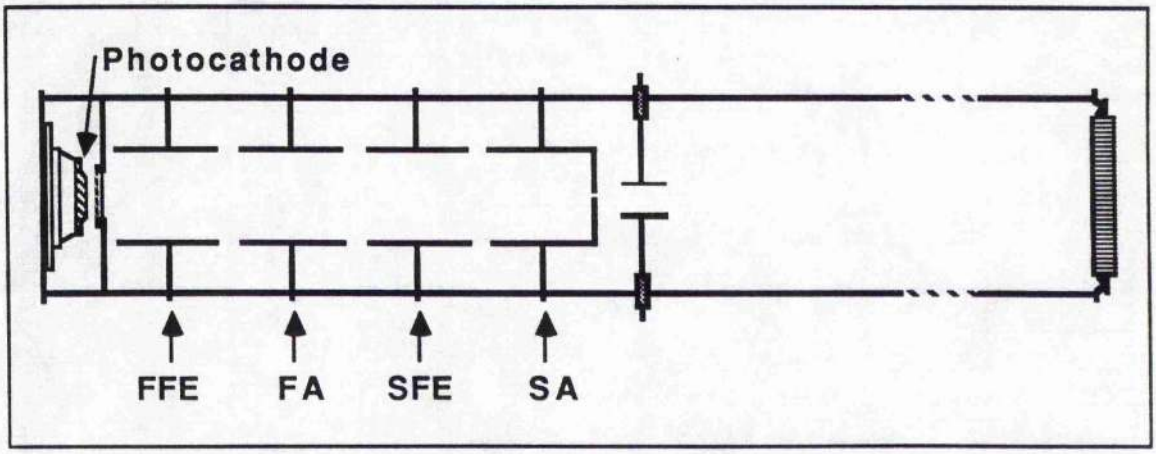

Figure 2.6 Schematic of Photochron IV streak tube: FFE = First focus electrode, FA = First anode, SFE = Second focus electrode, SA = Second anode.

2.4 COMPUTER AIDED DESIGN OF STREAK CAMERAS

The constantly increasing speeds available in computer technology has revolutionised the design of image tubes and the modelling of processes that occur within them [35]. As a consequence the remainder of this chapter is devoted to a brief outline of the techniques employed in generating new streak tube designs.

In order to design and develop any electrostatically focused imaging system, a complete knowledge of the potential distribution within the electrostatic lens is required so that its imaging characteristics can be determined. By applying standard numerical techniques and the use of a fast digital computer a program was developed at Imperial College to solve Laplace's equation for a given set of electron lenses [21,34,36]. This program, initially Fortran based and run on a VAX mainframe, was rewritten at St. Andrews by Dr. Killean to be operated on a Cromemco Microprocessor, the language environment being changed to Language C for more efficient coding. The result is a very useful and powerful development tool which not only can be utilised in the design of new streak camera systems, but also lends itself to a more thorough understanding of electron optics.

The following is a brief introduction to the mathematical techniques employed to solve Laplace's equation. A useful mathematical analogue is derived to show the equivalent optical lens system of a streak tube and finally the numerical techniques used to map electron trajectories through the camera are discussed. The Photochron II and IV streak tubes have been modelled with this program and the results are presented to show their static imaging properties.

2.4.1 SOLUTION OF LAPLACE'S EQUATION

A streak camera lensing system has rotational symmetry about one axis (defined as the z-axis) and thus the Laplace equation defining the electrostatic potential, $\phi(r,z)$ can be represented in cylindrical polar form and will be independent of azimuthal angle. Thus the equation whose solution is required becomes:

$$\frac{\delta^2\phi}{\delta r^2}+\frac{1}{r}\frac{\delta\phi}{\delta r}+\frac{\delta^2\phi}{\delta z^2}=0 \qquad \text{–eq(2.4)}$$

Analytical solutions of electrostatic lensing systems exist only for the most trivial of electrode configurations and, since the streak camera usually has a complex lens arrangement, a numerical technique of solution must be employed in order to solve equation 2.4. One such numerical technique, which is basic but extremely powerful, involves the application of finite difference equations and an iterative process of solution [37].

Initially the streak camera is represented two-dimensionally as shown in figure 2.7 and a grid or mesh superimposed over the region. The electrode structure can then be modelled by supplying the computer with potentials for grid points located at the electrodes, such points are defined as constant throughout the subsequent iterations. The potentials of the grid points on the boundary of the mesh must be defined and to do this it is assumed that the streak camera tube lies inside an earthed conducting cylinder.

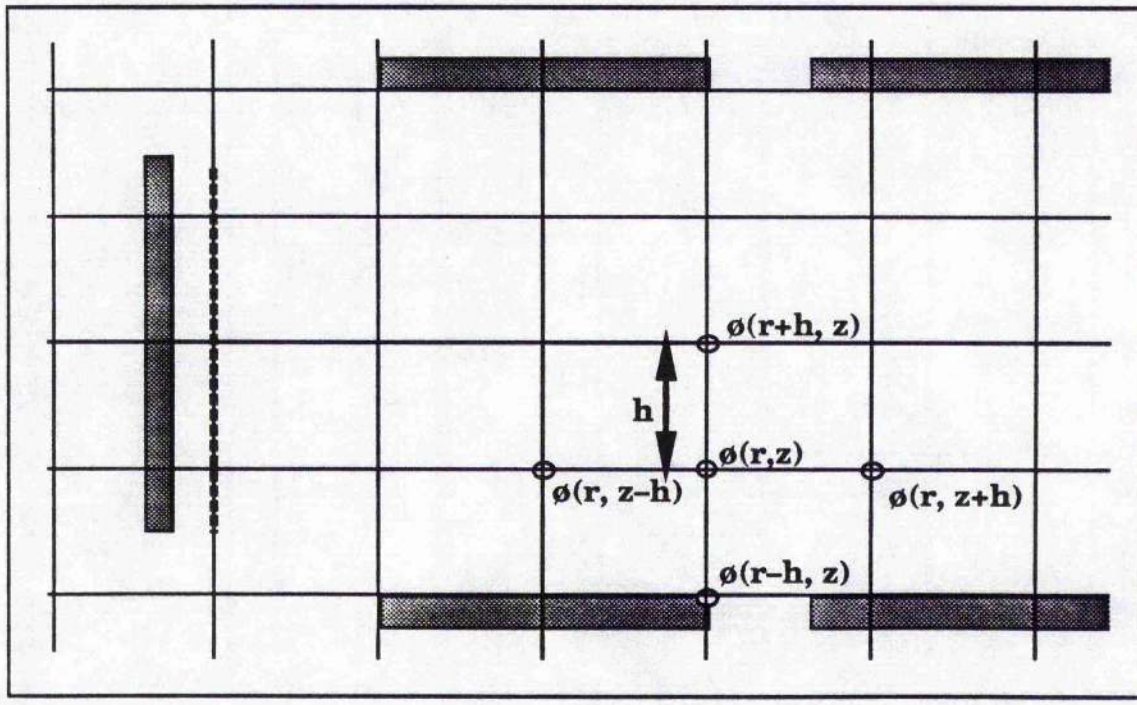

Figure 2.7: Notation of points on grid overlay

To set up the difference equations the potential at a grid point is represented as a Taylor expansion. Referring to figure 2.7 this gives:

$$\phi(r+h,z) = \phi(r,z) + \left[\frac{\partial\phi}{\partial r}\right] h + \left[\frac{\partial^2\phi}{\partial r^2}\right] \frac{h^2}{2!} + \ldots \qquad \text{–eq(2.5)}$$

Applying equation 2.5 to the grid points indicated on figure 2.7 yields five Taylor expansions which, by adding or subtracting relevant terms and ignoring differentials of higher than second order gives expressions for the differential operators in equation 2.4 solely in terms of the potentials at the various grid points. Substituting these equations into the Laplace equation we obtain the following five point difference equation:

$$\phi(r,z) = \frac{1}{4}[\phi(r,z+1) + \phi(r,z-1) + \phi(r+1,z) + \phi(r-1,z)] + \frac{1}{8r}[\phi(r+1,z) - \phi(r-1,z)] \qquad \text{–eq(2.6).}$$

This equation is not valid for points that lie on the z-axis ie for r=0. Along this axis one must revert to a cartesian representation and use the properties of rotational symmetry to collect terms. The difference equation in this case is:

$$\phi(r,z) = \frac{1}{6}[\phi(r,z+1) + \phi(r,z-1) + 4\,\phi(r+1,z)] \qquad \text{–eq(2.7).}$$

A further calculation is required specifically for streak camera applications due to the presence of regions of differing dielectric constant, ε within the streak tube, ie glass or ceramic envelopes surrounding the metal electrodes and regions of vacuum inside the camera itself. Using basic electromagnetic boundary conditions obtained from the Maxwell Equations [38], the following five point difference equation was derived for a grid point lying on the interface between two media of relative permittivity ε_1 and ε_2:

$$\phi(r,z) = \left[\frac{\varepsilon_1\,[1 - \frac{1}{2r}]\,\phi(r-1,z) + \varepsilon_2\,[1 + \frac{1}{2r}]\,\phi(r+1,z)}{2\,[\varepsilon_1\,[1 - \frac{1}{2r}] + \varepsilon_2\,[1 + \frac{1}{2r}]\,]}\right] + \frac{1}{4}[\phi(r,z+1) + \phi(r,z-1)\,] \qquad \text{–eq(2.8)}$$

This expression was an improvement to the previous difference equations as the values of the dielectric constant were found to have major effects on the potential distributions in the streak tubes.

The above equations relate the potential of a free point on the mesh to the potentials of its adjacent four grid points and thus every free point has a corresponding five point difference equation. Hence a mesh of N grid points will generate a series of N linear equations with N unknowns. In other words we have reduced the Laplace equation to a set

of linear difference equations which may now be solved by an iterative process described below. The free point potentials are initially set to a series of arbitary values which will almost certainly fail to satisfy the system of difference equations. In order to solve the set of equations the potential of the first free point is recalculated from the potentials of its neighbouring points using the above finite difference relation. This process is repeated for every free point in the mesh area until all the grid point potentials have been reevaluated; thus completing one iteration. Further iterations are then performed until eventually, as their number becomes large, the potential at any point converges towards a specific value; that which would be achieved after an infinite number of iterations. Such values will satisfy the set of difference equations exactly and hence the Laplace equation will be solved. Usually the iterative process is stopped when the grid point potential values satisfy eq(2.6–2.8) to a defined accuracy. The resulting potential distribution will be independent of the initial arbitary free point values, dependent only on the electrode structure and its fixed potentials.

Convergence to a final solution tends to be slow (ie very many iterations are required) but by applying the technique of *successive over-relaxation* [39] - in which a new set of potentials is obtained by extrapolation in the direction of the change in potential of the previous set - the speed of convergence can be substantially increased. The program is usually stopped when all grid points satisfy their difference equations to an accuracy of 1 part in 10^5. The actual error introduced by this method of solution of the Laplace equation is of the order h^4, where h is the unit mesh size [40]. Since all free points have this truncation error and over a large mesh region it will be of the same size, the total error for the camera system becomes $\sim h^2$.

At present the mesh consists of 20,000 grid points with h=1mm; thus the total truncation error is approximately 1 part in 10^6. It is intended in due course to increase this number of grid points and reduce h to 0.5mm. This would improve the total error by a factor of 4.

2.4.2 THE POTENTIAL DISTRIBUTION WITHIN A STREAK TUBE

The common representation of the Laplace solution of a given electrode structure is to plot equipotential contours. There exists, however, a highly concise mathematical analogy

between mechanics and optics which, when represented on the streak tube diagram makes the lensing properties of the camera that much more clear. This analogy was originally formulated by de Broglie and then later by Ehrenberg et al (1949) [41].

From mechanics one derivation of the differential equation governing the path of an electron (or any charge particle) in a electrostatic field can be obtained from the principle of least action:

$$\delta \int_a^b \mathbf{p}.\mathbf{ds} = 0 \qquad \text{–eq(2.9)}$$

This states that the path of an electron between points a and b is such that the integral of its momentum, **p**, over the path is a minimum or more generally a stationary value compared to the same integral over any neighbouring path.

By analogy in optics we have Fermat's Principle:

$$\delta \int_a^b n\,\mathbf{ds} = 0 \qquad \text{–eq(2.10)}$$

which implies that light in travelling from point a to b traverses an optical path length which is stationary with respect to variations of this path.

The mathematical form of these two statements are very similar and can be physically related. In an optical lensing system the imaging characteristics are determined by variations in refractive index along the path causing changes in the ray trajectory (such that Fermat's Principle is satisfied). Likewise, in an electrostatic lens the variations in electrostatic potential along the electron path cause changes in momentum and consequent changes in direction (such that the principle of least action is upheld). In a sense the momentum of the electron at a point in the electrostatic lens defines an *effective refractive index*, n_{eff} for that region. For a given potential distribution we need only derive the dependence of the electron momentum on potential in order for n_{eff} to be plotted. The electron trajectory in the streak camera could then be treated as an equivalent ray trajectory through an optical lens system.

From the Einstein equations in special relativity [42] the total energy of the electron in an electrostatic field is:

$$E = mc^2 = m_oc^2 + e\phi \qquad \text{–eq(2.11)}$$

We have also:

$$E^2 = (cp)^2 + m_o^2c^4 \qquad \text{–eq(2.12)}$$

Combining these equations and collecting terms we find:

$$n_{eff} = p = [2em_o\phi(1 + \eta\phi)]^{\frac{1}{2}} \qquad \text{–eq(2.13)}$$

where:

$$\eta = \frac{e}{2m_oc^2} \qquad \text{–eq(2.14)}$$

Figures 2.8 and 2.9 show plots of the regions of constant effective index calculated from the potential distribution of the Photochron II and IV streak tubes. Although the appearance of what are certainly recognizable optical components can be initially quite startling (particularly so in the Photochron IV with well defined concave and convex lenses), it is to be expected that the focusing region of an electrostatic imaging device should resemble a series of optical lenses when transformed to its optical equivalent.

2.4.3 Calculation of Electron Trajectories through Streak Tube

The differential equation defining the path of an electron through a given potential distribution can be derived via a number of routes. One method has already been mentioned, namely use of the principle of least action or more specifically employing the Euler equations [43] which is equivalent to invoking eq(2.9). Alternatively one can try direct relativistic analysis of the forces acting on the electron in the radial and axial directions to obtain a differential equation describing the electron path. The end result in either case is the general relativistic ray equation [43] as shown below:

$$r'' = \frac{(1+2\eta\phi)}{(1+\eta\phi)} \frac{[1+(r')^2]}{2\phi} \left[\left(\frac{\delta\phi}{\delta r} \right) - r' \left(\frac{\delta\phi}{\delta z} \right) \right] \qquad \text{–eq(2.15)}$$

which describes the dependence of the electron radial position, r as a function of its position along the camera axis, z and the electrostatic potential, ϕ through which it moves (all derivatives are with respect to z and η is as defined before in eq(2.14)). A different equation exists for skew trajectories but by suitable transformation of axes it can be made to be of the same form as the above.

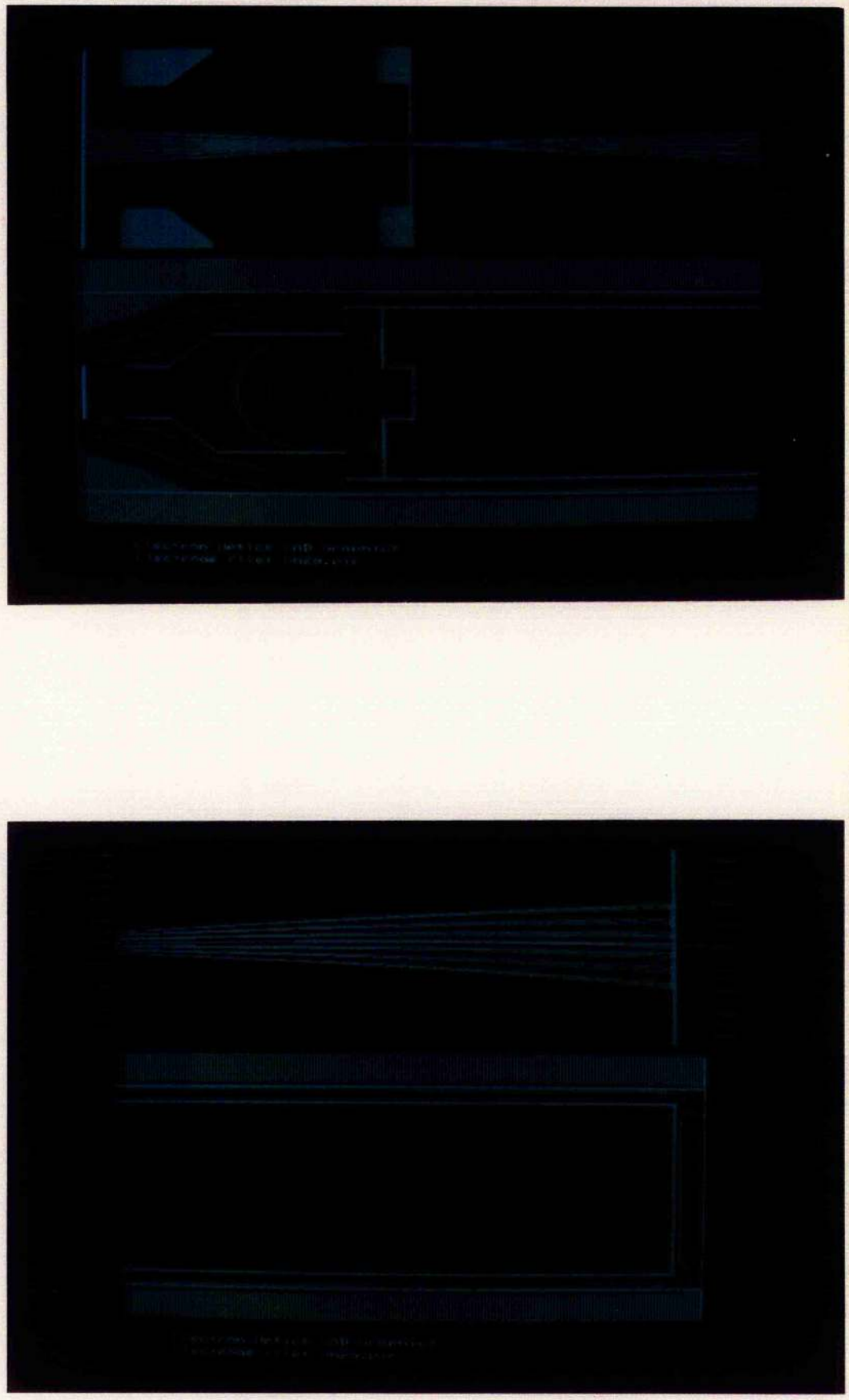

Figure 2.8 Equivalent lens system and electron trajectory in the Photochron II streak tube

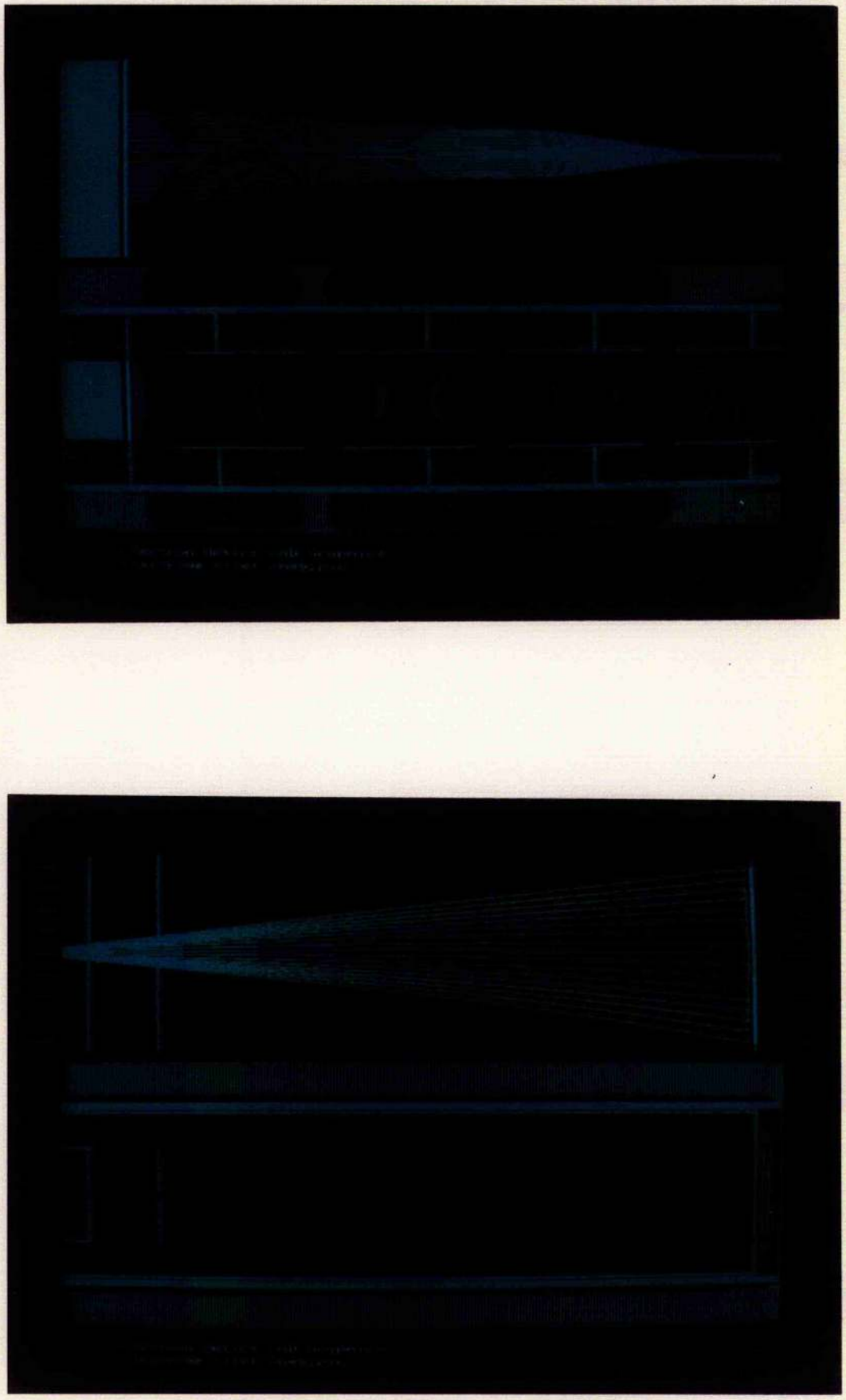

Figure 2.9 Equivalent lens system and electron trajectory in the Photochron IV streak tube

For a well designed, aberration free electrostatic lens the electron trajectories will be confined within a narrow tubular surface of revolution about the z axis. In this region we may neglect terms in r and r' of orders higher than the first in eq(2.15) - this is the *Gaussian approximation* [43]. Further in this region we have from Gauss' Law:

$$\left(\frac{\delta\phi}{\delta r}\right) = \frac{1}{2} r \phi'' \qquad \text{–eq(2.16)}$$

Substitution into eq(2.15) and removal of negligible terms yields the Gaussian ray equation:

$$\frac{(1+2\eta\phi)}{(1+\eta\phi)} r'' + \frac{1}{2}\frac{\phi'}{\phi} r' + \frac{1}{4}\frac{\phi''}{\phi} r = 0 \qquad \text{–eq(2.17)}$$

In any numerical solution of this equation it is preferable to remove terms containing ϕ'' and this may be achieved by the substitution:

$$R = r\,[\phi\,(1+\eta)]^{\frac{1}{4}} \qquad \text{–eq(2.18)}$$

For such a case we obtain the reduced ray equation:

$$R'' = -R\,T(z) \qquad \text{–eq(2.19)}$$

where:

$$T(z) = \frac{3}{16}\left(\frac{\phi'}{\phi}\right)^2 K(\phi) \qquad \text{–eq(2.20)}$$

and:

$$K(\phi) = \frac{\left(1 + \frac{4\eta\phi}{3} + \frac{(2\eta\phi)^2}{3}\right)}{(1+\eta\phi)^2} \qquad \text{–eq(2.21)}$$

This is the differential equation of the electron trajectory that we wish to solve. There is no analytical solution as the potential distribution is not an analytical function of the electron position. Instead a solution must be computed using numerical integration. Several methods are available, all of varying degrees of accuracy. They include methods due to Liebmann [44], Gans [43], Burfoot [45], and Runge-Kutta [43]. The latter, one of the more accurate procedures and less demanding in computational terms, requires only a knowledge of a single point on the electron trajectory and its direction. Using the reduced ray equation and an integration interval of length dz = h (the unit mesh size as before) we can calculate the values of R_{n+1} and R'_{n+1} (the normalised trajectory and its slope) at a point z_{n+1} on the grid from the previously calculated values at the point z_n using the following expressions:

$$R_{n+1} = R_n\left[1 - \frac{h^2}{6}(2T_n + T_{n+1})\right] + R'_n h\left[1 - \frac{h^2}{6}T_{n+1}\right]$$

$$R'_{n+1} = -R_n\frac{h}{2}(T_n + T_{n+1}) + R'_n\left[1 - \frac{h^2}{2}T_n\right] \qquad \text{–eq(2.22)}$$

An accuracy of better than 1 part in 10^6 can be achieved if the value of the function T at the centre of the integration interval is also determined and eq(2.22) modified accordingly [43]. The starting points of the electron trajectory are taken as lying on the mesh at equally spaced distances from the camera axis. Several angles of exit are used equivalent to mapping electron trajectories of differing initial velocities (this provides data on temporal dispersion effects). Using the above numerical technique the resulting electron paths are also plotted in the top sections of figures 2.8 and 2.9 for the Photochron II and IV respectively. It should be noted that the Photochron IV has superior spatial resolution compared to the Photochron II as is evident by the minimal spread in arrival positions at the phosphor by various electron trajectories.

2.5 CONCLUSIONS

The purpose of this initial chapter was to introduce streak cameras and the techniques used in their design and development. In general the criteria for the design of an image tube having improved temporal resolution in streak operation can be separated into four primary requirements. These are (i) a 'fast' photocathode from which the electrons are released with a narrow energy distribution, (ii) an electron-optical lens arrangement that provides optimised temporal and spatial characteristics, (iii) a high sensitivity deflector geometry, and (iv) a phosphor screen having an optimum quantum efficiency. In the main requirement (i) is the ultimate limiting factor.

Two tube designs, the Photochron II and IV have been addressed as these have been extensively used by the author as test beds for the development of electronic deflection systems and also since they are key tube designs per se satisfying the above prerequisites to atleast some degree.

REFERENCES

1 D.G.Parker, P.G.Say, A.M.Hansom and W.Sibbett, Electron. Lett. **23** 527 (1987).

2 K.J.Weingarten, M.J.W.Rodwell and D.M.Bloom, IEEE J. Quant. Electron. **24** 198 (1988).

3 D.H.Auston and P.R.Smith, Appl. Phys. Lett. **41** 599 (1982).

4 R.J.Manning and J.R.Hill, Optica Acta **33** 483 (1986).

5 A.Finch, Y.Liu, H.Niu, W.Sibbett, W.E.Sleat, D.R.Walker, H.Yang and R.Zhang, in *Ultrafast Phenomena VI* : Springer Series in Chem. Phys. **48** 159 (1988).

6 A.Frieberg, S.Savikhin and K.Timpmann, Proc. XVIIIth ICHSPP (to be published).

7 M.R.Baggs, R.T.Eagles, W.Margulis, W.Sibbett and W.E.Sleat, Adv. in Electron. and Electr. Phys. **64B** 627 (1985).

8 J.Rodney M.Vaughan, IEEE Trans. Electron. Dev. **35** 1172 (1988).

9 D.Welford, W.Sibbett and J.R.Taylor, Opt. Comm. **34** 175 (1980).

10 H.G.Ahlstrom in *Diagnostics of experiments on laser fusion*. Vol II. Lawrence Livermore Nat. Lab., Livermore Ca. UCRL–53106 (1982).

11 M.C.Jackson, R.D.Long, D.Lee and N.J. Freeman, Laser and Particle Beams **4** 145 (1986).

12 D.H.Auston, Appl. Phys. Lett. **26** 101 (1975).

13 W.Knox and G.Mourou, Opt. Comm. **32** 203 (1981).

14 W.Sibbett, Proc. XVth ICHSPP. SPIE **348** 15 (1982).

15 H.Niu and W.Sibbett, Rev. Sci. Instr. **52** 1830 (1981).

16 R.Kalibjian and G.G.Peterson, Proc. XVth ICHSPP. SPIE **348** 195 (1982).

17 E.K.Zavoisky and S.D.Franchenko, Appl. Optics **4** 1155 (1965).

18 Y.Liu, H.Niu, Q.L.Yang, and H.Zhang, Proc. 5th NCHSPP, China (1985).

19 J.A.Armstrong Appl. Phys. Lett. **10** 16 (1967).

20 D.J.Bradley, B.Liddy and W.E.Sleat, Opt. Comm. **2** 391 (1971).

21 K.W.Jones Phd Thesis, Imperial College, London (1986).

[22] V.S.Bulygin, Y.A.Drozhbin & B.M.Stepanov, Proc. XII ICHSP, SPIE **97** 68 (1976).

[23] P.T.Farnsworth, Electron multiplier: US Pat. N1.969.399 (1930).

[24] G.Holst, J.Boer and M.Teves, Physica **1** 297 (1934).

[25] J.S.Courtney-Pratt, Photograph. Journ. B **92** 137 (1952).

[26] M.M.Butslov, E.K.Zavoisky, A.G.Plahov, G.E.Smolkin and S.D.Fanchenko, Proc IVth ICHSP 230 (1958).

[27] F.Walters, R.A.Chippendale, R.P.Brown, Proc VIth ICHSP 357 (1963).

[28] D.J.Bradley, B.Liddy, A.G.Roddie, W.Sibbett and W.Sleat, Adv. Electron. and Elect. Phys. **33** 1145 (1972).

[29] M.Ya.Schelev, M.C.Richardson, A.J.Alcock Appl. Phys. Lett. **18** 354 (1971).

[30] D.J.Bradley and G.H.C.New, Proc. IEEE **62** 313 (1974).

[31] P.R.Bird, D.J.Bradley and W.Sibbett, Proc. XIth ICHSP 112 (1974).

[32] D.J.Bradley and W.Sibbett, Appl. Phys. Lett. **27** 382 (1975).

[33] W. Sibbett, H. Niu and M.R. Baggs, **53** 758 (1982).

[34] R.T.Eagles Phd Thesis, St. Andrews University (1985).

[35] *Image processing and computer aided design in electron optics*. Ed. P.W.Hawkes, Academic Press, London (1973).

[36] D.J.Bradley, K.W.Jones and W.Sibbett, The Royal Society - London 71 (1980).

[37] V.K.Zworkin, G.A.Morton, E.G.Ramberg, J.Hillier and A.W.Vance in *Electron optics and the electron microscope*, John Wiley & Sons (1945).

[38] B.Bleaney and Bleaney in *Electricity and Magnetism*, Oxford University Press (1984).

[39] B.A.Carré, Comp. J. **4** 73 (1961).

[40] C.Weber in *Focussing of charged particles.Vol. I.* Ed. A.Septier. Academic Press. New York (1967).

[41] W.Ehrenberg and R.E.Siday. Proc. Phys. Soc. B **62** 8 (1949).

[42] A.P.French in *Special relativity*. MIT Introductory Physics Series, Nelson (1981).

[43] P.Grivet in *Electron Optics I*, Trans. P.W.Hawkes, Pergamon Press, Oxford (1972).

[44] G.Liebmann, Proc. Phys. Soc. B **62** 753 (1949).

[45] J.C.Burfoot, Brit. Journ. of Appl. Phys. **3** 22 (1952).

CHAPTER 3: DYNAMIC OPERATION OF THE PHOTOCHRON II STREAK TUBE

3.0 INTRODUCTION

The first experimental demonstration of synchroscan operation of a streak camera was performed by Hadland et al. [1] using a flashlamp pumped, mode-locked Nd:YAG laser as the test source. Unfortunately no quantitative data were available as to the achieved temporal resolution because of the associated difficulties with the small number of streak images (~12) superimposed at the phosphor. In 1978 a Photochron I camera was operated in synchroscan mode using pulses from a CW dye laser which had been synchronously pumped by a mode-locked argon ion laser [2,3]. The synchronisation signal for the camera was derived from the 70 MHz electrical drive applied to the acousto-optic modulator in the pump laser. The temporal resolution obtained for input optical pulses of ~2 ps was in excess of 13 ps compared to an expected FWHM of 5 ps. This poor performance was ascribed to the deliterious effect of pulse-to-pulse jitter in the laser and possible RF interference between the camera deflectors and the drive signal to the mode-locker.

When the same camera was tested with pulses from a passively mode-locked CW dye laser the temporal resolution was significantly improved to a camera-limited value of 5.2 ps for input pulse durations of 0.2 – 0.3 ps [4]. In this experiment synchronisation was achieved at twice the laser repetition frequency (165 MHz) by using a tunnel diode oscillator and this technique is discussed in detail in Chapter 4. Interestingly when this synchroscan system was re-employed on the sync-pumped system of reference 3 there was only a marginal improvement in temporal resolution (12 ps) indicating that indeed laser source jitter was the main limiting factor to its performance.

Following on from this, with the advent of the Photochron II streak tube, application of the above circuitry yielded resolutions of less than 2.5 ps which was close to the estimated tube limiting resolution [5]. In this instance the test pulse source was a mode-locked CW ring dye laser with pulse durations of less than 200fs. Optimisation of the deflector geometry and inclusion of a microchannel plate (MCP) intensifier within the image tube envelope led to the Photochron IIA streak tube [6]. Deflection efficiency was improved

threefold compared to the original Photochron II and using a similar experimental arrangement as before a realtime FWHM resolution of 2.5 ps was obtained. When a 1 ms shutter was employed this value was reduced to 1.2 ps indicating on deconvolution that this streak camera had near picosecond resolution [7]. At the outset of this project this result was the best ever synchroscan resolution achieved.

3.1 PASSIVE SYNCHRONISATION

When the Sibbett research group was transferred to the University of St. Andrews (from Imperial College, London) a redesign of the synchronisation circuitry was initiated mainly because there were reservations as to the merits of the tunnel diode system. It was decided that the mode-locked CW laser pulse source should provide its own synchronisation rather than relying on a phase locked oscillator. Such a *passive* synchronisation scheme is represented in figure 3.1 and described below.

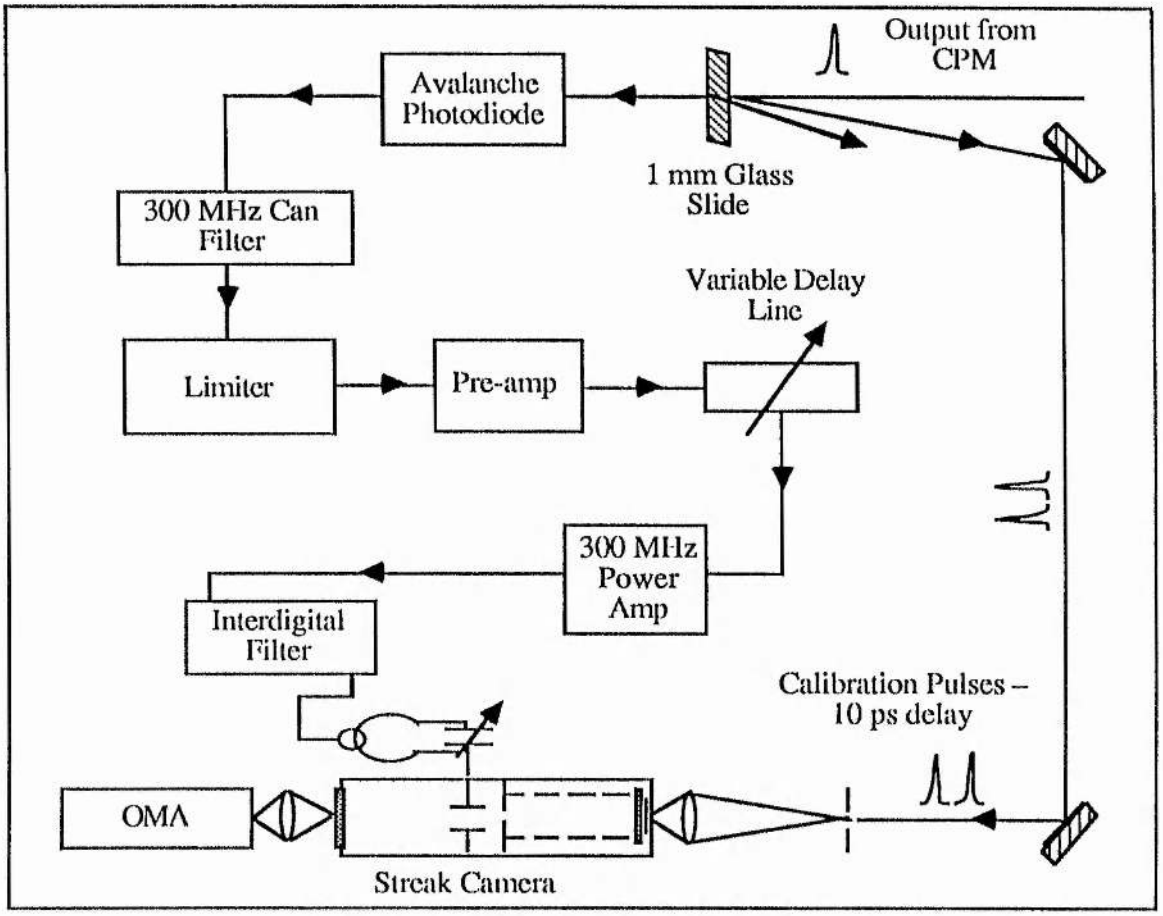

Figure 3.1 Block diagram of Synchroscan circuit and experimental set up

3.1.1 SYNCHRONISATION CIRCUITRY

One of the laser outputs was directed onto an avalanche photodiode (Telefunken BPW 28) and the resultant electrical pulse train passed directly into a 300 MHz band pass filter to generate an initial sinusoidal signal synchronous to the laser repetition rate. Advantage was taken of the fact that a comb of delta functions in time, separated by a constant time interval, transform into frequency space as a secondary comb of Fourier impulses extending to infinity separated by the reciprocal time interval. For the case of the photodiode signal where the electrical pulse comb consists of impulses of finite width, in frequency space this manifest itself as a roll off in the frequency-Fourier components. Figure 3.2b shows this for the photodiode employed, demonstrating a 3dB roll off at ~2.5 GHz indicating a electrical pulse width of ~ 200 ps. This should be compared to the recorded electrical pulsewidth of 450 ps measured using an oscilloscope (Tektronix 7559) which naturally includes the bandwidth limited response of the input amplifier.

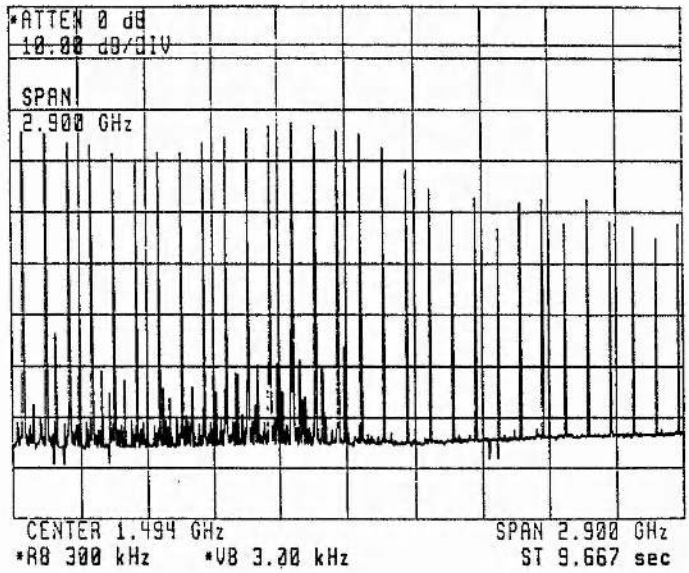

Figure 3.2 a) Fourier spectrum of photodiode electrical pulse train

Immediately following the 300 MHz filter the signal was amplified by ~ 40dB and limited in order to remove large amounts of amplitude modulation. This signal was then taken through a variable delay line (Sage Laboratories 6702-5) which allowed the relative phase between the drive sinusoid and the arrival of pulses at the camera to be varied and hence ensure that the streak images occupied the central, optimally linear region of the

phosphor screen. The signal was then passed to a broad band pre-amplifier stage (TRW CA-2820), followed by a tuned power amplifier (Microwave Modules MML 432/100 - retuned from 432 to 300 MHz) and finally inductively coupled to a tuned circuit across the deflection plates of the Photochron IIA streak tube. A circuit Q in excess of 50 was achieved giving adequate deflection power inputs of the order of 20 Watts.

3.1.2 PHOTODIODE AND LIMITER CIRCUIT

The input avalanche photodiode had an active area of ~250 μm^2 and to obtain adequate electrical signals it was necessary to reverse bias to 139V with the laser output focussed tightly by means of a 1 cm focal length lens. The bias voltage was provided by using two back-to-back transformers with the rectified and smoothed D.C. output stabilised by two Zener diodes (100V and 39V) in series. Additional capacitive smoothing was provided and <1% voltage regulation was acheived for average photodiode currents of up to 2mA. The photodiode was mounted on a strip of printed circuit board and the anode connected to a coaxial cable soldered securely to the board. The cathode end was terminated to ground via two 100Ω resistors in parallel. For light signal levels from the CPM of ~3 mW the peak diode output was 800 mV at an average current of 1.9 mA.

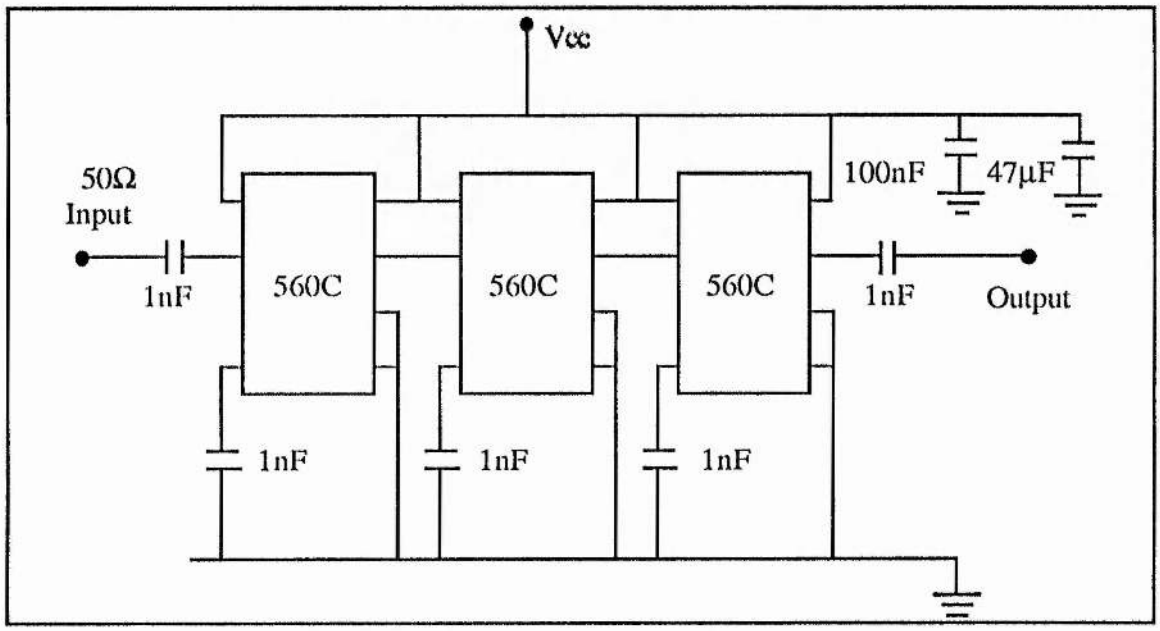

Figure 3.3: Initial limiter circuit diagram

After filtering to obtain the 300 MHz Fourier component the signal (which contained significant amounts of laser-induced amplitude fluctuations) was passed into a three high gain amplifiers (Plessey RS560C) to effectively limit the signal. The initial limiter circuit is represented in figure 3.3. For a rail voltage, V_{cc} of 9V the cascaded amplifiers provide a net (small signal) gain of 40dB, individual gains being in excess of 16dB.

3.1.3 FILTERS

Two types of filter were used within the synchronisation circuitry depicted schematically in figures 3.4 and 3.5. The input filter (figure 3.4a) placed directly after the photodiode can be seen either as a sub-quarter-wave transmission line resonator at 300 MHz – capacitive tuning being achieved by varying the length of the air-space back short – or alternatively as a simple LC circuit with a variable air-spaced capacitor and the inductor consisting of a double wire loop rotated about its centre axis to generate a cylinder. In either case this so called *can filter* had a 3dB bandwidth of 2.4 MHz and an insertion loss of 2dB at its centre frequency (figure 3.4b).

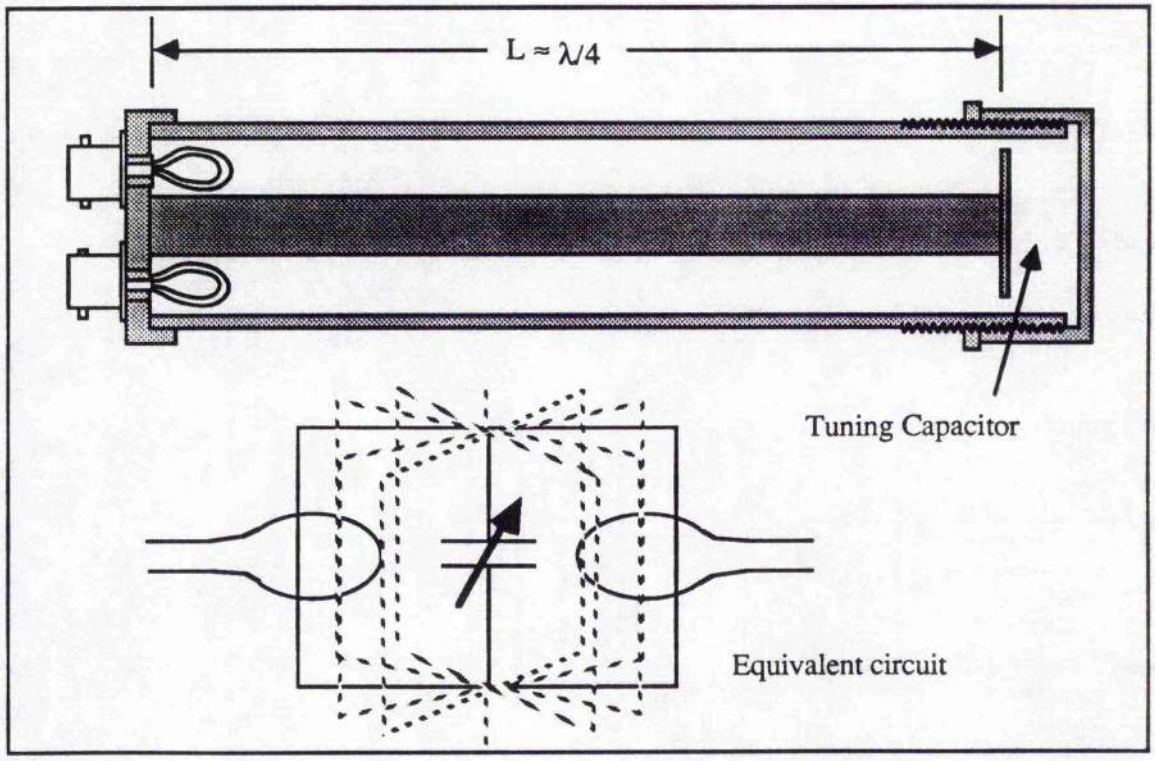

Figure 3.4a): Schematic of *Can* filter

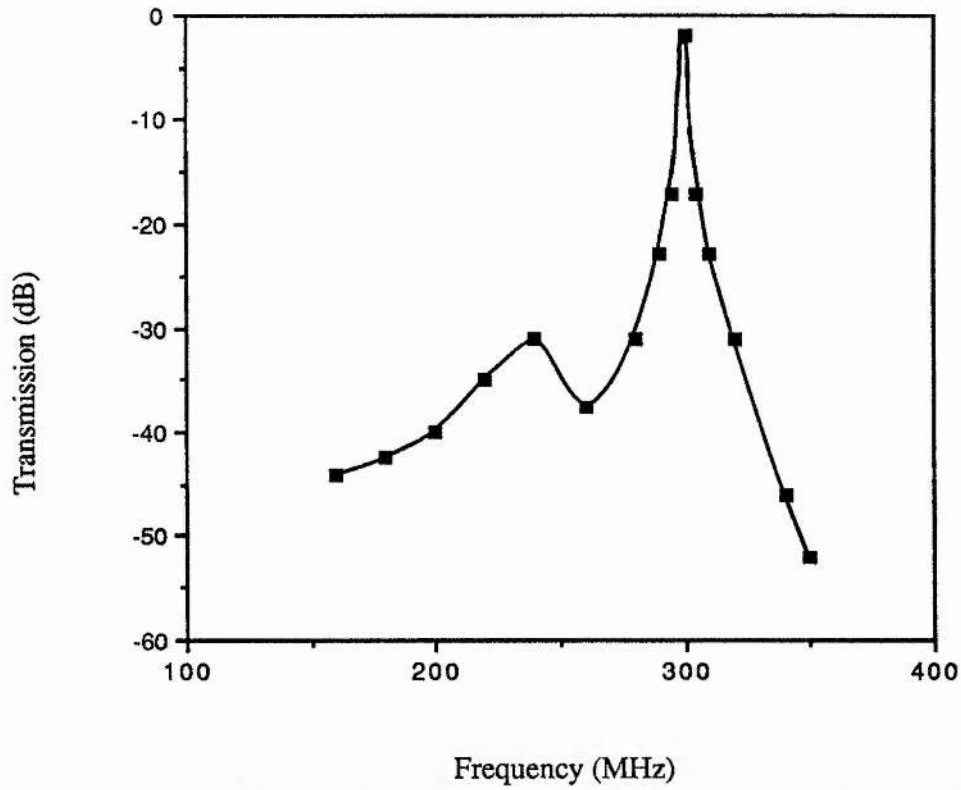

Figure 3.4b): Frequency response of Can filter tuned to 300 MHz

Between the power amplifier and camera a second filter was inserted to remove any distortion in the synchronisation signal. This 300 MHz *interdigital filter* comprised four 50Ω quarter-wave lines placed side by side in a brass container (figure 3.5a). Tuning was provided by screws at the end of each rod. Each rod would resonantly couple to its neighbour at the frequency defined by their quarter-wavelength. The Q of this filter was lower than the can filter (3dB bandwidth being 11 MHz) but its rejection of higher frequencies was improved with a 60dB bandwidth of 45 MHz (figure 3.5b). The construction of this filter was based on design criteria provided by Dishal [8,9] and can be readily adapted to any centre radio frequency and bandwidth requirement, limited mainly by practical quarter-wave dimensions. The pertinent dimensions for the 300 MHz filter are shown in Table 3.1 and the formulae used to calculate them can be found in reference 8. A ratio of h (the filter inside height) to d (the rod diameter) set to 2:1 gives an input impedance of 55Ω, ideal for standard coaxial cable coupling.

The measured frequency responses of the two filters are shown in each figure.

Table 3.1: Dimensions of 300 MHz Interdigital filter

Centre Frequency :	300 MHz	
Bandwidth :	11 MHz	
No. of Stages:	4	
DIMENSIONS (mm)		
Filter Length L:	250	
Filter Height h:	19.5	
Filter Width w:	111	
Rod Length:	237.5	
Rod Diameter d:	9.7	
Rod spacing:	$c_{12} = c_{34} = 27.3$	$c_{23} = 30.0$
	$c_{01} = c_{40} = 0.7$	$h = 13.7$
Tapping point t:	29.5	

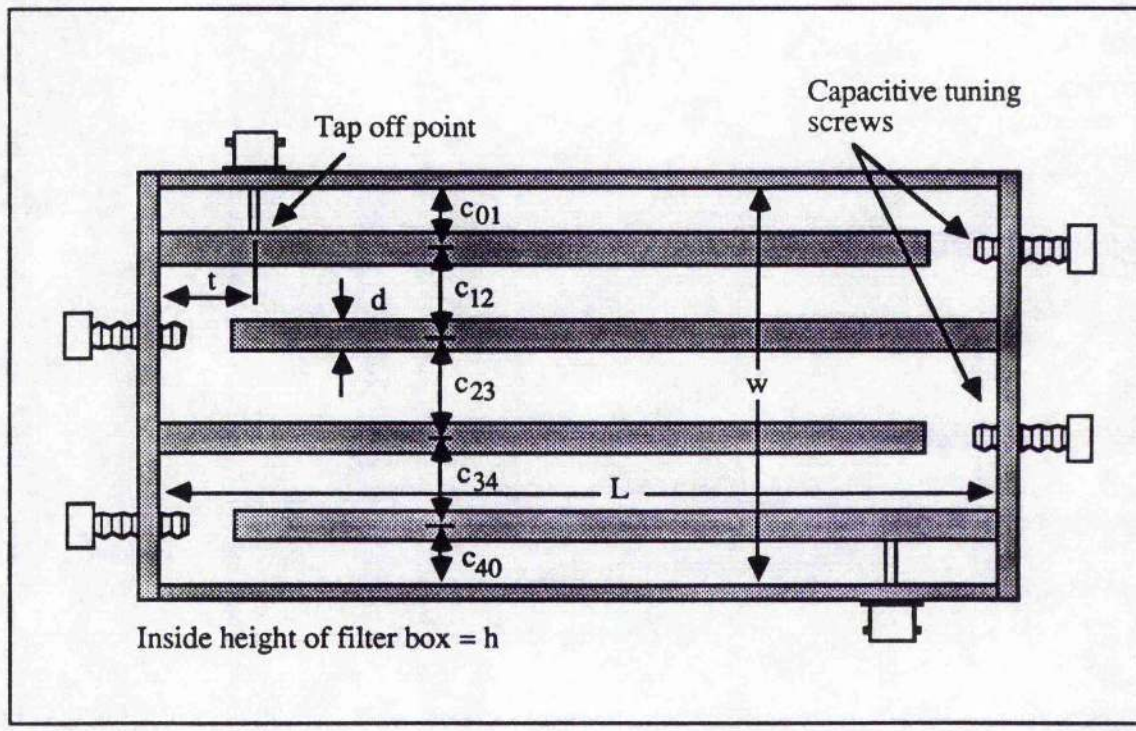

Figure 3.5a): Schematic of Interdigital Filter

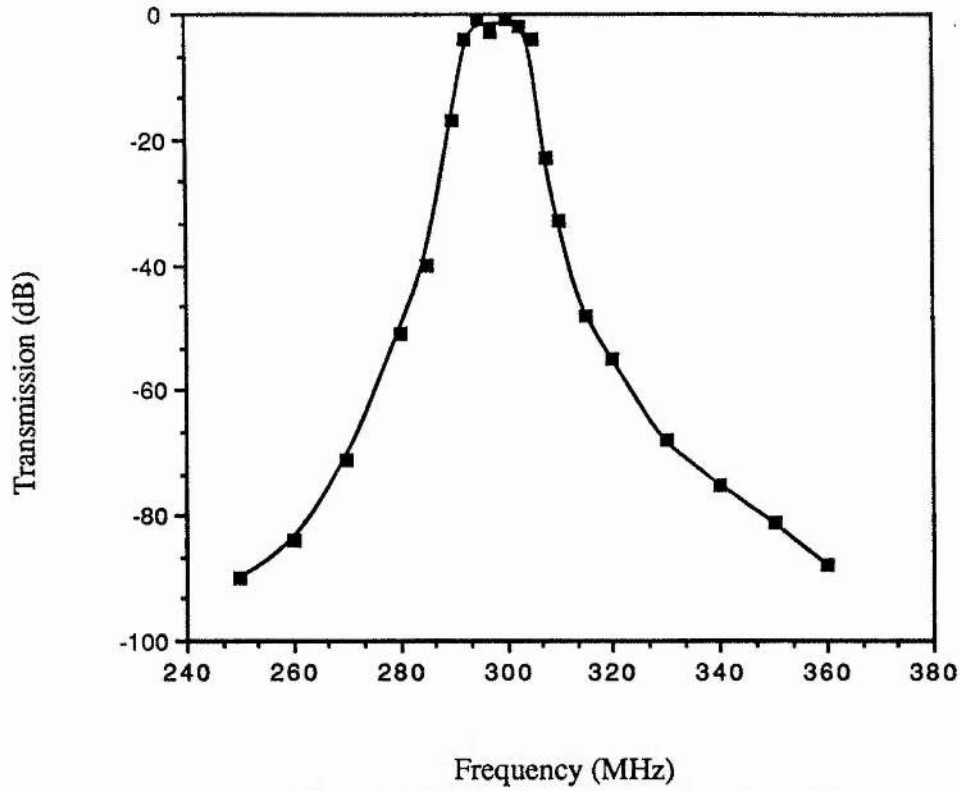

Figure 3.5b): Plot of 300 MHz interdigital filter frequency response

3.2 READOUT SYSTEM

In single-shot streak camera applications a commonly employed image recording medium is photographic film, but for synchroscan operation electronic readout systems are more suitable because they permit realtime monitoring. Such systems avoid the time consuming necessity of film processing, calibration, microdensitometry and linearisation of the resultant data. Throughout these experiments the streak records were read out using a B&M Spektronik OSA 500. The unit consisted of a silicon intensified target vidicon (SIT) [10] the output being accessed by a multichannel analyser. The target was divided into 500 channels each of 25μm width and height extending over approximately 2mm. Each channel was scanned by a probe electron beam and the resultant signal digitised to 12 bits by the analyser and displayed as a function of channel number on a CRT. Full frame scan times were 32ms ie) 64μs per channel giving a dark current of around 60 counts with a peak to peak noise level of ~ 8. Hence the dynamic range of the system was 2^9 but microprocessor controlled signal averaging over several scans allowed this figure to be improved. The

microprocessor could store several memories and cursor control allowed anaysis of the stored streak records. A hardcopy facility was also provided.

The streak camera input comprised a 100μm slit scribed on an aluminised glass slide which was imaged onto the photocathode with a x4 demagnifying lens. To ensure adequate resolution the phosphor image was focussed onto the SIT vidicon with a f1.4 lens operating at x2 magnification. The minimum static slit width measure with this system was 5.5 channels indicating a FWHM image of 140μm at the target or 70μm on the streak camera screen. This is consistent with a measured camera resolution of 17.5 lp/mm at the phosphor, some degradation in imaging arising due to cross-talk between channels.

3.3 PHOTOCHRON IIA PERFORMANCE

3.3.1 INITIAL EXPERIMENTATION

Initially the Photochron IIA was operated at 300 MHz. Two calibration pulses were obtained by quasi-normal reflection from a 1mm thick (1.00±0.002 mm) glass slide placed in the beam path. Hence for an incident angle of 10° the pulse separation was 10.0 ± 0.3% ps; this was later confirmed with a Michelson calibration delay arrangement. Early studies were prior to the inclusion of any dispersion compensating optics within the CPM laser and performance of the streak tube typically yielded a temporal resolution of ~4 ps. Since the laser was being used directly to generate the deflection signal, the 300 MHz Fourier component was scrutinised on a spectrum analyser (HP 8555B). It was at this point that some curious laser properties were first observed. It was found that the odd harmonics in the Fourier comb from the photodiode had a two-peaked spectrum, whereas the even harmonics were single peaked (Fig. 3.6a and b repectively). There then ensued an investigation in order to identify the source of this disturbing laser property where emphasis was primarily placed upon mechanical sources (eg. jet speeds were changed, pump power was monitored) but all were to prove fruitless.

One possibility was that a roundtrip modulation due to some scattering process in the dye jet, ie. some form of cavity transverse mode wander might exist. To investigate this,

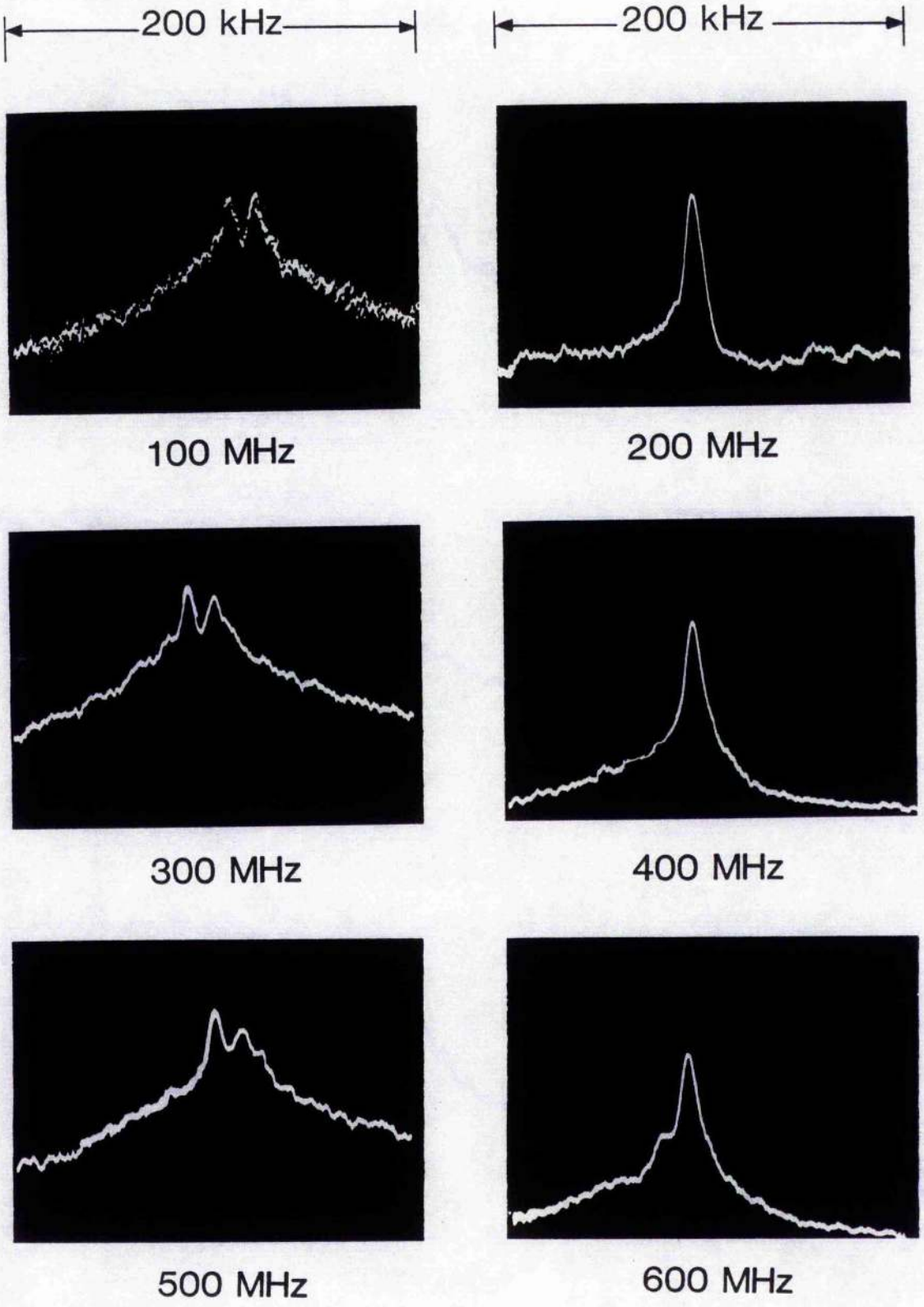

Figure 3.6 a) Odd and b) even Fourier components of electrical pulse train.

apertures were placed in the cavity and the 300 MHz Fourier component mixed with a 300 MHz crystal oscillator and the difference frequency input to a radio receiver to demodulate any amplitude sidebands. With no intracavity aperturing, no discernible "clean" signal was audible except very close to threshold. However with apertures present the noise spectrum as determined by the mixed and demodulated signal from the receiver quietened dramatically and adjustment of the laser jet lead to a steady beat frequency to be established between the laser and the receiver's local oscillator. It was presumed that the problem had been resolved and expected that on examining the Fourier components on the spectrum analyser this odd-even effect would have disappeared. This was true only to a limited extent, odd and even harmonics now had identical spectra, but each Fourier component had a set of strong sidebands distributed evenly around the relatively clean central carrier (Fig. 3.7a). The sidebands corresponded to gross amplitude modulation on the pulse train (Fig.

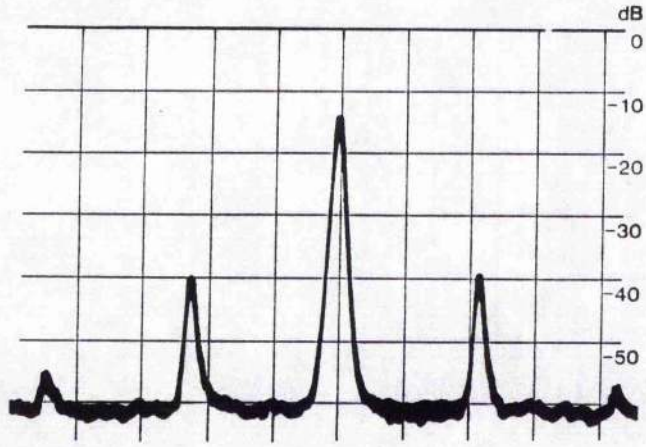

(a)

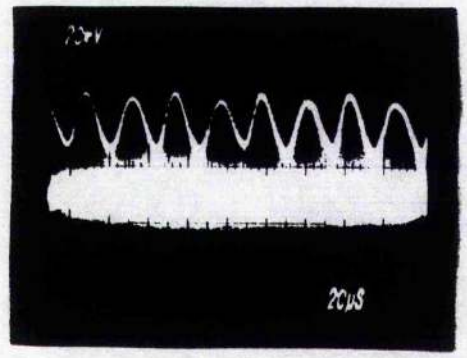

(b)

Figure 3.7 a) Sideband content in synchroscan carrier signal (20 kHz/div) and b) gross amplitude modulation of laser output.

3.7b) at a frequency of around 70 kHz.

The source of this curious effect has been ascribed to a semi-solitonic phenomena in the laser [11] and is discussed in Chapter 9; the apertures act more to control intracavity intensities rather than to prevent any transverse mode hopping as was initially thought. This strong amplitude modulation proved even more of a nuisance during synchroscan operation until the action of the limiter was considered.

It was found that adjustment of the input light intensity illuminating the photodiode could have a significant effect on the observable resolution of the streak camera, and optimum resolution (~ 3.5 ps) occuring not at maximum signal levels. So the question was asked why should the limiter have preferred input signal levels and what effect would limiting have on the deflection signal?

3.3.2 OPTIMISATION OF LIMITER CIRCUIT

Amplitude modulation will present only a minor limitation on achievable temporal resolution; the high power applied to the deflection plates implies a large region of linearity in scan and hence such fluctuations will have only a minimal effect on streak velocity. The amplitude modulation is effectively removed from the carrier by the limiter in the drive circuit. Streak camera performance is much more sensitive to phase fluctuations in the deflection signal. Since when the laser was showing this solitonic effect the third harmonic of its repetition rate gave a constant beat frequency with the crystal oscillator it was concluded that the phase fluctuations (ie. jitter in the pulse train) were minimal and the degradation in streak camera performance had its source in the synchronisation circuitry. It became our belief that the action of the limiter itself actually induces phase modulation to appear in the deflection signal since the outputs of the FET amplifiers within the limiter are driven into different levels of saturation, dependent upon input level. This will generate a varicap effect within the amplifier causing phase/frequency modulation to be present in the carrier which has some relation to input amplitude fluctuation. To provide some control of the limiting action the system was modified so that the first pair of the 560C amplifiers had a separate, variable rail voltage compared to the output chip (Fig. 3.8). To enhance gain a fourth final stage amplifier was incorporated with a 300 MHz tuned output. It was then

found that adjustment of these rail voltages could reduce the level of sidebands on the limiter output and have a marked effect on achievable resolution.

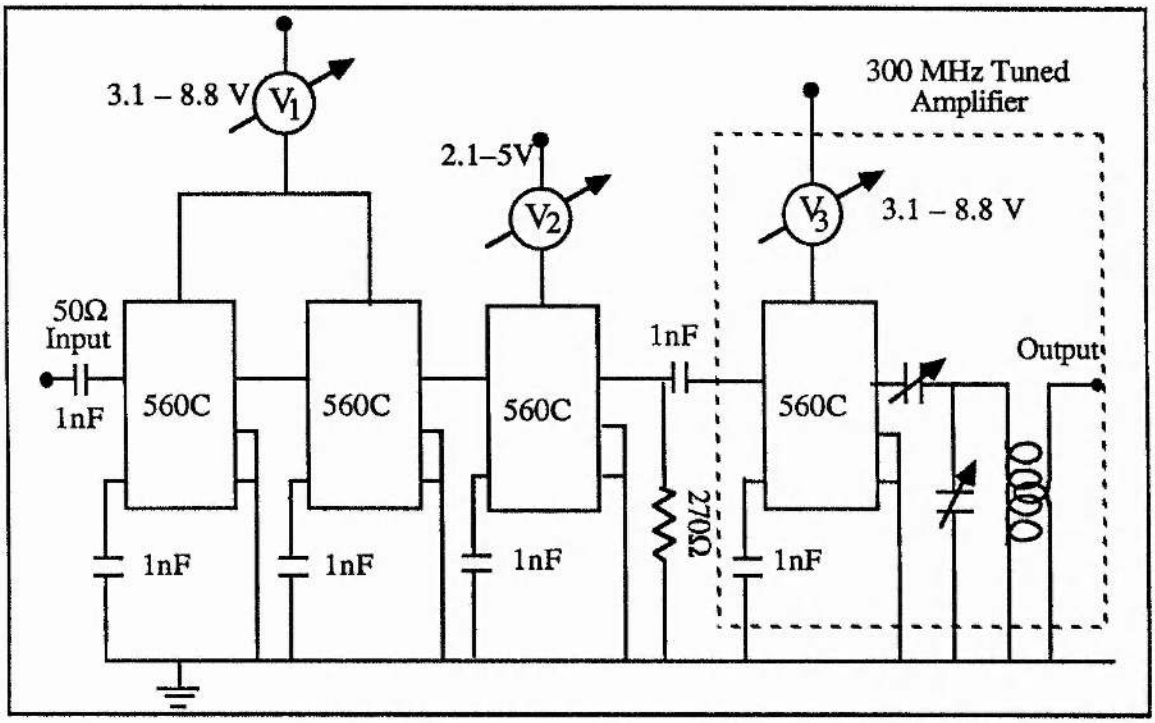

Figure 3.8 Redesigned limiter circuit

3.4 Effect of Phase Modulation on Streak Camera Performance

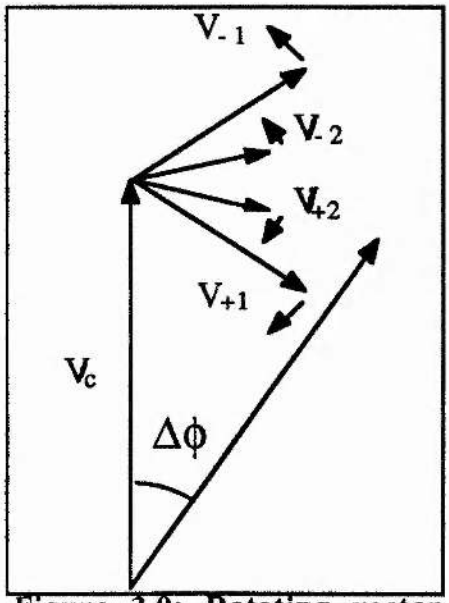

Figure 3.9: Rotating vector representation of carrier signal and deviating sidebands

Assuming that all of the sideband content after limiting is entirely due to frequency modulation – a reasonable assumption since no discernible amplitude modulation was ever present – its effect on synchroscan performance was then considered. It is useful to view the effect of frequency modulation sidebands on a carrier employing the *rotating vector model* [12]. Referring to Fig. 3.9 the phase of the main carrier having a signal level V_c will be deviated through an angle $\Delta\phi$ equal to the vector addition of the various sideband

signal levels. The maximum phase deviation $\Delta\phi_{max}$ will occur when all the sideband components are in phase with each other and in quadrature with the carrier. In this case:

$$\Delta\phi_{max} = \left[\frac{V_{-2} + V_{-1} + V_{+1} + V_{+2}}{V_c}\right] \qquad \text{–eq(3.1)}$$

Assuming that this maximum deviation corresponds to the limit of the synchroscan resolution the expected temporal resolution will be:

$$\tau_r = \frac{\Delta\phi_{max}}{f_o\pi} \qquad \text{–eq(3.2)}$$

where f_o is the deflection frequency.

There is an additional effect of the Q of the system which will act to amplify any frequency modulation thereby increasing the value of $\Delta\phi_{max}$. For the case of a basic resonant circuit [13], the phase shift for a frequency component f at the output of simple LC resonant filter with resonance f_o is given by:

$$\tan\delta\phi = \pm Q\left(\frac{f}{f_o} - \frac{f_o}{f}\right) \qquad \text{-eq(3.3)}$$

For small frequency deviations around f_o, $\tan\delta\phi \approx \delta\phi$ and thus:

$$\frac{\delta\phi}{\delta f} \approx Q\left(\frac{1}{f_o} + \frac{f_o}{f^2}\right) \approx \frac{2Q}{f_o} \qquad \text{-eq(3.4)}$$

After the limiter we have phase/frequency modulation defined by the sideband content which generates a phase deviation $\Delta\phi$. Thus the drive signal can be represented as:

$$V(t) = V_o\sin(\omega_o t + \phi_o + \Delta\phi.\cos\omega_m t) \qquad \text{-eq(3.5)}$$

The frequency content of the drive signal is defined by the derivative of the argument of the sine term in the above expression and thus the instantaneous frequency of the drive signal,

$$f = \frac{1}{2\pi}(\omega_o + \Delta\phi\ \omega_m.\sin\omega_m t).$$

Hence the maximum frequency deviation for a phase deviation $\Delta\phi$ is given by

$$\Delta f_{max} = \Delta\phi.f_m \qquad \text{-eq(3.6)}$$

Combining the above expression with equation 3.4 the frequency deviation induces an additional phase deviation at the output of the filter given by:

$$\delta\phi = \frac{2Q}{f_o} f_m\,\Delta\phi_{max} \qquad \text{–eq(3.7)}$$

where f_m is the sideband frequency separation. Insertion of this into equation 3.2 yields the expression:

$$\mathcal{T}_r = \frac{1}{f_o \pi}\left(1 + \frac{2Q}{f_o} f_m\right) \sum \frac{V_{sb}}{V_c} \qquad \text{--eq(3.8)}$$

By adjusting the limiting level of each FET amplifier the degree of saturation was varied which produced an alteration in sideband content, V_{sb}. Figure 3.10 shows how measured values of $\mathcal{T}_r$ vary with $\sum V_{sb}/V_c$ as measured on the Photochron IIA streak tube operated at f_o= 300 MHz. Also shown on the figure are the theoretical values of $\mathcal{T}_r$ calculated from eq(3.8). Good agreement is seen between theory and experiment which indicates that the above analysis represents a reasonable model and demonstrates the importance of phase noise in limiting synchroscan performance. (The fact that the measured values of $\mathcal{T}_r$ are slightly greater than those predicted by theory probably implies the presence of additional deliterious factors associated with the RF signal which is expanded upon in the next chapter.) From this analysis it becomes apparent that in order to achieve subpicosecond temporal resolution it is necessary to reduce the sideband content to less than 80 dB below the carrier power level (dBc).

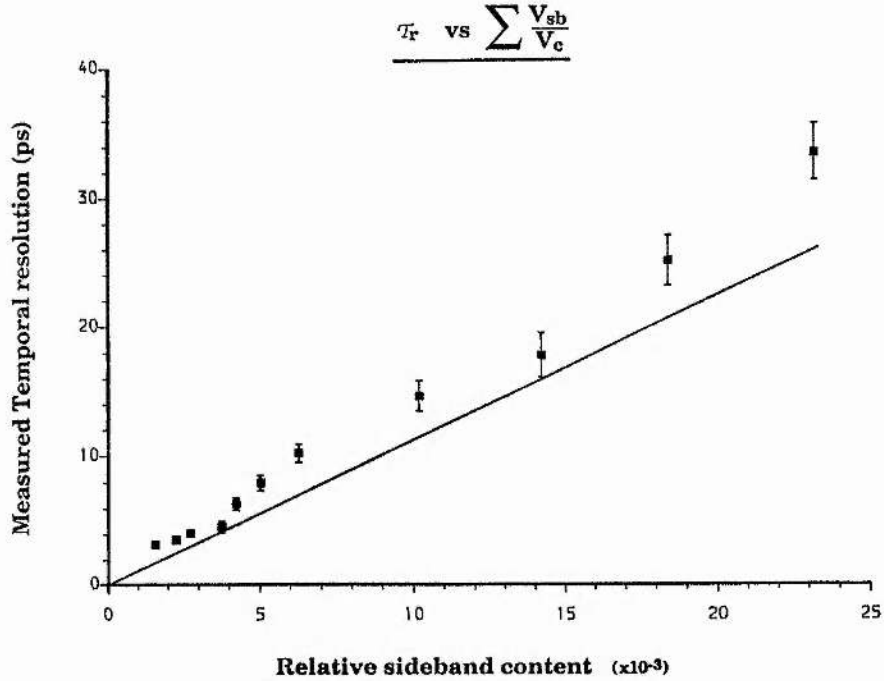

Figure 3.10 Measured temporal resolution (points) and theoretically-predicted (solid line) temporal resolution values as a function of sideband content in deflection signal.

With the laser in this solitonic mode and limiter rail voltages adjusted to minimise sidebands to around 70 dB below the carrier the best resolution achieved realtime was 2.8 ps and with a 1ms mechanical shutter, optimum resolution of 2.4 ps was achieved as is shown in figure 3.11.

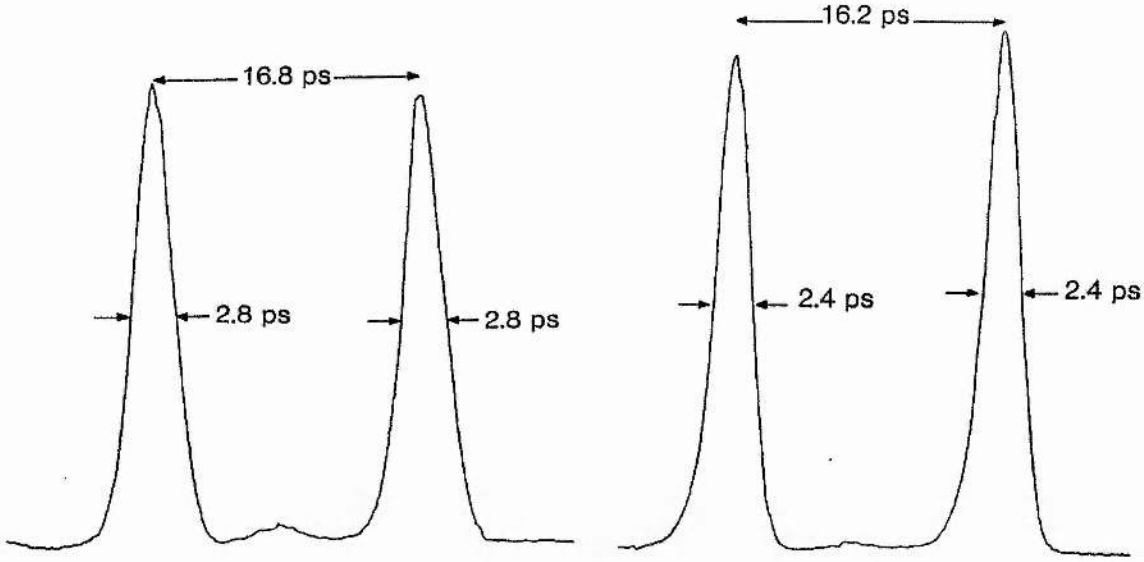

(a) (b)

Figure 3.11 a) Optimum realtime and b) 1ms shuttered streak records with laser operating in soliton mode.

3.5 SYNCHROSCAN OPERATION AT 200 MHZ

Because of the inherent difficulties in operating at 300 MHz streak frequencies (mainly due to RF heating effects in deflector feed-through pins) it was decided to scan the Photochron IIA at twice the laser repetition rate ie) 200 MHz. This required the retuning of the final stage tuned amplifier in the limiter, the construction of a 200 MHz power amp (Mullard BGY45C) and the modification of the can filter. The power amplifier was supplied with a adjustable rail voltage thus allowing its gain to be controlled. To bring the can filter to the lower resonance of 200 MHz required its end capacitance to be increased by reducing the air gap. Low resonant transmission loss of 2dB was maintained by pushing the inductive loops closer to the centre rod to improve coupling. Inductive coupling to the streak tube deflectors was modified; the inductance loop area was increased and the double

plate wide air gap tuning capacitor replaced with a variable 8 plate narrow gap capacitor stack.

Initially results were very similar to those achieved at 300 MHz operation but camera handling was much easier since settling times and detuning due to RF heating were much reduced. It became fairly clear that if better temporal resolutions were to be achieved the phase noise in the drive signal had to be improved and, since its origin was in the main part due to amplitude fluctuations in the laser output, time was taken to improve the CPM laser performance. This involved the inclusion of a 4-prism sequence in the laser cavity to control group velocity dispersion (GVD) and the development of realtime intensity and interferometric autocorrelation monitoring equipment. These are discussed in some detail in Chapter 9.

Control of the dispersion in the cavity enhanced laser performance significantly. Pulse durations were reduced almost threefold and amplitude fluctuations were largely removed apart from a few percent constant ripple associated with argon ion pump 3-phase regulated power supply. There was a higher frequency modulation (Figure 3.12a) at around 1 MHz which manifested itself as amplitude modulation sidebands about the 200 MHz carrier (figure 3.12b) but these could be readily removed by the limiter. The origin of this

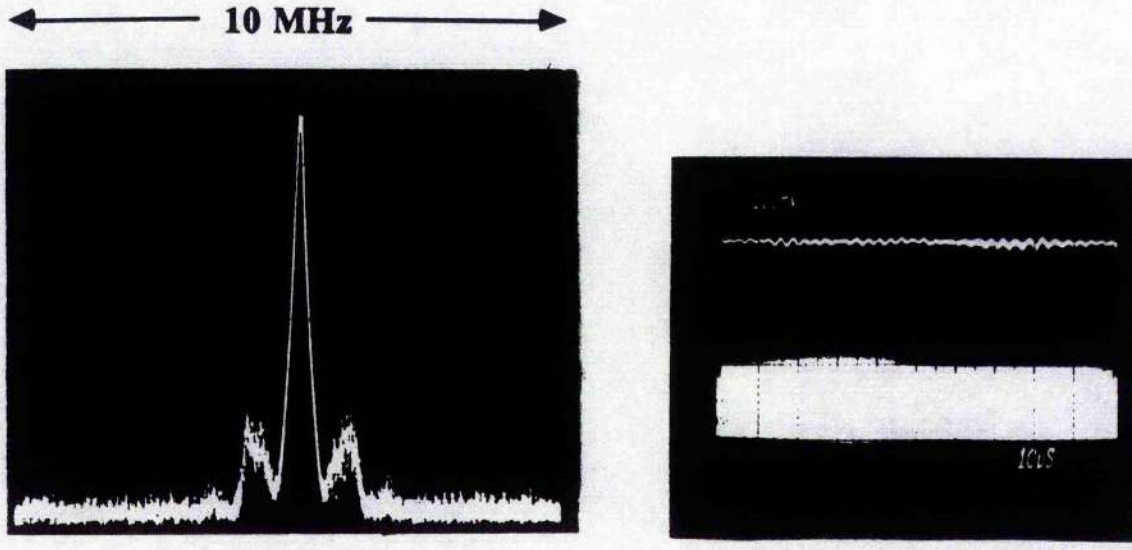

(a) (b)

Figure 3.12 a) High frequency modulating sidebands on 200 MHz Fourier component and b) associated modulation present in electrical pulse train.

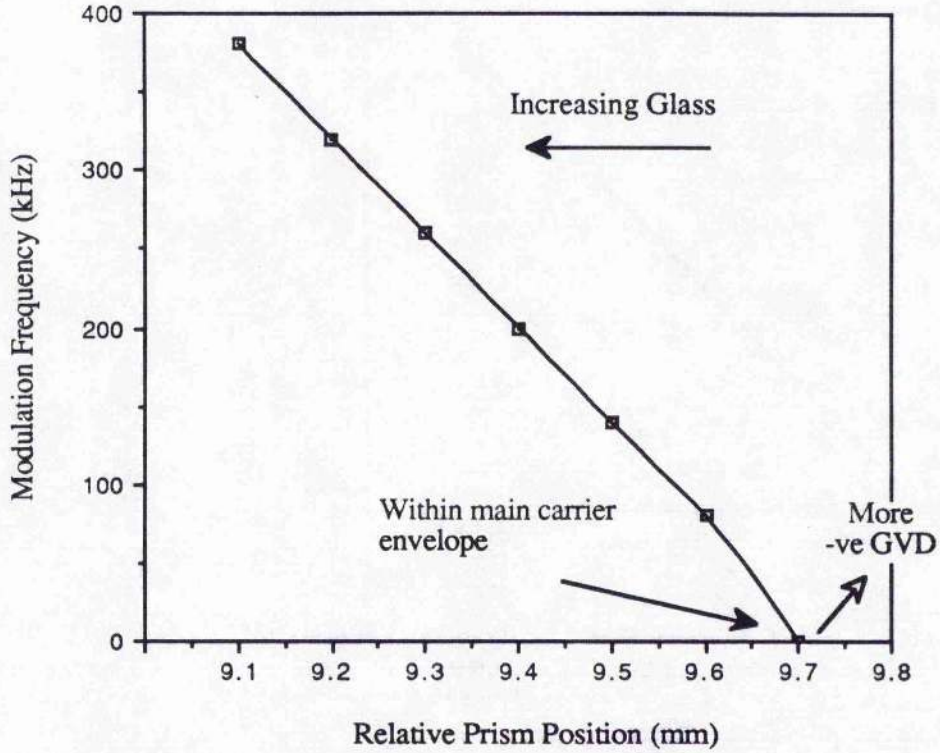

Figure 3.13: Modulation frequency as a function of prism position

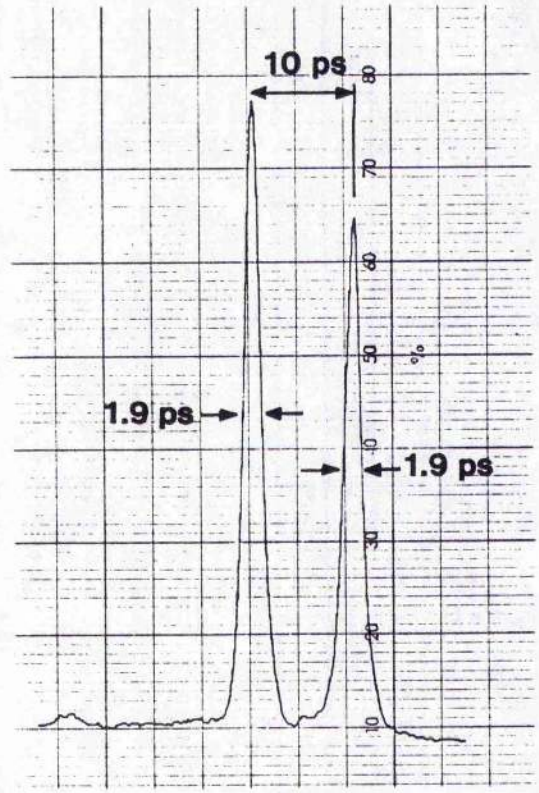

Figure 3.14 Optimum realtime temporal resolution obtained Photochron IIA streak tube

modulation is unknown as it does not originate from the pump laser. The modulation frequency has a dependence upon the amount of dispersion in the cavity as is shown in figure 3.13. Adding excess negative GVD (removing prism glass) had the effect of reducing the modulation frequency thus pushing the sidebands closer towards the central carrier until they disappeared inside the latter's envelope. Further removal of glass caused the sidebands to reappear and increase in frequency. Optimum synchroscan temporal resolution was usually observed when the modulation frequency was a minimum. With the limiter rail voltages adjusted to minimise sideband content the best temporal resolution measured on the Photochron IIA was 1.9 ps realtime (Fig. 3.14).

3.6 CONCLUSIONS

A passive synchronisation system has been developed which has proved simple to use and applicable to many mode-locked sources. As previously observed with synchronously-pumped systems [2] laser stability is vital if optimum synchroscan results are to be obtained. Furthermore, it is important that the synchronisation circuitry itself does not introduce any jitter into the system. This point is examined in more detail in the next chapter.

REFERENCES

1 R.Hadland, K.Helbrough and A.E.Huston, Proc XIIth ICHSP 107 (1974)

2 M.C.Adams, W.Sibbett and D.J.Bradley, Opt. Comm **26** 273 (1978).

3 M.C.Adams, D.J.Bradley, W.Sibbett and J.R.Taylor, Phil. Trans. R. Soc. Lond. **A298** 217 (1980).

4 W.Sibbett, Proc. XVth ICHSPP SPIE **348** 15 (1982).

5 M.C.Adams, D.J.Bradley, W.Sibbett, Adv. in Elect. and Electron Phys. **52** 265 (1979).

6 W.Sibbett, W.Sleat, J.R.Taylor and J.P.Willson, Proc. XVth SPIE **348** 278 (1982).

7 J.P.Willson, W.Sibbett and W.E.Sleat, Opt. Comm. **42** 208 (1982).

8 I.White, Rad. Commun. (1984).

9 M.Dishal, IEEE Trans. **MMT-3** 696 (1965).

10 M.J.Eccles, E.Sim and K.P.Tritton, *Low light detectors in astronomy*. Cambridge University Press (1983).

11 F.Salin, P.Grangier, G.Roger and A.Brun, Phys. Rev. Lett. **56** 1132 (1986).

12 D.S.Evans, G.R.Jessop, *VHF - UHF MANUAL* Radio Society of Gt. Britain, London 5.30 (1976).

13 F.Langford-Smith, *Radio Designers Handbook*, Iliffe & Sons, London (1957).

CHAPTER 4: SYNCHROSCAN OPERATION OF THE PHOTOCHRON IV STREAK CAMERA

4.0 INTRODUCTION

Experimentation was extended to the Photochron IV tube design for several reasons. Primarily the camera was of enhanced design with proven temporal resolution (single-shot <800fs [1]) better than its Photochron IIA counterpart and consequently ultimate limiting synchroscan performance should be improved. Further it was proposed to carry out some initial tests of external CCD readout systems. Having no intensifier the sensitivity of the CCD head was relatively low compared to the SIT Vidicon OSA system and so a high brightness streak image at the phosphor was most appropriate. The Photochron IIA with its MCP intensifier would saturate for large input intensities and so of little use in CCD evaluation studies, whereas the Photochron IV containing no internal intensifier had a much larger dynamic range and peak phosphor intensity.

4.1 STATIC PERFORMANCE

The streak tube, constructed by EMI, had an excellent electron-optical imaging system. Typical operating voltages are higher than the Photochron IIA and are summarised in the table below.

Table 4.1 Typical operating voltages (kV) of the Photochron IV

Photocathode	First Focus Mesh	First Electrode	Second Focus Anode	Second Electrode	Anode
-15	-6.5	-8.02	+5.05	-10.38	0

The camera tube is designed specifically for streak applications; electron-optic lensing aberrations are minimal and voltages are maintained high throughout the lensing section to minimise transit time dispersion. It was recognised at an early stage, employing the computer modelling programs discussed in Chapter 2, that increasing the photocathode to mesh differential voltage would improve the static resolution. Increasing this voltage caused the electron beam waist to be focussed closer to the anode aperture. Table 4.2

shows the measured static resolution of the Photochron IV for three different mesh voltages and corresponding axial E-fields (E_{pc}). Resolution was measured using a standard USAF resolution chart (see §5.5). The large error in the quoted value of E_{pc} is due to a manufacturing uncertainty in the mesh to cathode separation (3.5-4.0 mm). The spatial resolution quoted is that seen at the photocathode screen and should be compared to the static performance of the Photochron IIA of less than 35 lp/mm.

Table 4.2 Spatial resolution of Photochron IV at different mesh Voltages

Mesh Potential relative to Photocathode (kV)	E_{pc} (kV/cm)	Spatial Resolution at Photocathode (lp/mm)	Magnification
8.5	22.7 ± 1.4	50	2.2
11.0	29.3 ± 1.9	60	2.1
13.5	33.8 ± 2.3	70	2.0

4.2 DYNAMIC PERFORMANCE

The streak tube deflectors were made part of a 200 MHz resonant circuit. Problems were initially encountered in making good electrical contact with the deflector feed-through pins. Whereas in the Photochron IIA tube each feed-through had screw threads available for connection, the Photochron IV was fitted merely with smooth kovar pins. By bonding selectro-plug fittings to these pins with silver loaded epoxy good electrical contact was made and allowed the facility for the air-spaced tuning capacitor to be connected via a push-on fitting. RF power required for full screen deflection was noticeably higher at 5 Watts than for the Photochron IIA which is to be expected for the higher tube operating voltages and hence increased electron velocity at the deflectors.

Operating with the identical input lens/slit arrangement and OSA readout the camera was synchronously streaked as before. Results were quite perplexing at first in that the normal calibration streak images were double humped in nature as shown in fig.4.1 (These

results were recorded using a CCD camera/framestore system which is discussed in Chapter 5.)

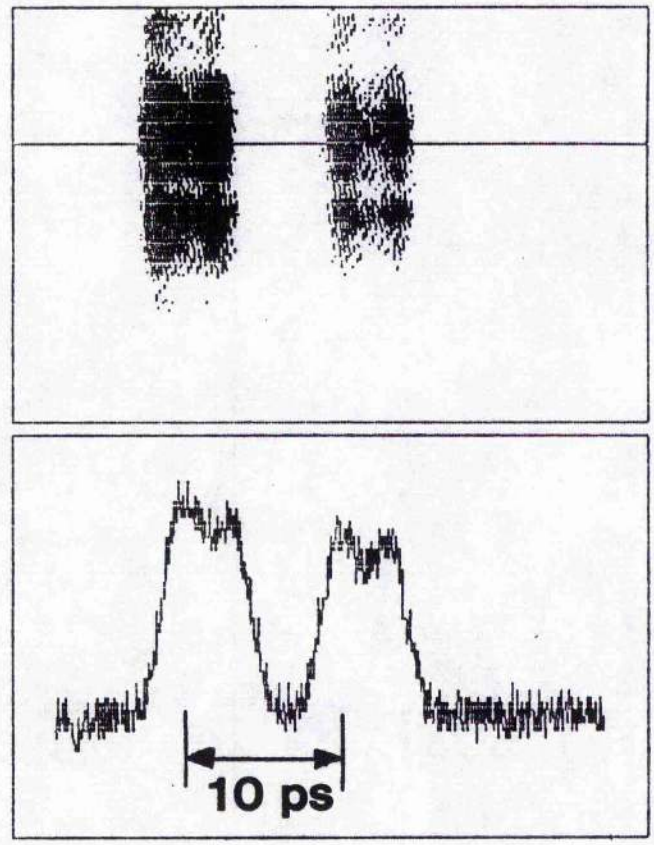

Figure 4.1 Double humped streak image readout by a CCD digitisation system

The two pronounced peaks on each pulse were very stable and independent of the illumination angle at the slit and their source was not traced until refocussing was attempted. It was found that by adjusting the mesh voltage the splitting of the two peaks could be varied and it was concluded that the problem was due to RF coupling into the mesh and possibly other electrodes. The RF voltage developed at the mesh would act to modulate the electron velocity and hence its arrival time at the phosphor. The solution was to connect high voltage capacitors between the front end tube electrodes and by screening all voltage leads, the tube chassis could be effectively decoupled from any RF influence. Such action removed this RF power splitting and thus the streak resolution was enhanced considerably.

Under optimum operation with rail voltages in the limiter adjusted to remove nearly all sideband content the best synchroscan temporal resolution obtained for the Photochron IV streak tube was 1.3ps realtime and 1.1ps for a 1ms shutter period (see fig. 4.2). Typical operating resolution was 1.4 ps.

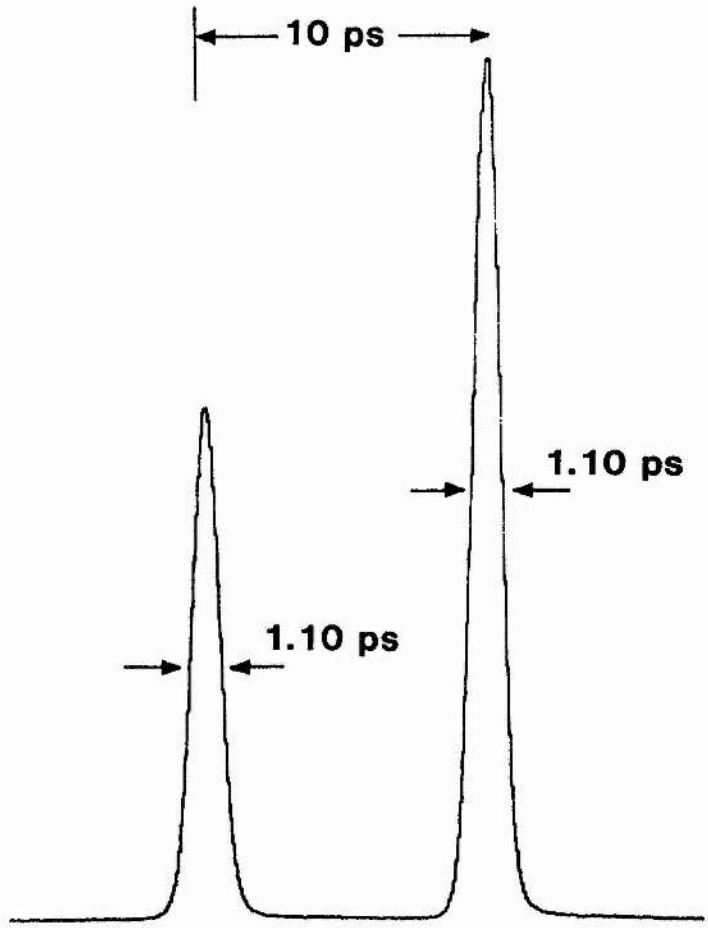

Figure 4.2 1ms shuttered streak images of Photochron IV operating with passive synchronisation

4.3 ACTIVE SYNCHRONISATION

As a comparative study it was decided to re-employ the tunnel diode synchronisation system in conjunction with the limiter circuit (Fig. 4.3). Generating our own terminology this type of synchroscan operation was labelled *active synchronisation* since the deflection

signal source was effectively an oscillator driven by the laser system. Conversely the direct photodiode-200 MHz filter circuit system was termed *passive synchronisation.*

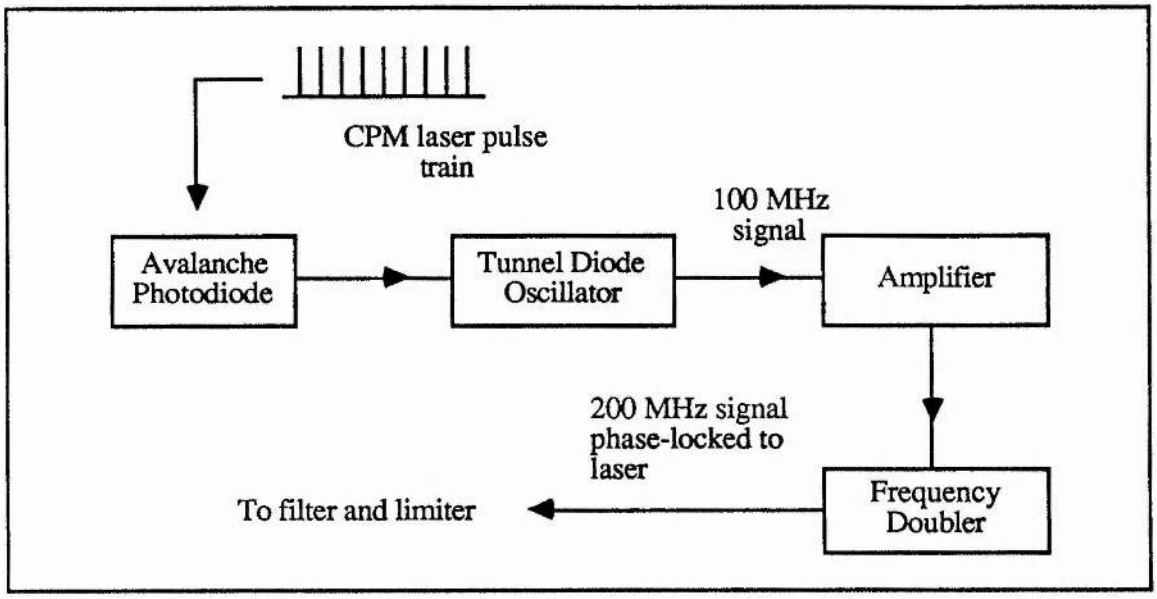

Figure 4.3 Active synchronisation system

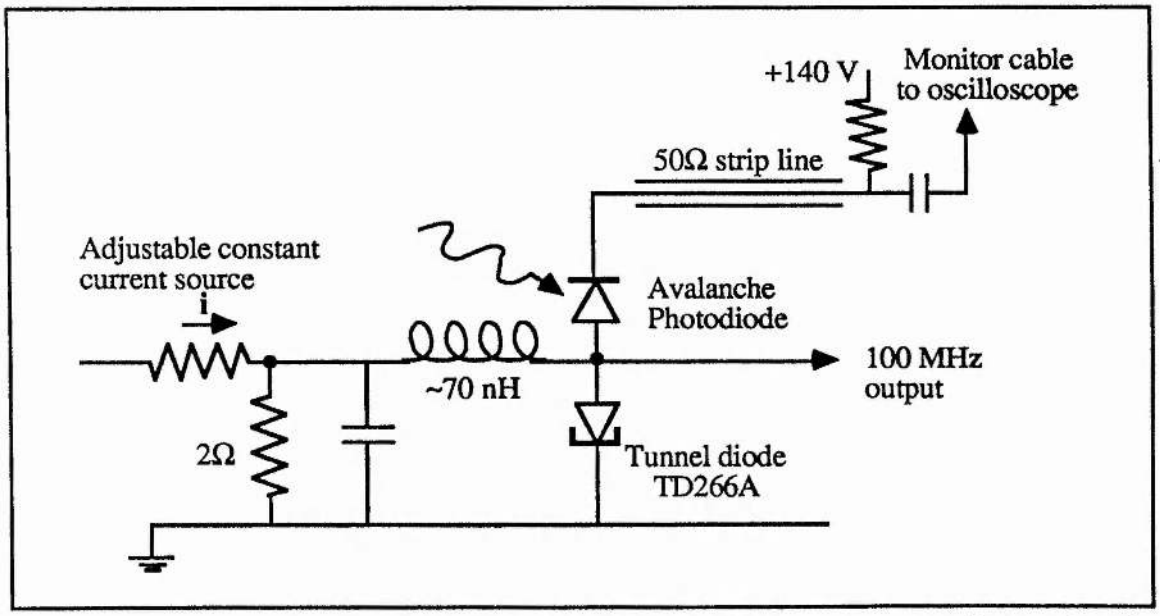

Figure 4.4 Tunnel diode oscillator trigger circuit

The tunnel diode circuit is shown in detail in Fig. 4.4 and is based on a countdown oscillator used in the trigger synchronisation circuit for the Tektronix 519 oscilloscope [2]. The tunnel diode, having an intrinsic negative resistance, will show monostable operation when formed part of the above resonant circuit and loaded accordingly. Fig. 4.5 shows the

I-V characteristic of the tunnel diode employed (General Electric TD266A [3]). The 2Ω load provides a single stable operation point at A which is just below the diode's region of negative resistance – the actual bias position being determined by the current supplied from an adjustable constant current supply.

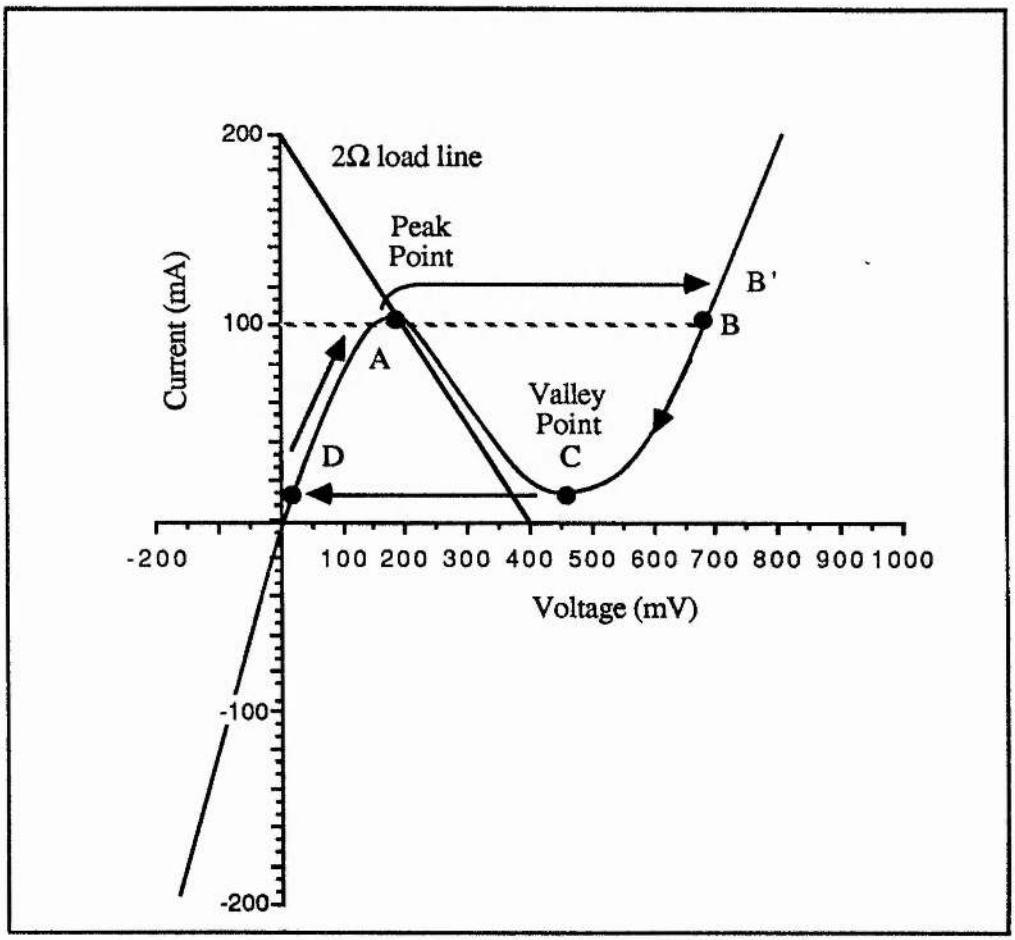

Figure 4.5 I-V Characteristic of TD266A Tunnel Diode

When a light pulse is incident at the avalanche photodiode additional current is supplied to the tunnel diode and its operating point switches to the high-voltage point B' along the constant current path AB', the current held constant by the action of the inductance. When the photodiode transient current is removed between light pulses the operating point moves to B. At this point the energy in the inductance must be dissipated before the circuit can be returned to its original operating point. As the inductance energy decreases the operating point moves along the forward diode characteristic to the valley point C where the presence of the inductance causes switching to occur along a constant current path to the operating

point D. The cycle of operation is then completed by a recovery period during which the inductance energy builds up and the operating point moves up the diode characteristic to the starting position A before the next light pulse arrives at the photodiode.

Choosing a inductance value such that its combined discharge and recovery time is around 10 ns allows the monostable circuit to switch at precisely the repetition rate of the CPM laser. This inductance value is not too critical, as long as the circuit can recover in less than one cavity roundtrip the switching of the photodiode will act to phase-lock the oscillation to the cavity frequency. Following the tunnel diode output the signal is amplified and then frequency doubled before being inputed to the 200 MHz filter and limiter circuit as before.

Operation of this form of synchronisation circuit is not as straightforward as the passive configuration. Optimum temporal resolution was found to be dependent not only on limiter rail voltage but also on the photodiode monitor cable length. This effect may be due to a resonant reflection of a higher Fourier component of the pulsetrain spectrum which will act to cancel out a ringing voltage on the electrical pulse or alternatively enhance the pulse risetime. Once properly adjusted, however, the system consistently gave better temporal resolutions compared to the passive system, these results are discussed in section §4.4.

4.4 PHASE NOISE SOURCES AND EFFECTS

As already discussed in Chapter 3 the ultimate synchroscan resolution is limited by phase noise in the drive signal. Since the tunnel diode system showed improved performance compared to the passive system the effect of phase noise in the drive signal was examined in more detail, the deviating effect of noise being extended to accommodate a general noise floor distribution rather than the specific sidebands considered in the previous chapter.

There are several possible sources of phase noise in the synchronisation circuitry; part is laser-related and part is generated internally in the electronics. Laser pulse train amplitude fluctuations are monitored as a modulation in the initial photodiode electrical signal. The effect of ampliude modulation inside the limiter has already been discussed, but there is an

analogous effect in the tunnel diode system. Any variation in switching current implies a triggering jitter between points A and B' and hence once more laser amplitude fluctuations are mapped into phase modulations in the synchroscan drive signal. Thus, although the laser source is inherently stable in terms of phase noise, severe constraints are placed upon the constancy of its pulse train amplitude for both synchronisation techniques.

The active system has the advantage over its passive counterpart in that relatively high signal levels are maintained throughout and thus the system has a improved signal-to-noise ratio at the input. This will only be important if the main noise source is not from laser amplitude fluctuations but from the photodiode itself. In addition the active circuit will also be less susceptible to electromagnetic interference which can be a problem with the high gain and high deflection powers employed. Fundamental noise sources, eg. Johnson noise in the input stage, may also be less influential in the active system which has a lower source resistance, although it is difficult to quantify this figure for the two systems.

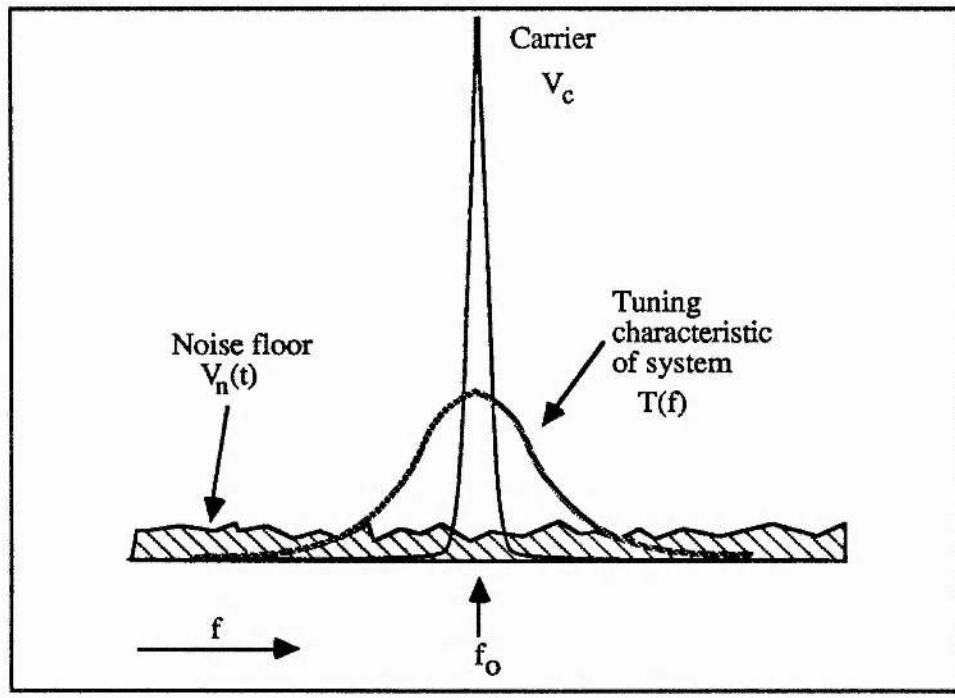

Figure 4.6 Representation of phase noise and drive signal in synchroscan circuitry.

To determine the effect of such broadband noise sources on the achievable temporal resolution during synchroscan operation a more detailed theoretical analysis was

performed.[4] In this analysis the input drive signal is treated as a single component of frequency f_o which sits on a noise floor having an instantaneous amplitude $V_n(t)$ and random fluctuation (See Fig. 4.6). The noise floor is assumed to originate from many sources but can be taken to have a uniform spectral distribution which will be tailored by the tuning characteristics of the circuit, T(f). (This is not necessarily true for a nonlinear limiting circuit but for the purposes of this preliminary analysis this was ignored.) The instantaneous integrated deviating voltage is given by :

$$V_N(t) = \int_0^\infty V_n(t).T(f).\exp\{i[\emptyset(f,t)]\}df \qquad \text{–eq(4.1)}$$

where $V_n(t)$ is the instantaneous amplitude of a noise sideband frequency component at frequency f and $\emptyset(f,t)$ is its instantaneous phase. T(f) is the tuning characteristic of the electronic circuit which will act to tailor the noise floor frequency distribution. Effectively $V_N(t)$ is the sum of a continuous set of uncorrelated oscillators weighted by the bandpass response of the system. Evaluation of the distribution of deviating voltages represented in equation 4.1 is extremely difficult using numerical techniques without knowledge of the noise floor distribution. Nonetheless, since noise content in a signal is often measured in terms of noise power within a given bandwidth it is instructive to represent V_N by a Gaussian distribution:

$$\mathcal{P}\{V_N(t)\} = \frac{1}{\Delta V_m\sqrt{2\pi}}\exp\left[-\frac{1}{2}\frac{(V_N - V_m)^2}{\Delta V_m{}^2}\right], \qquad \text{–eq(4.2)}$$

where V_m is the root mean square voltage obtained from the noise power appearing at the deflector plates and its variance, $\Delta V_m{}^2$ taken as a fixed percentage of the mean. Hence the instantaneous drive signal applied to the deflector is given by the sum of the carrier and the deviating noise contribution such that:

$$V_S(t) = \text{Im.}[V_c\exp\{i(2\pi f_o t)\} + V_N(t)\exp\{i\emptyset\}] \qquad \text{–eq(4.3)}$$

where $\emptyset$, the phase of the deviating integrated noise voltage, will be uniformly distributed between 0 and 2π. For a particular streak operation the deviating voltage is calculated by a Monte-Carlo method.

The electron trajectory within the streak tube was calculated by the Runge-Kutta technique (§2.5) where the potential distribution of the Photochron IV was determined by a finite difference solution of the Laplace equation. The computational process and the various distribution functions used are summarised schematically in Fig.4.7.

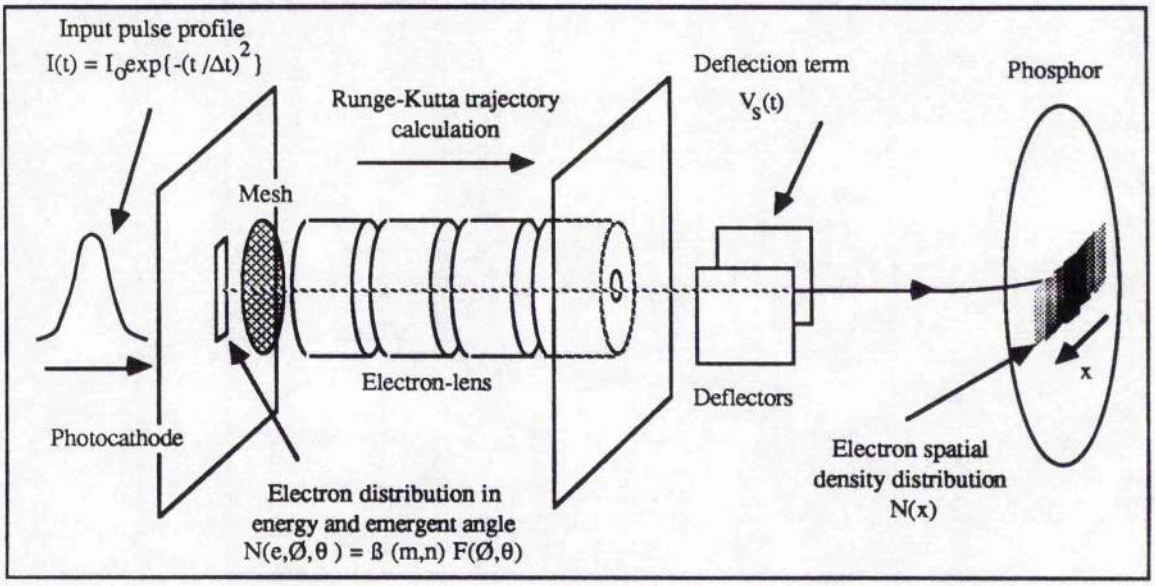

Figure 4.7 Schematic of calculation process used in computer model.

A Gaussian input optical pulse profile of duration 300 fs was assumed. The distribution of electron energies leaving the photocathode was modelled by a Beta function and the distribution in exit angles modelled by a Lambertian function giving uniform and cosine distribution for angles in the photocathode plane and normal respectively [5]. Again a Monte-Carlo technique was used to generate the initial values. For each streak the electron density distribution appearing at the deflectors was computed and the above expression representing the total deflection voltage was then mapped onto this distribution to generate a spatially varying electron density profile at the phosphor screen. The magnitude and phase of the deviating noise voltage was assumed not to vary as the electron distribution was deflected on the basis that the bandwidth of the deflection system would limit fluctuations to a few megahertz and consequently during the transit time of the electrons through the plates (~0.5 ns) any additional variation of the deviated deflection voltage would be minimal. Provision was made for a second term in the input pulse profile to represent jitter between the laser and the deflection signals. These calculations were then performed over a

total of 10^4 streaks and an integrated spatial electron density profile N(x) was generated. With a knowledge of the streak velocity (0.65×10^9 cms^{-1} @ 15 Watts) N(x) was transformed into a temporal spread distribution from which the temporal resolution was deduced. This process was repeated for a range of noise powers.

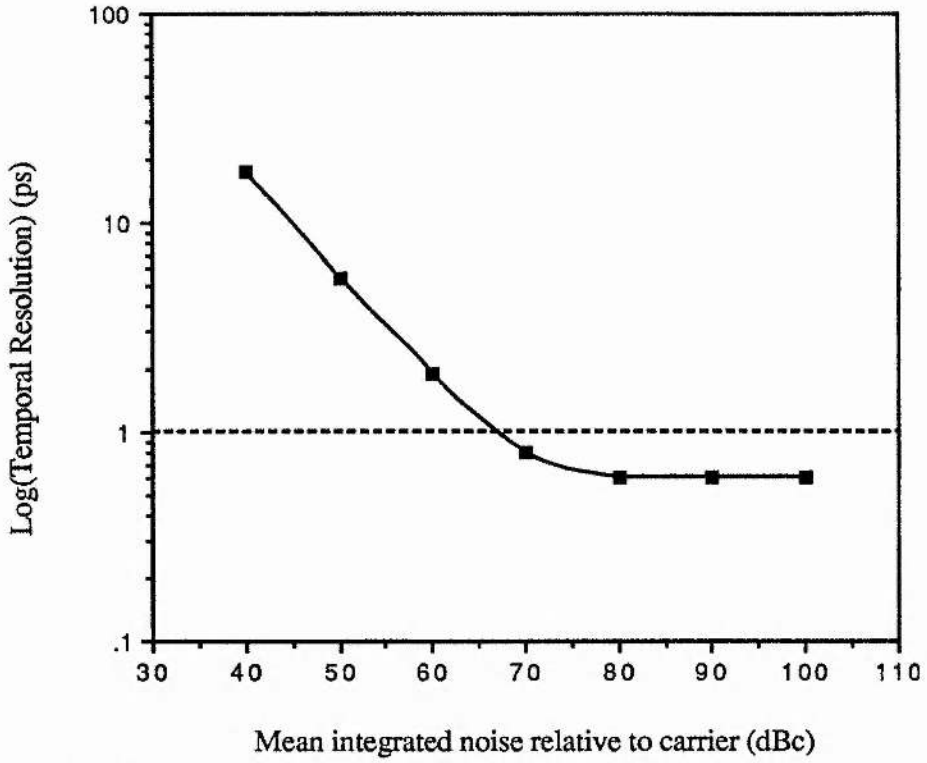

Figure 4.8 Achievable temporal resolution as a function of integrated noise level with respect to carrier signal.

Figure 4.8 shows the expected temporal resolution as a function of integrated noise level with respect to the carrier signal ($20\log_{10}(V_C/V_N)$). Note that for noise levels below 80 dB with respect to the drive signal the achievable resolution is almost equal to the theoretical tube limiting temporal resolution. Between 80dB and 70dB temporal response begins to be degraded until at 60dB the available resolution is nearly 2 ps which exceeds the limiting temporal resolution by a factor of more than three.

4.5 Noise levels in passive and active synchronisation systems

The actual integrated noise floor values for the two synchronisation systems was estimated by examining the 200 MHz drive component on a high resolution spectrum

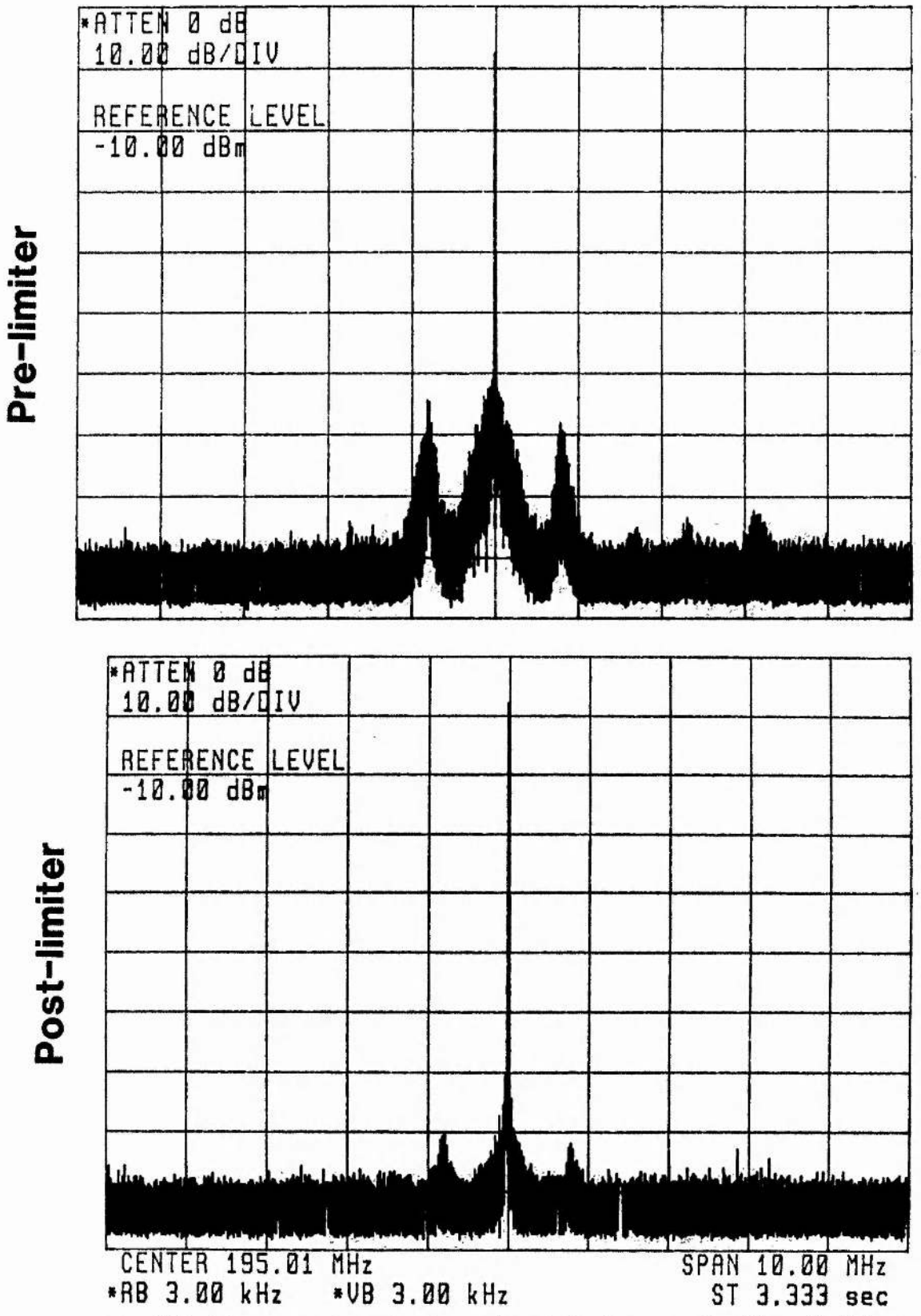

Figure 4.9 200 Mhz synchronisation signal before and after limiting obtained from passive system.

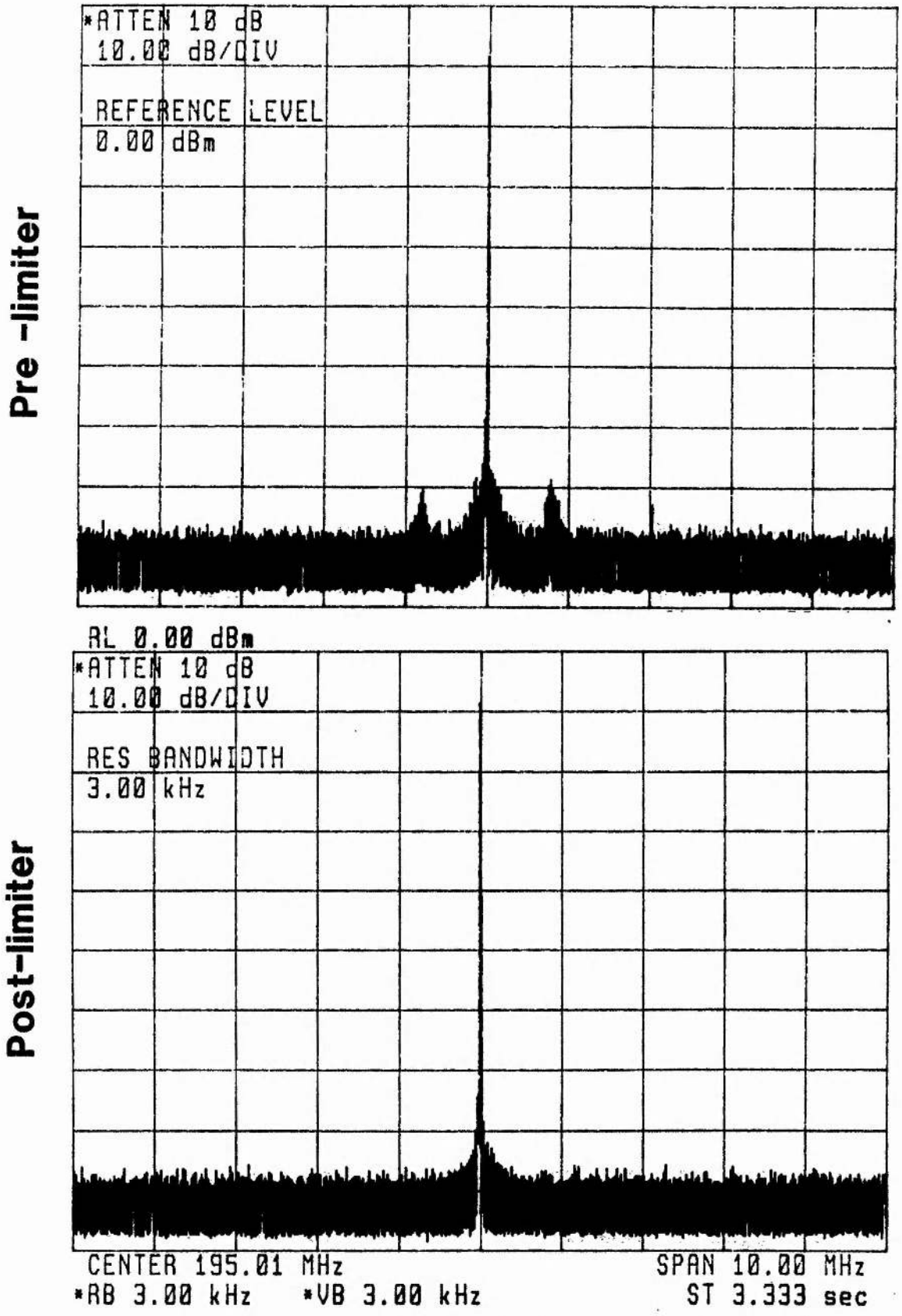

Figure 4.10 200 Mhz synchronisation signal before and after limiting obtained from active system.

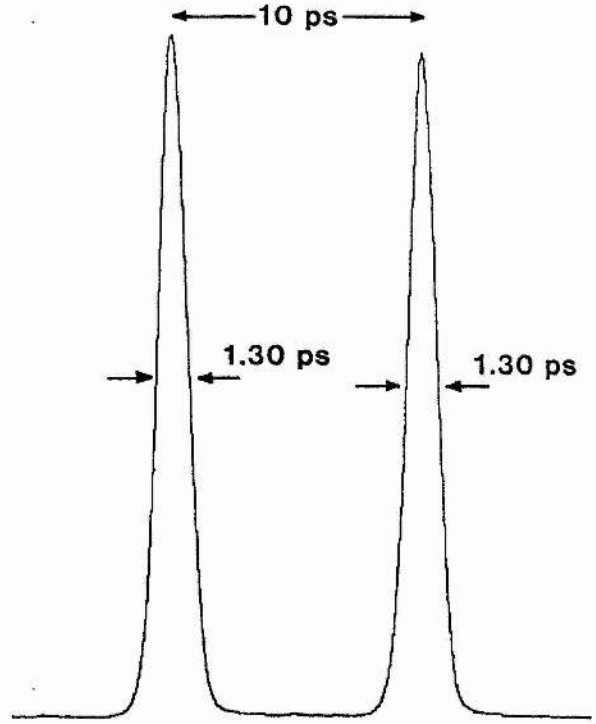

a)

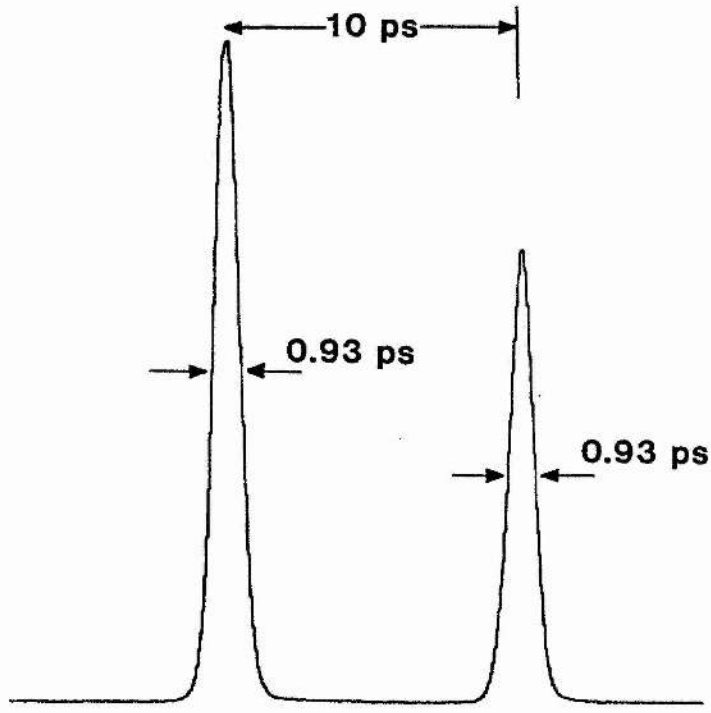

b)

Figure 4.11 a) Realtime and b) 1 ms shuttered streak images employing active synchronisation.

analyser (HP70900). Figures 4.9 and 4.10 show the 200 MHz components for the passive and active synchronisation systems respectively both before and after the limiter. It can be seen clearly that in the tunnel diode system the limiter has to remove a much lower sideband content and consequently the saturation effects discussed in §3.3 will be lessened compared to the passive circuitry. Typical integrated noise powers for the passive system were estimated to be 65dB below the carrier whereas for the active system this was improved to around 70dBc. These values would indicate, from the above calculation, temporal resolutions of 1.1 and 0.87 ps respectively for a shutter time of 100μs (10^4 streaks). Actual values for the passive system with a 1 ms shutter time have been shown to be the same between 1.1 and 1.2 ps. When the active system was fully optimised realtime resolutions were consistently around 1.3 ps and when shuttered for 1 ms the resolution limit was as low as 0.93±.01 ps (see figure 4.11) This is the best synchroscan temporal resolution ever reported and the experimental value is close to the above calculation.

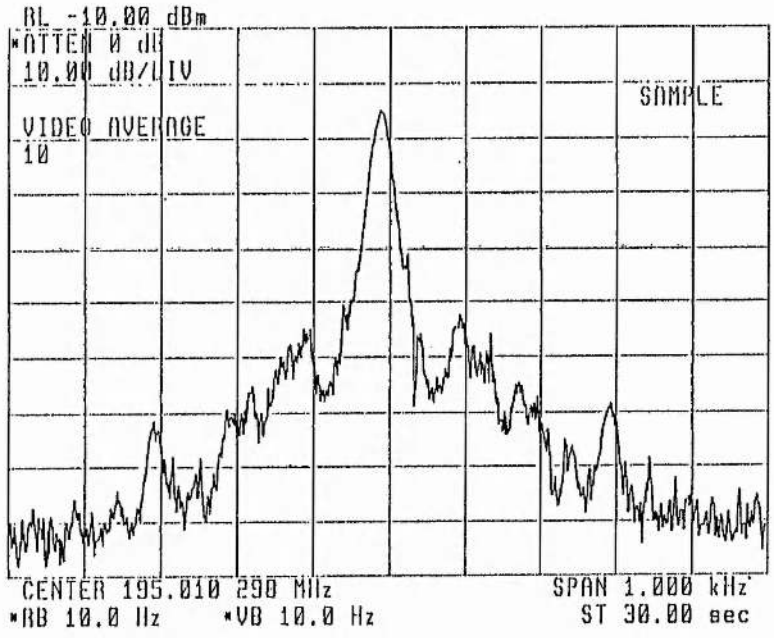

Figure 4.12 Close in noise content of 200 MHz Fourier component.

The effect of shuttering is to remove the deviating effect of phase noise near (<1kHz) to the 200 MHz carrier. Figure 4.12 shows a high resolution spectrum of the avalanche photodiode signal. Most of the noise is low frequency amplitude variations due to pump

laser modulation and possibly some phase modulation due to dye jet turbulence. The intrinsic noise content of the diode detector itself is yet to be assessed.

4.6 CONCLUSIONS AND FUTURE WORK

The correlation of both experimental and theoretical data between synchroscan temporal resolution and noise content in the drive signal implies that all noise sources should be identified and removed or their effect minimised. The improvement in synchroscan performance using the tunnel diode in conjunction with the limiter is encouraging but operation is not simple or optimised. The dominant phase noise source is, in all likelihood, the avalanche photodiode, its cascade gain process being inherently noisy. Currently available GaAs photodiodes with risetimes of ~ 5-10ps [6] deliver peak currents of order 1mA into 50Ω for illumination with CPM laser pulses. Use of these input photodetectors as the initial switching current source and the construction of a resonant circuit employing a tunnel diode with a lower peak point current (10mA-TD263B) should offer several advantages. The photodiode has excellent phase noise properties since no avalanche processes occur and charge transport only is involved. The extremely fast photodiode risetime coupled with the lower tunnel diode inductance (0.15 nH as opposed to 1.5 nH) reduces the amplitude-dependent trigger jitter and hence the whole circuit will be less susceptible to laser amplitude fluctuations and fundamental noise sources.

It follows that, with this circuitry development, a complete characterisation of noise sources in the laser and electronics is required. This can be achieved by detailed spectral analysis of mixed harmonics of the diode Fourier components with reference oscillators [7] or Fourier analysis of high harmonics of pulse train spectra [8,9]. If it is possible to reduce the integrated noise power to 80dB below the carrier then, in theory at least, we should observe synchroscan temporal resolutions which are limited by the tube design (ie in the femtosecond regime) rather than the deflection electronics. Naturally as the tube designs improve this noise minimisation criterion must be made more rigorous. Conversely, once optimised the synchroscan system can be used to characterise and quantify noise content in other mode-locked laser sources and/or photodetectors. This will aid the design and

development of low phase noise photodetectors which currently is of prime importance if short pulse high repetition rate laser sources are to be implemented in telecommunications and optical data processing applications.

REFERENCES

1 M.R.Baggs, R.T.Eagles, W.Margulis, W.Sibbett and W.E.Sleat, Adv. Electron. and Electron Phys. **64B** 617 (1985).

2 Tektronix, *519 Instruction manual.*

3 *Semiconductor data handbook* 2nd Ed. General Electric Company, New York P.120 (1973).

4 A.Finch, Y.Liu, W.E.Sleat, W.Sibbett and G.Chen, Proc XVIIIth ICHSPP (1988) To be published.

5 O.Klemperer and M.E.Barnett, *Electron Optics* 3rd Ed. Cambridge University Press (1971).

6 D.G.Parker, P.G.Say, A.M.Hansom and W.Sibbett, Electron. Lett. **23** 527 (1987).

7 *Phase noise characterisation of microwave oscillators*. Hewlett Packard Product note 11729C–2.

8 U.Keller, K.D.Li, M.J.W.Rodwell and D.M.Bloom, IEEE J.Quant. Electron. To be published.

9 *Measuring phase noise with the HP3585A spectrum analyser*. Hewlett Packard, application note AN 246-2.

CHAPTER 5. SOLID-STATE STREAK CAMERA READOUT SYSTEMS

5.0 INTRODUCTION

The full impact of Charge Coupled devices (CCD's), as solid state image sensors, is only just beginning to manifest itself in the commercial world. Since their invention in the early seventies [1] CCDs have found many uses both as imaging devices and memory stores. With the advent of new large format, high pixel number area CCD's in the not too distant future a new generation of imaging devices will appear. Computer interfacing of such devices, allied with sophisticated image processing has generated an enormous market. Predicted sales of imaging systems in the US industry alone by the early nineties are in excess of £1bn with a growth rate of over 15 percent per annum [2]. Many applications are in medicine, robotics, industrial processing, intelligent monitoring and telecommunications. Indeed even over the period of this research use of CCD's have become widespread in the field of high speed photography and photonics [3,4] and particular interest has been shown in their use as alternative readout systems for ultrafast electron-optical imaging instruments such as streak cameras. CCD's have several distinct advantages over their vidicon counterparts including: no geometric distortion, uniform spatial resolution across the entire image area, large dynamic range and linear response, in addition to which they are physically compact.

Our research efforts have been primarily concerned with developing CCD readout systems for the recording of streak images where two approaches have been adopted. One has been the preliminary development of electron-sensitive photodiode/CCD arrays with both linear and circular formats for inclusion inside the vacuum envelope of a streak tube and thus dispensing with the tube phosphor and associated readout system. (This work was done in collaboration with C.Claeys and I.Debusschere at the Interunivestair Micro-Electronics Centrum (IMEC) in Belgium, who manufactured these devices). The other approach was related to the implementation of an area CCD array readout system for external readout of the streak image with a facility for subsequent digitisation and signal

processing. (This work was done with the aid of Professor R.Zhang and J.Wade who designed and constructed much of the electronics.)

The impetus for this research effort was initially born from an European Space Agency project to build a space-borne laser ranging system [5]. A streak camera based upon the *Photochron IIC* picosecond image tube is intended to form a major sub-component of this instrument [6]. The data from this camera will be read out via a CCD array designed to achieve an overall instrument time resolution of less than 6ps which is equivalent to a distance resolution of 1mm in free space. This chapter describes the operating principles of two separate area array CCDs image digitisation systems that have been constructed. The space project is described in outline (§6.0) and in greater detail in Appendix A. A detailed analysis of the main noise sources in CCD devices and a feasibility study for their use as readout device for laser ranging is given in a conference reprint in Appendix B. The design concept and preliminary evaluation of a pre-prototype internal readout system is the subject of the next chapter.

5.1 Charge coupled devices – an overview

As far as the use of CCDs for streak camera readout is concerned the parameters that need to be considered are the solidstate sensor's responsivity, limiting spatial resolution, dynamic range and saturation level. Associated with this is the prerequisite ease of interface to data processing be it hardware or computer generated. However it is perhaps worthwhile to discuss the underlying structure and mechanism of readout of the CCD in order to explain the various circuitries designed to run these devices and to enable an estimate to be made of a given CCD's expected performance.

5.1.1 Principle array types

There are three main types of commercially available area array imager all of which are designed with a compatibilty to the conventional 625/525 line TV technology. These array types are 1) inter-line transfer (ILT) arrays, 2) X-Y addressed (XY) arrays and 3) frame transfer (FT) arrays. Line-transfer sytems are manufactured mainly by Fairchild and Sony

and transfer photo-generated charge from pixels along shielded columns spaced between the active vertical photosensitive regions to a readout register clocked at TV line frequencies. X-Y addressed arrays usually store photogenerated charge in MOS capacitor pairs and readout of the signal achieved by monitoring voltage changes on the capacitance of the X and Y address registers. Manufacturers include Hitachi and General Electric who use photodiode detectors with the MOS pairs (these are called Charge Injection devices - CIDs). Frame transfer arrays integrate the image charge in one section of the device and then transfer the whole frame to a storage section which is then sequentially read out while the next frame is integrated in the image section. There are several manufacturers - EEV, RCA, Sanyo, Philips, Thomson-CSF, Tektronix and just recently Polaroid and Kodak. This device has the advantage that variable integration and slow clocking speeds can be used and offers the best resolution and sensitivity. ILT and XY arrays have poorer noise specifications compared to FT systems mainly due to a large fixed pattern noise contribution. For this reason the streak camera readout system that has been developed is built around an EEV FT array CCD chip, namely the P8602 [7].

5.1.2 BASIC OPERATING PRINCIPLES

An excellent review of the operating principles of CCD's has been given by Barbe [8]. CCD's in their simplest form are metal oxide semiconductor (MOS) structures as shown in figure 5.1. When a voltage is applied to the polysilicon/metal electrode of a MOS type capacitor band bending occurs at the Si-SiO_2 inteface. The effective voltage across the capacitor, $V_G - V_{FB}$ is distributed between the semiconductor (s/c) (giving rise to band bending) and the SiO_2 (causing the 'tilt' in energy bands). Since, for this p-type semiconductor, V_G is negative the electron potential at the s/c-insulator interface is lower under the electrode than in the bulk of the s/c. Hence a potential well is formed in the conduction band of depth $\emptyset_{so}$ which is the difference of the Fermi energies at the interface and in the bulk. Minority charge carriers can be collected and stored in these localised potential wells as a result of input diffusion, photogeneration or thermal generation and this redistributes the potential across the capacitor as is also shown in figure 5.1. These charge

packets can be transfered along the length of the structure (figure 5.2) by the movement of the potential wells using suitable adjustment of the voltages applied to the electrodes and

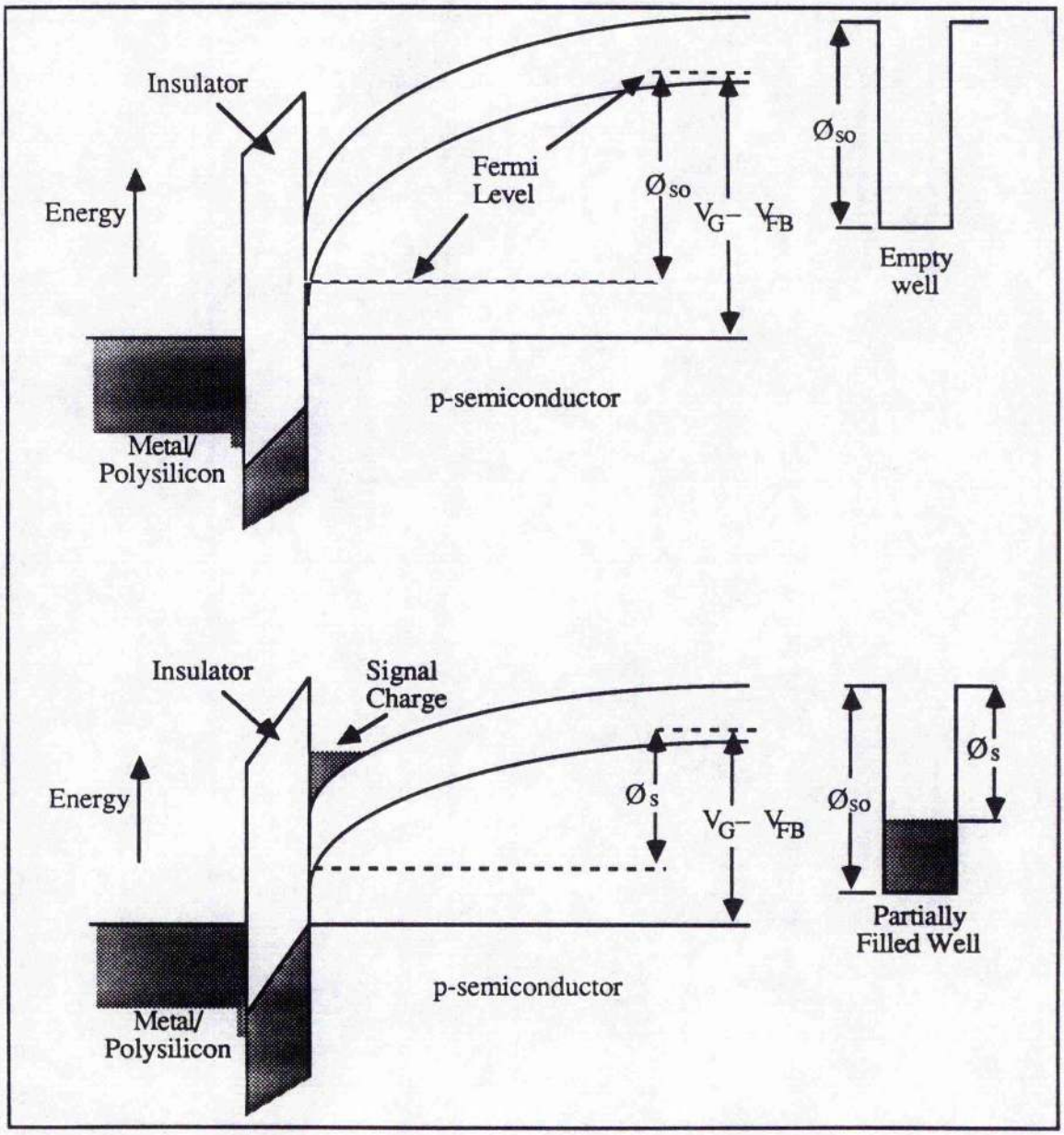

Figure 5.1 Energy band diagrams for a MOS capacitor (surface channel)

then detected at the output by charging a capacitor and monitoring its voltage. In effect the CCD acts as an analogue shift register - indeed this was the principal idea behind their initial development until it was soon realised that they could also be used as imaging devices. The potential well depth $Ø_{so}$ is controlled by gate voltage, doping density and

oxide thickness and consequently two methods of channel confinement (channel stops) are available – heavy doping implants and stepped oxide layers. Such techniques provide charge flow directionality in two phase CCD's and most kinds of area arrays. The problem of *blooming*, where signal charge from saturated wells spills over into adjacent cells, can also be suppressed by use of channel stops.

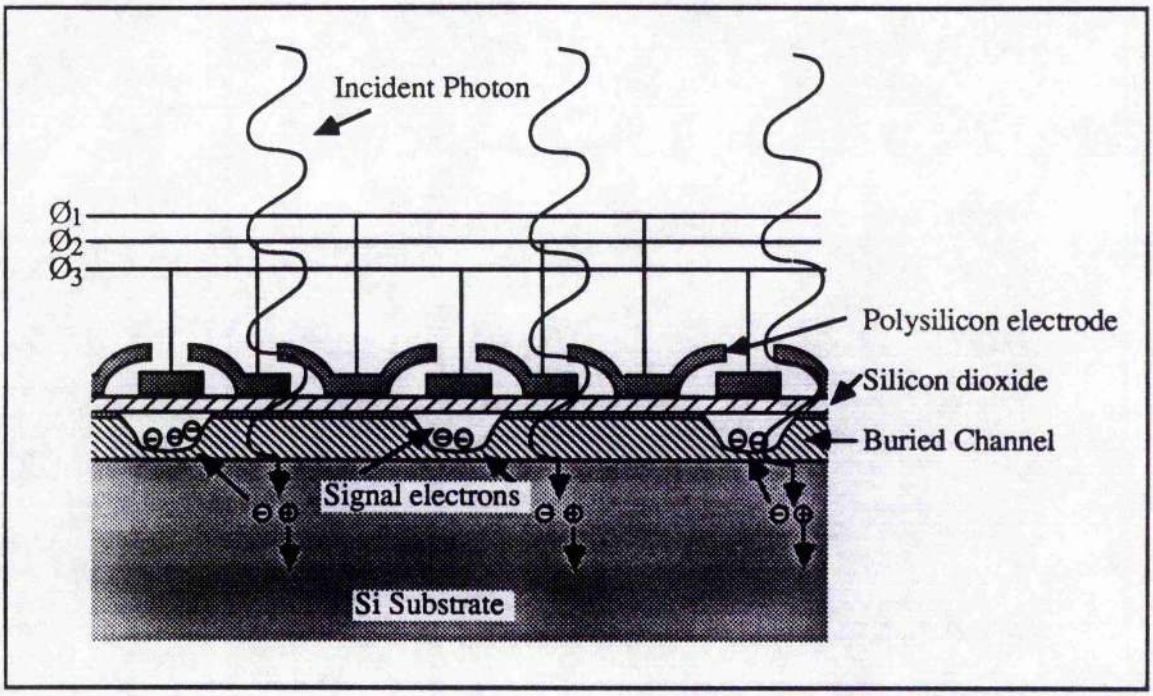

Figure 5.2 Section of a 3-phase CCD image sensor

Figure 5.2 differs in structure from the MOS capacitor represented in figure 5.1 in that a secondary layer of n-type silicon is formed between the oxide and p-type silicon. Such a *buried channel* device (bcd) is the usual format for CCD's nowadays. This format has several advantages in that lower electrode voltages are required for charge confinement and charge transfer is not susceptible to surface state trapping (see §5.1.3). Its main disadvantage is that the full well capacity is approximately one order of magnitude lower at ~5 x 10^5 electrons per cell as opposed to ~2 x 10^6 electrons for surface channel devices (scd). In general a CCD has three sections:

1) *The input section* - containing a diffusion acting as a source of minority charge carriers and whose potential can be varied, along with an input gate which can be turned on or off thereby controlling the flow of charge into the first potential well.

2) *The transfer section* - containing a series of electrodes which control the potential at the Si-SiO_2 interface. By suitable adjustment of the electrode voltages the potential wells can be made to move towards the output and the charge packets will follow.

3) *The output section* - in principal a reversed biased p-n junction capacitance whose voltage is changed when a charge packet is transfered into it. Diode reset is achieved via a reset switch to prepare the diode for the next charge packet. The output diode is usually connected to an on-chip MOS amplifier.

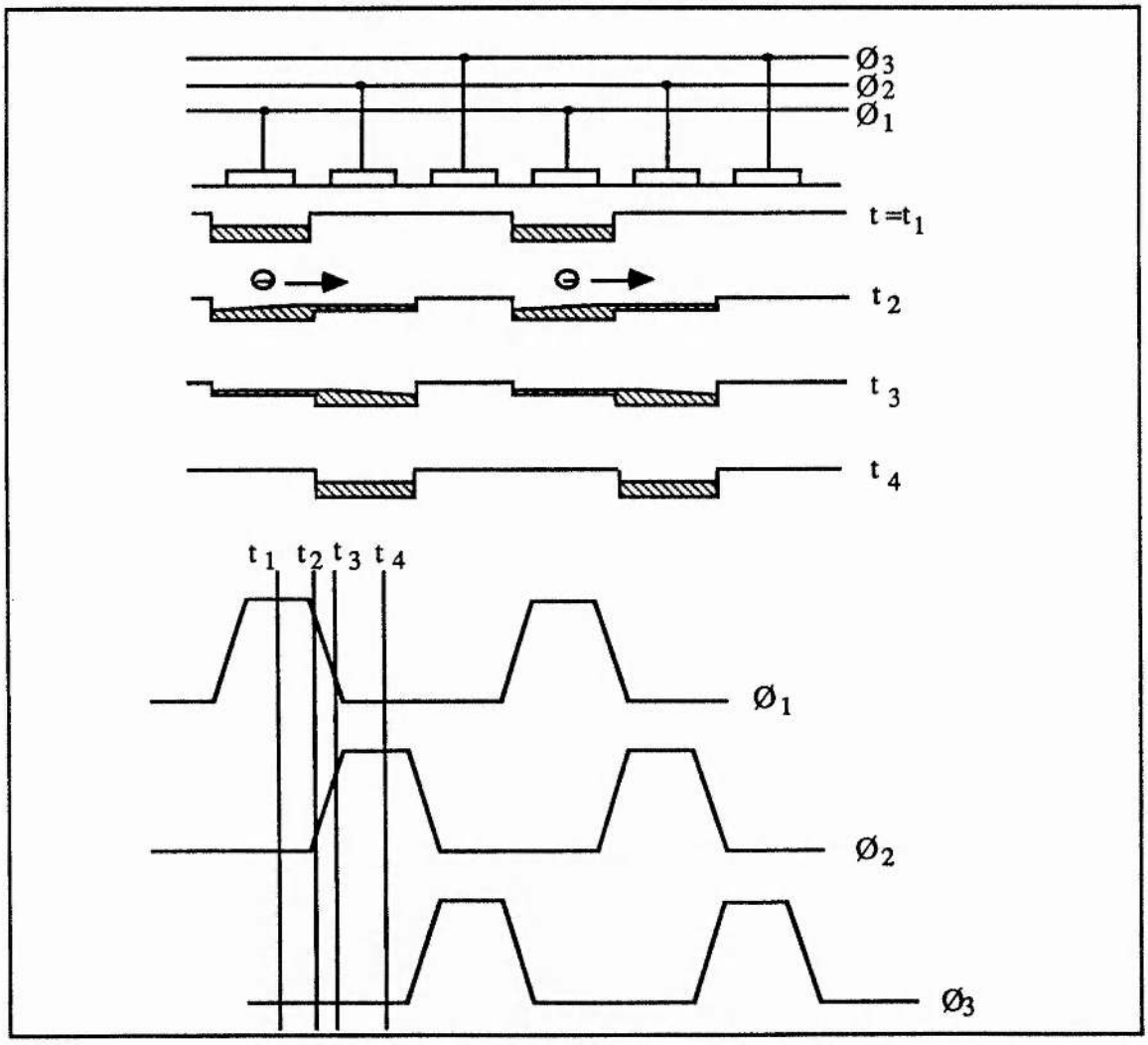

Figure 5.3 Transfer of charge in CCD over one clocking period

Minority charge can enter a well either via the input diffusion or by the absorption of photons or thermal generation within a diffusion length of the potential wells. Assume that a charge distribution exists as shown in figure 5.3. For a device with planar oxide and

uniform substrate doping, three sets of voltages or phases are required to transfer this charge - one phase to maintain a potential barrier behind the charge packet, one phase to maintain the potential well in which the charge resides and the other phase to provide a deeper well in front of the charge packet into which the charge will flow. Figure 5.3 also shows the clocking waveform diagram. At $t = t_1$ charge resides under the $\emptyset_1$ electrodes. At $t = t_2$ the potential on $\emptyset_2$ is made positive forming wells under these electrodes and charge then flows from the $\emptyset_1$ well into the $\emptyset_2$ well. At $t = t_3$ the potential at the $\emptyset_1$ electrode is reduced to a lower value and the remaining charge is "pushed" into the $\emptyset_2$ wells. This sequence is repeated such that the charge distribution moves from one cell to the next every clock period. Hence the clock rate is equal to the data rate.

Since the charge packets follow the movement of the potential wells which are in turn controlled by external voltages, by the construction of suitable electrode configurations, charge transfer may be achieved in two dimensions. The device can have multiple inputs and non-destructive outputs. It is an inherently low power device, requiring relatively low voltages for operation ($\emptyset_1 < 25$ V) and has a high packing density. As a result it is ideally suited for many imaging applications.

5.1.3 CHARGE TRANSFER MECHANISMS

Charge transfer has two contributors namely drift and diffusion. However in well designed CCD's drift processes are dominant in the transfer of charge from well to well - diffusion being minimised by suitable use of channel stops etc. Drift current has two components: 1) *Self induced drift* - caused by the electric field due to a non-uniform distribution of electrons under two equipotential electrodes and 2) *Fringe field drift* - caused by the electric field between two electrodes of differing potentials.

In general self induced drift is the dominant process at the onset of charge transfer whereas during the final part fringe field drift becomes important. Buried channel devices with n-type channel thicknesses >5μm can achieve very short charge transfer times compared to surface channel devices. The reason for this is that for the scd the surface potential in the p-type semiconductor is determined almost solely by the electrode voltage

above it and influenced little by neighbouring electrodes except at its extreme edge. For bcd formats the minimum potential is relatively far from the electrode plane and the potential under a given electrode is affected by adjacent electrodes. Hence during clocking the potential profile will have a greater degree of slope and the fringe field is larger in bcd fromats with a consequent faster transfer time compared to scds. In practice clocking speeds are usually limited by RC time constants of area array electrode structures in buried channel formats. For the particular case of the P8602 [9] frame transfer speeds up to 4MHz have been achieved.

A further disadvantage of scd formats over bcd, which limits the efficiency of charge transfer, is trapping at the Si-SiO_2 interface. The emission time of such interface states of energy E_t is proportional to $\exp[(E_c-E_t)/kT]$. Whether a state contributes to charge transfer inefficiency depends on its emission time relative to the clock frequency f_c. States near the conduction band edge rapidly emit trapped electrons after the charge transfer process has begun and so these electrons can rejoin the main charge packet. ie) traps with emission times $<< 1/f_c$ do not effect transfer efficiency. States having emission times $>> 1/f_c$ likewise do not effect charge transfer on a steady state basis as they result in almost permanent trapping. Transfer efficiency is effected predominantly by intermediate states (with emission times $\approx 1/f_c$) which trap electrons from one packet and emit them into a trailing packet.

Transfer inefficiency due to interface trapping can be offset to a certain extent by filling each well to a certain level - about 10 to 20 percent of saturation. This bias charge is often denoted by the term *fat zero* and it helps to keep the interface trapping states under the gates filled so that they do not trap signal charge. Each charge packet receives approximately the same number of electrons from the preceeding packet that it loses to the trailing packet. Interface states at the edges of the elctrodes however are not covered by the fat zero charge since the potential well wall is not vertical. The reduction in offset of the fat zero charge in these regions is called the *edge effect.*

A typical curve of transfer inefficiency, ε verses clock frequency has two regions. At low frequencies ε is limited by trapping processes and is nearly independent of f_c, whereas

at high frequencies ε is limited by free charge transfer processes - electron mobility etc, and increases sharply with f_c. Trapping processes are also present in bcd in the bulk of the device but their contribution towards ε is much smaller than the above interface trapping and fat zero offsetting is not required.

The effect of transfer inefficiency is to smear the signal charge being clocked out and, since it is a cummulative effect, is only important for large format CCD's.

5.2 THE P8602 AREA ARRAY

The CCD imager we have employed in the external streak camera readout system is the *EEV P8602* area array which offers high sensitivity (pixel saturation at video rates of 3 lux which is more than three times the sensitivity of any known alternative commercial device). It also has good spatial resolution (23 lp/mm) having 288 x 385 active elements, pixel dimensions being 22 μm square. The active area of the chip is 8.5 x 6.4 mm. The device is

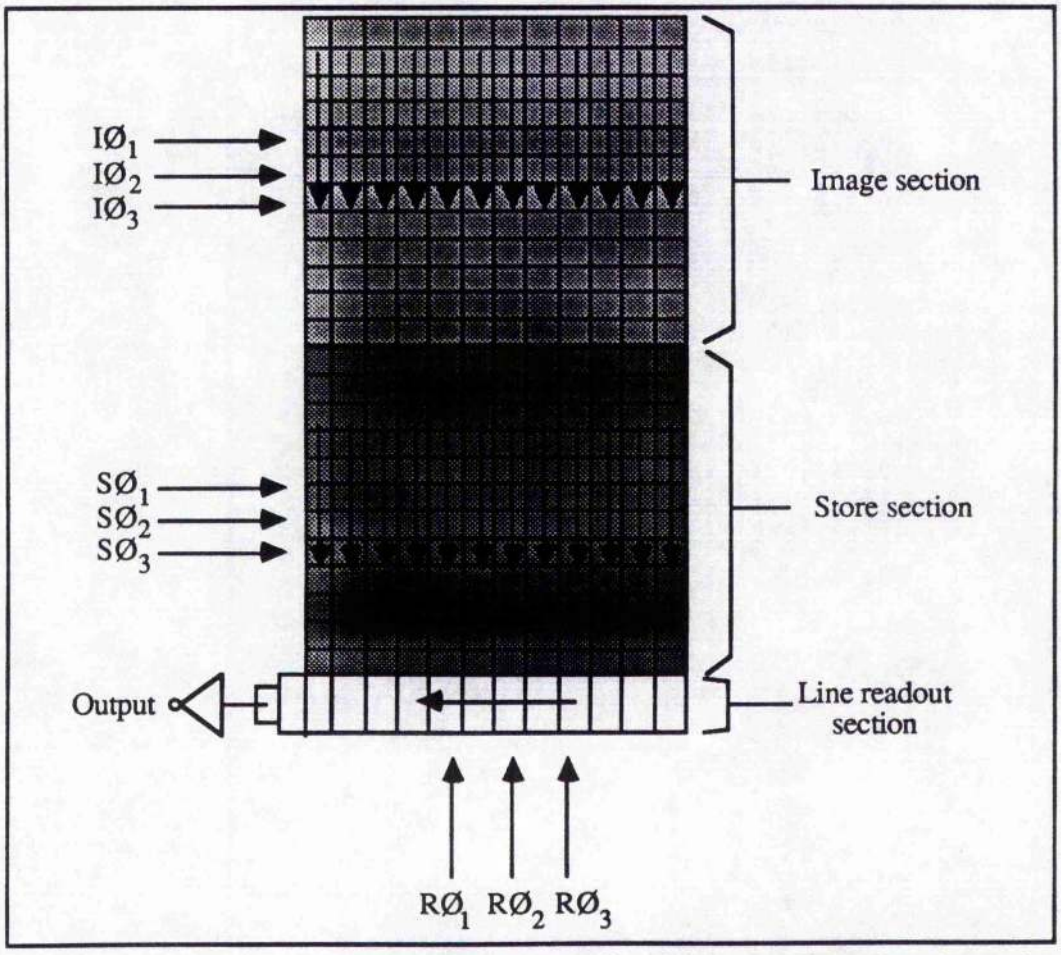

Figure 5.4 Schematic of Frame Transfer Area Array

widely used in astronomy at both room and liquid nitrogen temperatures. Chips are available with half or full frame active windows, fibreoptic coupling blocks and peltier coolers. A schematic of the chip structure is shown above in figure 5.4. Three different sets of clocking waveforms are required for its operation which are applied to the image, store and readout sections (designated IØ, SØ, and RØ repectively). In half frame operation the store and readout sections are masked off from incident light. During image integration the previous frame is readout line by line from the storage section to the line readout section which sequentially transfers the signal charge of each pixel to the on-chip amplifier which converts the signal into a voltage modulated video signal. In fact the CCD chip has two outputs a signal output from the line readout section and a dummy output which has no signal content. Differential amplification of these two outputs effectively removes the clocking waveform from the signal. Once the stored frame is readout the integrated frame from the image section is quickly transfered to the storage region and the whole process is repeated. Fast transfer is imperative to prevent the pick up of spurious signal from the incident illumination still present on the CCD.

TV systems usually display the detected image using a odd/even frame interlace technique. This can be accommodated for in a 3-phase CCD chip by adopting pseudo-interlacing where between alternate frames the central cell position is moved down the chip by a single electrode spacing (ie a third of the pixel length). Thus an odd and even frame is generated every two frame scans compatible for video interlacing and the verical spatial resolution of the chip is effectively doubled.

Two imaging systems have been constructed for interfacing to 12-bit and 8-bit video digitising systems (figures 5.5a and b respectively); each will be discussed in turn.

5.3 12-BIT DIGITISATION SYSTEM

5.3.1 CCD DRIVER AND DIGITISATION UNIT

The first system constructed is represented schematically in figure 5.6. All timing for clocking waveforms is derived from a 24 MHz crystal oscilliator and the circuitry can be run at 8, 4, 2, 1 and 0.5 MHz pixel clocking rates (8 MHz being the normal video rate).

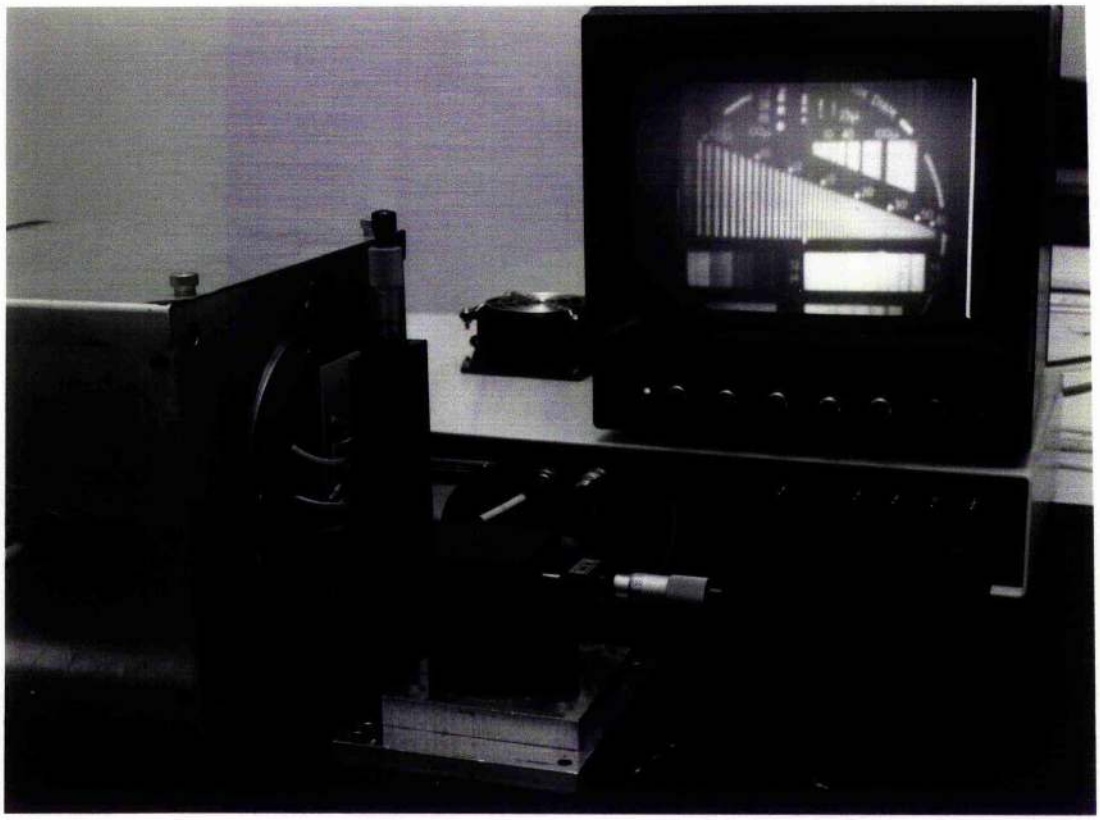

Figure 5.5a) (upper) 12-Bit CCD readout system with sensing head fibre-optically coupled to Photochron IV streak camera phosphor and b) (lower) 8–Bit imaging system showing camera head and framestore.

The drive circuitry is very similar to the circuitry found in the EEV P4310 camera with slight modifications to enable slow clocking to be performed. Variable video gain was provided at the capacitively coupled output and the signal was sent in part to a video driver for monitor display and to a sample-&-hold amplifier before being input to the 12 bit A-to-D converter. The CCD chip was mounted separately from the driver unit as small stand alone detecting head. By this means various P8602 CCD arrays could undergo evaluation and in particular streak images could be recorded employing either lens or fibre-optic coupling.

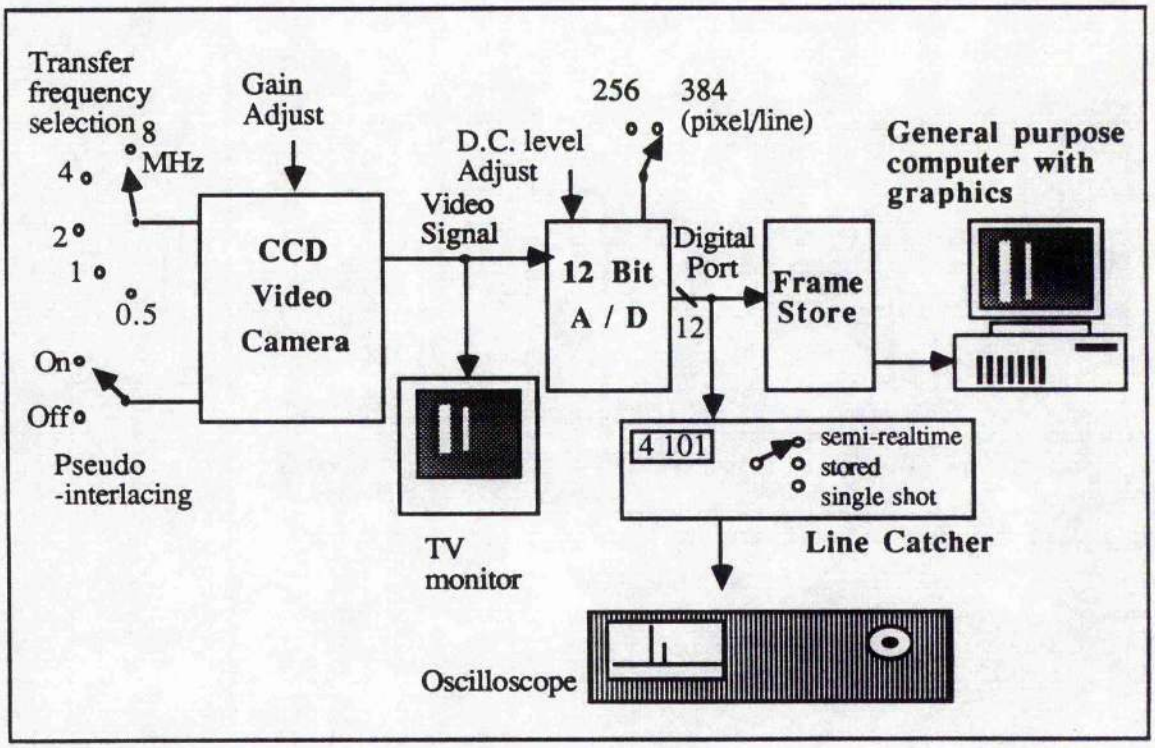

Figure 5.6 Block diagram of 12-bit image digitisation system

To achieve CCD image digitisation requires a fast data conversion rate coupled with a facility for dumping the digitised data into a large block of memory, often termed a frame store. The frame store is necessary since currently available computers have insufficient speed to read in the image information at the data conversion rate of the A-to-D. In other words the bottleneck in data transmission is at the input port of the computer. This situation is changing with the appearance of 32-bit processor computers, SCSI based I/O ports and 16/32 bit DMA cards, but cost is still prohibitive for most laboratory based applications.

To digitise a full frame (288x385 pixels) to 12-bit precision in a time sufficiently short before pixels become swamped by dark current (§5.6) requires a conversion rate of better than 1 MHz at room temperature. A review of the available converters was first made and this is summarised in table 5.1. The A-to-D purchased was the HAS 1201, a hybrid device manufactured by Analog Devices which has maximum conversion rate of 1.1 MHz. Input fsd voltages are 5 or 10 V and outputs are TTL compatible. The circuitry built around the device allowed two digitisation modes where either 256 or 385 pixels per line were digitised. This facility was provided since external memory size was initially limited but this was soon overcome with the availability of high density dynamic RAM memory chips. Once enabled by the frame store or readout device the digitisation circuit would wait for the next TV field before conversion commences and then signals the start and finish of a line digitisation by the toggling of a status line. A variable DC offset voltage can be applied to the input signal for masking dark current levels. The digital output is presented to the rest of the readout system via a buffered 25-way D-type port.

Table 5.1 Fast 12 bit A-to-D converters available

Maanufacturer / serial no.	Type and output compatibility	Speed (MHz)
Analog Devices:		
MOD 1205	Module – TTL	5
CAV 1220	Module – ECL	20
CAV 1202	Module – TTL	2
HAS 1201	Hybrid – TTL	1.1
HAS 1202	Hybrid – TTL	0.6
Burr Brown:		
AD 600	Hybrid – ECL	10
Micro Network:		
MN 5247	Monolithic – TTL	2
MN 52245A	Monolithic – TTL	1

5.3.2 12-BIT FRAME STORE AND COMPUTER CONTROL INTERFACE

The complete frame 385 x 288 12-bit data is transfered to 256 KBytes of dynamic RAM at the 1 MHz rate. The data is stored in two parts - an 8-bit word representing the

eight most significant numbers of the data and the lower numbers are recorded as 4-bit information. The memory buffer is interfaced to a 8 MHz IBM AT clone (ITS X86) via three 8 bit input/ouput ports (Intel 8255 I/O card). The computer graphics driver is an EGA high resolution card giving a two page display of 640 x 350 pixels and 16 colours, this is adequate for most graphical display of the stored data. Programs were written in Turbo Pascal (version 4.0). Frame transfer and subsequent analysis is controlled from the keyboard by a series of single keystrokes selected from a menu. Total access time for digitisation of a full frame, transfer to buffer and then to computer RAM is around 6 seconds. The 1 Megabyte of computer RAM can allow several frames to be stored and manipulated at once. A series of graphics procedures are included to display the image data including a colour pixel map which displayed the intensity level of each pixel using a 16 level pseudo gray scale and a three dimensional plotting program which displays the intensity values in the horizontal and vertical directions as is shown in figure 5.7. The data shown, a two dimensional sinc function, was generated in the computer for testing purposes. Stored frames can be dumped onto hard disc and read back. Full cursor control is provided in both display modes to allow the selection of single vertical or horizontal lines and the subsequent plotting of intensity versus position (figure 5.7c).

5.3.3 VIDEO LINE CATCHER

A very compact video line-catcher was also built as a useful complement to the CCD driver and digitiser. This device has two 8 Kbyte memory chips and a 12-bit D/A converter allowing the access of a total of 16 TV lines in the 384x12-bit data format to be displayed on a simple oscilloscope and hard-copied on a chart recorder. The starting line number in a frame and the line spacing between adjacent lines to be caught can be selected independently thus allowing all parts of the CCD image area to be accessed.

There are several facilities provided by the line-catcher. Firstly, when combined with the CCD driver and A/D converter, it represents a compact 2-dimensional readout system which does not require any peripheral frame store or computer for graphical display. Secondly, even if a frame store and computer are available, use of the semi-realtime

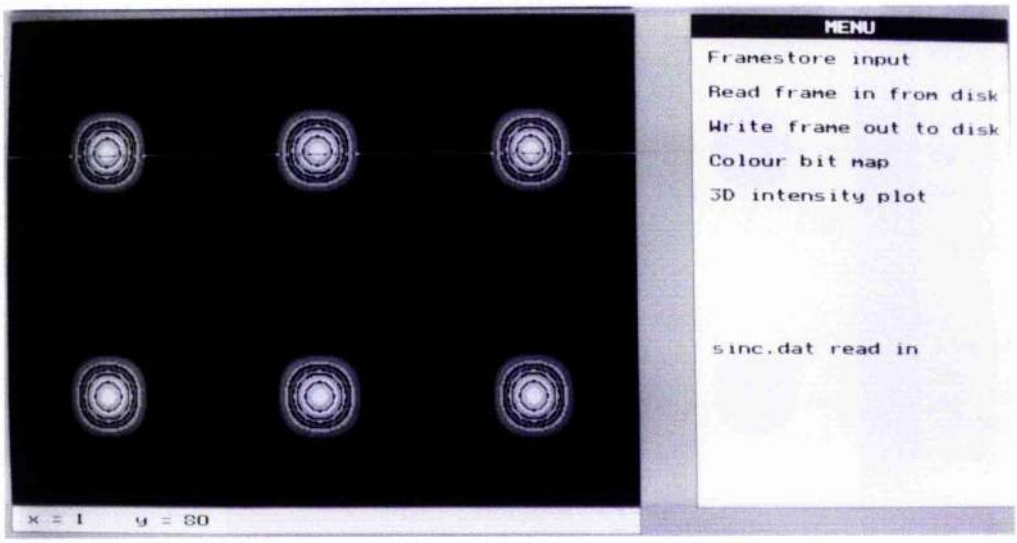

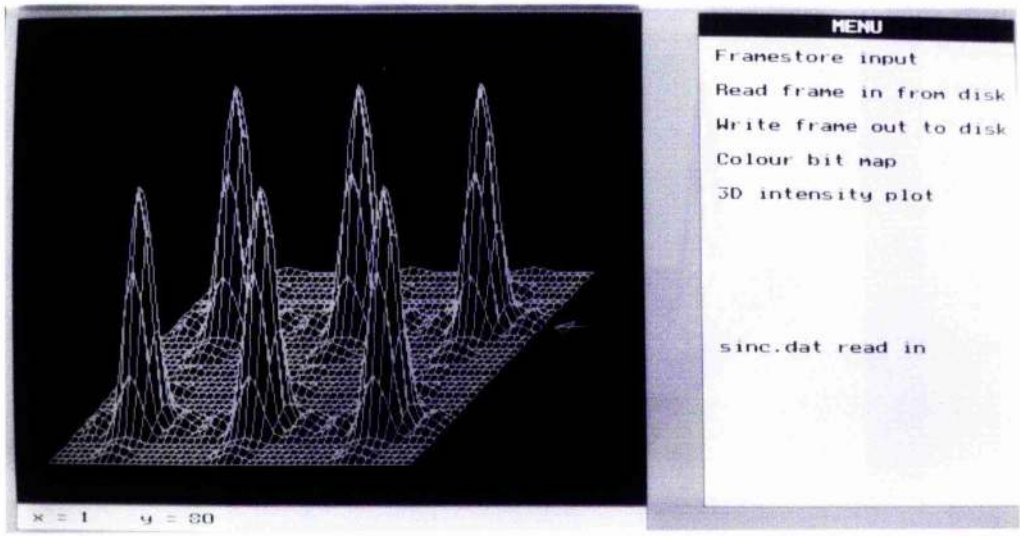

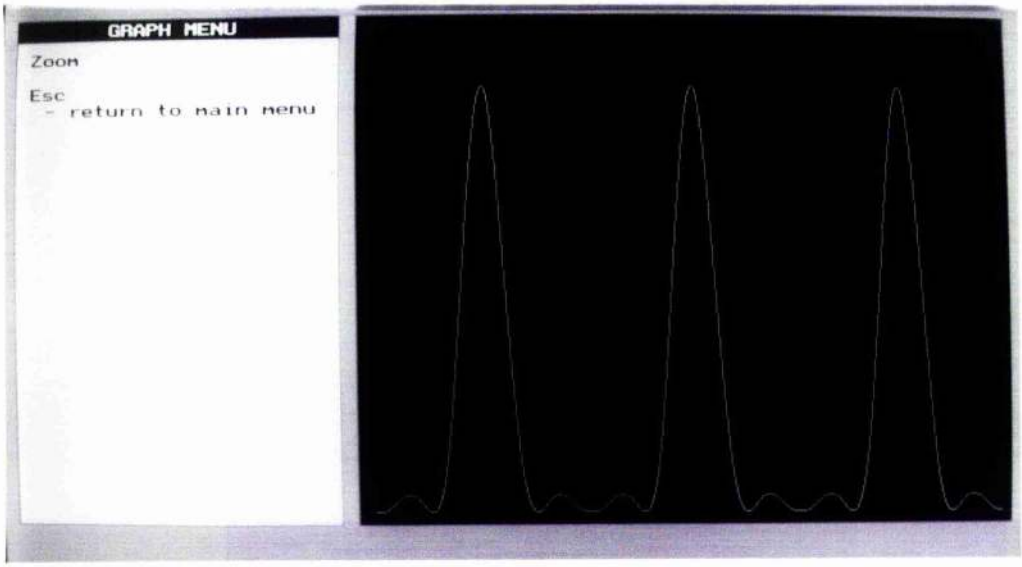

Figure 5.7 Demonstration of graphical software with computer generated sinc function intensity pattern: (upper) Pseudo-grey scale, (middle) intensity vs X-Y and (lower) intensity cross-section.

function of the line-catcher, which constantly updates the displayed video line on the scope, allows optimisation of CCD video gain and D.C. offsets on the A/D converter to ensure that the dynamic range of the CCD lies within the voltage range of the converter. Thirdly, this device represents an excellent trouble-shooting system which permits rapid fault-finding in the readout system and this is particularly important in the case of a relatively complex CCD driver/frame-store/computer configuration.

5.4 8-BIT IMAGING SYSTEM

5.4.1 CAMERA HEAD

The CCD detecting head and waveform driver developed above was simplified and made into a self contained unit requiring only low power DC voltage supplies. Again the output is provided with high, adjustable video gain and gives a standard 8 MHz video output. Only one clocking speed is available since it was intended to employ a fast video 8-bit A-to-D converter. The array is lens coupled to the streak tube by a $f0.7$ 50 mm lens (Fujimoto 44546).

5.4.2 FRAMESTORE

The video signal from the CCD camera head is digitised into 8 bit words and stored in a 256 kbyte static RAM frame store. The system at present provides, via a D/A converter, a video picture of the stored frame on a TV monitor and this image is up dated at video rates. The digitised frame can be transfered to the IBM computer via the 8255 port as before but with the added advantage that processed image data could then be sent back to the image store for true 256 gray level display. This frame store coupled with a CCD camera proved to be very useful in other applications including monitoring the linewidth of a DFB dye laser and use as a star tracking facility in the astronomy department. The trace showing the effect of RF drive signal coupling into the streak camera mesh (§4.2) was recorded with this system.

5.5 SYSTEM SPATIAL RESOLUTION

5.5.1 P8602 CCD RESOLUTION

The P8602 chip was illuminated with a standard resolution chart in order to ascertain its limiting spatial resolution and to compare this with its specification and thereby check the CCD driver performance. Operating at 8 MHz normal video rates the image displayed by the 12-bit system CCD driver on a TV monitor indicated resolution was lost above 23 lp/mm. On digitisation at 1 MHz rates the images were obtained in which the test chart was projected both horizontally and vertically (Figure 5.8a shows the horizontal example). Analysis of the modulation depths of a single line intensity distribution from each of these images (figure 5.8b) allowed the Modulation Transfer Functions (MTF) of the CCD chip to be generated as shown in figure 5.9. The pixel size in both horizontal and vertical directions is 22 μm and thus the pixel line spacing is 45 lp/mm. Consequently unambiguous resolution is lost above half this spatial frequency (Nyquist sampling theorem) and the image is further degraded by aliasing effects. The agreement between predicted and observed spatial resolution and the near identical MTF functions between horizontal and vertical directions shows that clocking waveforms are adequate, transfer efficiency is high and minimal vertical image smearing is prevalent. The latter is not a problem in the horizontal direction because of the presence of channel stops. The vertical resolution can be increased by a factor of 2 using pseudo-interlacing (§5.2).

5.6 DEVICE SENSITIVITY

The chip was illuminated with a Helium Neon laser to a measure its sensitivity and check the linearity of its response. Data was measured for different input intensities employing various ND filters and the beam spot size estimated from the CCD digitised image. It should be pointed out that the chip was found to be extremely sensitive; employing a 2.2 mW HeNe with a 1mm spot size required initially over a 10^5 reduction in intensity before the CCD was just under saturation @ 1MHz clocking rate. All measurements are for 633 nm light and the estimated error in these values is approximately 5% allowing for ND filter value tolerances. The measured system sensitivity was found to be 10.8 V/μW/cm^2 at 1Mhz clocking rates, which indicates a saturation energy density of

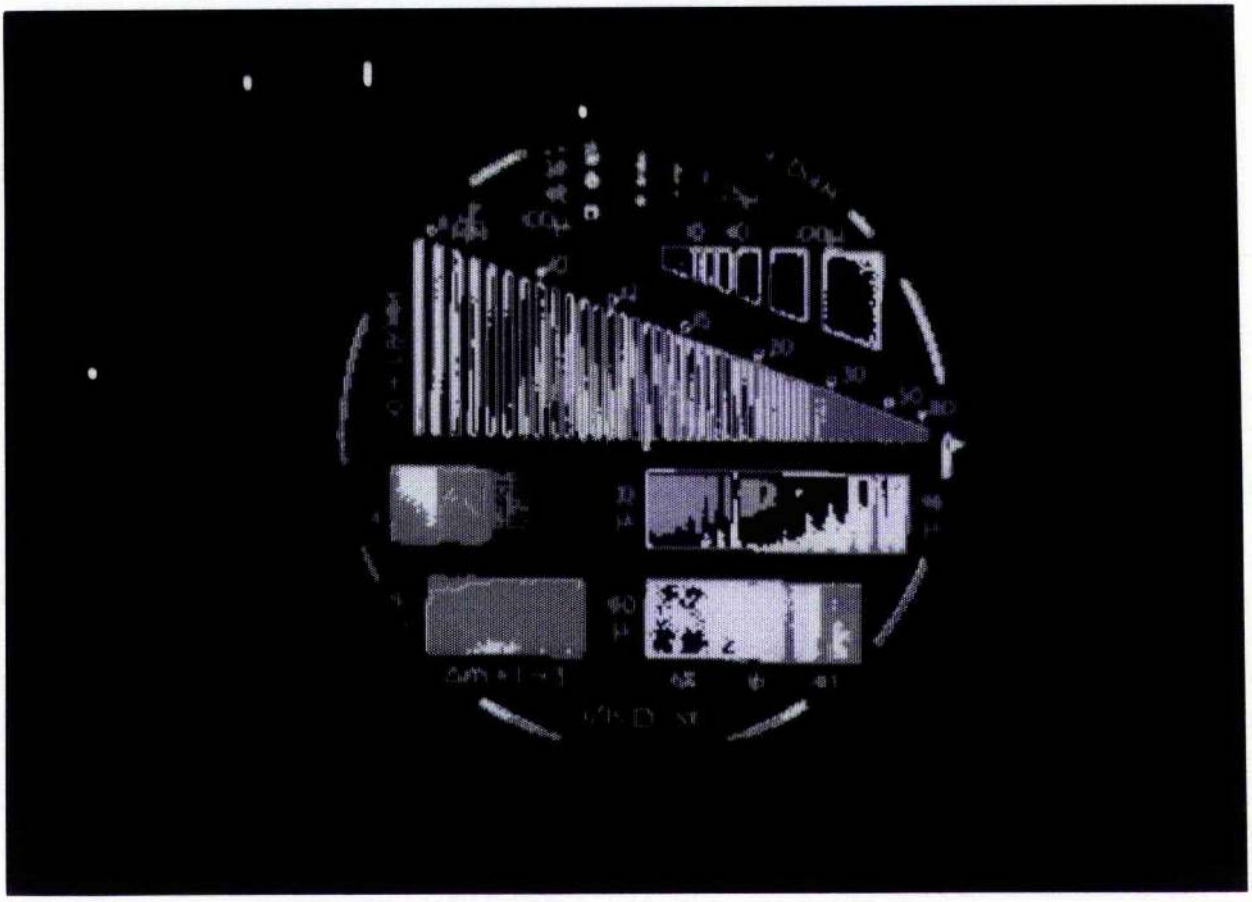

Figure 5.8a) (upper) digitised image from P8602 CCD illuminated by USAF resolution chart and b) (lower) intensity cross section across central region.

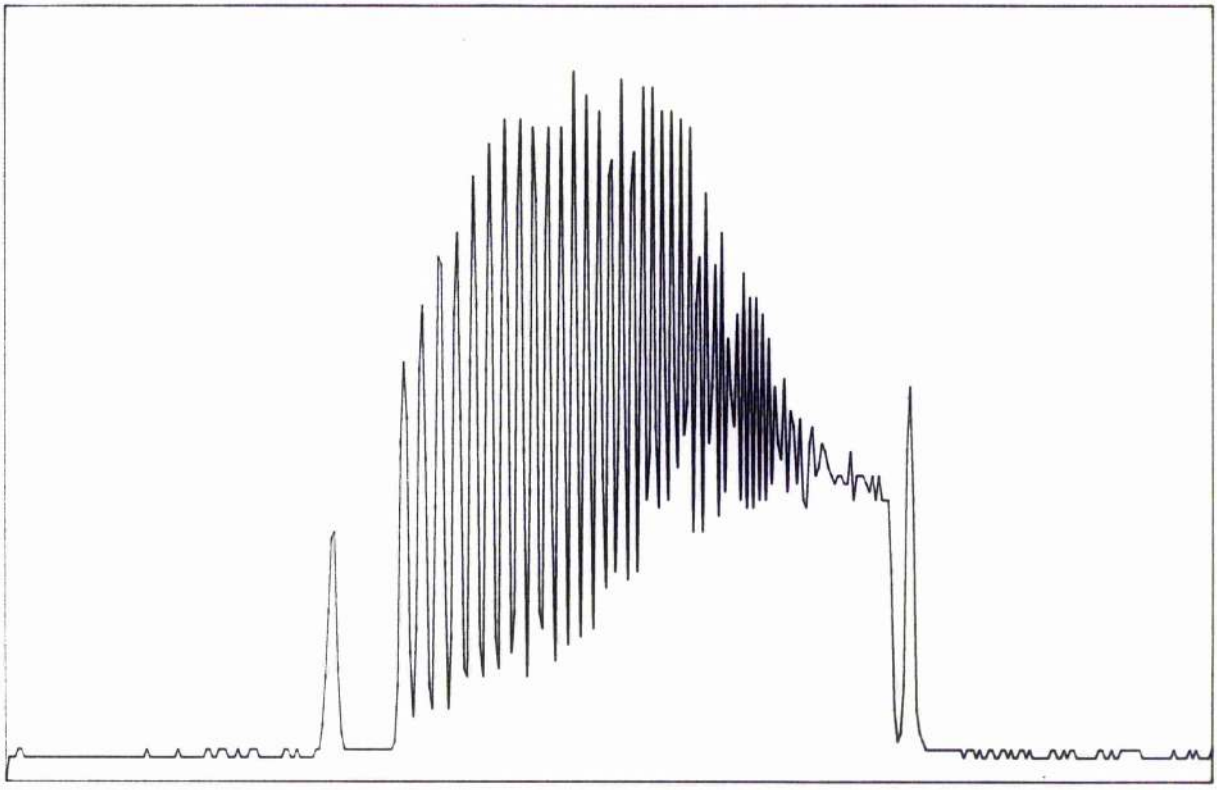

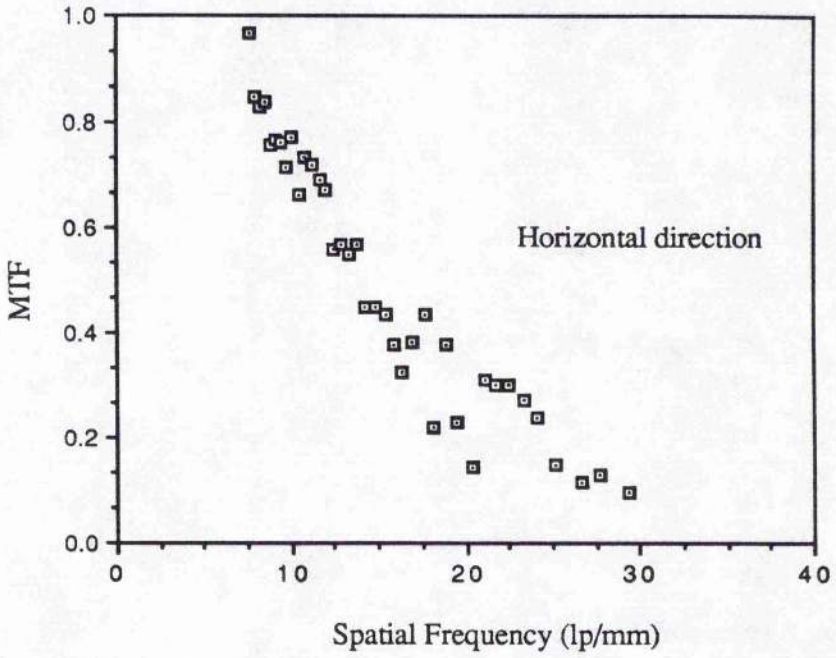

a)

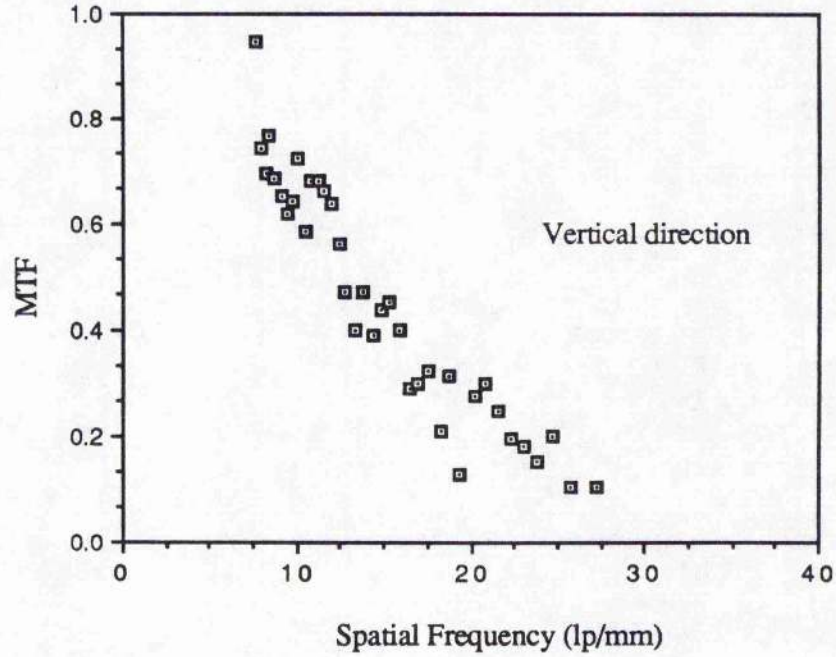

b)

Figure 5.9 a) Modulation transfer functions of CCD imaging system in a) horizontal and b) vertical directions.

0.71 μJ/cm^2 or 0.34 pJ per pixel (assuming a 22 μm square active area). Taking the pixel capacity to be 3x10^5 electrons the quantum efficiency of the device is calculated to be 28%; this value is lower than the specification (36%) at this wavelength and may be due to the fact that a set up grade CCD was used for these tests. Figure 5.10 shows the system response as function of intensity.

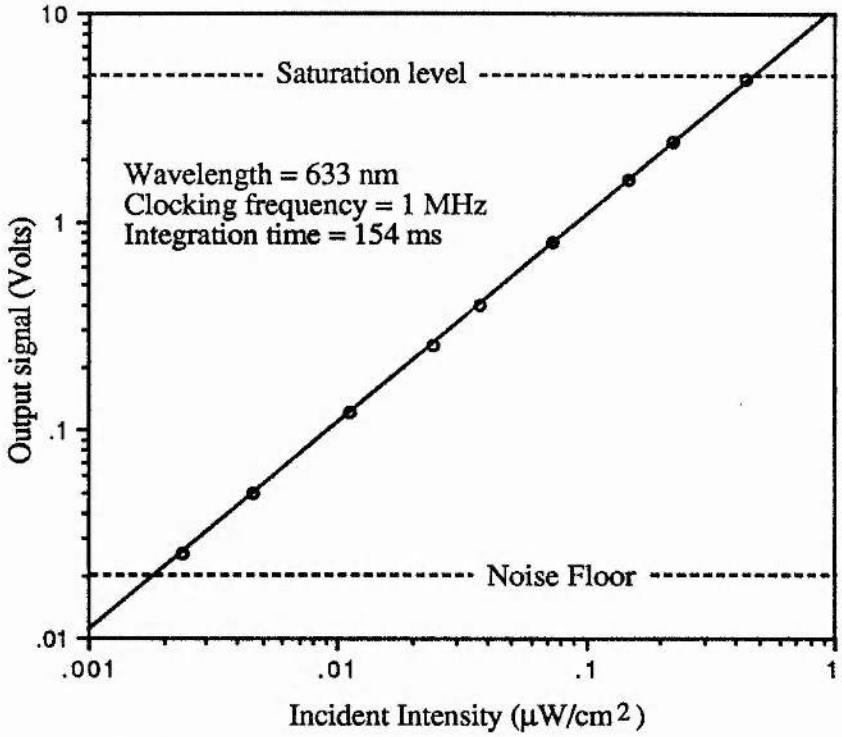

Figure 5.10 System response as a function of incident intensity

The average noise floor of the system can be offset by a DC voltage and set at 20 mV for this particular measurement and in reality the dark current level is ~100 mV. The actual noise level is defined not by absolute dark current value but by pixel to pixel variation in this value due slight differences in pixel size – so called fixed pattern noise. This is discussed further below.

5.7 CCD NOISE

A detailed analysis of CCD noise sources is provided in Appendix B. Three main noise contributions are present:

(i) dark current – random fluctuations in the thermally generated electrons signal level,

(ii) fixed pattern noise – fluctuations in dark current due to small geometric differences in pixel size, channel depth etc, and

(iii) reset noise – uncertainty developed in reset voltage level of output gate due to Johnson noise in transistor leading to noise transfered to the pixel signal.

For low frequency scan operation (< 10 kHz) 1/f noise in the output transistor is dominant [9]. When the CCD is at a pixel transfer frequency of 1 MHz or below, dark current can also lead to serious limitations. In a video field output period the image section of the CCD is integrating image charge while the storage section transfers the previously stored field line by line into the output register. Dark current is also being accumulated in the storage section during this period and the slower the transfer frequency, the larger the dark current will become. Two problems therefore arise. Firstly, dark current levels in lines which are clocked out later are higher than those which appear earlier but, since this noise variance is fixed-pattern in nature, it can be removed by background subtraction or data processing. Secondly, there is a certain amount of dark current remaining in the storage section at the end of each field output. During fast vertical frame transfer where the integrated image frame is put into the storage section, this dark current is clocked into the output register. For normal clocking rates the output register capacitance is sufficient to accommodate this charge and it is only necessary to transfer this line out before commencing the next field output. However, when the transfer frequency becomes slower, the storage section dark current is large enough to saturate the output register and spill over into several adjacent storage section lines. This causes blooming to appear at the top extreme of the monitor screen. A solution to this is to run the output register continuously during vertical frame transfer thus clocking out any accumulated storage section dark current and preventing build-up in the output register. Implementation of this solved the problem even at transfer frequencies as low as 0.5 MHz.

The dark current mean voltage level as a function of line number for a transfer frequency of 1 MHz is shown in figure 5.11. As can be expected the mean noise level increases linearly with line number since lines further up the CCD array take longer to be clocked out and thus the dark current integration time is increased. This problem in slow

scan operation can be reduced by cooling the chip. For approximately every ten degrees cooling of the CCD the dark current level is reduced by a factor of two (see Appendix B)

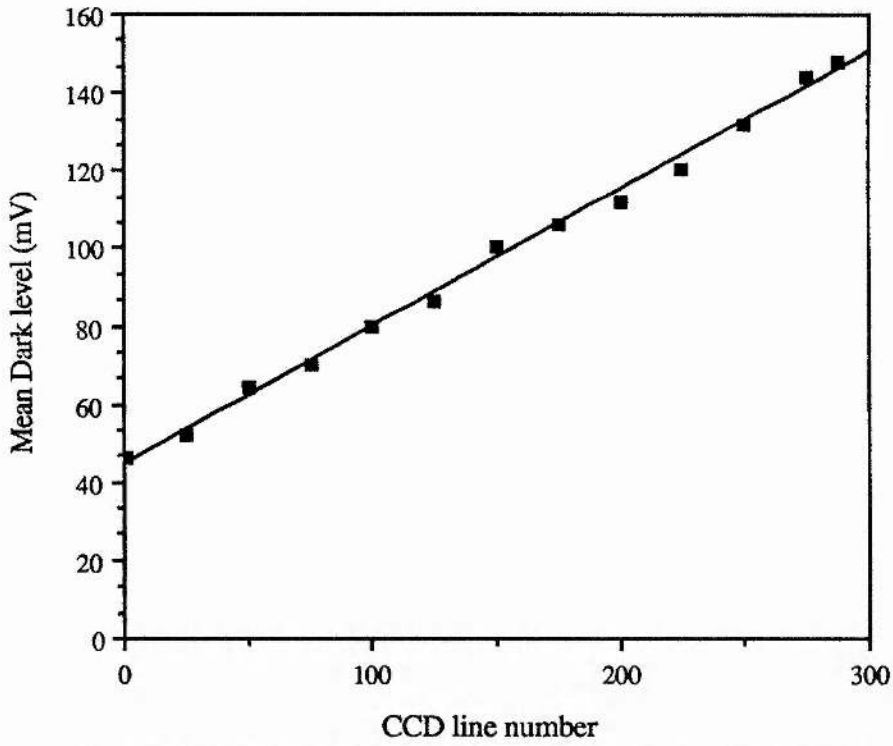

Figure 5.11 Mean dark level as a function of CCD line number

and thus if the full 12-bit digitisation is to be usefully realised future detector heads will require peltier cooling devices. The measured noise variation (fixed pattern and reset noise) of ~10 mV p-p associated with the complete readout system is quite reasonable in view of the fullscale output of 5V. This noise level is equivalent to 600 electrons and gives a dynamic range (at room temperature) of ~500. Other noise sources eg) reset noise will be removed at a later date employing double correlated sampling techniques [9,10].

5.8 STREAK IMAGE READOUT

The CCD was fibre optically coupled to the Photochron IV streak camera phosphor (Figure 5.5) with only a small degradation of resolution, achieving a static limiting resolution of 42 lp/mm measured at the photocathode. For lens coupling with a f0.7/50 mm lens operated with X3 magnification no loss of resolution was detected for f stops

greater than 5.4, but less than this lens distortion was noticeable at the edge of the image. Although fibre-optic coupling offers a compact readout system with good coupling efficiency (35%) the lack of image magnification implies only a very few pixel elements across one resolution element of the camera and thus it is of little use for picosecond streak events. Lens coupling is much more convenient in this respect.

Figure 5.12 shows a streak image recorded on the Photochron IV streak camera using the 8-bit image digitisation system. This result was taken after the mesh and photocathode had been decoupled from RF influences (§4.2). Experimentation using the CCD imaging systems during synchroscan operation was also somewhat limited due to RF inteference effects from the 20W synchroscan drive signal. To reduce this problem it will be necessary to house the CCD within a well shielded container and to reduce RF emission from the streak camera. A second more serious problem was that the CCD sensitivity was measured to be 250 times less sensitive than the SIT vidicon detector and consequently signal levels were small. However with low noise peltier cooled detector this lack of sensitivity can be offset by provision of high gain at the output.

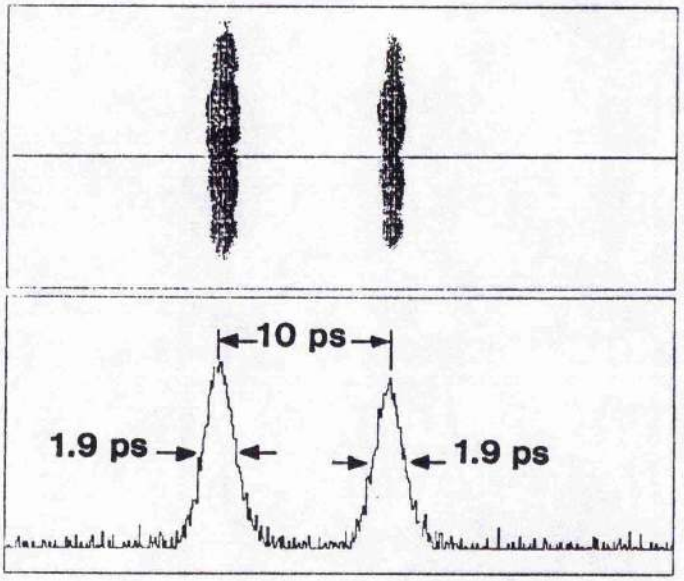

Figure 5.12 Recorded streak image from Photochron IV streak camera

5.9 CONCLUSIONS

A two dimensional image readout system has been developed which has involved the successful interfacing of a P8602 CCD detector to a host computer via an 8-bit and 12-bit framestore system. The possible applications of this sytem extend beyond the initial requirement of streak camera operation and include framing camera readout and a new interest in molecular structure diagnostics using X-ray diffraction techniques.

REFERENCES

1 W.S.Boyle and G.E.Smith, Bell Syst. Tech. J. **49** 587 (1970).

2 L.E.Ravich, Laser Focus p.148 (Dec. 1987).

3 C.Cavallier Proc XVIth ICHSPP SPIE **491** 706 (1984).

4 B.Speyer and D.Bowley, Proc. XVIIIth ICHSPP (1988) to be published.

5 H.Lutz, W.Krause and G.Barthel, *Space 2000* Amer. Inst. of Aeronautics and Astronautics, New York, p.236 (1983).

6 W.Sibbett, W.Sleat, W.Krause and J.R.Taylor, Proc. ESA workshop on Space Laser Applications and Technology ESA **SP-202** 171 (1984).

7 *P8602 CCD image sensor*. EEV tech. note (1984).

8 D.F.Barbe, Proc. IEEE **63** 38 (1975).

9 *CCD Imaging III*. EEV publication (1987).

10 Y.Endo, A.Furukawa, Y.Matsunga, N.Harada and O.Yoshida, IEE conf. on Photoelectronic Imaging, suppl. to publ.no. 253, London (1985).

CHAPTER 6: PHOTOCHRON IIC STREAK CAMERA WITH ELECTRON SENSITIVE PHOTODIODE / CCD READOUT – PRELIMINARY INVESTIGATIONS

6.0 INTRODUCTION

As mentioned in the previous chapter much of the CCD research has been concerned with a specific project for spaceborne laser ranging using an adapted Photochron II (see §2.3) streak tube as an integral part of the measuring system. Precise measurement of the separation between a satellite and selected ground-based retroreflectors can facilitate the remote monitoring of geodynamic processes on the earth's surface. An elegant technique for the determination of these straight line distances uses a laser, emitting picosecond pulses at a pulse repetition frequency of the order of 10Hz, in conjunction with a detector capable of accurately measuring the pulse round trip time between the satellite and the ground-based retroreflectors. A correction factor is required for the pulse retardation due to atmospheric refraction and this can be estimated using data obtained from of the laser, emitting short pulses on two different wavelengths, combined with a theoretical model for the atmosphere. The general concept of precise two-colour spaceborne laser ranging is well established [1] and is based on the use of a circular-scan streak tube to obtain the fraction of the final count period of a counter, triggered at the emission time of the laser pulse and stopped by the reflected pulse. Effectively the streak camera is operating as a vernier measuring system complementary to the low precision coarse 'period' counter. Other possible applications for this type of system include monitoring coastline erosion and ranging of large space structures.

The existing experimental circular-scan streak camera, the Photochron IIC [2] incorporates a microchannel plate (MCP) intensification stage and the streak images are recorded from its phosphor screen via photographic film and subsequent microdensitometry. It was recognised, however, that for a spaceborne application it would be essential to use a readout , such as a CCD – either externally or internally, which has inherent ruggedness, small size and low power requirements.

6.1 IMAGE TUBE CONFIGURATION

The basic electrode configuration of the Photochron IIC streak tube is illustrated schematically in Figure 6.1a. For this particular application the two pairs of orthogonally oriented deflection plates are supplied with 300MHz voltage sinusoids in phase quadrature to give a circular sweep of diameter 30mm. The Photochron IIC camera [3], has demonstrated a temporal resolution of 6 ps. In laboratory experiments performed to date the available input signal intensity has not been limited and so the signal-to-noise ratio and overall detection sensitivity of the tube have not been fully evaluated or optimised. In a spaceborne application these parameters are of prime importance. One possible approach, currently being investigated, that should provide improved signal detection is to dispense

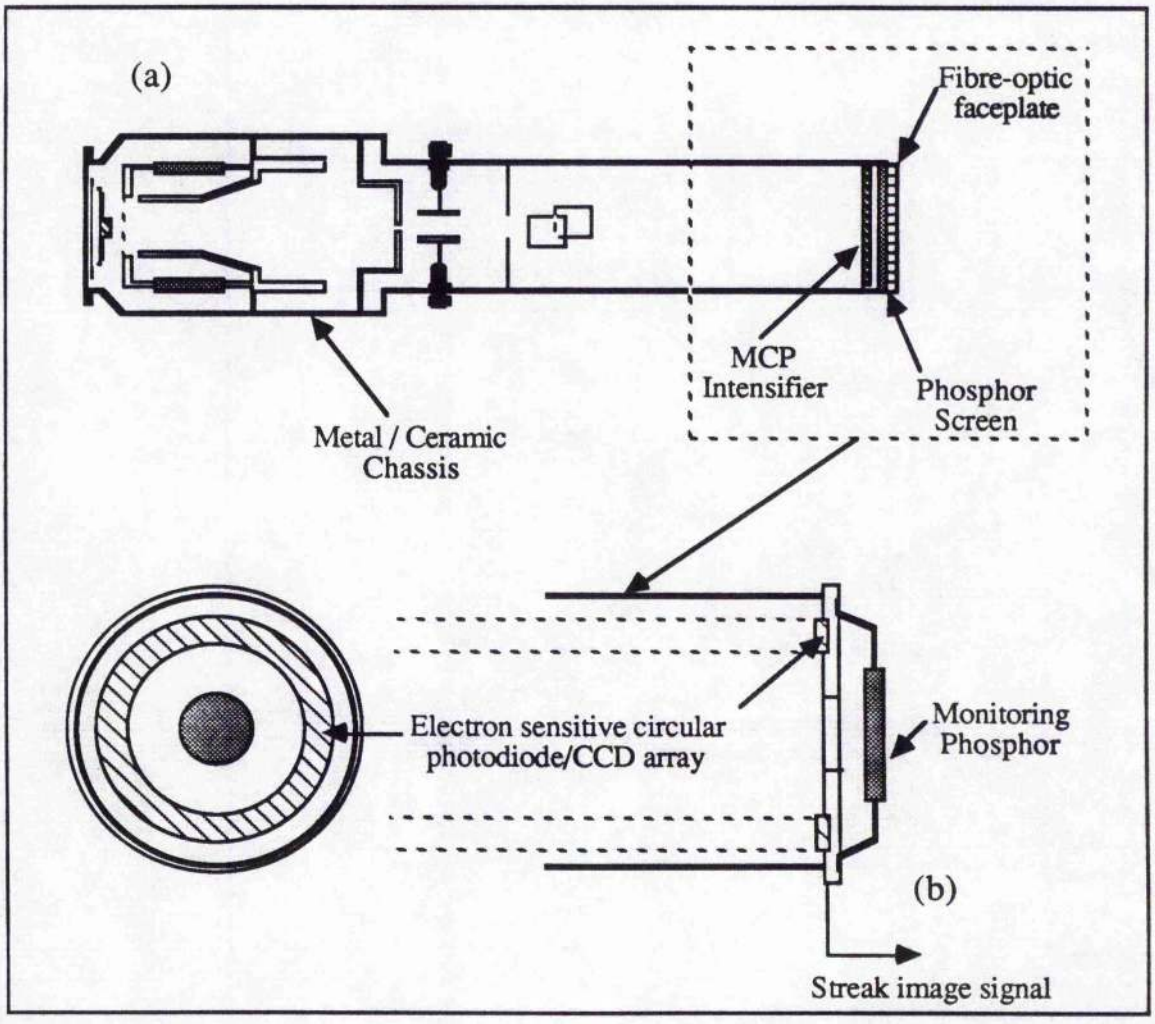

Figure 6.1 (a) Photochron IIC circular streak tube and (b) modified back assembly for internal CCD readout

with the MCP, phosphor, and associated optics and incorporate a direct readout system in the form of an electron sensitive circular photodiode/CCD array mounted within the vacuum envelope of the tube. For effective use in the laser ranging application the readout system (Figure 6.1b) must satisfy the high sensitivity requirements and have sufficient spatial resolution to reliably match the performance of the Photochron IIC. These features along with pertinent details of the readout system are discussed below.

6.2 READOUT FORMAT

Several possible CCD readout formats were considered, each having relative advantages and disadvantages. Of these, (i) a circular CCD array, (ii) an internal area CCD array, and (iii) a circular CCD/diode array have been compared.

6.2.1 CCD CIRCULAR ARRAY

Using MOS capacitors as sensing elements for electrons has the advantage that the readout of the signal can be effected by transfer of charge around the circular array to the output. The loss incurred at the gate oxide and electrodes of the MOS device, however, make front-side electron sensing impractical. There is also the problem of radiation damage where impinging electrons create trapping centres in the oxide layer which will seriously degrade the characteristics of the sensor with respect to charge capacity and dark current. Using *backside* irradiation [4], the device must be precisely thinned because the signal electrons, incident on the rear of the device, generate electrons within the bulk silicon which diffuse to, and are collected in the pixel potential wells. An array of too great thickness would therefore have poor efficiency due to recombination losses.

6.2.2 CCD AREA ARRAY

An internal area CCD would have the advantage that there would be no registration problems of the circular electron beam on the active area of the detector. Also the large circle diameter would necessitate use of a large format area CCD which is costly and inefficient in terms of clocking requirements since large regions of the device will contain no signal of interest. Furthermore the need for backside irradiation and the consequent uniform thinning of the rear of the device is difficult to achieve for large area formats.

6.2.3 CCD/DIODE ARRAY

Most attempts at including internal solid-state readout systems in streak tubes have adopted commercially available CCDs and modified their design accordingly but with marginal success. It was recognised that in order to develop such an internal readout system requires a specialist design customised to streak camera operation and processing. With this in mind researchers at Interunivestair Micro-Electronics Centrum (IMEC) in Leuven, in collaboration with St. Andrews University, designed a circular photodiode/CCD array which was tailored to streak camera needs. The configuration avoided the problems already mentioned as it uses a photodiode as the sensing element and a CCD as a shift register to read out the resulting charge. Photodiodes as electron sensors have the advantage over MOS capacitors in that they have superior detection efficiency and are less susceptible to electron damage. Each diode is covered with a thin oxide layer which absorbs only a small amount of the electron energy and has no electrical function. The separation of the sensing and transfer operations also improves manufacturing yield since two output shift registers can be provided, one on each side of the sensor, and either the inner or the outer register can be used for readout. Some redundancy can therefore be introduced without increased fabrication difficulties.

Improved yield can also be achieved by subdividing the circular array into small sections and this technique has the additional advantage that it avoids some of the transfer loss. A buried channel CCD has a typical transfer loss of 2×10^{-5} per transfer and therefore about 20% of the charge would be lost if it had to be transferred along the complete circle of 3600 elements. Subdividing the readout arrays into 8 sectors each of 450 cells will reduce the transfer loss to ~5%. The device was denoted a *self-scanning circular electron detector array* (SSCEDA) and is discussed in detail below.

6.3 DESIGN FEATURES OF THE SSCEDA

The sensing elements of the array are required to detect single photoelectrons with energies of 11keV (Appendix B and reference [5]). This generates two design criteria (i) the relatively low energy of the electrons implies there must be minimal energy loss through the

surface protective oxide layer of the sensor ie. this must be as thin as possible, and (ii) since only a few (~5) photoelectrons are expected per streak event during spaceborne laser ranging the whole of the sensor surface must be active, ie. there can be no oxide isolation between pixels which would mask on average 20% of the sensor area. The sensing element adopted which meets these design constraints is the depletion-isolated sensor (DEPLI sensor) which was originally developed at the ESAT laboratories in Belgium [6].

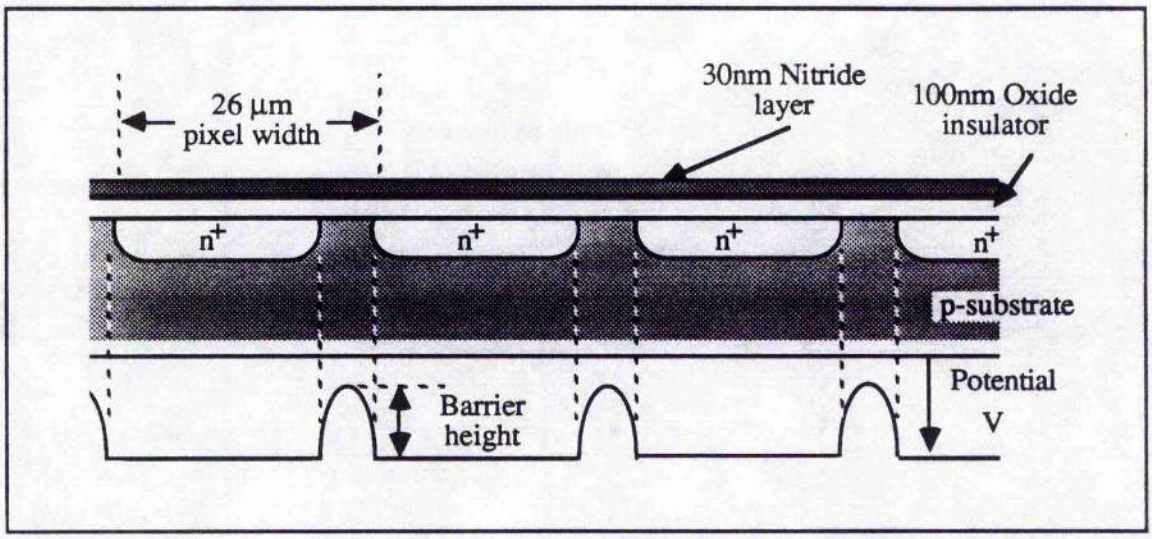

Figure 6.2 Cross-section of DEPLI electron sensor

6.3.1 THE DEPLI SENSOR

A schematic of this type of sensor is shown in figure 6.2. The sensors essentially consist of photodiodes of width 26 μm and radial dimension 500 μm. The large radial extent is necessary to allow for registration of the circular streak trace if slight ellipticity is present in the drive signal [3] and assumes that the signal electrons will fall within a segment with a Gaussian distribution with a deviation of ~ 50 μm. Between each diode there is a 4 μm insulating region of low-concentration substrate material. A suitable doping concentration, N_A at the silicon suraface is ~6×10^{14} cm^{-3}, the photodiode concentration, N_D being ~3×10^{16} cm^{-3}. For normal operation the region between two diodes is entirely depleted by reverse biasing. Thus the isolation between sensors is performed by the potential barrier which is built up in this depletion region and the pixel boundary will lie at the minimum of this potential barrier. A thin, 30 nm nitride layer is deposited on a

protective oxide layer yielding a uniform insulator thickness of 130 nm. Impinging signal electrons will lose approximately 1.5 keV of their energy in transit through this insulating layer and will penetrate ~0.7 μm into the silicon substrate generating ~2500 electon hole pairs per incident electron [5]. From the noise analysis detailed in Appendix B the signal charge thus accummulated in the photodiode pixel will be sufficient for single photoelectron detection under these conditions.

6.3.2 CIRCULAR ARRAY STRUCTURE

The DEPLI sensors were configured around a circle of radius 15 mm and were divided into eight sectors. Surrounding this anulus were a series of CCD shift registers, eight inside and the same number outside the circular array (see figure 6.3a and b). Between each CCD cell and DEPLI sensor pixel a transition structure consisting of a small buried channel shift register was constructed perpendicular to the readout registers. Input structures were provided on each CCD array to allow functional testing and provision of a fat zero if required. To limit transfer noise the width of the shift register was made as narrow as possible. Two output structures were provided, a standard output diode connected to an on-chip double source follower (DSF) and an additional operational amplifier with a feedback capacitance which could be connected to the DSF off-chip. The second configuration would give an output voltage of ~0.2V for 2500 signal electrons whereas the single DSF device will only give 20 mV. Because it was uncertain whether the 'op-amp' configuration would be stable due to the extremely small feedback capacitance both output systems were constructed and the op-amp system suitability tested after processing.

6.3.3 SSCEDA MOUNTING SUBSTRATE

The design of a mounting substrate for such a complex structure as the above SSCEDA was a non-trivial exercise. Certain requirements had to be met by IMEC in that for inclusion of the device into a Photochron IIC the number of feedthrough contacts that had to be made was limited to around thirty, the substrate must be of a tube compatible material eg. ceramic and its dimension should be a small as possible. The format that was designed

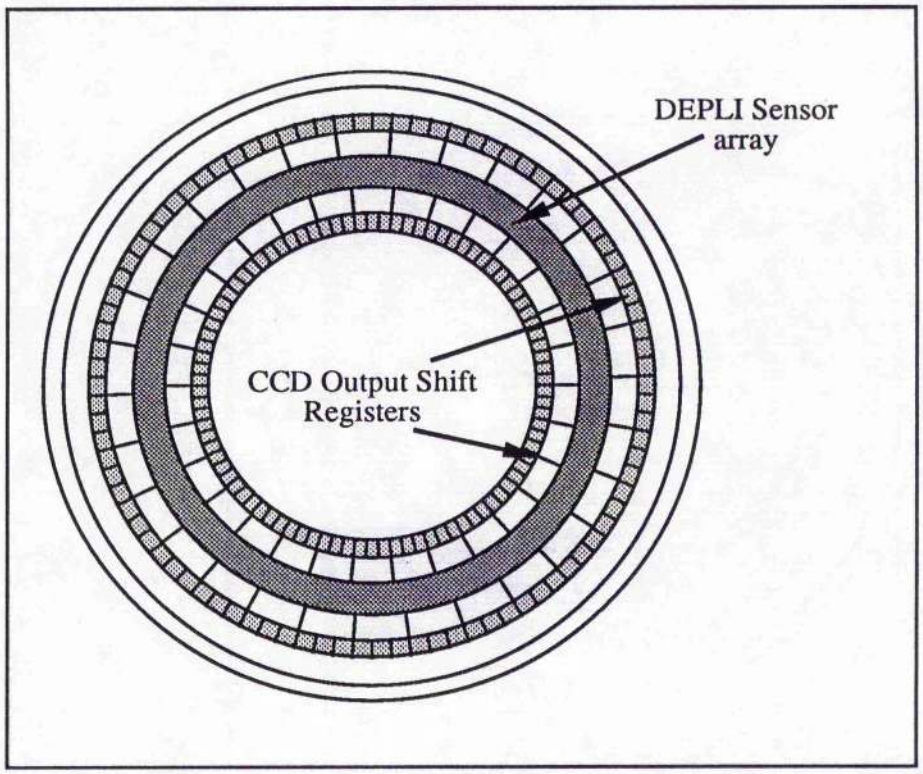

Figure 6.3 Schematic (above) and photograph (below) of SSCEDA sensor and readout structure

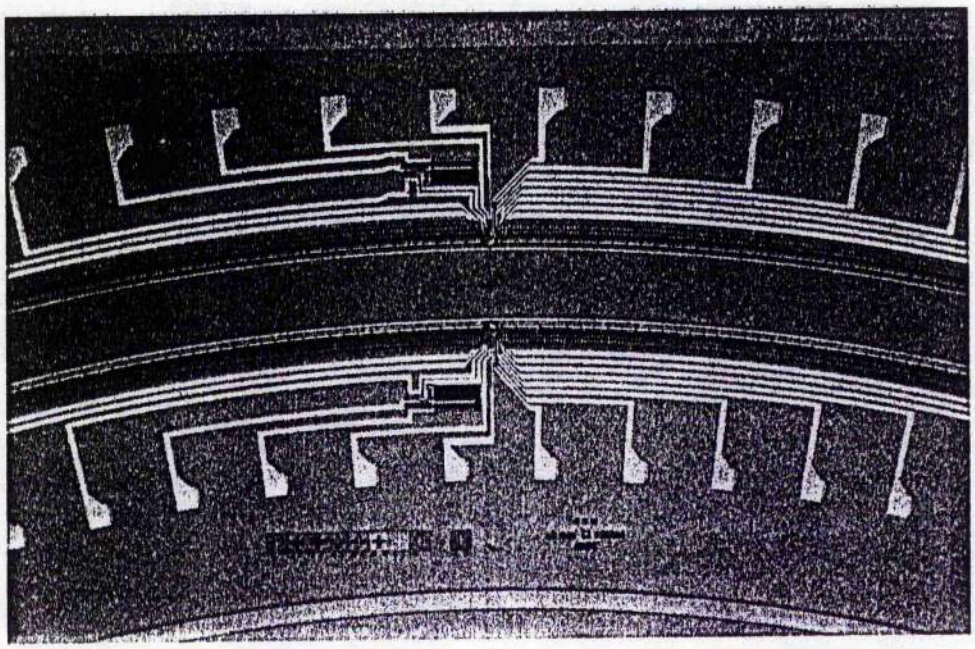

at IMEC consisted of an octagonal ceramic tile with a 6-level glaze process to provide all required bonding pads both external and on-chip. The thick film substrate is shown in figure 6.4 and a schematic of the conductors and inter-level vias shown in figure 6.5.

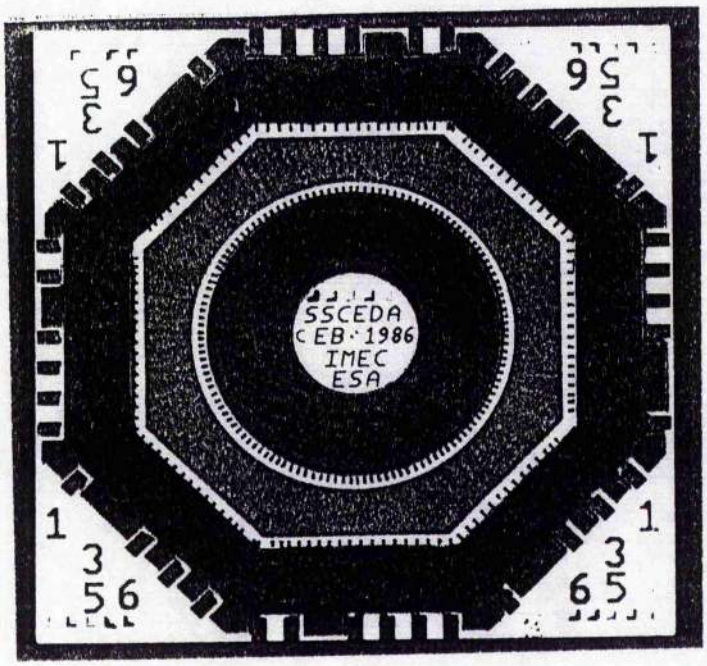

Figure 6.4 Photograph of thick-film ceramic SSCEDA substrate

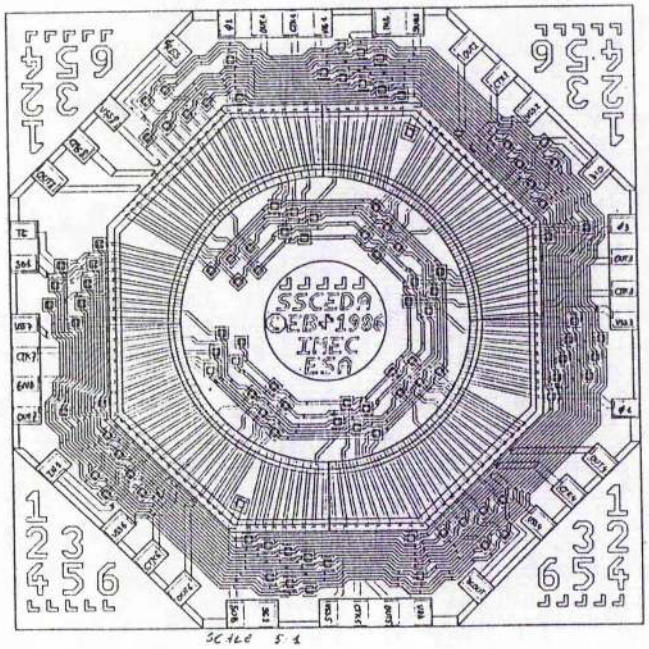

Figure 6.5 Schematic of conductor bonding configuration

The minimum width and spacing of the conductors is 250 μm and were made from gold paste. On the substrate 256 bonding pads were provided but only 128 will be used since there is a redundancy factor of 2 in the shift registers. If the op-amp output system is chosen then the total number of tube feedthroughs required will be 30; for the single DSF output either 23 or 30 feedthroughs will be required depending on whether 8 separate or one single pin is provided for the reset transistor source voltage.

6.4 TUBE CONSTRUCTION

It is proposed that the tube will be of the metal and ceramic construction in order to benefit from the improved manufacturing tolerances and ruggedness that this technique has to offer. The tube design will be very similar to the original Photochron IIC structure but the MCP will be removed and a separate SSCEDA back assembly fitted. This structure must include the following aspects (i) vacuum-compatible mechanical support and electrical feedthroughs for SSCEDA, (ii) window access to a 10 mm diameter phosphor screen and (iii) compatibility of subunit to suitable cooling schemes for noise-floor suppression.

A suggested structural design of the CSST-SSCEDA subunit is illustrated in figure 6.6. This is based on the IMEC SSCEDA thick film substrate format that has already been described. The approach here has been to devise a vacuum-compatible ceramic annular interface such that the already-designed SSCEDA can be attached to a prefabricated subsection of the streak tube. Electrical interconnects would then be made between the diode array and the tube feedthroughs. The central circular section of the SSCEDA substrate will be removed by laser to allow electron signal to be incident on a rear end phosphor screen for focussing and/or low amplitude scan appraisals.

Because this suggested construction differs substantially from what had been envisaged initially, it may be that an alternative design will be more practical in the first instance. For this scheme, (see figure 6.7), the feature of electrical feedthrough pins on the output end of the streak tube are retained together with the possibility of adapting the technology so that a small phosphor screen can be incorporated.

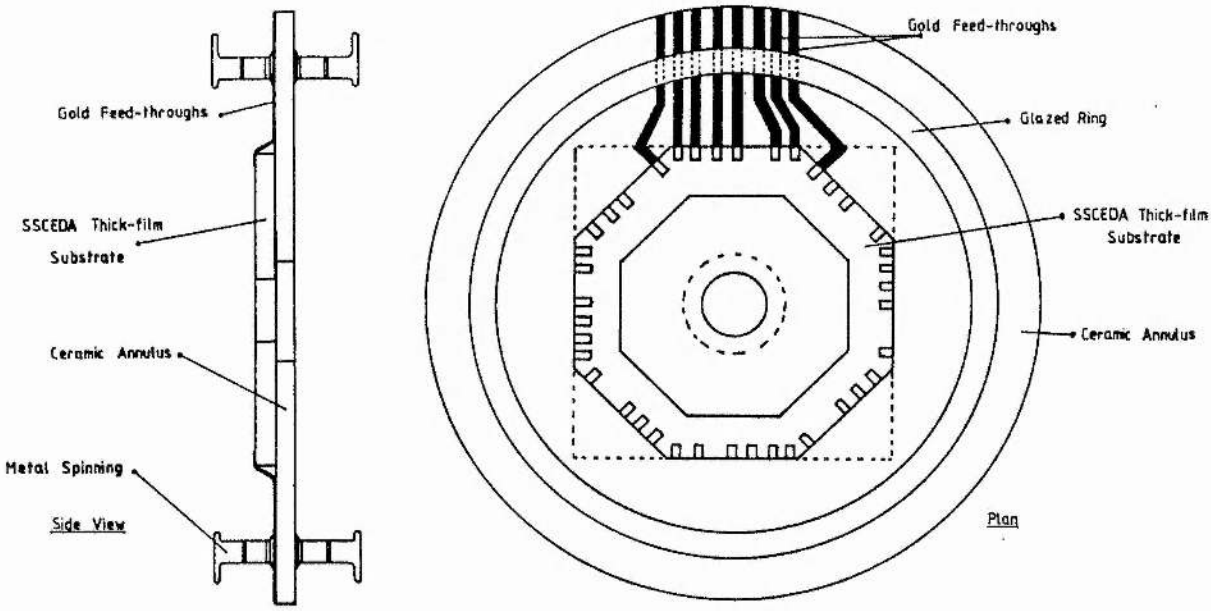

Figure 6.6 Modular SCCEDA mounting system.

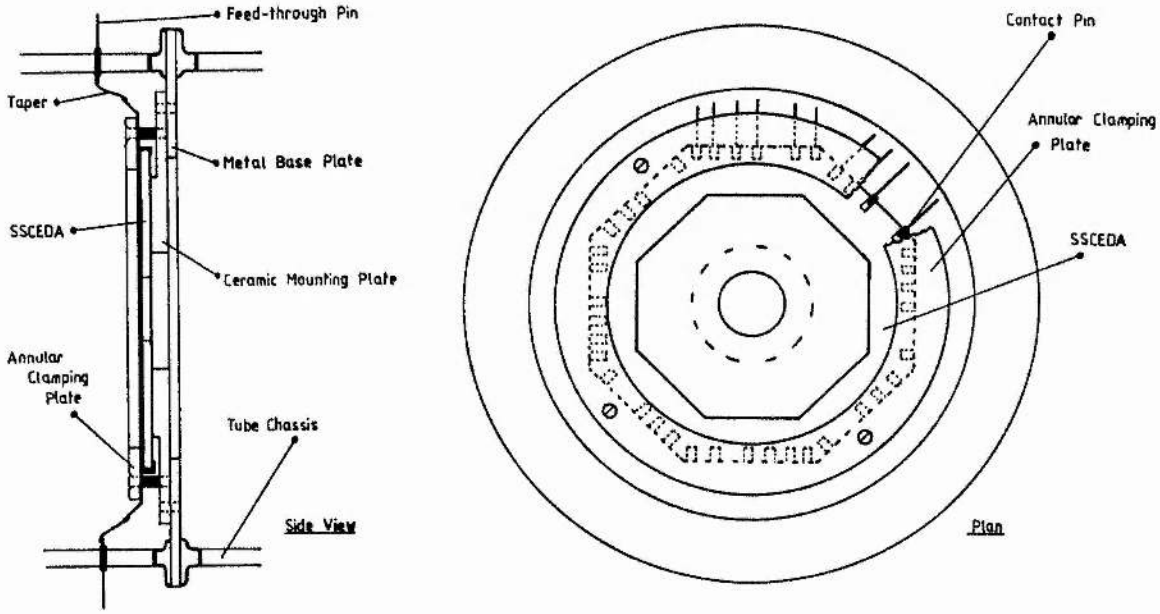

Figure 6.7 Pin feed-through mounting system.

6.5 TUBE PROCESSING COMPATIBILITY TESTS

6.5.1 BAKEOUT CONSIDERATIONS

It was recognised that some further optimisation of the tube processing procedures would be required. The sustained high bake-out temperatures that are normally necessary during processing could cause damage to an internally mounted CCD and slight impurity contamination from cathode materials may impair performance. Some research has been reported [7] in this field, but it should be noted that in this particular case small image intensifier tubes were processed at a reduced temperature of 275°C which is a lower temperature than that normally used when manufacturing the Photochron series of tubes. These lower bake-out temperatures would have serious photocathode lifetime implications. The so called bake-out procedures involve the heating of the image tube through a number of temperature cycles while maintaining a high vacuum condition. As a result the electrodes and tube body are progressively out-gassed and effectively passivated. This means that good electrical insulation and low photocathode contamination levels are ensured. A typical bake-out cycle is illustrated in figure 6.8. In some instances the appropriate vacuum conditions can only be achieved by applying a longer bake with perhaps temperature excursions that exceed 400°C.

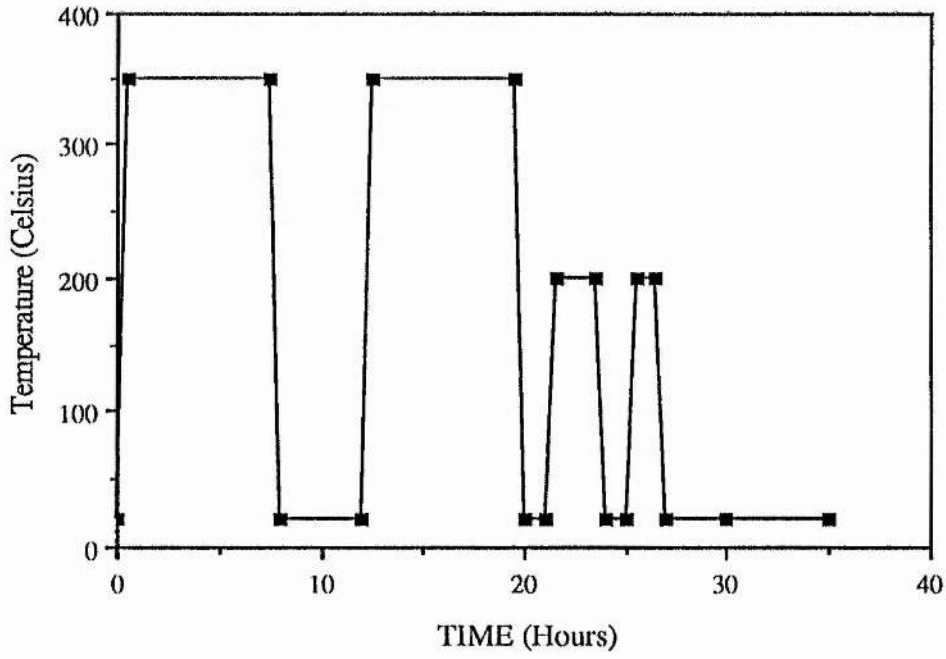

Figure 6.8 Streak tube bake-out temperature cycle

During the processing of the photocathode (type S25) onto the entrance window of the streak tube, alkali metals are evaporated which may diffuse in some measure throughout the volume of the tube. If any of the evaporants, particularly sodium, come into contact and chemically attack the silicon structure of the photodiode array then the performance of the array will be adversely affected. Conversely, it is imperative that the chemical equilibrium of the photocathode does not become disturbed by any outgassing of the photodiode array or its packaging. One of our initial objectives has therefore been to establish whether the proposed circular photodiode array is compatible with tube fabrication and processing techniques. In other words, whether the CCD can survive the rigours of bake-out and photocathode production and in turn whether the image tube can tolerate the presence of this internal sensor.

Although the vacuum pump port is generally located near the photocathode, appreciable amounts of evaporants can be absorbed onto electrode and wall surfaces. The exposure of the SSCEDA to these alkalis is to be avoided so means will be devised by which the diffusion can be suppressed or eliminated from the sensor region of the tube. The mechanisms under current consideration involve either a spring-loaded metal 'shutter' or the 'ball-stop' constraint located at the anode aperture. It follows that it would be necessary to evacuate both of the quasi-independent regions and some differential heating could also be applied. Whenever the photocathode has been processed the obstruction is suitably removed from the anode aperture so that the integral device can be tested.

An alternative considered was the inclusion of a electron transmissive mica window within the tube (using techniques developed for fabrication of Spectracon tubes [8]) which would effectively partition the photocathode and CCD from each other. A review of early literature allowed an empirical formula relating critical transmission thickness, t (in microns) to incident electron energy E_c (in keV) to be adapted from reference [8]:

$$t = 0.028 \times E_c^{1.65} \qquad \text{–eq(6.1)}$$

Comparison of this equation and Kanters universal transmission curve for mica [9] generated the plot shown in figure 6.9. As can be seen for the typical electron energies of 11 keV for the Photochron IIC streak tube an extremely thin mica window would be

needed to provide sufficient transmission of signal electrons. The stringent avoidance of any differential pressure between the photocathode and CCD regions in order to prevent rupture of this mica film would not be practicable. Also scattering processes in the mica would imply loss of image resolution. Consequently this photocathode isolation technique was not considered further.

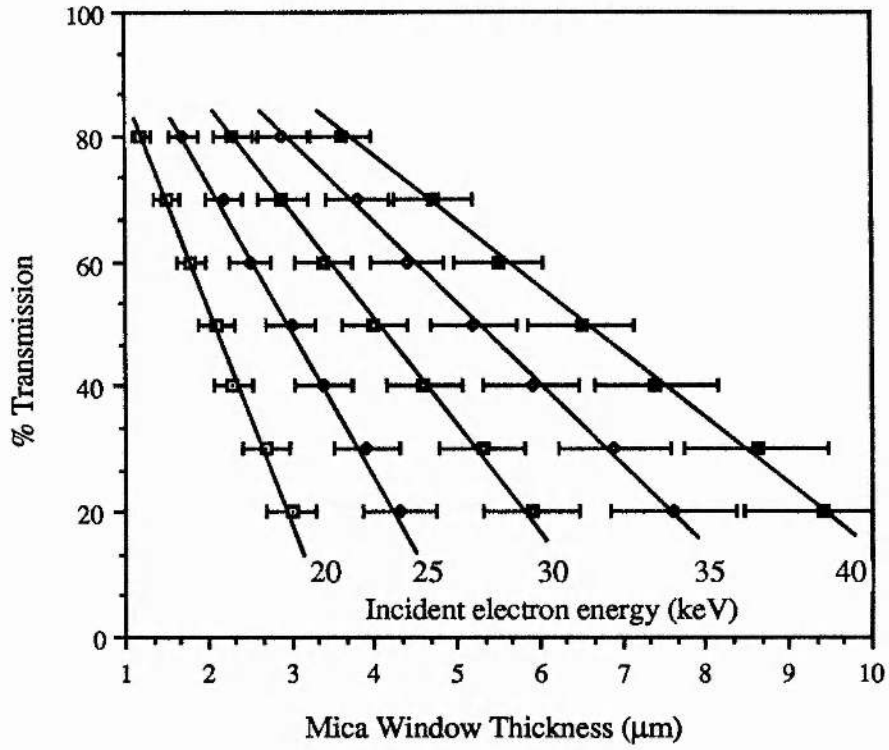

Figure 6.9 Electron transmission through mica as a function of thickness and incident electron energy

In the longer term it is proposed to use a 'photocathode transfer technology', whereby the cathode is processed outside the streak tube environment. The cathode can then be subsequently tested before being transferred and vacuum-sealed (eg. with cold indium seals) onto the tube body. This offers the advantages of preselection of high-sensitivity photocathodes and near avoidance of alkali contamination. Whereas this scheme has been exploited for smaller imaging photon-counting detectors its application to the relativity larger streak tubes would require the design and development of a dedicated transfer system.

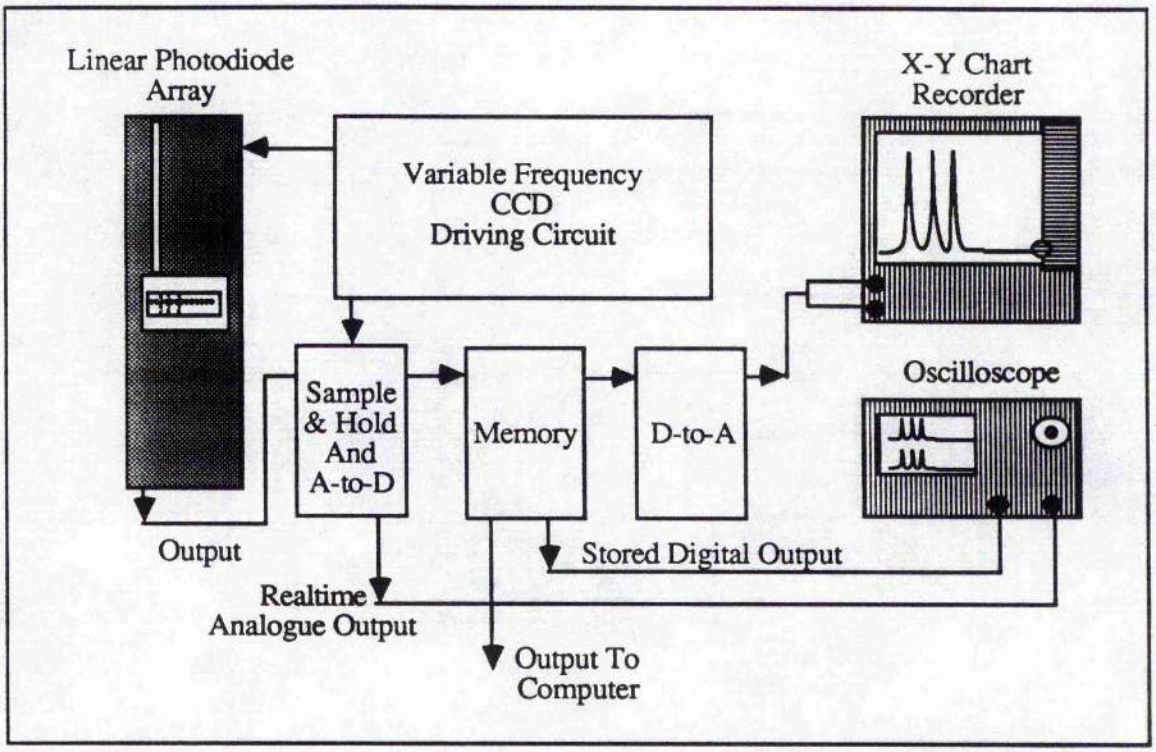

Figure 6.10 Linear Array Readout System

6.5.2 MOCK-UP LINEAR PHOTODIODE/CCDARRAYS

Before committing the specialist SSCEDA to the procedures detailed above preliminary tests were carried out on linear diode arrays that have been manufactured by IMEC using similar technology to that which will be employed for the circular device structure. Each array consisted of 512 photodiode pixels with two CCD shift registers above and below. One shift register would collect and clock out signal charge from the odd photodiode pixels and the other from the even pixels. These linear arays are controlled with the circuitry featured in figure 6.10 such that the output can be examined using a conventional oscilloscope. The drive circuitry was adapted from an original design provided by IMEC. Prior to any tube-compatibility tests the performance of each array was checked for the existence of 'dead' pixels, uniformity of photoresponse, darkcurrent and saturation level. (See figure 6.11a.).

6.5.3 TEMPERATURE TESTS

Several test linear diode arrays were subjected to the temperature excursions (figure 6.8) experienced in image tube bake-out schedules. Each array was covered with a

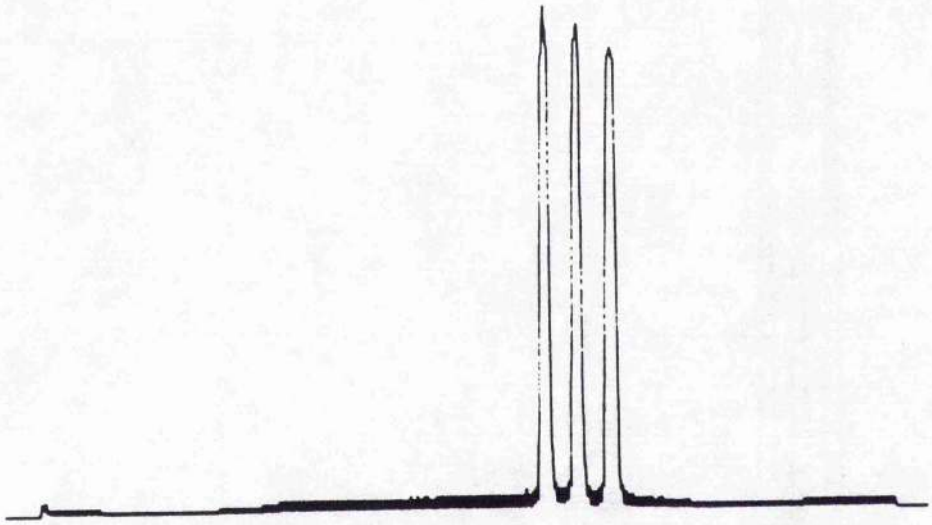

a)

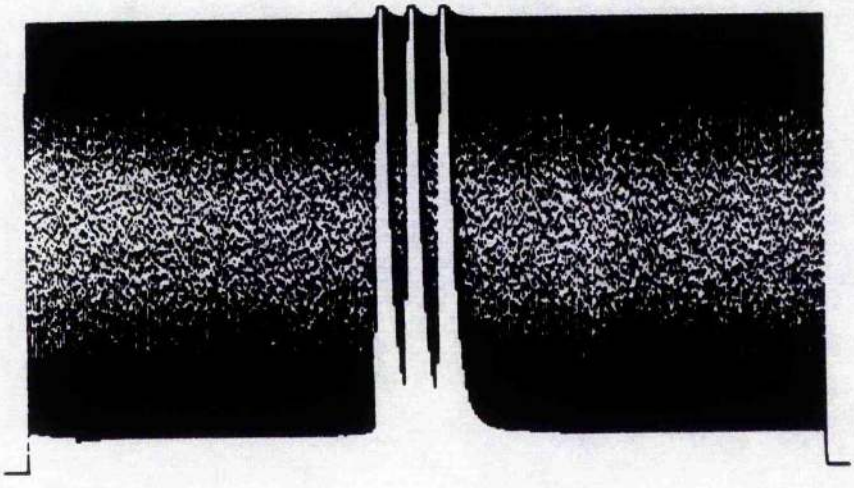

b)

Figure 6.11 3-slit test image displayed on linear photodiode array a) prior to bake-out and b) following bakeout with one channel saturated.

microscope slide, wrapped in aluminium foil (thereby avoiding electrostatic effects) and placed inside a sealed, evacuated glass ampule. This was then located within the oven that contained a streak tube that was passing through the bake-out and processing phases of production at Instrument Technology Ltd. (ITL). Upon subsequent removal and testing the array outputs were observed to be saturated with dark current (figure 6.11b). After examination using an optical microscope it was concluded that failure to survive was likely to have been due to the harmful influence of residual epoxy adhesive remaining after the removal of the array's protective glass window. During heating this epoxy would sublime, char and contaminate the array structure. IMEC arrays without protective windows were then tested. It was found that while they could withstand heating to 300° C for 1 hour they were inoperable at the end of the complete bake-out cycle unless a negative bias was provided to the substrate.

These results caused some concern because it was expected that the silicon structure should readily cope over these temperature ranges. It was later realised that the silicon wafer itself was bonded to its ceramic package by what appeared to be silver loaded epoxy and it was recognised that this was also a likely source of problems. This clearly has important implications in respect of the SSCEDA to be incorporated into the streak tube because this epoxy would otherwise have been used for bonding the silicon wafer to the ceramic substrate. This technique is therefore not acceptable because the epoxy vapour would doubtless seriously impair and probably destroy the performance of the diode array, the photocathode and also contaminate the vacuum pumping system used by ITL. Epoxy is therefore to be avoided at all costs in the context of image tube processing technology.

Alternative approaches to the bonding of the diode array to the ceramic substrate were therefore investigated. Several possibilities were suggested including the use of a eutectic adhesive layer of indium or indium-tin alloy and an interim solution whereby a purely mechanical constraint between the silicon wafer and ceramic substrate could be implemented. A more simple solution was found by discovering a temperature resistant polyimide bonding epoxy which was stable to above 400°C. In tests at ITL it was observed that appreciable sublimation of adhesive material still existed but it had a different nature.

With the original epoxy bonded arrays after bake-out carbon could be seen lying on the array structure and the ampules had a characteristic charred aroma, whereas with the new arrays no epoxy debris was observed but a definite phenolic sublimant could be detected. This is encouraging in the sense of possible damage to the silicon wafer (such high impedance structures are very susceptible to short-circuit by the patially conductive carbon and thus charring of epoxy must be avoided). However the effect of the epoxy sublimant on the photocathode processing and its subsequent lifetime was still uncertain.

On retesting the arrays after bakeout the devices initially showed the same problems as with the previous arrays ie) saturation on one or both channels. Isolating the on-chip test FETs - this proved a remedy in some cases for earlier tested CCD's - had no effect in this case. However if a negative bias of approximately 1.2 volts was applied to the substrate the devices could be made to work perfectly with no apparent deterioration compared to their prebake-out performance. The conclusion is that the new adhesive, although an improvement on the previous epoxy, still has some effect on the linear array's performance. (The reliance on substrate biasing was due to an contamination of the input diode causing it to switch on for normal ground voltages and fill the CCD register).

6.5.4 PHOTOCATHODE PROCESSING COMPATIBILITY

It was decided to attempt a photocathode process in the vicinity of the array. To this end a test cell was designed where both photocathode and array could be tested after the process and their subsequent performance monitored indefinitely. The test cell (see figure 6.12) consists of the rear pin section of an EMI photomultiplier tube providing 21 feed-through pins for electrical connections to the CCD. To these pins stainless steel tapers were spot welded and at the other end small pins taken from DIL sockets attached. The whole rear assembly was drop sealed to a piece of glass tubing with a nilo flange at one end. The linear array was push fitted to the DIL pins and was tested before photocathode processing was attempted. The front of the test cell comprises the photocathode substrate, evaporators and an anode plate accommmodating a sliding shutter which should prevent the effusion of evaporants to the rear of the cell during photocathode processing. A test pattern,

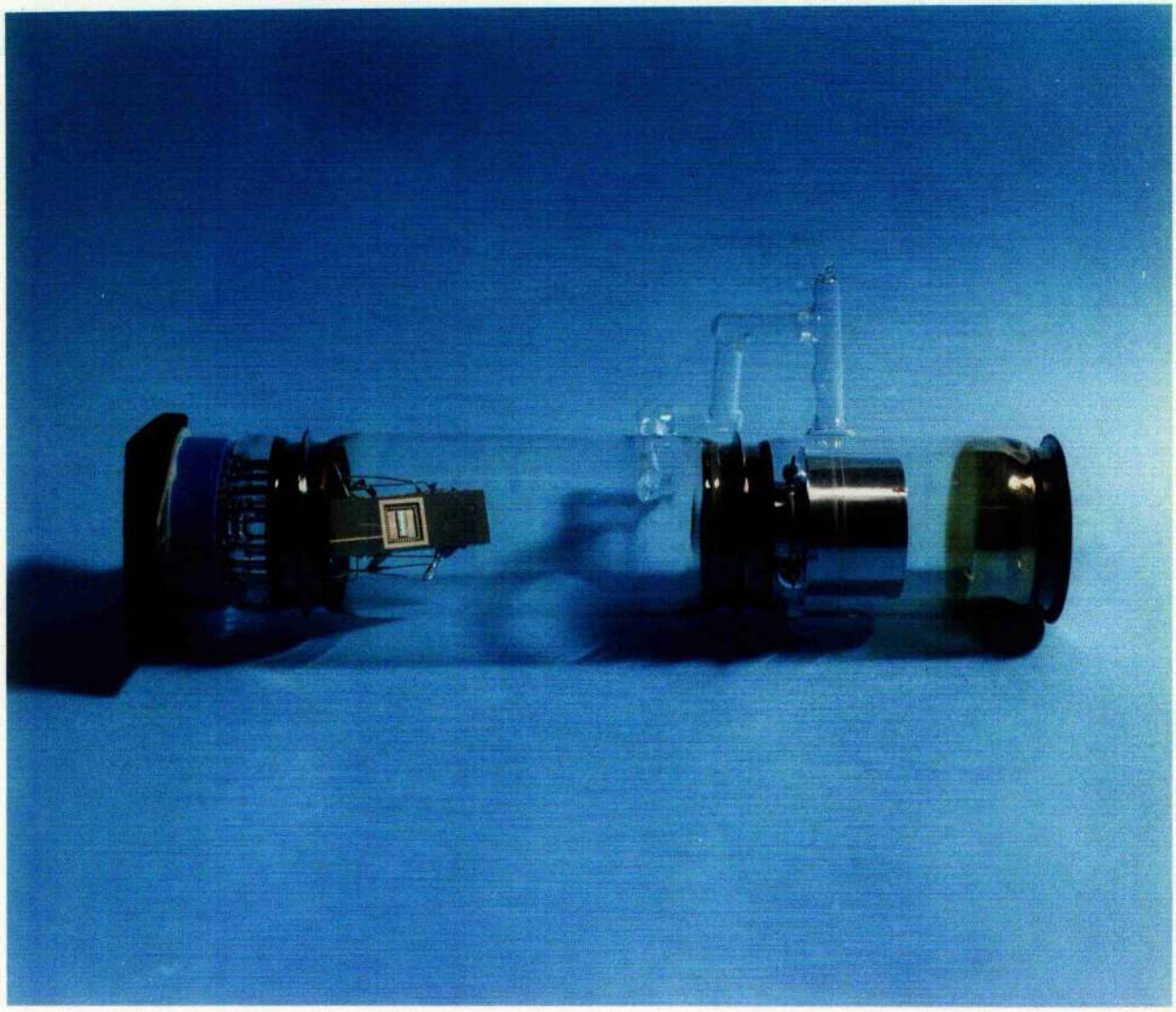

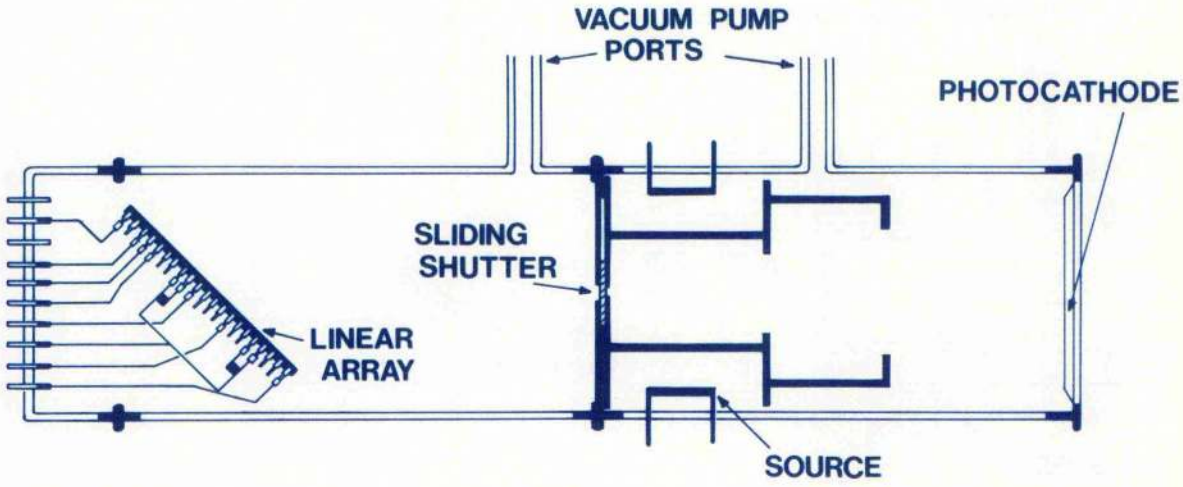

Figure 6.12 Photograph and schematic of vacuum test cell containing linear photodiode array and processed S20 photocathode.

comprising three narrow slits, was then projected onto the array and the intensity adjusted to a level slightly less than that required to achieve saturation on peak signal. This confirmed that the array was operating correctly.

The first tube produced was only partially successful. A good (>100mA/L) S25 photocathode was obtained but unfortunately no lifetime studies were possible due to a stress fracture in one of the glass pumping stems of the glass envelope. When the array was removed and tested it was found to be working properly on just one register. The other register was completely non-functioning which would imply that the device had withstood the photocathode manufacturing procedure and that failure arose through a faulty electrical interconnect. There was always the possibility that the physical stresses associated with the temperature cycling had contributed to mechanical failure.

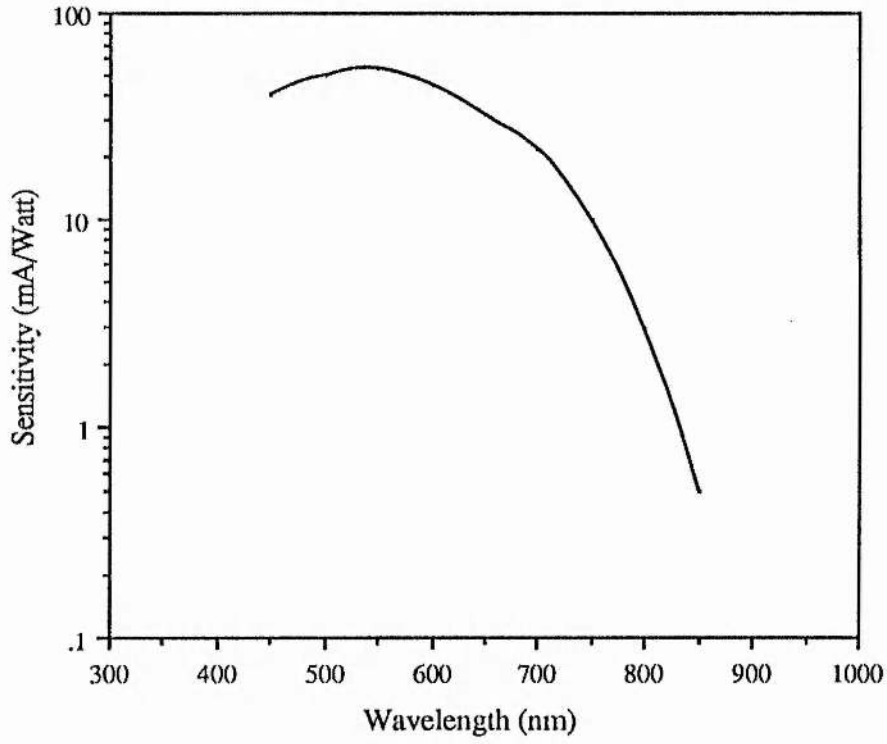

Figure 6.13 Spectral response of S20 photocathode processed in test cell.

It was therefore necessary to repeat the experiment using another array in a new test cell. The cathode obtained was of the same quality as that achieved during the previous process having photosensitivity of approximately 100mA/Lumen. The spectral response of this second photocathode is shown in Figure 6.13.

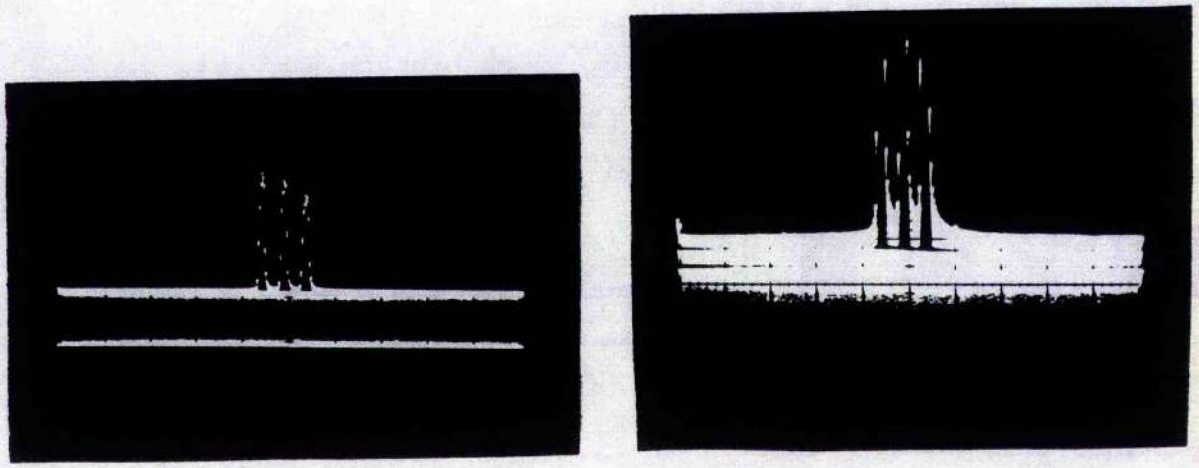

a) b)

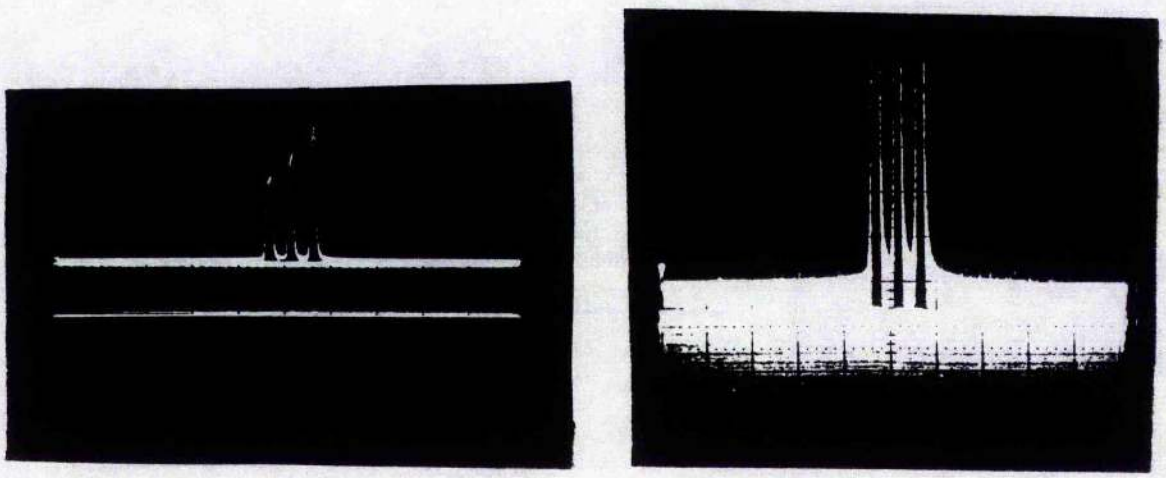

c) d)

Figure 6.14 3-slit test image of linear array inside test cell a) prior to photocathode processing, b) expanded scale, c) after processing and d) expanded scale.

After three days the array was checked and found to have similar performance to that obtained prior to inclusion in the glass envelope. Figure 6.14a and b shows the performance of the array prior to processing, figure 6.14b being an identical trace to a) but on an increased oscilloscope sensitivity. This highlights the small (≈5mV) random noise content present in the dark level of the array. Figures 6.14c and 6.14d are similar readouts for the array after photocathode processing. Note the slight increase in random noise content both in amplitude and generation rate.

The test cell was tested over a period of several months and the linear array is still working with no obvious degradation in performance and similarly the photocathode is showing no signs of deterioration.

6.6 PRESENT STATUS OF SPACE PROJECT

After extensive processing runs IMEC were partially successful in manufacturing the SSCEDA in that arrays were produced that showed some electron sensitivity, but a fully working device was not produced. The problems encountered in generating masks with circular geometries and stringent location tolerances proved problematical. It is intended for future stages of the space project to commission photolithographic masks from the professional market.

Nevertheless, the above preliminary assessments indicate that it should be possible to incorporate an array into a streak camera tube without seriously impairing the performance of either the array or the S25 photocathode. It should, however, be remembered that the array performance was evaluated solely as a light-sensitive device. The observable increase in the random noise at room temperature could represent an unacceptable decrease in performance when the device is required to detect small numbers of electrons, even when used at reduced temperature. Further tests on the actual devices to be incorporated in the streak tube will therefore be required. The next test cell should therefore incorporate an appropriate focussing electrode configuration and electron sensitive linear photodiode array such that it could be characterised as an electron imaging device.

REFERENCES

1 H.Lutz, W.Krause and G.Barthel, *Space 2000* Amer. Inst. of Aeronautics and Astronautics, New York, p.236 (1983).

2 W.Sibbett, W.Sleat, W.Krause and J.R.Taylor, Proc. ESA workshop on Space Laser Applications and Technology ESA **SP-202** 171 (1984).

3 W.Sibbett, W.Sleat, W.Krause and J.R.Taylor, Proc. XVIth ICHSPP SPIE **491** 76 (1984).

4 M.Leomonier, J.C.Richard, C.Piaget, M.Petit and M.Vittot, Proc. IEE conf. on Photoelectronic Imaging **253** 74 (1985).

5 A.Finch, W.Sibbett, W.E.Sleat, C.Claeys, I.Debusschere and W.Krause,Proc. Conf.on Solid State imagers and their applications, SPIE **591** 31 (1985).

6 G.J.Declerck, J.Bosiers, J.Sevenhans and L.Van den Hove, IEE Trans. on Elect. Dev. **ED–22** 1551 (1985).

7 E.L.Dereniak, M.N.Salcido, D.H.Pommerrenig, R.A.Simms and J.M.Abrahams, IEE conf. on Photoelectronic Imaging **253** 71 (1985).

8 J.D.McGee, A.Khogali and A.Ganson, Proc. III Symposium on photoelectronic image devices, Adv. in Electron. and Electron Phys. **22A** 331 (1966).

9 H.Kanter, Phys. Rev. **121** 461 (1961).

SECTION II

NONLINEAR PULSE MEASUREMENT

– SECOND HARMONIC GENERATION –

– AUTOCORRELATION –

CHAPTER 7: SECOND HARMONIC AUTOCORRELATION TECHNIQUES

7.0 INTRODUCTION

The commonly used method of laser pulse duration measurement by autocorrelation in a second harmonic crystal (SHG) was first reported by Maier et al [1] in 1966 and shortly afterwards by Armstrong [2]. The technique was eclipsed initially by the Two-Photon Fluorescence (TPF) method [3,4] of pulse measurement, beacause this latter method offered single-shot, single-pulse measurement whereas SHG autocorrelation required several shots while the pulse overlap within the crystal was varied to complete the autocorrelation. Hence the TPF method was ideally suited for the evaluation of the early flashlamp pumped modelocked lasers.

With the advent of CW passive mode-locking the SHG autocorrelation technique became more popular and provided a simple and inexpensive monitor of pulse duration. It offers the highest temporal resolution in the characterisation of ultrashort pulses but, due to its nonlinear nature, it does not provide a direct measurement of the pulsewidth, nor can pulseshape be readily discerned. Moreover, for the pulsewidth to be determined with any degree of accuracy, pulse spectra must be simultaneously investigated. For this reason streak cameras have several advantages over autocorrelation in the picosecond regime, but in the femtosecond regime, at present, there is no rival. Indeed when the interferometric detail is retained this nonlinear scheme can give quantitative measurement of pulseshape and chirp content. These aspects will be shown later to be of vital importance to the optimisation of passively mode-locked dye laser operation.

7.1 INTENSITY AUTOCORRELATION

A schematic of a basic second harmonic generation autocorrelator is included in figure 7.1. In essence it is a Michelson interferometer but with a lens, a SHG crystal (Type I, angle tuned) and filter to cutoff the unconverted fundamental light. The intensity of each pulse from the mode-locked pulse train is split into two subcomponents by the beam

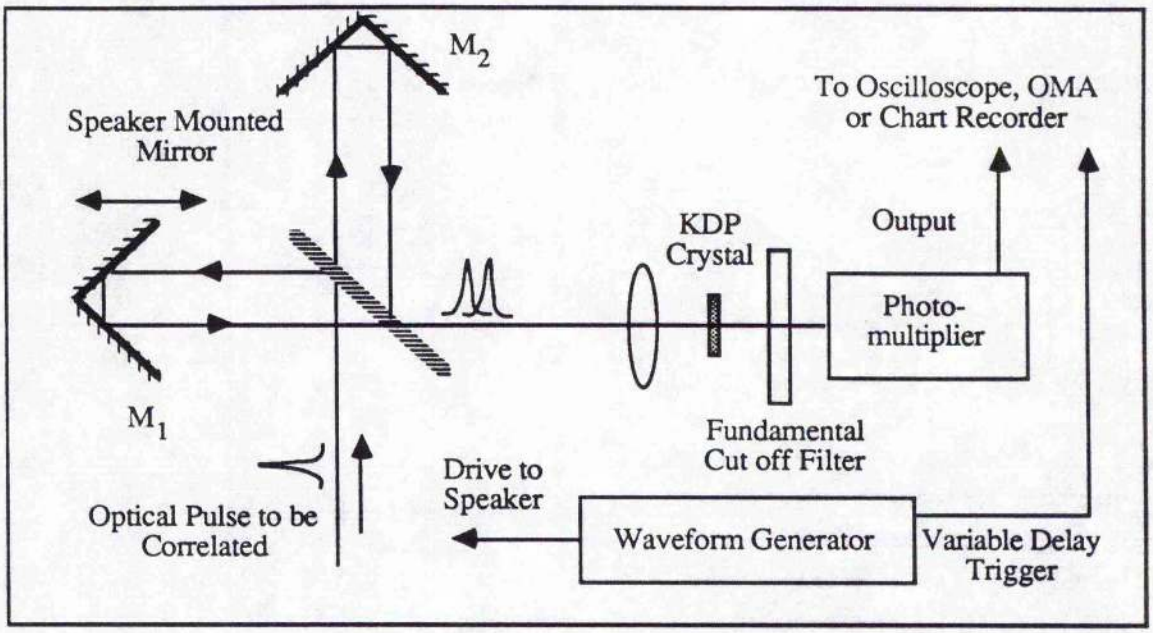

Figure 7.1 Schematic of basic Optical autocorrelator

splitter, and each travels to the separate retroreflectors, M_1 and M_2, to be reflected, recombined and focused into the SHG crystal. The translation of mirror M_1 has the effect of introducing a variable delay, τ into one arm of the autocorrelator. Thus one subcomponent pulse arrives slightly later (or earlier) at the crystal. Variable delay is usually provided by the movement of one retroreflector mirror either by a slow-scan, single-sweep stepping motor or repetitively via a loudspeaker or shaker mounting – the latter providing realtime monitoring.

The second harmonic signal generated within the crystal will consist of a background level due to the frequency doubled light from the separate subcomponents and an additional signal corresponding to the enhancement in the SHG process when the pulses overlap in transit through the crystal. This signal enhancement is a function of the differential path length between the two interferometer arms and reaches a maximum when the two path lengths are equal. The functional form of the second harmonic signal as τ is varied becomes in effect the autocorrelation of the intensity pulseshape and can be represented by:

$$G_2(\tau) = 1 + 2 \frac{\int_{-\infty}^{+\infty} I(t)I(t-\tau)\,dt}{\int_{-\infty}^{+\infty} |I(t)|^2 dt} \qquad \text{–eq(7.1)}$$

where I(t) is the intensity distribution of the pulse.

For the CPM laser operating at around 630nm the SHG signal from the crystal is passed through a filter, type Kodak BK3, to remove the fundamental frequency and then detected with a photomultiplier tube (PMT) which provides an electrical signal for an oscilloscope, chart recorder or multichannel analyser. If M_1 is translated at a constant rate then the signal displayed is directly proportional to the above formula. Referring to figure 7.2 which shows a calculated intensity autocorrelation of a sech^2 pulse, we see that the peak signal to background level is in the ratio of 3:1 which is characteristic of this type of autocorrelation and offers a useful check during actual measurement for correct interferometer alignment and optimal phase matching within the SHG crystal.

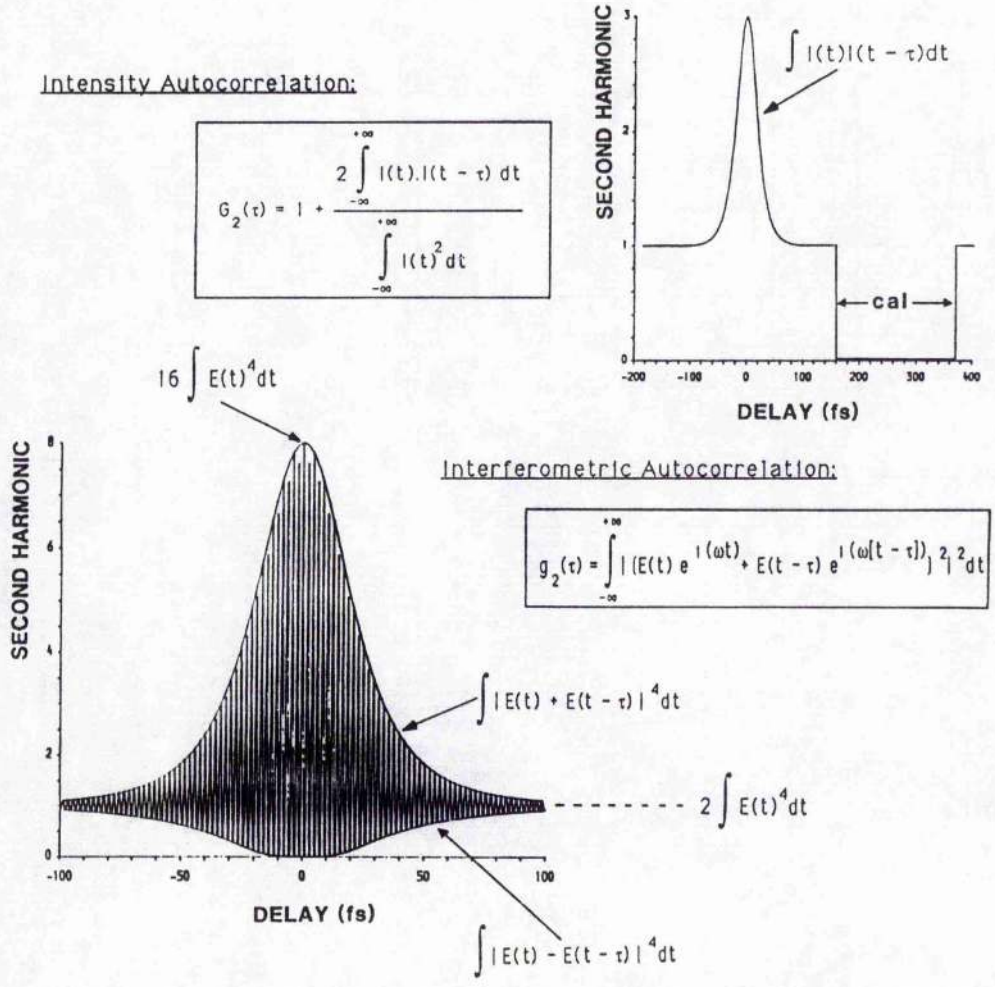

Figure 7.2 Properties of intensity and interferometric autocorrelation functions

To deduce a pulse duration from this measurement requires a knowledge or assumption of the pulseshape. For a given pulseshape the ratio between the FWHM pulse duration, Δt and the FWHM of the autocorrelation, $\Delta\tau$ is a constant. As mentioned previously, the $sech^2$ pulse intensity profiles that are often assumed have the $\Delta\tau/\Delta t$ ratio of 1.543. Dividing the autocorrelation FWHM by this correction factor gives the actual pulse duration. However it is inadvisable to assume a given pulseshape without some experimental back-up and the common method adopted is measurement of the pulse FWHM spectral bandwidth, $\Delta\nu$ by means of a scanning monochromator. The bandwidth-duration product, $\Delta\nu\Delta t$ is also a constant for a given pulseshape and hence this complementary spectral measurement provides an important cross-check.

The intensity autocorrelation is impervious to frequency chirp content and relatively insensitive to pulseshape – the FWHM of the autocorrelation always gives a measure of the pulse duration irrespective of the frequency sweep across the optical pulse. This is useful when one is only concerned with pulse durations but for pulse characterisation intensity autocorrelations can give only a limited amount of information.

7.2 Interferometric Autocorrelation

The intensity autocorrelation is more widely employed due to frequency response limitations on the detection and recording systems (see Chapter 8). The main disadvantage of the intensity autocorrelation, being in its very nature a time-averaged recording, is that it can conceal many vital pulse parameters including laser amplitude instability and frequency chirp. It is also more prone to inaccuracy due to incorrect calibration of the delay introduced by imprecise mirror translation.

A better and in some ways more fundamental measurement technique is termed *interferometric autocorrelation* [5]. If the detection system (PMT and monitor) has sufficient frequency response with respect to the rate of mirror translation then it is possible to resolve the constructive and destructive interference effects between the electric fields of the recombined subcomponents as the delay is varied. For this reason this type of pulse measurement is sometimes labelled *fringe resolved autocorrelation.*

For a pulse with field envelope E(t) and centre optical frequency w_o the time dependent electric field of the pulse can be written as

$$\xi(w_o,t) = E(t)\, e^{iw_o t} \qquad \text{–eq(7.2)}$$

where: $I(t) = |\, E(t)\, e^{iw_o t}\, |^2.$

In this case the SHG intensity signal will be proportional to the function $g_2(\tau)$:

$$g_2(\tau) = \int_{-\infty}^{+\infty} |\xi(w_o,t) + \xi(w_o,t-\tau)|^4\, dt$$

$$= \int_{-\infty}^{+\infty} |E(t)e^{iw_o t} + E(t-\tau)\, e^{iw_o(t-\tau)}|^4\, dt \qquad \text{–eq(7.3)}$$

This expression has the form shown in figure 7.2. It has a characteristic peak-to-background ratio of 8:1 and is more sensitive to pulseshape and, as will be shown later, various types of pulse chirp will produce distinctive patterns in the autocorrelation. In common with the intensity autocorrelation (which is in effect the fringe average of the above), pulse duration is determined by a correction factor specific to a given pulse profile – for the $sech^2$ pulseshape $\Delta\tau/\Delta t$ is equal to 1.897. Within the interferometric autocorrelation the delay between two fringe maxima corresponds to one optical cycle within the pulse. Providing the central wavelength of the pulse is known, and there is not excessive chirp present, this fringe spacing enables the autocorrelation to be self-calibrating. The necessity for high frequency response of the monitoring system implies that pulse-to-pulse instabilities, be they phase or amplitude fluctuations, will become apparent. This is in contrast with the intensity autocorrelation where the time-averaging (effected by inserting a low-pass filter at the PMT output) conceals such laser instabilities and presents a more aesthetically pleasing but often unrealistic pulse measurement.

Having performed an interferometric autocorrelation, the pulseshape and duration may be determined by undertaking iterative fitting onto the autocorrelation envelope about the loci of fringe maxima and minima. This eases computation since less data points need be generated than if a fit to the complete autocorrelation were attempted. The envelope integrals are simply derived from eq(7.3) by replacing the frequency-dependent terms as follows:

$$g_2(\tau) = \int_{-\infty}^{+\infty} |E(t) \pm E(t-\tau)|^4 \, dt \qquad \text{-eq(7.4)}$$

where the maxima loci correspond to the addition of the electric field envelopes and the minima loci correspond to their subtraction.

The effects of pulseshape on intensity and interferometric autocorrelations and also the corresponding pulse spectra are illustrated in the following sections. Additional sections are concerned with the addition of chirp to the pulse. Although the data have been generated using a computer program the results are relevant to Chapter 9 where an analysis of the CPM laser properties is presented.

7.3 PULSESHAPE MODELLING

When autocorrelations are used to determine pulse duration a certain pulseshape is generally assumed and a corresponding correction factor applied to the recorded FWHM of the autocorrelation. The result is then cross-checked with the pulse spectral bandwidth to verify that the $\Delta\nu\Delta t$ product corresponds to the pulseshape adopted. A widely assumed pulseshape is the $sech^2$ – this is probably due to the fact that this shape is a solution of the early theoretical and rather simplified studies applied to passively mode-locked CW lasers [6].

It is important, however, to fit various computed autocorrelation curves to the measured data for more comprehensive proof that the assumed pulseshape resembles reasonably the actual pulse detected. As will be presented in Chapter 9 we have demonstrated strong evidence for pulse asymmetry within our CPM dye laser. Since no tabulated $\Delta\nu\Delta t$ values or deconvolution factors were available for asymmetric pulseshapes – apart from the rather contrived single-sided exponential profile – a program suite was devised for the calculation of these pertinent constants and it also performs the necessary integrations to generate autocorrelation profiles (either intensity, fringe resolved or envelope) and corresponding spectra to allow fitting to be performed to measured data. The programs were written in Fortran and access several NAG routines which perform relevant numerical integrations. The suite is operated on a Digital VAX 11/785 mainframe.

Table 7.1 shows the various correction factors and constants referred to above. The values were calculated from an analytical pulseshape which can have differing degrees of asymmetry and was expressed in the form:

$$E(t) = \frac{1}{[\exp\{rt\} + \exp\{-t\}]} \qquad \text{–eq(7.5)}$$

It was termed the *asymmetric sech² function.* For $r = 1$ the pulseshape is symmetrical and has an intensity profile identical to the sech² pulseshape. As r increases the trailing edge of the profile steepens and the opposite effect occurs on the leading edge. Eventually as r approaches infinity the intensity profile approaches that of the single-sided exponential (these properties are represented in figure 7.3).

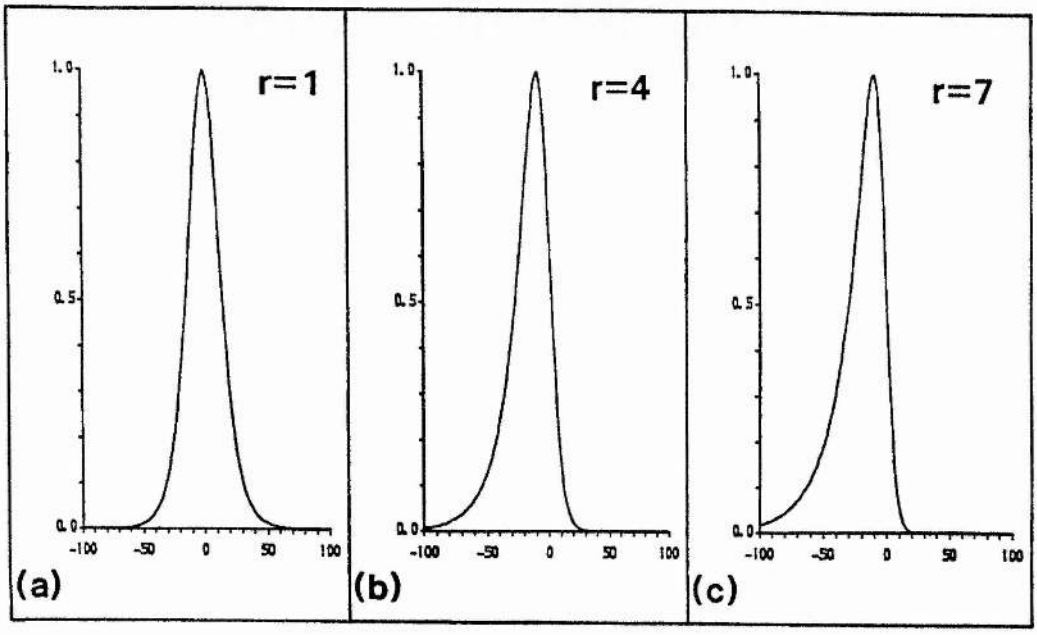

Figure 7.3 Asymmetric pulse profiles a) $r = 1$, b) $r = 4$ and c) $r = 7$

Table 7.1 Correction factors and bandwidth-duration products for pulseshapes or varying asymmetry

r	∂t_o	Bandwidth-duration product	Intensity a.t. correction factor	Interferometric a.t correction factor
1	1.7627	0.3148	1.543	1.897
2	1.2580	0.2996	1.545	1.902
3	1.0430	0.2784	1.549	1.991
4	0.9183	0.2598	1.554	1.920
5	0.8354	0.2444	1.559	1.931
6	0.7755	0.2317	1.565	1.942
7	0.7300	0.2212	1.571	1.954
8	0.6941	0.2125	1.577	1.965
9	0.6650	0.2050	1.584	1.977
10	0.6408	0.1986	1.590	1.989
11	0.6204	0.1931	1.597	2.001
12	0.6029	0.1883	1.603	2.012
13	0.5878	0.1840	1.610	2.023
14	0.5745	0.1802	1.616	2.035
15	0.5628	0.1769	1.623	2.045
16	0.5523	0.1738	1.629	2.056
17	0.5429	0.1711	1.635	2.066
18	0.5345	0.1686	1.641	2.076
19	0.5168	0.1666	1.647	2.086
20	0.5198	0.1642	1.652	2.095
25	0.4922	0.1559	1.678	2.137
30	0.4728	0.1500	1.700	2.172

The spectral bandwidth required to generate these pulses also changes with r, as can be readily observed from the bandwidth-duration product. At $r=1$ we have the classic sech^2 $\Delta\nu\Delta t$ value of 0.315, while as r increases $\Delta\nu\Delta t$ decreases to approach the single-sided exponential product of 0.110 for $r=\infty$. Table 1 displays this variation of bandwidth-product with pulseshape, together with a value labelled ∂t_o which is simply the FWHM of the pulse intensity profile that is represented in eq(7.5) in arbitrary time units. Scaling to a real duration, Δt is achieved by modifying the above equation to yield:

$$E(t) = \frac{1}{[\exp\{rft\} + \exp\{-ft\}]} \qquad \text{–eq(7.5b)}$$

where $f = \partial t_o/\Delta t$. Bandwidth-duration products naturally remain identical.

E(t) merely represents the electric field envelope; however the full oscillatory expression relevant to an optical pulse is most usefully represented as:

$$\xi(w_o t) = E(t)\, e^{i(w_o t + \emptyset(E,t))} \qquad \text{–eq(7.6)}$$

where w_o is the central frequency of the pulse spectrum and $\emptyset(E,t)$ a term describing the chirp content within the pulse. Physically there are various specific causes of frequency chirp within an optical pulse which manifest themselves as a particular functional form of $\emptyset$. These are most conveniently split into two types: (i) *linear chirp* – generated by passage of an optical pulse through a weakly dispersive medium (eg. glass) and is dependent solely on *t.*, (ii) *nonlinear chirp* – generated by interaction of the pulse for example with a Kerr-like medium or one with saturable gain or absorption, (both of which occur in the CPM dye laser). In this latter case $\emptyset$ has a further functional dependence on the pulse profile, E(t) aswell as a temporal dependence.

All of these examples will be dealt with in subsequent sections of this chapter.

7.4 PULSE AUTOCORRELATION AND SPECTRAL CHARACTERISTICS

The interferometric and intensity autocorrelation profiles have a certain dependency on the input pulseshape. The additional presence of chirp within the pulse can have a considerable effect on the interferometric autocorrelation which requires a high degree of coherence across the pulse in order to generate the constructive and destructive interference

of the fundamental electric fields within the SHG cystal. This is not so for the intensity counterpart whose insensitivity to chirp thus provides a definitive method for pulse duration determination. There is also an effect in the frequency domain, chirp content producing broadening and modulation of the pulse spectra and these effects will now be expanded upon in the following subsections.

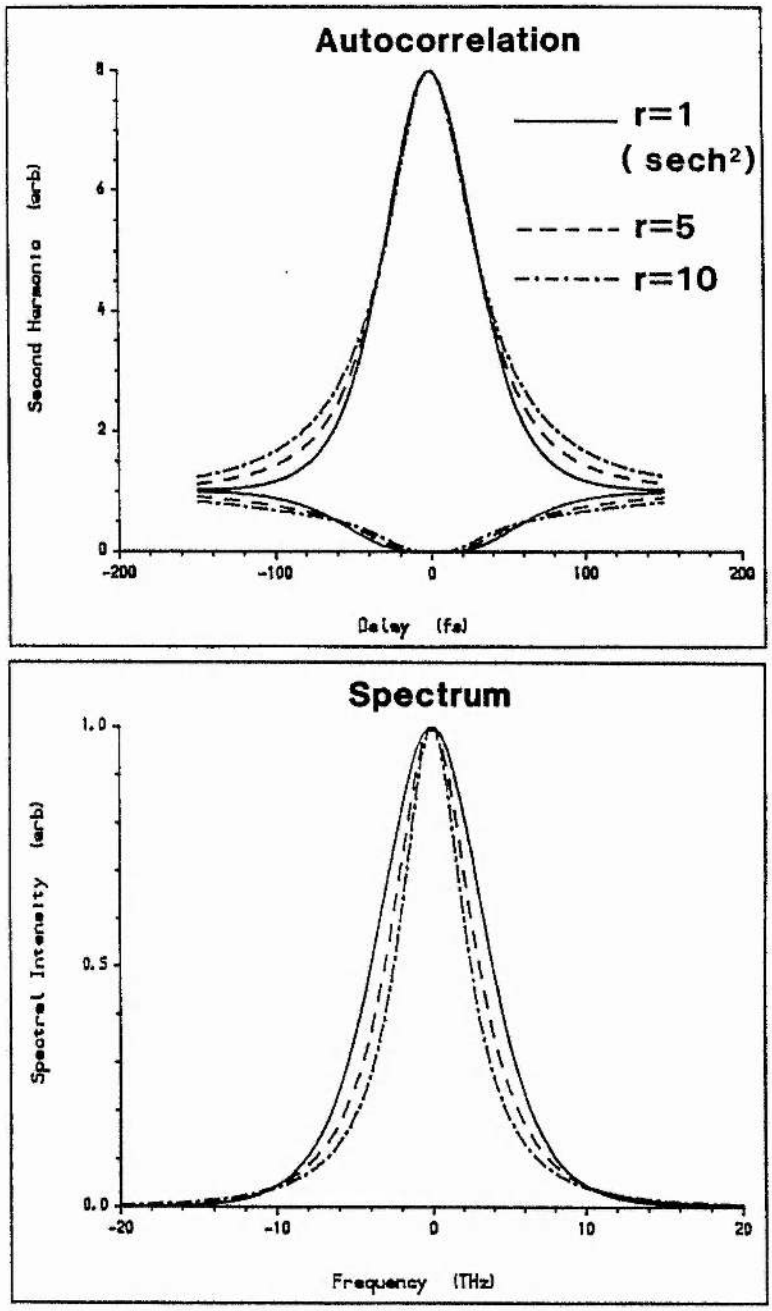

Figure 7.4 Interferometric autocorrelation profiles and spectra for pulses of varying asymmetry factor *r*.

7.4.1 PULSESHAPE EFFECTS

In a detailed analysis carried out by Diels [7], who has pioneered interferometric correlation techniques, several pulseshapes were analysed, namely gaussian, $sech^2$ and asymmetric functions of particular form which lend themselves to analytical solutions when calculating their autocorrelations. Calculation of the autocorrelation with the pulseshape depicted in equation 7.5 can only be performed by use of numerical methods to solve the relevant integrations. As can be seen from Table 7.1 the actual FWHM deconvolution factors do not change drastically with asymmetry indicating that the central region of the autocorrelation sees little dependence on pulse asymmetry. The same cannot be said for the wings of the correlation which, as the pulse asymmetry increases, extend to larger delays as illustrated in figure 7.4 which shows the envelopes of interferometric autocorrelations of different pulse asymmetries, together with the corresponding intensity autocorrelations. Shown also in figure 7.4 are the Fourier transforms of the pulseshapes listed. Note that the more asymmetric the pulse the wider the spectral base but the more narrow the central FWHM region. This is to be expected because the sharp asymmetric edge in the pulse will require the existence of higher frequency components within its Fourier transform.

7.4.2 LINEAR CHIRP

The propagation of optical pulses through dispersive media (eg. fused silica) has the effect of imposing a linear chirp on the pulse as was demonstrated analytically [8] and experimentally [9] for Gaussian pulses. In mathematical terms this is equivalent to the presence of a time-varying quadratic phase term in eq(7.5),

$$\emptyset_L(t) = \mathcal{A}t^2 \qquad \text{–eq(7.7)}$$

which represents a linear sweep in frequency across the pulse. Substitution of the phase term into eq(7.4) yields, after expansion:

$$g_2(\mathcal{T}) = \int_{-\infty}^{+\infty} |E(t)^2 + E(t-\mathcal{T})^2 + 2\,E(t)E(t-\mathcal{T})\cos(w_o\mathcal{T}-\mathcal{A}\mathcal{T}^2+2\mathcal{A}t\mathcal{T})|^2\,dt \qquad \text{–eq(7.8)}$$

This expression is somewhat cumbersome for numerical analysis, but calculable. An approximation of its envelope function can be generated by looking for maxima and

minima within the kernel. This will obviously occur whenever the argument of the cosine is equal to an integer number of pi. Assuming that the largest contribution to the integral occurs around t=0 then the locus of maxima and minima will occur when:

$$\tau_n = \frac{w_o - \sqrt{(w_o^2 - 4Aq)}}{2A} \qquad \text{–eq(7.9)}$$

with q = 2nπ for maxima and (2n+1)π for minima, with n as integer. Calculating the integral of eq(7.8) for the specific values of τ_n given in eq(7.9) yields the envelope function shown in figure 7.5 which should be compared to the full fringe function also shown on the figure. Good agreement is possible for small values of chirp and τ.

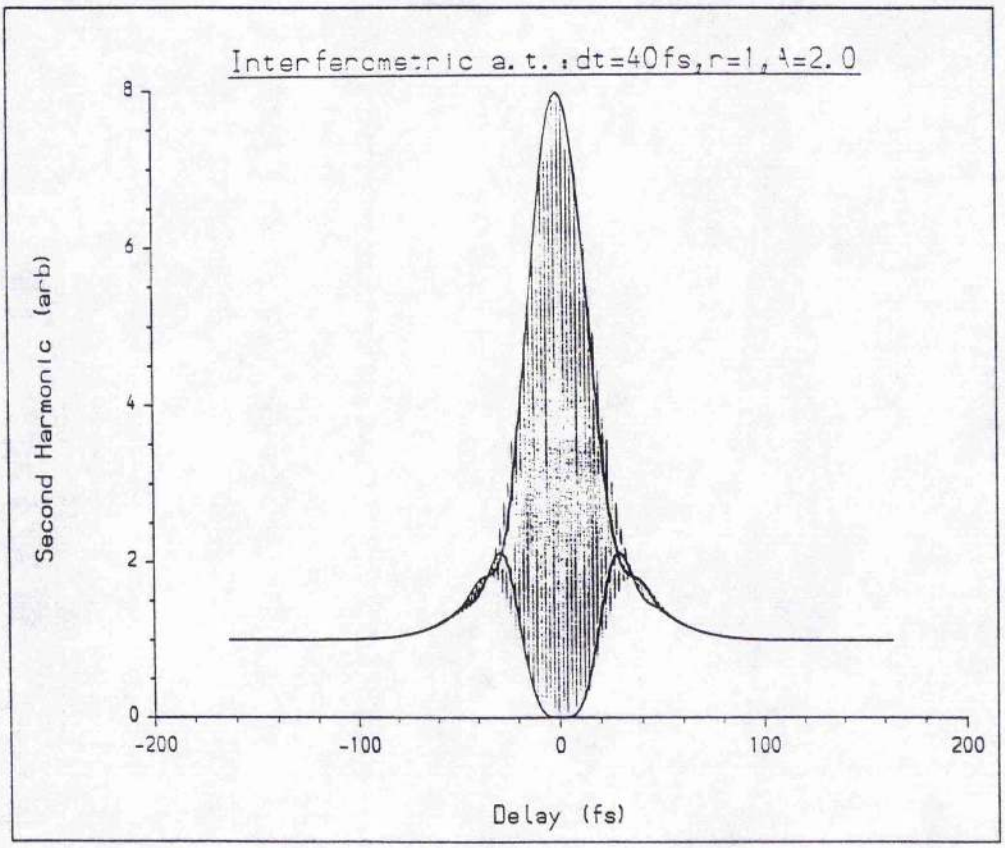

Figure 7.5 Envelope and full fringe linearly-chirped autocorrelations

Figure 7.6 shows a montage of full fringe interferograms for a $sech^2$ pulse (r =1) with different amounts of linear chirp, together with the corresponding spectra. The modelled pulse is of 40fs duration and has a central wavelength at 630 nm. Two effects can readily be observed as the chirp content is increased. The region of interference across the

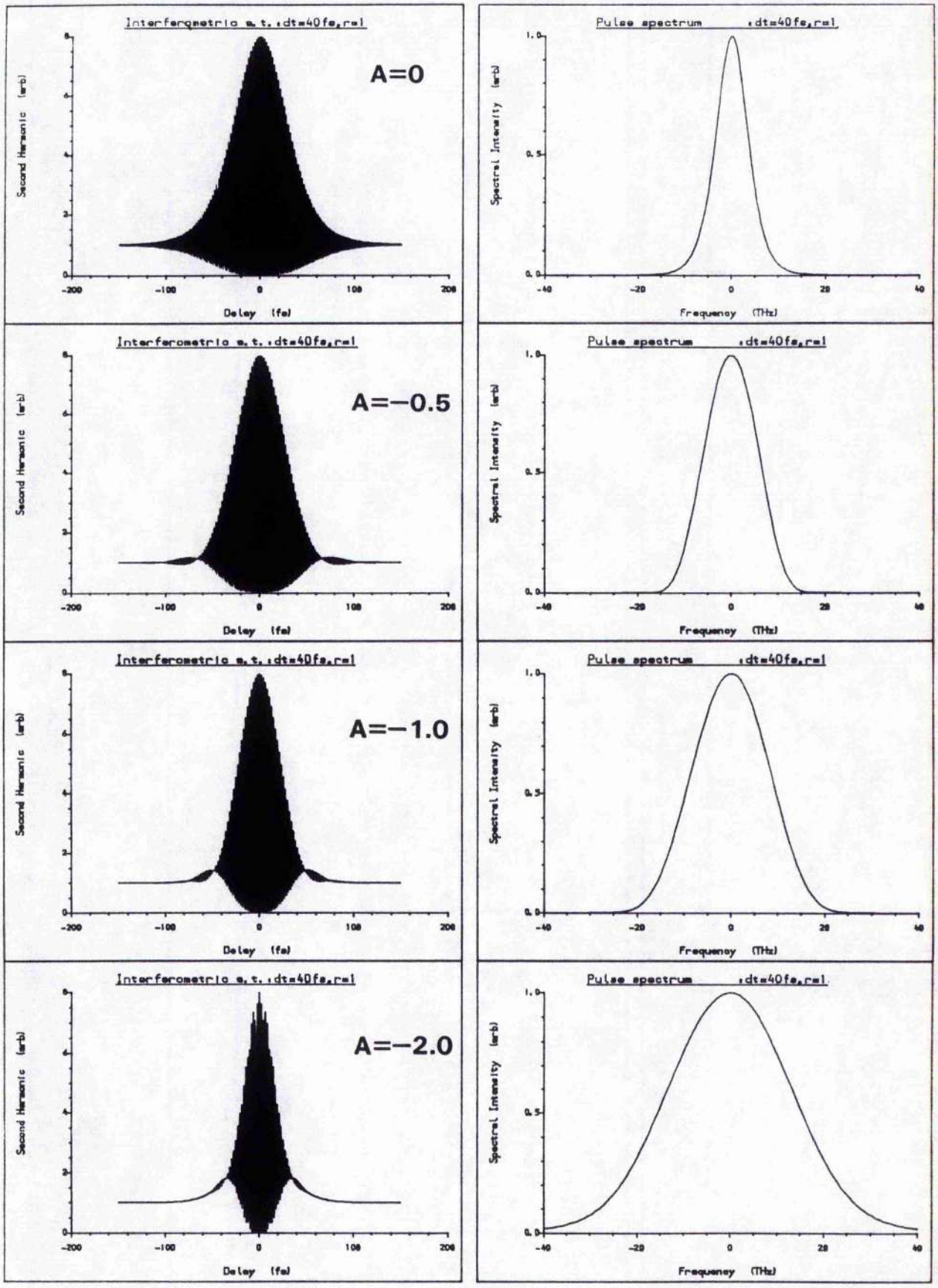

Figure 7.6 Autocorrelation and spectral data for sech^2 pulses with linear chirp

autocorrelation decreases, the fringe visibility is lost for large delays and in these regions the profile approaches that of an intensity autocorrelation. This is to be expected since the destructive and constructive superposition of the subcomponent electric fields within the SHG crystal depend upon interacting fields having closely related frequencies. In the wings of the autocorrelation the signal is generated from the overlap of leading and trailing parts of the optical pulse, where the linear chirp is largest and opposite in sign and thus the signal here becomes proportional to the subcomponent intensities. This can be seen in figure 7.7 where both the interferometric and intensity autocorrelations of a highly chirped $sech^2$ pulse are shown. The effect is analogous to the generation of *white light fringes* in a Michelson interferometer which are resolved only near zero path difference (equivalent to zero delay in the autocorrelation set up).

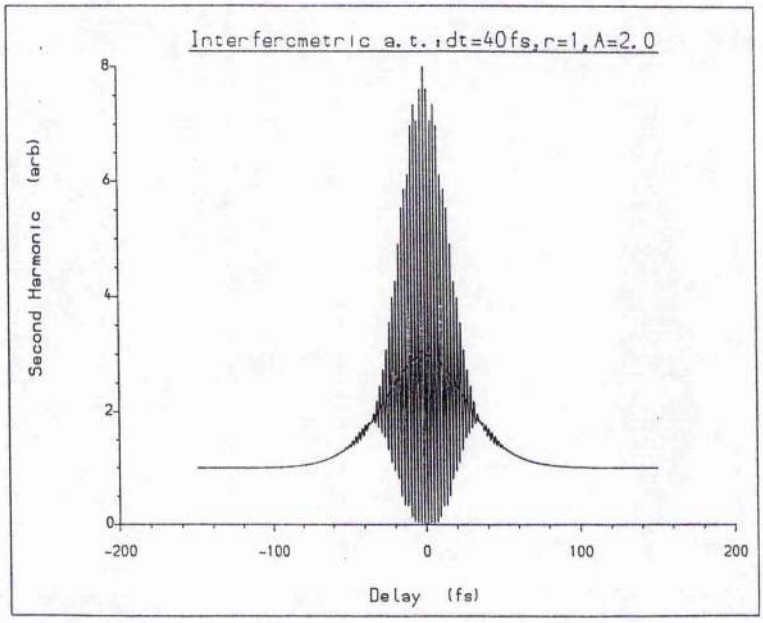

Figure 7.7 Coherence loss in wings leading to intensity autocorrelation resemblance (dotted lines)

The second effect is that on pulse spectrum. For the $sech^2$ pulse linear chirp generates a symmetric broadening of the Fourier spectrum compared to the unchirped pulse. Figures 7.8 show a similar montage for an asymmetric pulse ($r = 5$). Here again there is a loss of fringing in the wings of the autocorrelation but the effect is less severe than for the $sech^2$ pulse – note the values of $\mathcal{A}$ used. However there is an interesting effect on the pulse

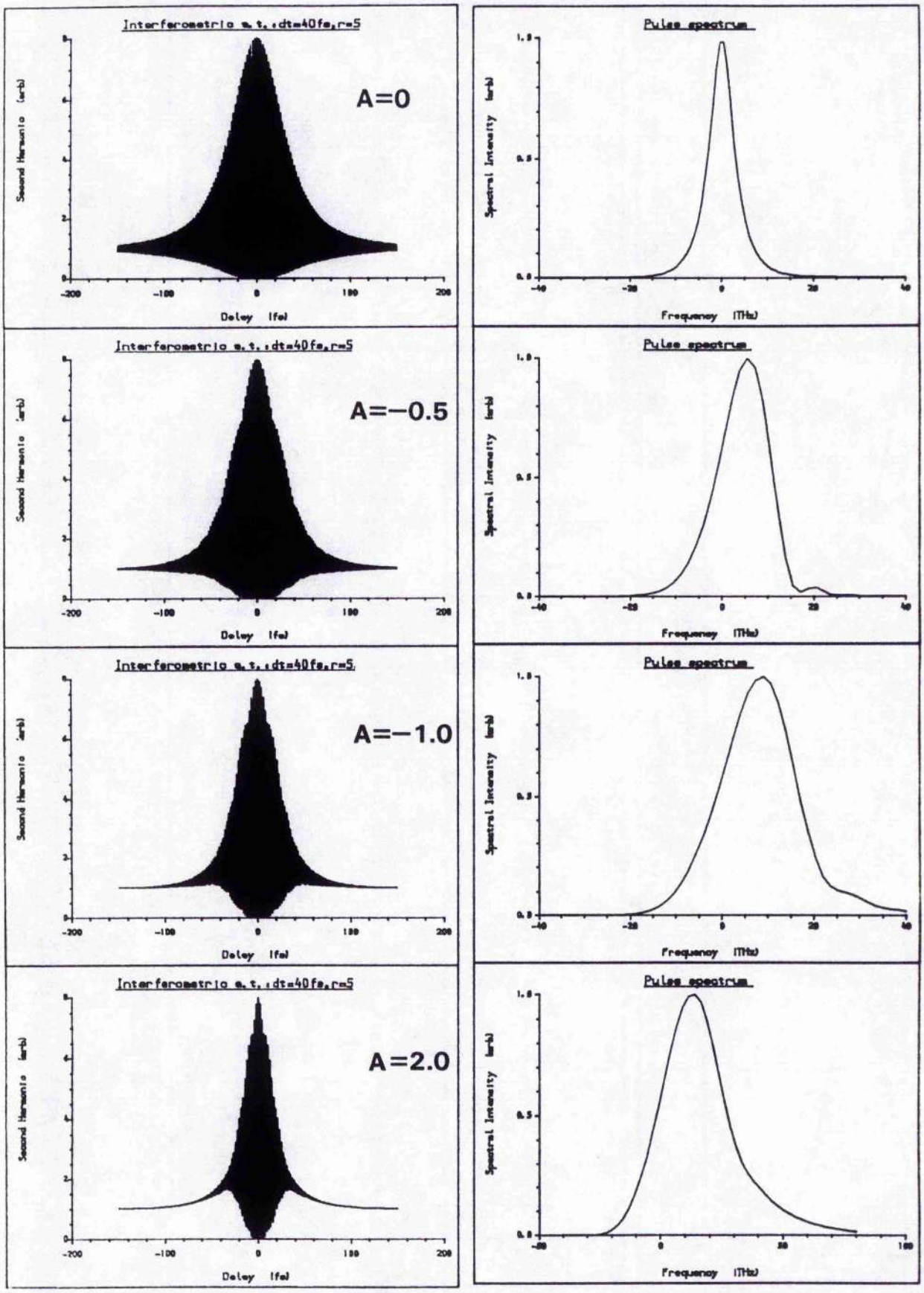

Figure 7.8 Autocorrelation and spectral data for asymmetric pulse (r=5) with linear chirp

spectrum yielding a preferential broadening towards longer or shorter wavelengths depending on chirp sign and nature of pulse asymmetry ie) which edge of the pulse is steeper. In the case shown we have $\mathcal{A}$ negative corresponding to an downchirp across the pulse and the trailing edge of the pulse steeper which yields spectral broadening towards higher frequencies (shorter wavelengths). If the sign of $\mathcal{A}$ is reversed then so is the spectrum, positive values of $\mathcal{A}$ yielding asymmetric broadening towards longer wavelengths. Alternatively if the leading edge of the pulse is made steeper then the Fourier spectrum is reversed. These effects are summarised in figure 7.9.,

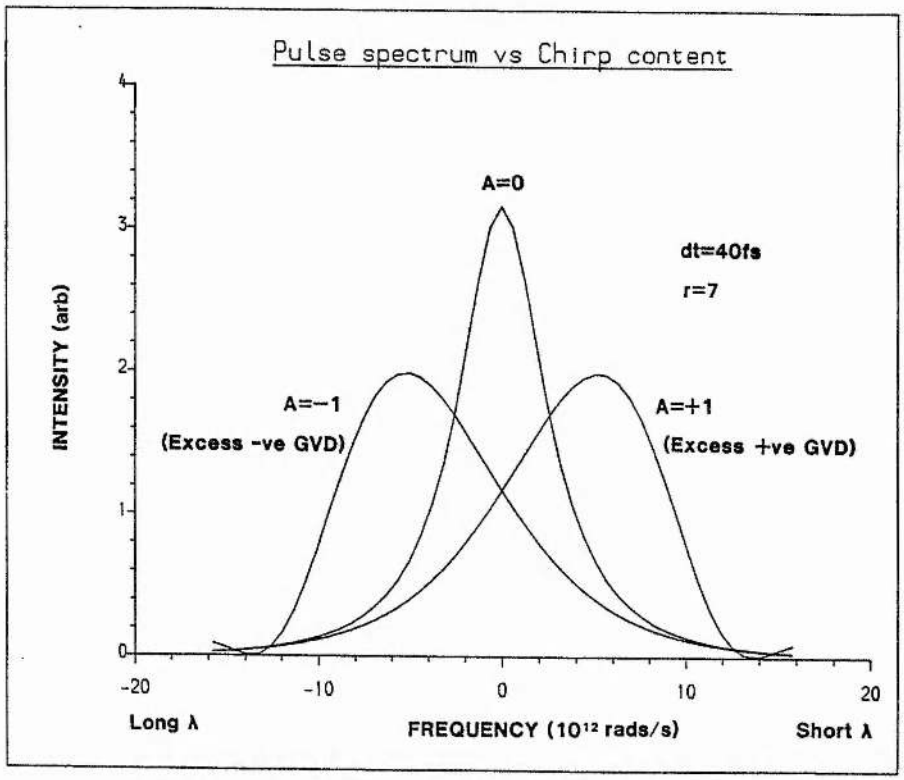

Figure 7.9 Spectral shape as a function of chirp sign and pulse asymmetry

The spectral asymmetry dependence on absolute pulseshape and linear chirp has interesting consequences in the analysis of passive mode-locking in the CPM laser. It is quite readily seen in the CPM laser discussed in Chapter 9 and reference [9] that when the prism system is configured to give large amounts of excess negative GVD within the cavity the pulse spectrum shows an asymmetric broadening towards shorter wavelengths. Negative group velocity dispersion (GVD) has the effect of overlaying a negative linear

frequency sweep across the pulse [8] and thus such pulse spectra would be consistent with the presence of asymmetric pulse within the cavity having a steeper trailing edge compared to the leading edge. The measured values of $\Delta\nu\Delta t$ have consistently agreed with the fact of pulse asymmetry but we have have as yet been unable to determine the absolute pulseshape.

7.4.3 NON-LINEAR CHIRP - KERR EFFECT

Nonlinear self-phase modulation (SPM) effects are commonly encountered in ultrashort pulse generation due to the optical Kerr effect and gain or absorber saturation whereby the refractive index of a medium is modulated by the passage of the optical pulse through it. All of these mechanisms have their own characteristic effect on the pulse spectrum and autocorrelation profile as discussed below.

Self phase modulation due to Kerr effect is relatively straightforward to model because the phase term in eq(7.6) is proportional to the intensity of the pulse and hence we have [10]:

$$\emptyset_k(E,t) = -\frac{n_2 w_o \ell}{ac} I(t) \qquad \text{–eq(7.10)}$$

where n_2 is the nonlinear refractive index of the medium (cm^2/W), ℓ is the transit length and a the beam area. The corresponding instantaneous frequency across the pulse due to this SPM is given by the differential of $\emptyset_k$ with respect to frequency which gives:

$$f(t) = \frac{1}{2\pi}\left[w_o - \frac{n_2 w_o \ell}{ac}\frac{dI(t)}{dt}\right] \qquad \text{–eq(7.11)}$$

For the purposes of modelling the effect of this term on autocorrelation profiles eq(7.10) is simplified to:

$$\emptyset_k(E,t) = -\emptyset_{max}\, I(t) \qquad \text{–eq(7.10b)}$$

where $\emptyset_{max}$ represents the maximum phase shift in radians ocurring at the peak of the pulse intensity and I(t) is the normalised pulse intensity. In this case eq(7.3) becomes:

$$g_2(\tau) = \int_{-\infty}^{+\infty} |E(t)^2 + E(t-\tau)^2 \qquad \text{–eq(7.12)}$$

$$+2\, E(t)E(t-\tau)\cos(w_o\tau - \{I(t)-I(t-\tau)\}\emptyset_{max})|^2\, dt$$

This autocorrelation function was calculated numerically for $sech^2$ and $r = 5$ pulses of 40fs duration as before together with the pulse spectra and the results are displayed in figures 7.10 and 7.11. Again as in the case for linear chirp, the $sech^2$ pulse spectrum is symmetrically broadened by the Kerr effect and for large values of $\emptyset_{max}$ it becomes modulated. This is due to the inteference of regions of the pulse having identical rates of change in intensity which map into the Fourier spectrum as interfering frequency components. Increase in the value of $\emptyset_{max}$ is equivalent to an increase in pulse power density in the Kerr medium or a increase in the nonlinear factor n_2. It can be seen from figure 7.10 that as the maximum phase shift increases the autocorrelation narrows in its central region. In the central regions of the pulse where dI/dt is largest there will exist the largest frequency shift and hence there will be a loss of visibility of fringes near the centre of the autocorrelation. As $\emptyset_{max}$ increases further the wings of the autocorrelation disappear at first and then reappear for large nonlinear chirp values.

For the asymmetric pulse the autocorrelation traces show similar features but the spectra again differ in that asymmetric broadening is seen. For the case of this pulse with a greater dI/dt in its steeper trailing edge the pulse spectrum is preferentially broadened towards higher frequencies (shorter wavelengths). If the pulse asymmetry was reversed then the spectrum would adjust correspondingly to give spectra with extended broadening towards longer wavelengths. Indeed this latter case has been experimentally reported by Kean and coworkers [11] in which they studied SPM effects in fibre launched Nd:YAG laser pulses. For large pulse powers spectral broadening was observed to be extended in the long wavelength region due to the depletion of the front (red shifted) region of the pulse by stimulated Raman scattering processes.

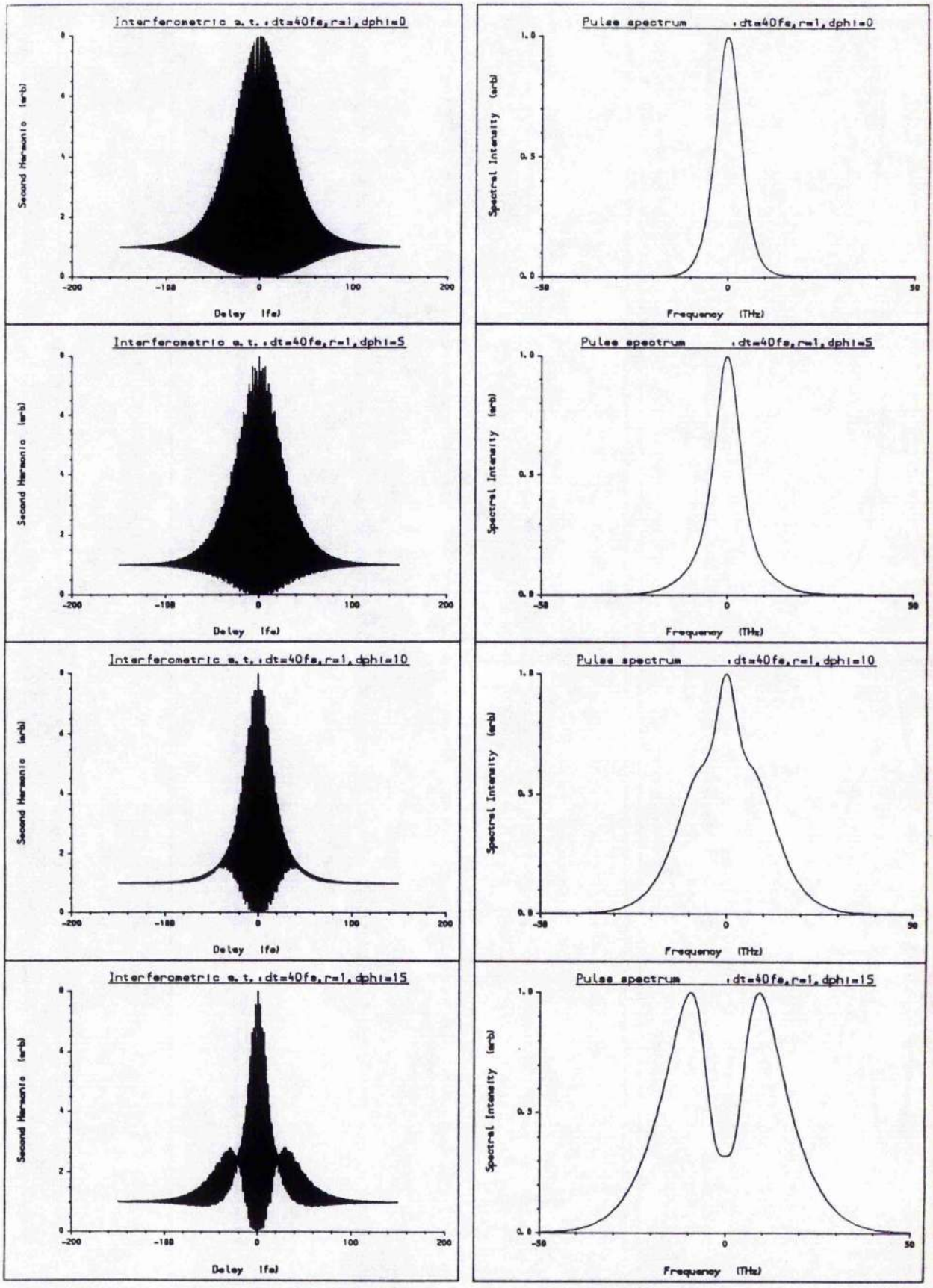

Figure 7.10 Autocorrelation and spectral data for sech^2 pulse with Kerr type chirp

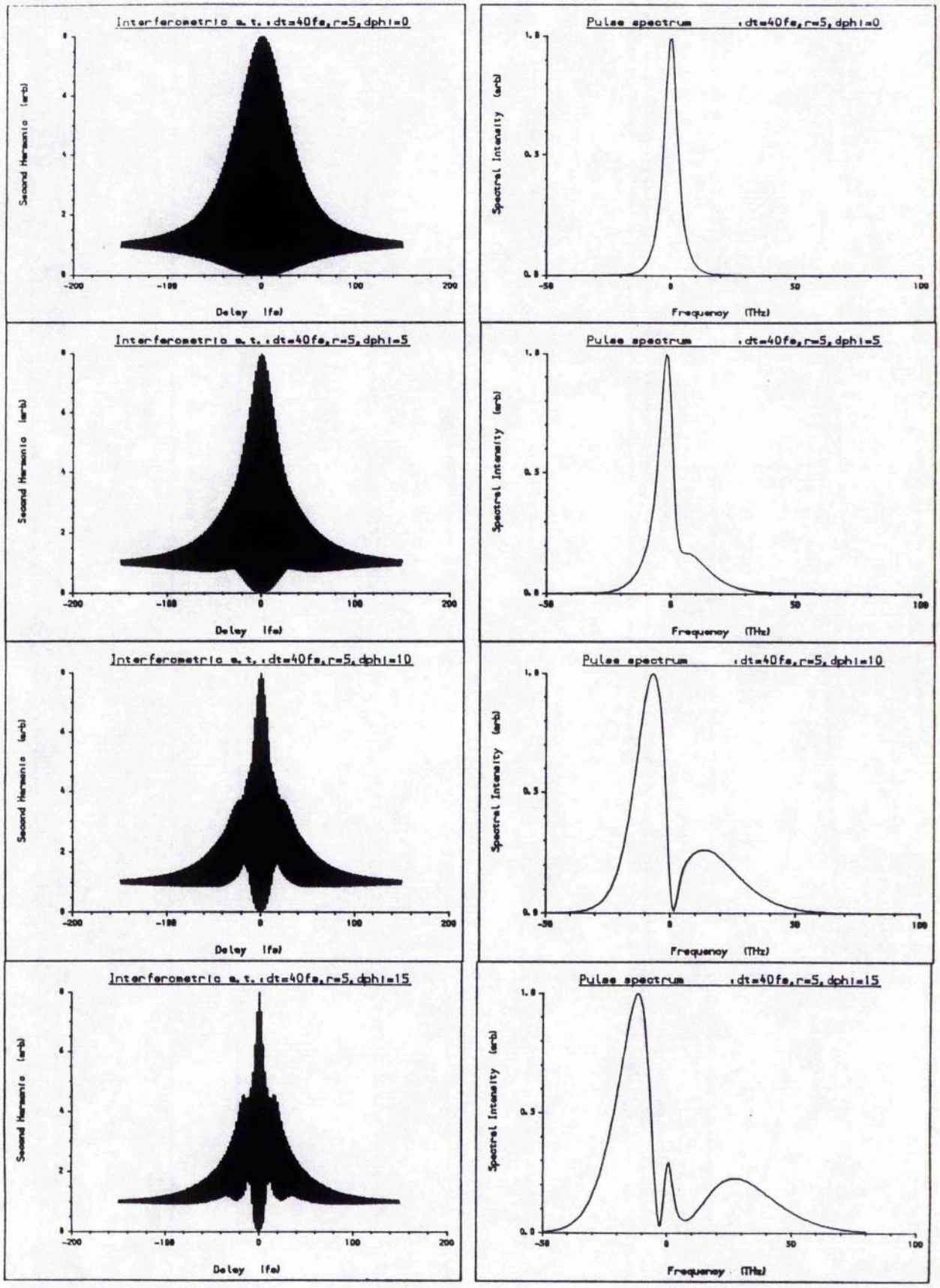

Figure 7.11 Autocorrelation and spectral data for asymmetric pulse with Kerr type chirp

7.4.4 NONLINEAR CHIRP - ABSORBER / GAIN SATURATION

The modelling of this form of chirping process is difficult in that attention must be made to several parameters: the operating wavelength and its proximity to the absorbing/gain region, the pulse energy and the saturation energy of the absorber/gain medium. The following is based on an analysis given by Miranda et al [10] (which in turn is taken from a preliminary investigation by Silvestri et al [8]) which considered the case of gaussian pulseshapes interacting with the saturable medium and was restricted to the spectral region around 610nm. The generalised case given here is for an absorbing medium but the analysis is identical for a gain medium and requires merely the change of the chirping sign.

Taking the absorption line shape $g(w)$ to be Lorentzian, where:

$$g(w) = \frac{2}{\pi \Delta w \left\{1 + \frac{4(w_c - w)^2}{\Delta w^2}\right\}} \qquad \text{–eq(7.13)}$$

with w_c the line centre and Δw the linewidth, the contribution of this resonant transition to the refractive index of the medium at a frequency w is:

$$n_R = \frac{\pi(w_c - w)c}{2w_c}\, \alpha\, g(w) \qquad \text{–eq(7.14)}$$

where α is the time-dependent saturated absorption coefficient which can be represented by:

$$\alpha(t) = \alpha_o \exp\left(- \frac{a \int_{-\infty}^{t} I(t')dt'}{E_s} \right) \qquad \text{–eq(7.15)}$$

Here α_o is the optical absorption coefficient at line centre, a is the beam area and E_s the saturation energy of the absorber. Hence the time-dependent phase factor representing the chirp due to absorber saturation can be written from eq(7.14) as:

$$\emptyset_S(E,t) = - G(w) \frac{wl}{c} \alpha(t) \qquad \text{–eq(7.16)}$$

where:

$$G(w) = \frac{\pi(w_c - w)c}{2w_c} g(w) \qquad \text{–eq(7.17)}$$

Examination of eq(7.15) reveals that for pulses with central wavelengths on the long wavelength side of the absorption line centre then absorber saturation yields an blueshift at the leading edge of the pulse which decreases as the absorber becomes bleached. For small values of saturation energy or for highly intense pulses the initial blue shift will only appear at the extreme leading foot of the pulse – the remainder of the pulse being predominatly unchirped. However for larger saturation energies/weaker pulses the frequency shift can extend further into the pulse yielding a predominant down-chirp across the central region of the pulse.

For the purposes of the autocorrelation modelling eq(7.16) was simplified to give:

$$\emptyset_s(t) = -\emptyset_{init} \exp\left(-\frac{a\int_{-\infty}^{t} I(t')dt'}{E_{sat}}\right) \qquad \text{–eq(7.16b)}$$

Figures 7.12 and 13 show the calculated interferometric autocorrelations and spectra for various values of peak phase deviation for the two cases of sech^2 pulses with E_p/E_{sat} = 0.5 and 2. Although the saturation energy was kept at a typical value of 1nJ, it should be noted that E_{sat} and $\emptyset_{init}$ are related via the wavelength dependence of the absorber cross section [12]. Higher values of the above ratio imply that the blue shift is confined to nearer the front of the pulse; higher values of $\emptyset_{init}$ yield larger blue shifts. In both cases the absorber saturation causes a narrowing of the central region of the interferometric autocorrelation trace and, for larger values of $\emptyset_{init}$ loss of fringes in the wings and winging effects. The striking effect in the pulse spectra is that asymmetry is observed whereas for previous types of chirp such an effect was restricted to asymmetric pulse shapes. The absorber saturation causes broadening towards the blue part of the spectrum and for large $\emptyset_{init}$ values secondary peaks appear as if the highly chirped front region of the pulse can be seen as a separate blue shifted narrow pulse lying at the foot of a broader unchirped pulse.

Figures 7.14 and 7.15 show the equivalent montage for the asymmetric pulses. For small saturation values the spectra and correlation data resemble that seen for linear chirp with the parameter $\mathcal{A}$ set negative. This is not the case when E_p/E_{sat} is increased to 2. The

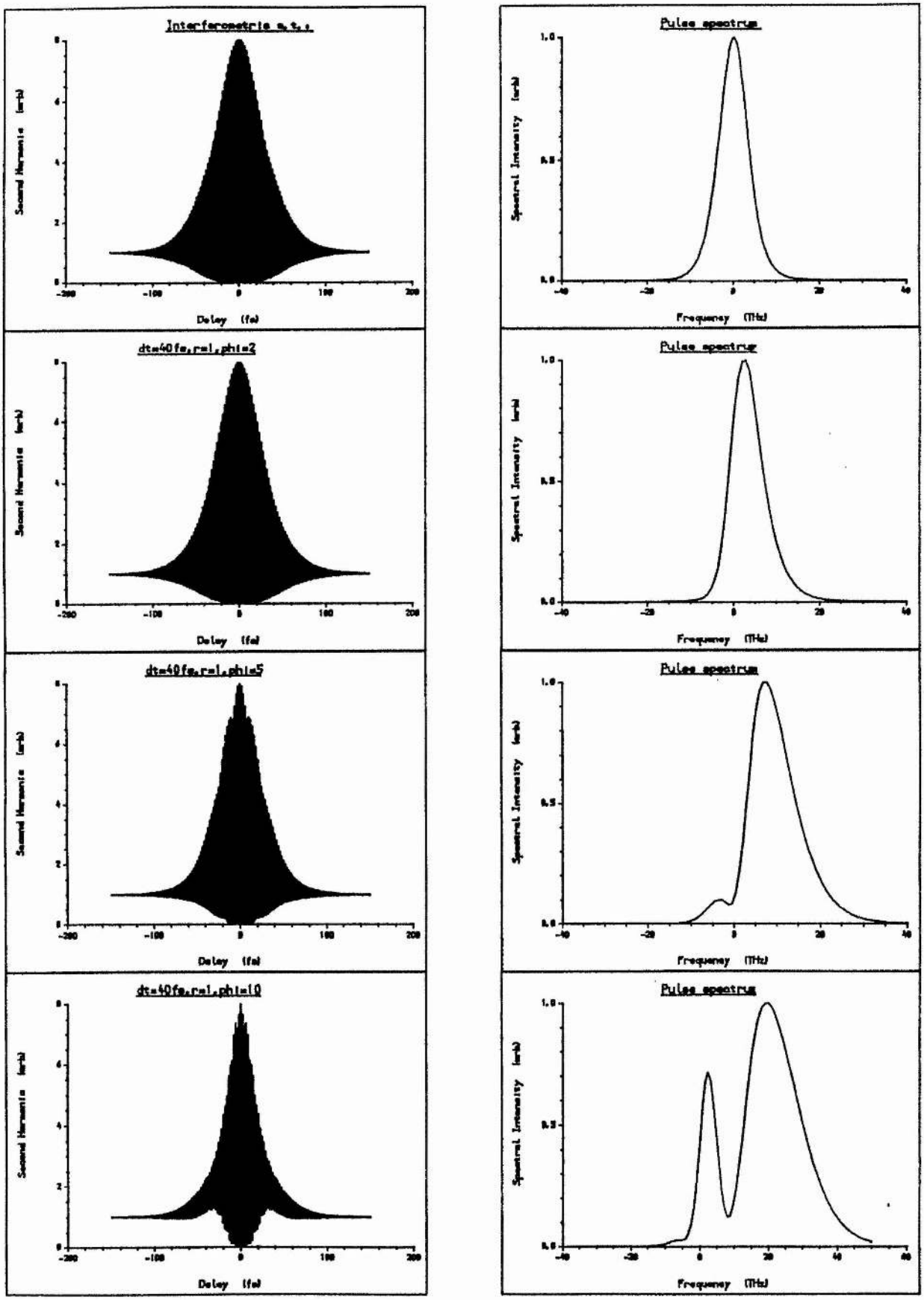

Figure 7.12 Autocorrelation and spectral data for sech^2 pulses with nonlinear chirp due absorber saturation (E_p/E_{sat} = 0.5).

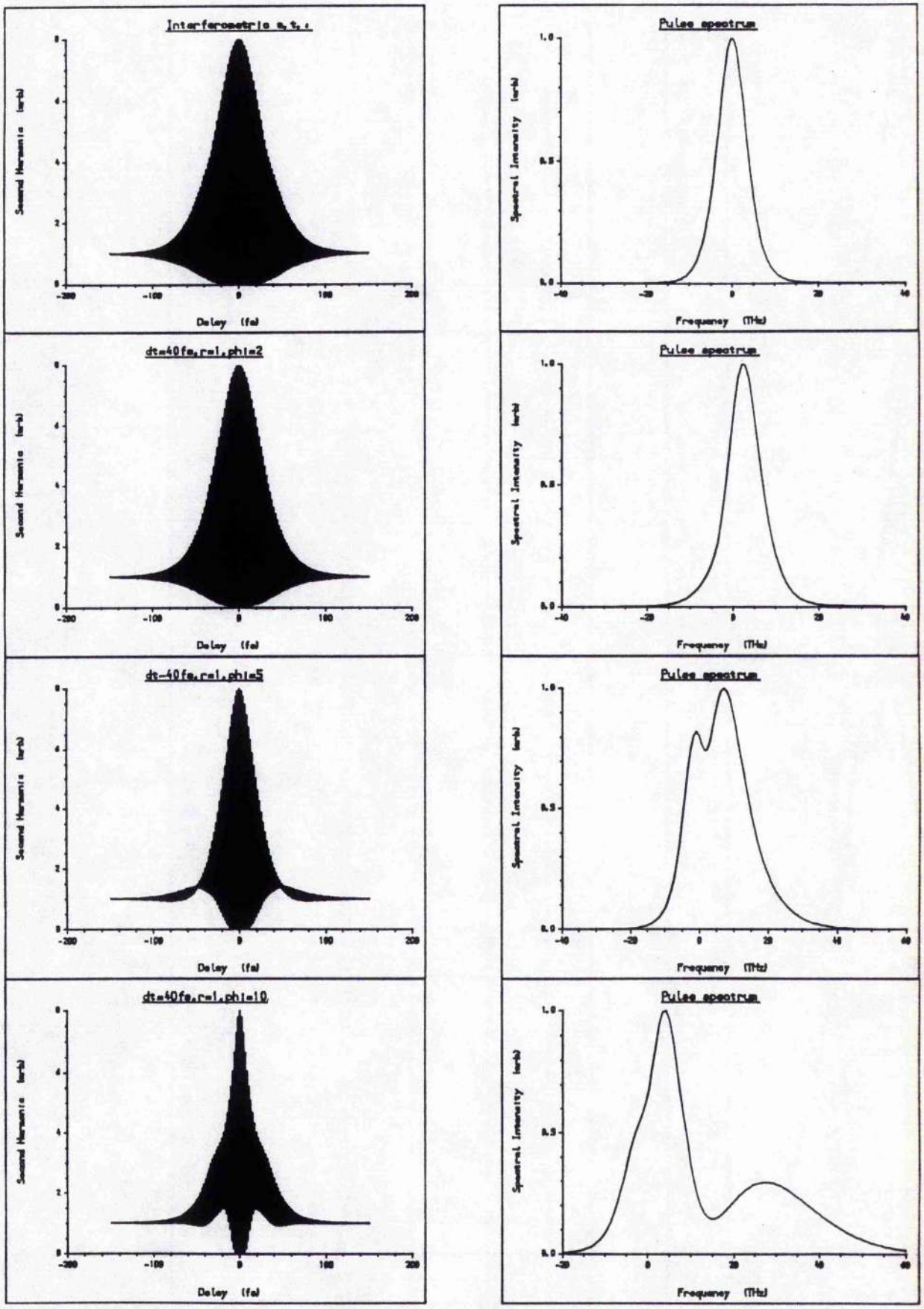

Figure 7.13Autocorrelation and spectral data for sech^2 pulses with nonlinear chirp due absorber saturation (E_p/E_{sat} = 2).

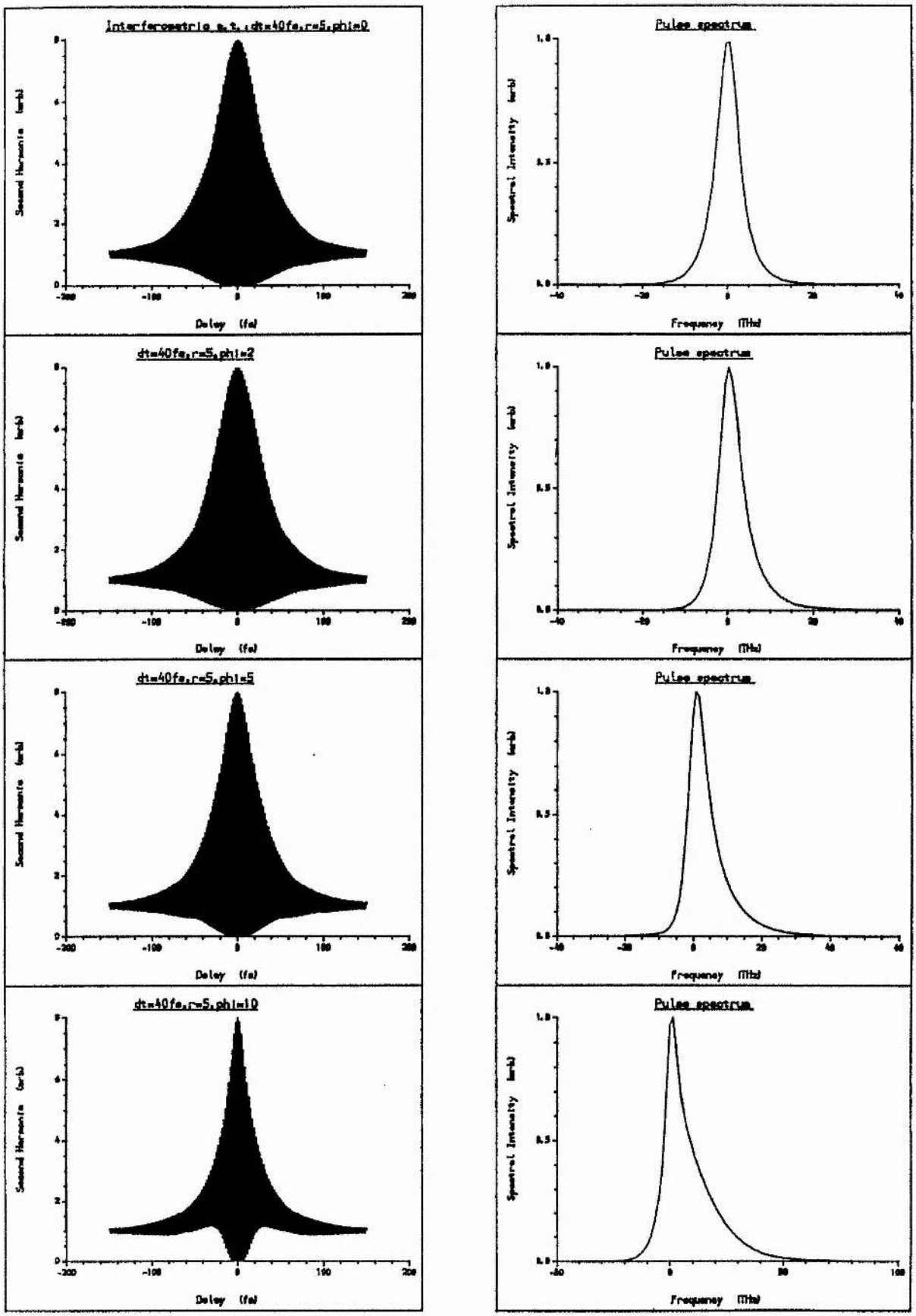

Figure 7.14 Autocorrelation and spectral data for asymmetric pulses with nonlinear chirp due absorber saturation (E_p/E_{sat} = 0.5).

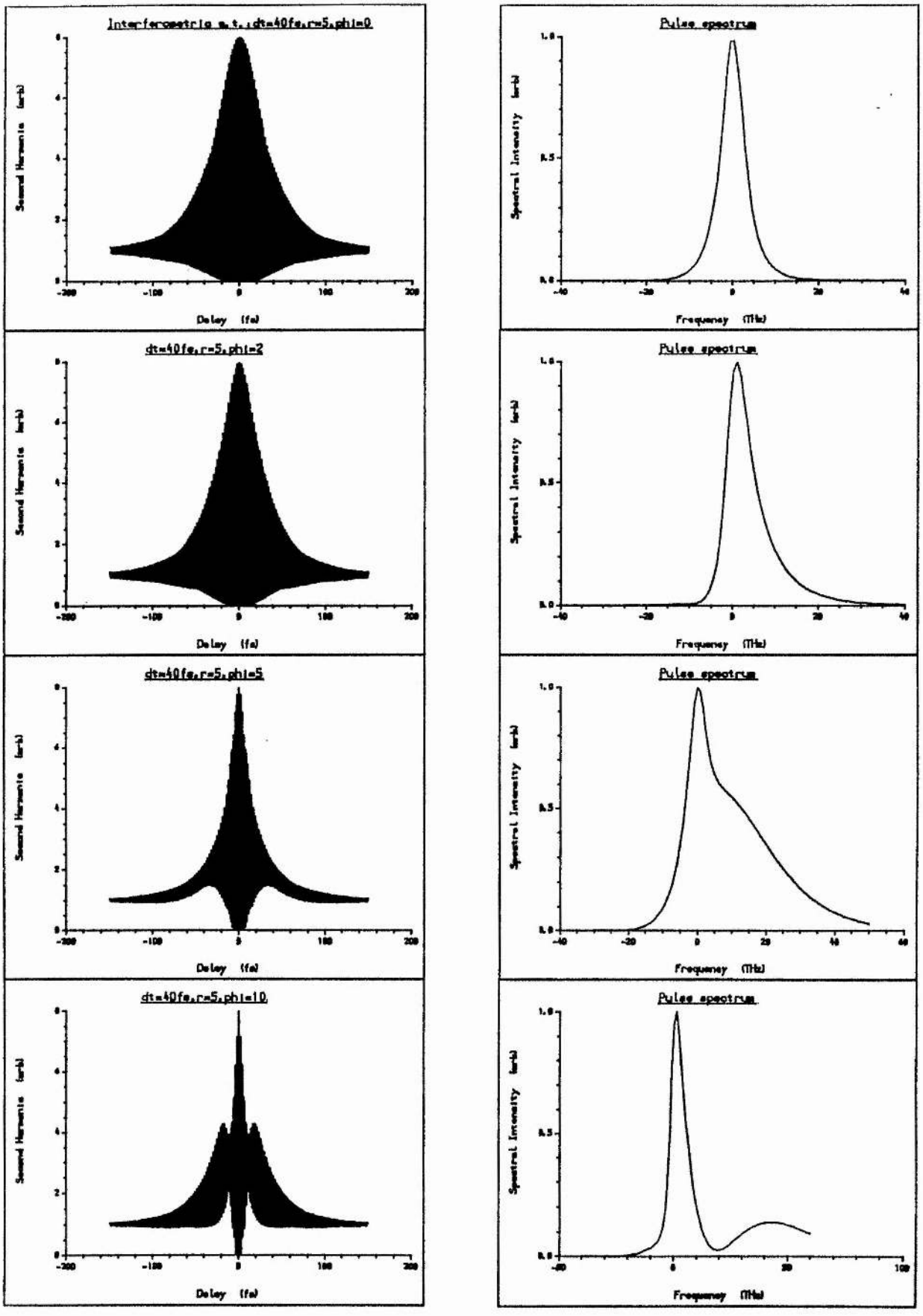

Figure 7.15 Autocorrelation and spectral data for asymmetric pulses with nonlinear chirp due absorber saturation (E_p/E_{sat} = 2).

winging effect in the autocorrelation function is much more enhanced and secondary blue shifted maxima appear in the spectra.

7.5 CONCLUSIONS

The relevant mathematical formulism used to described interferometric autocorrelation functions has been presented. The effect on the resulting correlation and spectral shapes has been numerically calculated for pulses of differing shape and chirp content. It has been shown that the type of chirp can radically effect the interferometric autocorrelation shape and hence the development of such a measurement technique is vital if chirping effects in mode-locked lasers are to be investigated.

REFERENCES

1 M.Maier, W.Kaiser, and J.A.Giordmaine, Phys. Rev Lett. **17**, 1275 (1966).

2 J.A.Armstong, Appl. Phys. Lett. **10** 16 (1967).

3 E.P.Ippen and C.V.Shank, in *Ultrashort Light Pulses*, S.L.Shapiro Ed. New York: Springer-Verlag 83 (1977).

4 J.A.Giordmaine, P.M.Rentzepis, S.L.Shapiro and K.W.Wecht, Appl. Phys. Lett **11** 216 (1967)

5 J.C.Diels, E.W.Van Stryland and D.Gold, in *Picosecond Phenomena I* :Springer series in Chem. Phys. **4** 117 (1978).

6 H.A.Haus, J.Appl. Phys. **46** 3049 (1975).

7 J.C.Diels, J.J.Fontaine, I.C.McMichael and F.Simoni, Appl. Optics **24** 1270 (1985).

8 S.de Silvestri, P.Laporta and O.Svelto, IEEE J.Quant. Electron. **QE-20** 533 (1984).

9 A.Finch, G.Chen, W.Sleat and W.Sibbett, J. Mod. Optics **35** 345 (1988).

10 R.S.Miranda, G.R.Jacobovitz, C.H.Brito Cruz and A.F.Sarpara, Opt. Lett. **11** 224 (1986).

11 P.Kean, K.Smith and W.Sibbett, Proc. IEE **134** 163 (1987).

12 O.E.Martinez, R.L.Fork and J.P.Gordon, J.Opt. Soc. Am B **2** 753 (1985).

CHAPTER 8: PULSESHAPE CHARACTERISATION - CORRELATION AND SPECTRAL MEASURMENT TECHNIQUES

8.0 INTRODUCTION

Although the use of interferometric autocorrelation techniques for pulse train monitoring was demonstrated in the early 1980's [1] the technique was slow to be taken up by other workers and is only now gaining popularity [2,3,4]. In our CPM system a realtime fringe-resolved autocorrelator was developed two years ago because we were interested in pulseshape detail. The autocorrelator design has been installed in other systems in the group and is proving very reliable and useful in determining pulse shaping dynamics in a wide range of lasers. It is of relatively simple design, low cost and reliable and the pertinent design criteria are given below.

8.1 DESIGN ASPECTS

The system requirements to achieve realtime autocorrelation are two-fold: (i) Provision must be made for the periodic scanning of one of the correlator mirrors, one half scan being over a distance sufficient to exceed the physical extent of the optical pulse and occuring in a time period short enough for a realtime collation of data to be displayed to the user (~10-20ms), and (ii) adequate frequency response must be provided in the photomultiplier and monitoring system such that the fringes of the interferogram can be resolved. There is the additional problem of how to adequately digitise and store the data of the interferogram.

8.1.1 WAVEFORM GENERATOR

A schematic of the waveform generator developed to drive the mirror is shown in figure 8.1. The scanning system that was designed is based around an EPROM which contains the hexedecimal values of a periodic waveform. A total of 216 points are recorded corresponding to three cycles of triangular waveform with rounded parabolic peaks. A

counter provides sequential addresses to the EPROM which then generates the 8-bit digital values along the waveform which are supplied to a digital-to-analogue (D-to-A) converter.

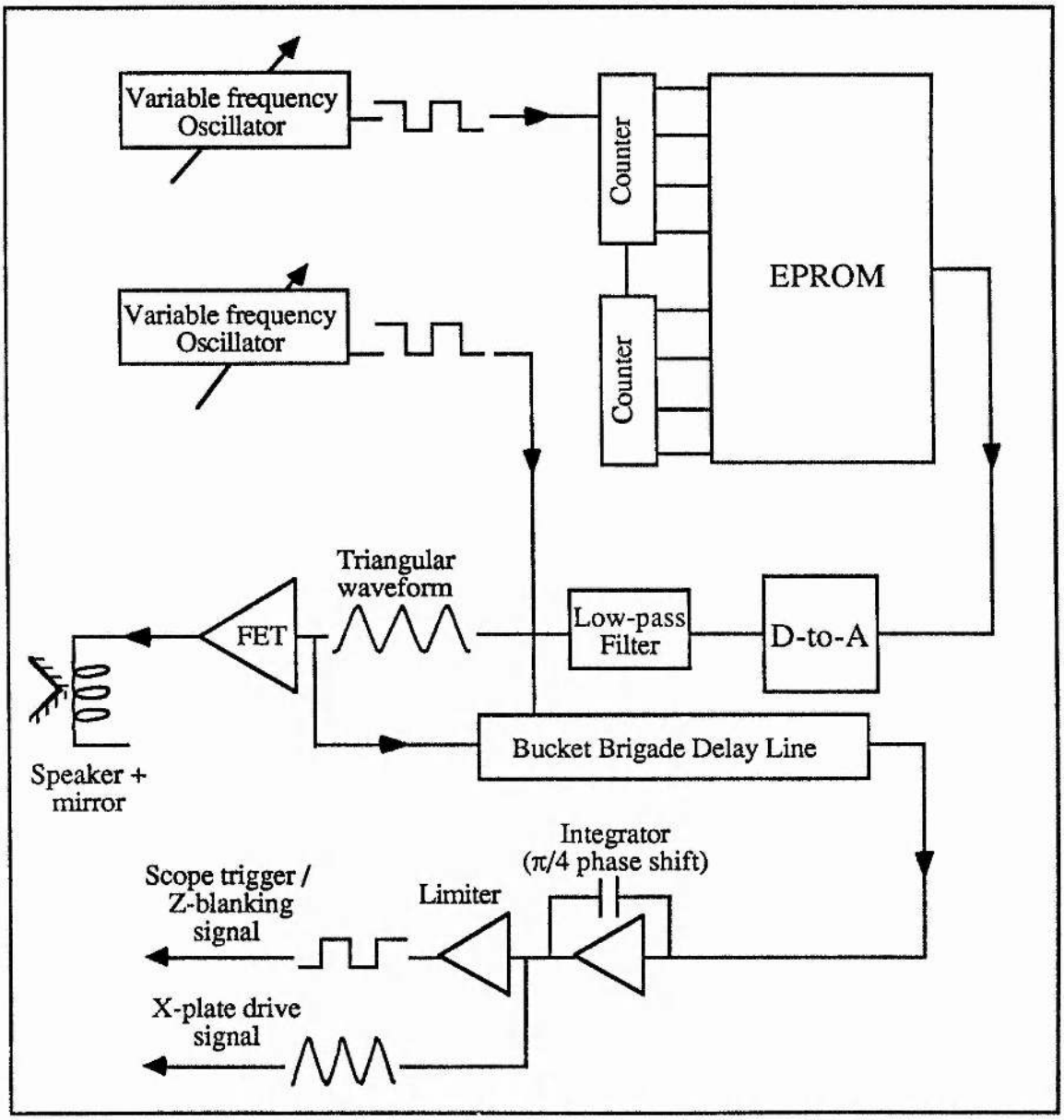

Figure 8.1 Block diagram of autocorrelator drive circuitry

This voltage signal is then smoothed by a low pass filter, amplified, before being applied to a bass response loudspeaker (Tanoy S31083) on which the retroreflector is attached (this has proved perfectly adequate as a mirror translation stage). Once the counter has reached a count of 216 it is reset to zero and the waveform is repeated. A triangular waveform was chosen to maximise the scan linearity across the half period; the particular waveform

chosen scans the mirror at constant velocity for >90% of the period. The counter is toggled by a variable frequency oscillator and part of the signal is passed to a square-wave generator and placed in phase quadrature to the drive signal. This is then passed through a variable delay line (TDA-1026) and acts as the trigger source for the monitoring scope to synchronise the scope to the autocorrelator and allow the centralisation of the interferogram on the screen. There is a secondary waveform generated which can be used to drive the scope in XY mode (or a multichannel analyser) in which case the trigger signal can be used for Z-blanking to remove the return correlation signal.

The scanning frequency can be varied from 20Hz to 4Hz and, by running the counter with 3-step increments, this frequency range can be condensed to between 8 and 1Hz. The counter can be toggled from external frequency sources which is particularly useful when dealing with chopped light eg) from a mode-locked LiF:F_2^+ colour center laser. Maximum scan amplitudes are around 1.5 cm, limited by the speaker throw.

8.1.2 SIGNAL DETECTION

The photomultiplier (EMI 9603QC-S11) has a typical output impedance of ~1MΩ. Coupled with the intrinsic capacitance of coaxial connections the frequency response of this detection system is severely limited. Assuming approximately 1 metre of cable (standard uniradio-43) @ ~100 pFm^{-1} and a 1MΩ input impedance of the monitoring scope the combined RC of the detecting system is approximately:

$$RC = (1\ M\Omega \times 100\ pF)$$
$$= 100\ \mu s$$

which gives a 3dB cutoff frequency of ~1.5 kHz.

Typical pulse durations from the CPM laser are around 30-40 fs but can be adjusted to above 500 fs. Setting 200 fs, say, as our upper limit such pulses will contain, for central wavelengths of 630 nm, around 500 optical cycles. The entire autocorrelation trace will contain ~ twice this number of fringes and, so in order to observe detail in wings, a single sweep of the speaker could present >1000 fringes at the detector system in a time period @20 Hz of ~5ms (thereby confining the correlation to the linear portion

of the scan). In fact for the triangular waveform generated by the above circuitry over 90% of the scan is linear and thus the scan time window is extended to ~9 ms. Hence in order to resolve these fringes the monitoring system must have a frequency response greater than ~200 kHz. Naturally for shorter pulses this upper limit on frequency response will be less stringent but, nevertheless, the direct coupling of the PMT to a scope monitor severely degrades the system response and makes the recording of interferometric autocorrelations impossible.

One simple solution is to terminate the cable with a low value resistor effectively lowering the RC time constant of the cable. Although this will increase the frequency response it will lower the signal presented at the scope input in the ratio of the terminating resistor to the scope impedance. If the second harmonic signal is limited in strength then this solution is not adequate. Clearly what is required is a device to lower the source impedance to that of the coaxial cable, ie a simple impedance matching circuit. Figure 8.2 shows the circuit adopted.

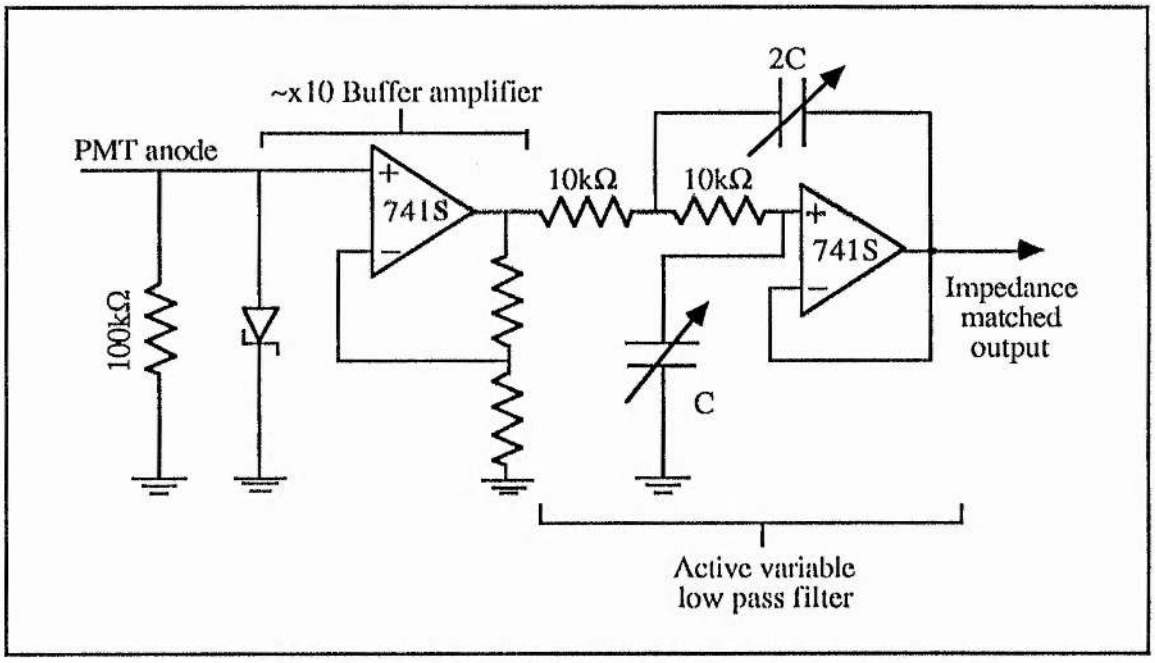

Figure 8.2 Impedance matching circuit with variable Butterworth filter

The impedance matching circuit is mounted inside the PMT housing and the anode connection to the circuit input is kept as short as possible to minimise cable capacitance. An input resistance of 100 kΩ was chosen and the ten-fold loss of signal that this entails was

regained by operating the buffer amplifier at X10 non-inverting. An -15V Zener diode is also included to protect the 741S op-amp which was selected for its enhanced frequency response. Directly after the impedance matcher an active low-pass filter was built in (2-pole Butterworth) with variable cut-off frequencies determined by the capacitive values of C (3dB frequency cut-off $\approx 1/2\pi RC$). Frequencies of 100 Hz, 1kHz and 10kHz were chosen. If the capacitance was left open circuit then the filtering action was removed and the output amplifier became a simple unity gain inverter. In this case the maximum frequency response could be obtained and interferometric autocorrelation could be displayed and recorded on the monitoring scope (figure 8.3a). If the active filter is switched in then fringe averaging occurs and the displayed trace becomes an intensity autocorrelation (figure 8.3b).

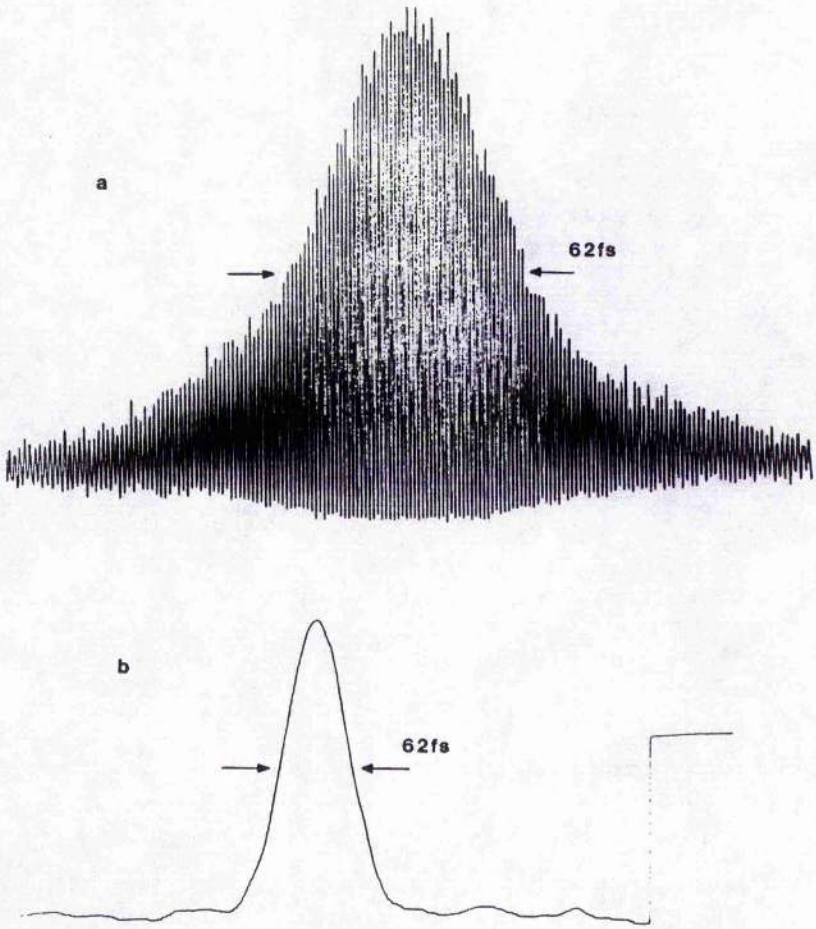

Figure 8.3a (upper) Example interferometric autocorrelation trace and b (lower) corresponding intensity autocorrelation employing variable cutoff Butterworth filter

The open circuit frequency response of the impedance matcher had a 3dB roll off of approximately 50 kHz. This allows the display of ~150 fs pulses at 20 Hz scan rates and obviously longer pulses at slower rates.

8.1.3 Data acquisition

Although the PMT detector head had sufficient frequency response to resolve long duration interferometric autocorrelations, the recording of this data often presented a problem. Use of a digitising scope immediately places frequency constraints on the system since each fringe requires atleast ten sampling points for unambiguous storage and so the sampling rate of the scope must be at least 1MHz. Furthermore, to capture a complete interferogram many data points are required. Most reasonably priced digital storage oscilloscopes (DSO) (eg. Hameg 405) have 2048 sampling points per channel which in reality limits the maximum recordable interferometric autocorrelation to pulse durations around 150 fs at 630 nm. We currently employ a Gould 4044 digital storage oscilloscope which has a 5000 data point storage capacity and hence autocorrelations of pulses with durations up to ~500 fs may be recorded.

If detailed analysis of longer duration pulses is required then a data logger could be interfaced which can easily store up to 128 kbytes of data. This system has the disadvantage that the data can only be then displayed via computer graphics or after hardcopying via a D-to-A and chart recorder, ie no realtime facility is available. However by using a combination of digital oscilloscope and data logger with switchable inputs one can have both facilities.

8.1.4 Calibration

Although the interferometric autocorrelation is self-calibrating – the delay between two fringe maxima corresponding to one optical cycle (2.1fs for 630nm) – a secondary calibration can be provided by a stepping motor fitted to the fixed mirror. By moving the mirror a known distance and noting the distance moved by the correlation trace on the scope, the time base axis can be calibrated. In the system developed for the CPM laser a

more accurate calibration is provided by a Burleigh 'Inchworm' which is a high precision piezo-electric stepping motor with single step increments as small a 2μm.

8.2 THE SHG CRYSTAL

For the autocorrelation of ultrashort pulses with inherent large spectral bandwidths it is vital that the second harmonic generation efficiency is constant over the entire spectral bandwidth of the pulse. Conversion efficiency is dictated by the phase matching of the fundamental and frequency doubled light and any dispersion in the doubling crystal will naturally place an upper limit on the bandwidth the crystal can accommodate and hence the minimum pulse duration it can resolve. To ensure adequate bandwidth a short conversion length should be used either by using extremely thin nonlinear crystals, tight focussing or a combination of the two. If this requirement is not met then the measured correlation functions will be broadened and distorted.

Specification of what exactly is an adequate crystal length for a given pulse duration has been open to much detailed analysis [5,6] and can lead to wildly differing results depending on the accuracy of data fitting to the crystal dispersion curve! Using a 3-pole Sellmeyer [7] fit for KDP a 200 μm thick crystal will have a 50% drop in second harmonic conversion efficiency for a $sech^2$ pulse of ~26fs duration [8]. In our experiments preliminary data was taken with a KDP crystal length of <100μm and later with a 200μm KDP crystal which limited the minimum resolution to ~15 and 25 fs respectively (these are pessimistic estimates).

8.3 SPECTRAL MEASUREMENTS

As a complement to the development of the realtime interferomeric autocorrelator, realtime measurement of the pulse spectrum is vital for pulse shape determination and as a practical tool for the optimisation and adjustment of the CPM laser in its day-to-day operation. As a spin-off of the CCD research discussed in the section I a linear photodiode array was configured [9] to detect the output of a grating monochromator (1m Hilger-Watt, Monospek) used to measure CPM laser pulse spectra. The sensing head consisted of a

Thomson-CSF diode array (7403) having 1728 pixels arranged along a 13μm x 22mm line. By removing the output slit of the monochromator the complete pulse spectrum could illumuninate the array. For this particular grating the array could access a 17 nm spectral window. The array head was driven at variable clocking speeds and the output signal digitised to 8 bits. A Z80 microprocessor based system stored the digitised information and allowed basic data manipulation (removal of backgrounds, cursor facilities, smoothing etc) displaying the memory contents and realtime spectra on a basic oscilloscope. All memory calculations were performed to 16 bit accuracy. Hardcopy facilities were provided and a twin-parallel computer interface was also installed. The device proved an extremely useful spectral monitor for the laser output.

8.4 CROSS-CORRELATION TECHNIQUES

As has been seen in the previous chapter the interferometric autocorrelation technique gives useful information regarding the shape and frequency chirp content of optical pulses. When coupled with spectral information it is possible to perform pulse shape and chirp characterisation with a high degree of certainty by employing an iterative fitting process. The measurement is not completely unambiguous because it is possible to envisage very different combinations of pulse shape and frequency chirp which would give identical measured data – such cases can only be differentiated by the interaction of the pulse with a known amount of dispersion (eg. a length of glass rod) and comparing autocorrelation results prior to and after such a procedure.

The only completely unambiguous technique of pulse characterisation in the femtosecond regime is that of *cross-correlation*, first described by Diels et al [10]. This technique performs a correlation of an optical pulse with itself having been modified by a known amount of dispersion and allows determination of all relevant data concerning the input pulse. On the whole this method is not commonly used and does not lend itself to the realtime monitoring of modelocked pulse trains – deconvolution being performed via computer based iterative fitting and numerical processing – but the technique provides all the pertinent data allowing the pulse to be reconstructed both in amplitude and phase. This

technique will be applied to the CPM laser system in the near future and the preliminary correlator design and initial experimentation is outlined below.

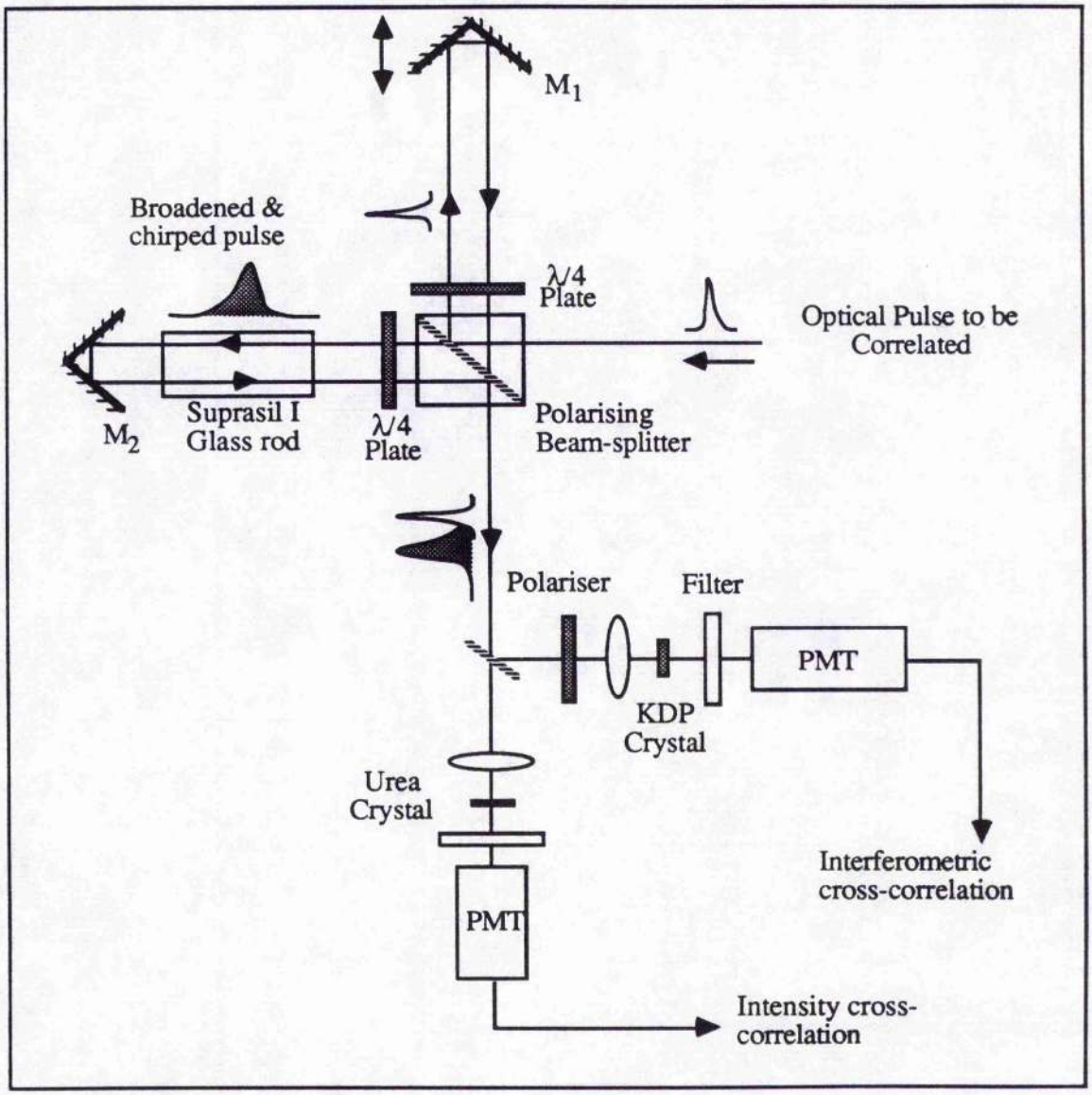

Figure 8.4 Schematic of dual interferometric and intensity cross-correlator

8.4.1 PROPOSED CROSS-CORRELATOR SETUP

A schematic of the proposed correlator is shown in figure 8.4. The system will be almost identical to a system devised by Diels [11]. Ignoring the action of the glass rod initially, the linearly polarised input beam is equally split into orthogonally polarised parts by the polarising beam splitter cube. Each beam is then sent through a quarter-wave plate before being reflected. The secondary passage through the quarter-wave plates rotates each

of the two orthogonally polarised beams through 90°. If these beams are then focussed into an Urea crystal which is angle tuned for Type II phase matching then second harmonic generation will only occur when the two orthogonally polarised subcomponent pulses have some degree of overlap ie) there is no background signal. If on the other hand a polariser is placed to transmit polarised light at 45° to the two beam's E-field then normal Type I phase matching can occur in a KDP crystal. By suitable incorporation of electronics into each PMT detector the KDP arm of the correlator can provide interferometric correlation data and the urea path will generate *background free* intensity correlation data. Considering now the action of the glass rod in one arm of the correlator, as the pulse passes through the dispersive material it is broadened and has a linear chirp imposed upon it. Consequently the signal detected at the photomultipliers will be the cross-correlation of the original pulse and the broadened pulse. By iterative analysis of the intensity and interferometric data and a precise knowledge of the dispersive properties of the glass rod it is possible to reconstruct the amplitude and phase of the original pulse [10]. The process is non-trivial requiring intense computation and for reasonable accuracy the correlation data must be sampled sufficiently. A reasonable sample size would be ~32,000 data points per interferogram and hence such digitisation and storage can only be performed by a suitably tailored data-logger. This project is at present in its early stages of development (it is outlined here for completeness – some preliminary experimentation will be discussed in the next section), but it is hoped that in the near future a complete characterisation of pulse shape and chirp content can be performed to facillitate a further understanding of the pulse shaping dynamics that occur inside the CPM laser.

REFERENCES

1 J.C.Diels, W.Dietel, J.J.Fontaine, W.Rudolph and B.Wilhelmi, J.Opt. Soc. Am. B 2 680 (1985).

2 R.L.Fork, C.H.Brito-Cruz, P.C.Becker and C.V.Shank, Opt. Lett. 13 129 (1988).

3 F.W.Wise, I.A.Walmsey and C.L.Tang, Opt. Lett. 13 129 (1988).

4 W.L.Nigham Jr., T.Gong and G.Fauchet in *Ultrafast Phenomena VI*: Springer Series in Chem. Phys. **48** 110 (1988).

5 I.S.Ruddock, Phd Thesis - Imperial College (1976).

6 R.C.Miller Phys Lett. **26A** 177 (1968).

7 D.Marcuse, Appl. Opt. **19** 1653 (1980).

8 D.Crust (private communication).

9 R.Zhang, A.Finch, W.Sleat and W.Sibbett, Proc. XVIIIth ICHSPP (to be published).

10 J.C.Diels, J.J.Fontaine, I.C.McMichael and F.Simoni, Appl. Optics **24** 1270 (1985).

11 J.C.Diels, J.J.Fontaine, N.Jamasbi, L.Ming and J.Mackey, Proc. CLEO paper MD3 14 (1987).

CHAPTER 9: PERFORMANCE CHARACTERISATION OF THE COLLIDING PULSE MODE-LOCKED RING DYE LASER

9.0 INTRODUCTION

The purpose of this chapter is to present experimental details and performance characteristics of the CPM laser developed at St. Andrews. Initial data will be concerned with the laser operating without any dispersion compensation optics. Following this the inclusion of Gires-Tournois interferometers components and a four-prism sequence will each be discussed in turn. The latter process enabled pulses as short as 19 fs to be generated. Finally an analysis of pulseshapes generated by the laser system will be made and evidence will be presented to show that their shape is distinctly asymmetric.

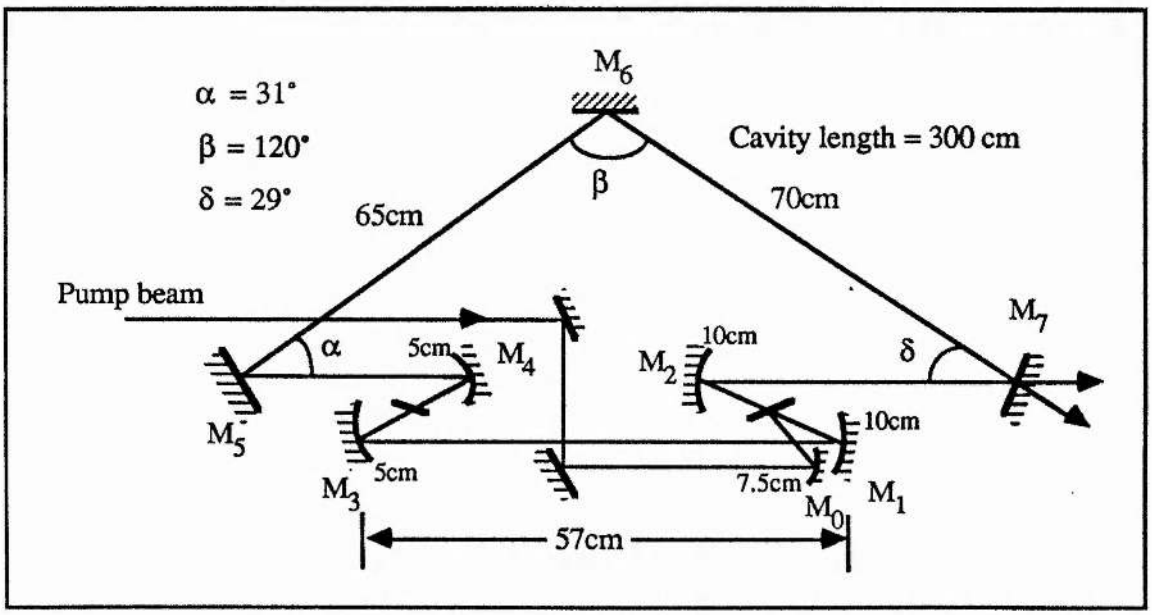

Figure 9.1 CPM laser cavity dimensions

9.1 CONSTRUCTION OF THE CPM CAVITY

Referring to figure 9.1 the CPM laser developed at St. Andrews employed Rhodamine 6G and DODCI as gain and absorber dyes respectively. Optimum operating dye concentrations were 1.9×10^{-3} mol/litre for the gain and $2.2 - 2.7 \times 10^{-4}$ mol/litre for the absorber media, both dissolved in ethylene glycol. The dyes were circulated through

standard commercial jet nozzles with 250 μm apertures. Laminar flow was maintained by inclusion of accumulators in the circulator circuit consisting of baffle plates surrounded by silicone rubber impregnated with lead shot. The dye reservoirs were kept at a constant temperature in a refrigerated water bath. The dye jets were orientated horizontally at Brewster's angle in two Z-fold focussing sections and hence the laser operated with its E-field vector polarised vertically to the plane of the optical table (p -polarisation at the jets and s -polarisation at mirror surfaces). Maintenance of a tight folding angle provided astigmatic compensation [1] and allowed non-elliptical TEM_{00} mode operation. The folding section mirrors M_1, M_2 and M_3, M_4 have 10cm and 5cm radii of curvature respectively and are coated for 100% reflectivity at 45° angle of incidence at 620 nm and a bandwidth from 600–710nm. Mirror M_0 had 7.5 cm radius of curvature and 100% reflectivity between 510 – 620 nm. Mounted on a precision translation stage this mirror independently focusses the argon ion pump laser (a Spectra–Physics 170 – later to be upgraded to a 2030 – operated at 514.5 nm) onto the gain jet. The plane dielectric mirrors M_5 and M_6 were coated identically to those in the folding section mirrors, whereas the output coupler was designed for 98% @ 620nm with normal incidence. Both M_6 and M_7 are operated at incident angles which are wider than their coating specifications and consequently act as red cut-off filters. These mirrors act to constrain the laser wavelength from extending too far into the red due to the absorption of the DODCI photoisomer. Conversely M_5 is operated at a smaller angle of incidence than its coating specification and hence acts a yellow cut-off filter thus constraining the lasing wavelength to exceed 600nm. Thus the single-stack cavity mirrors combine to restrict the lasing bandwidth to within the mode-locking regime of the DODCI absorber without the need to resort to lossy or bandwidth-limiting intra-cavity tuning elements.

9.2 LASER PERFORMANCE

When operated without any absorber dye the laser would operate at ~590 nm with a threshold of 300 – 350 mW. At optimum absorber concentrations the mode-locked threshold was between 4 – 4.5 W, typical pulse durations were 80–90 fs with central

wavelengths ~630nm (a typical autocorrelation trace and spectrum is shown in figure 9.2) and the output power of each beam was 2 –3 mW. In general, as evidenced by poor synchroscan streak camera performance (§3.2), the laser lacked good stability; random fluctuations measured on the avalanche photodiode and Tektronix 7834 storage scope reaching as much as 10% of the peak signal, depending strongly on laser alignment.

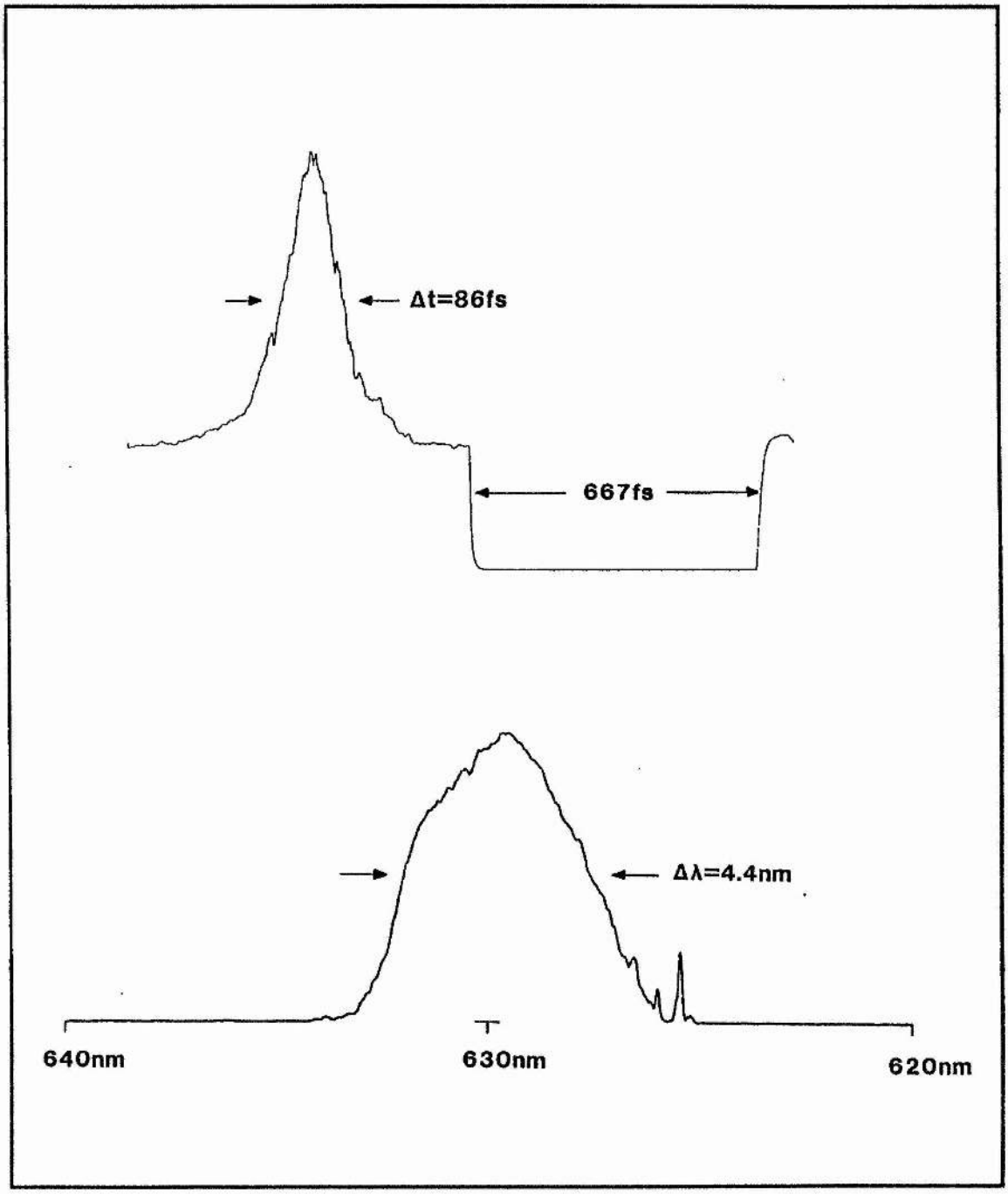

Figure 9.2 Typical autocorrelation and spectrum of a CPM laser pulse

9.2.1 PULSE TRAIN SPECTRAL ANALYSIS

As discussed in Chapter 3 when the photodiode electrical pulse train was examined on a spectrum analyser distinct splitting could be seen on the odd Fourier harmonic components whereas this was not observed for even harmonics (figures 3.7 a-b). To gain some understanding of this effect as a simple exercise a similar spectral comb was modelled on a BBC computer and a Fast Fourier Fransform (FFT) [2] performed on the data to generate the equivalent temporal pulse train. It must be stated that this was an extremely approximate analysis no effort was made to apodise the data set and the mark-space ratio of Fourier component width-to-spacing was several orders of magnitude less than the experimental case. Further no phase information was included. Figure 9.3 shows the input data set and FFT result.

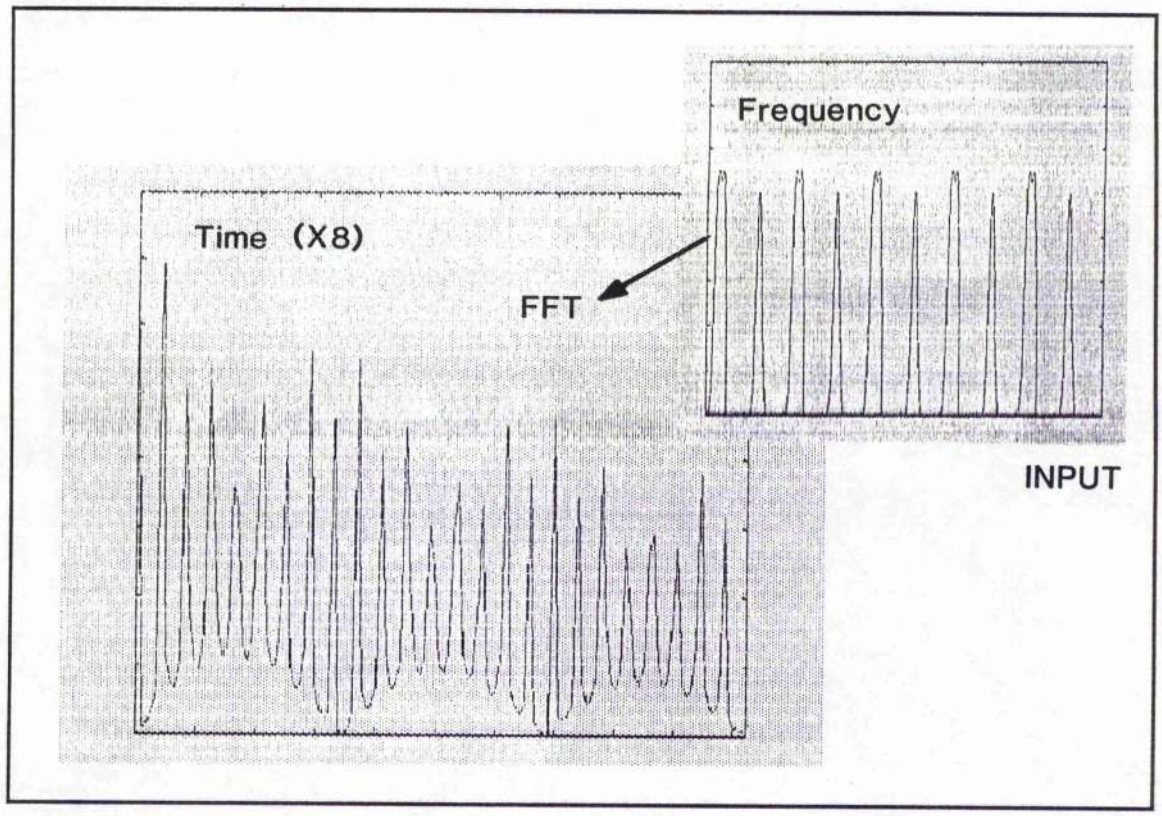

Figure 9.3 FFT of pulse train spectral characteristics

From the above computation there is a clear indication that this type of Fourier spectrum transforms to some form of pulsewidth modulation but whether this is a real effect in the CPM laser is uncertain. Although it is of some interest it is not a particularly

useful property and steps were taken to try to stabilise the laser. It was during these attempts that the laser was seen to operate in its *solitonic* mode.

9.2.2 "SOLITON-MODE" OPERATION

Assuming that the above effect could be due to a transverse mode instability, intracavity apertures were included to constrain the beam path. This had a marked effect on laser performance in that the Fourier component spectral width was considerably narrowed (>100 kHz to ~5kHz at the 60dB point) and odd and even harmonic components were rendered identical. Unfortunately large sidebands also appeared which were due to gross amplitude modulation (>20% modulation depth) of the pulse train (see figures 3.8a and b) and a large increase of the pulse duration to ~500 fs was observed (Figure 9.4). Such effects were reported almost simultaneously by Salin et al. [3] and later Avrampoulis and coworkers [4] although these workers employed cavity dispersion compensation elements.

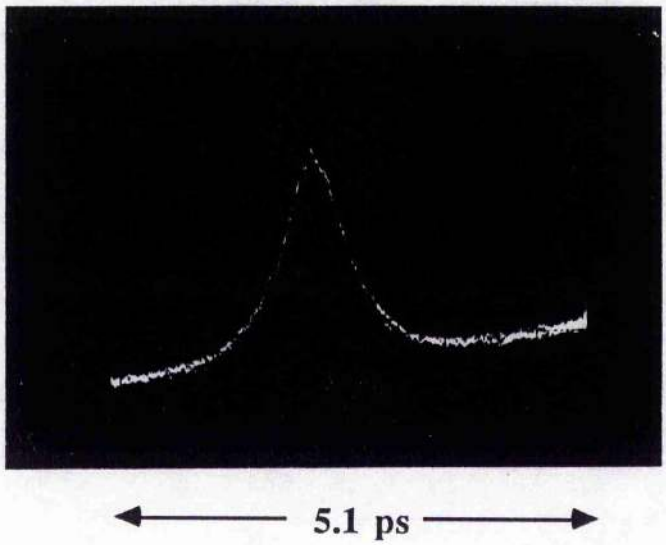

Figure 9.4 Realtime intensity autocorrelation for laser pulses in Soliton-mode operation

Salin ascribed this phenomenon to the propagation of a N=3 soliton inside the cavity with a periodical evolution characterised by the amplitude modulation frequency (70 kHz in this case) observed in the pulse train output. In his analysis use was made of the formal equations describing the properties of solitons in nonlinear media developed by Zakharov

and Shabat [5]. Solitons are particular solutions of a nonlinear wave equation for example the Nonlinear Shrodinger (NLS) Equation [6,7]:

$$u_{xx} + i\, u_t + 2\, u\, |u|^2 = 0 \qquad \text{–eq(9.1)}$$

Application of this equation to the propagation of ultrashort pulses in optical fibres where peak powers are sufficient to generate nonlinear effects implies certain steady-state solutions, ie solitons in which the pulses can propagate without any change in pulseshape (N=1) or a periodic pulsewidth modulation (N=2). Higher-order solutions exhibit complex evolutions in which multiple splitting and recombination occurs. Such optical solitons were indeed observed in fibres by Mollenauer and Stolen [8]. In these analyses the length of the nonlinear medium, Z_o over which the pulse shape is restored is defined by [8]:

$$Z_o = \frac{\pi^2 \mathcal{T}_p^2\, c}{\lambda^2\, \mathcal{D}} \qquad \text{–eq(9.2)}$$

where $\mathcal{D}$ is the GVD of the medium (fs/km.nm) and $\mathcal{T}_p$ a measure of the pulse duration as defined in eq(1.6). Salin applied this relation to the CPM laser cavity in which case a relevant parameter is the GVD per round trip $\mathcal{D}\ell$, where ℓ is the length of the nonlinear medium in the cavity ie) the jet thickness. Transforming $\mathcal{D}$ to the usual representation of the cavity dispersion Ø" (units are time^2):

$$Ø" = \frac{\lambda^2}{2\pi c}\, \mathcal{D}\ell \qquad \text{–eq(9.3)}$$

then the pulse shape in the cavity will be restored after $N_o = Z_o/\ell$ round-trips, and hence:

$$N_o = \frac{\pi\, \mathcal{T}_p^2}{2Ø"} \qquad \text{–eq(9.4)}$$

For a cavity round-trip time, T_{cav} the characteristic soliton frequency becomes:

$$f_o = \frac{1}{N_o T_{cav}} = \frac{2Ø"}{\pi\, \mathcal{T}_p^2 T_{cav}} \qquad \text{–eq(9.5)}$$

The interpretation that a N=3 soliton was propagating within the CPM laser cavity was based on appearance of two modulating sideband frequencies, the higher frequency being twice the lower and a triple-humped intensity autocorrelation. During its propagation a third order soliton will periodically transform from its initial sech^2 shape to a narrow pulse, then broaden and split into two pulses (generating a triple-hump in the autocorrelation),

recombine and narrow to a short duration pulse, before finally returning to the original $sech^2$ shape. By gating the photomultiplier of the autocorrelator at the modulation frequency and varying the sampling point Salin was able to resolve broad and narrow traces as well as a triple humped autocorrelation which is in good agreement with the above assertion [3]. Also as a consequence of the cyclic change in pulse shape and hence peak pulse powers there will be a periodic variation in gain and absorber saturation which could explain the observed modulation in the pulsetrain envelope.

As is apparent from eq(9.5) the characteristic frequency of the soliton should be proportional to the amount of cavity dispersion and so by varying the dispersion it should be possible to change the modulation frequency. This was achieved in our system by inserting thin glass slides into the CPM laser cavity at Brewster's angle. Stacking the slides and contacting their surfaces with index matching fluid allowed up to 3mm of glass to be added in 0.1 mm increments corresponding to an addition of over 150 fs^2 to the cavity GVD. Figure 9.5 shows the measured modulation frequency as a function of dispersion added.

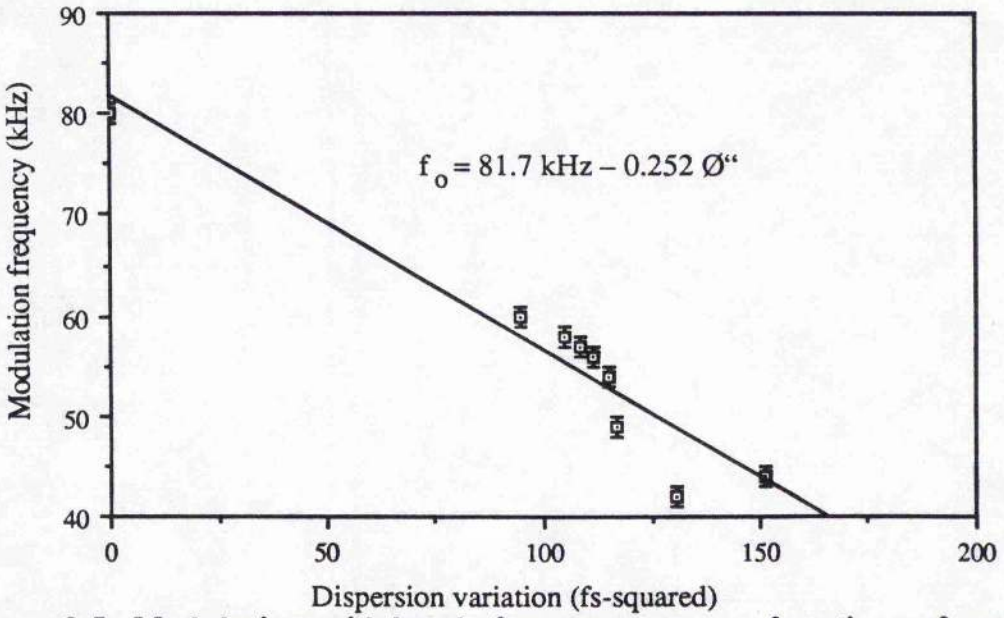

Figure 9.5 Modulation sideband frequency as a function of cavity dispersion

A simple linear fit gives a gradient of 0.25 kHz/fs^2 which when compared to equation 9.5 suggests for a N=3 soliton a initial pulse duration (FWHM = τ_p/1.76) of 1.2 ps. Our

results differed from Salin in that although triple-humped autocorrelations could be obtained by adjusting focussing in the absorber jet, operation was never stable whereas a stable single-peaked, broad correlations were readily achieved. Consequently we concluded that the soliton propagation was probably N=2 type and recalculation of initial pulse duration then gives 0.89 ps closer to the measured autocorrelation value of 0.51 ps which would represent an average pulse width over the soliton cycle.

Salin's assertion of soliton propagation seemed to fit his measured data very well but concern was raised over the arbitrary application of the Soliton relations which were derived for the particular case of pulse propagation through lossless nonlinear media. The NLS equation is not really an adequate model of the situation inside the CPM laser as it takes no account of saturable gain and loss, spectral filtering and linear and nonlinear frequency chirping processes. Hence, following similar observations in Rh110 / HICI and DASBTI CPM dye laser, Avrampolous et al [4] developed a detailed numerical model of the CPM laser taking the above factors into account and were able to reproduce most of their experimental results. There indeed exists various solutions which exhibit periodic pulse evolution but these are quite distinct from classical soliton propagation. The triple-humped autocorrelation is explained by the periodic decay of the main pulse and the simultaneous growth of a satellite pulse which then dominates before the cycle is repeated. The model has some ambiguity in that in order to perform the calculations in a reasonable computation time the cyclic frequency had to be increased ie) nonlinearities had to be scaled up and thus the actual CPM laser parameters were not modelled directly but rather an artificial situation was created. One interesting result that appeared from the modelling was a slight dip in the linear dependence of modulation frequency with cavity dispersion and this was experimentally observed in our laser as can be seen in figure 9.5.

To generate stable modulation of the pulse train the absorber jet usually had to be moved away from the beam focus so it was concluded that strong absorber saturation was not ideal for this mode of operation ie the mode-locking effect has to be partially suppressed. This is why the pulse durations observed are always several 100 fs and may be due to the existence of a narrow bandwidth regime over which stable propagation can

occur. Evidence for this comes from observations by Wise and Tang [9] who see in their CPM laser unstable operation in soliton mode but with a twin-peaked pulse spectrum. If the longer wavelength peak is removed by filtering the transmitted pulse shows stable tripled-humped autocorrelations. The real situation in the laser is still open to conjecture; a detailed numerical analysis will be performed at St. Andrews which will be backed-up with high temporal resolution streak camera studies.

9.3 GVD COMPENSATION IN THE CPM LASER

The CPM laser as it stood could produce sub 100 fs but in general its stability was not good and alignment and day-to-day handling were time-consuming. As a test source for synchroscan streak cameras, even when in so-called soliton-mode, it was a severe limiting factor. Following the work by Diels et al. [10] and Martinez and Fork [11] we soon considered it necessary to have some means of controlling the GVD inside the cavity if the laser performance was to be improved.

Two approaches were adopted for optimisation of the laser system: the inclusion of four Gires-Tournois interferometers and, separately, the construction of a four-prism sequence.

9.3.1 GIRES-TOURNOIS INTERFEROMETER PERFORMANCE

A set of four Gires-Tournois interferometers (GTI's) were manufactured by Queens University for inclusion inside the CPM laser. Their structure consisted of a spacer layer (figure 9.6a) of ZnS mounted on a silvered glass substrate with a covering layer of MgF_2 . The four GTI's were included in the cavity mounted on a table which allowed the angle of incidence to be varied to a small tolerance without changing laser alignment (figure 9.6b). The thin film thicknesses d_1 and d_2 were 180.3 nm and 80.3 nm respectively. Computation of the GVD contribution per substrate using eq(1.8) gave the result shown in figure 9.7 which was calculated for a central wavelength of 630 nm. From this figure it can been seen that the GTI's will introduce enough negative GVD into the cavity equivalent to compensate for approximately 1 mm of glass.

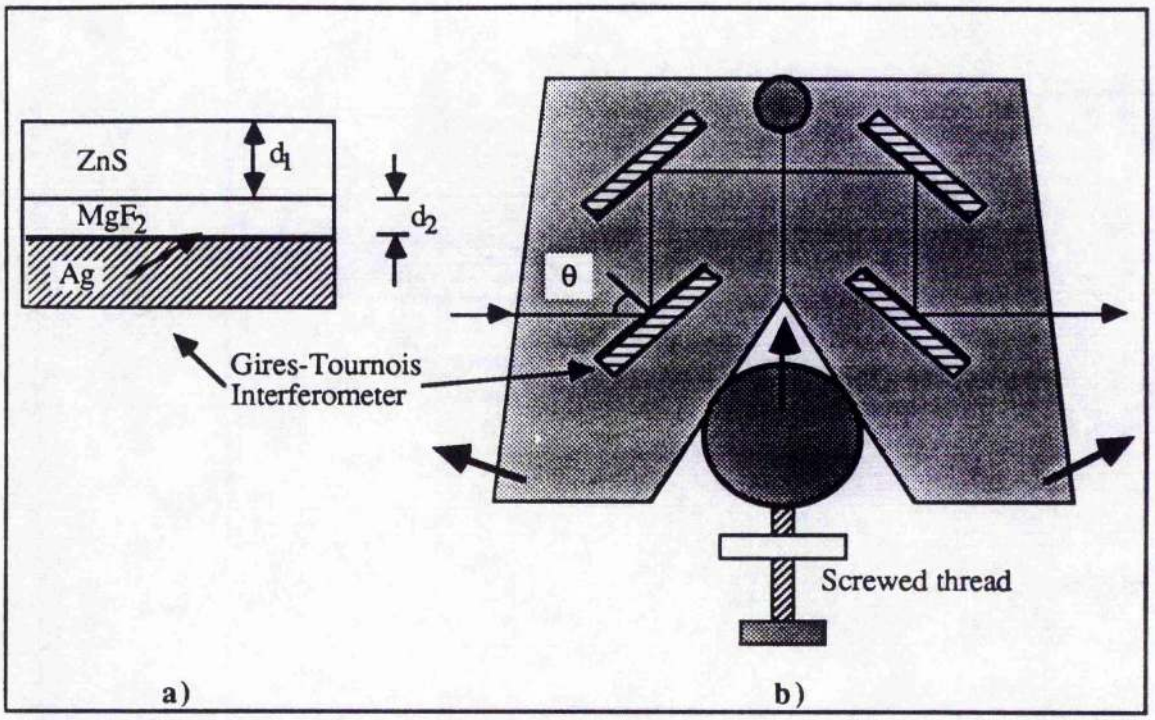

Figure 9.6 a) GTI substrate structure and b) schematic of mounting system.

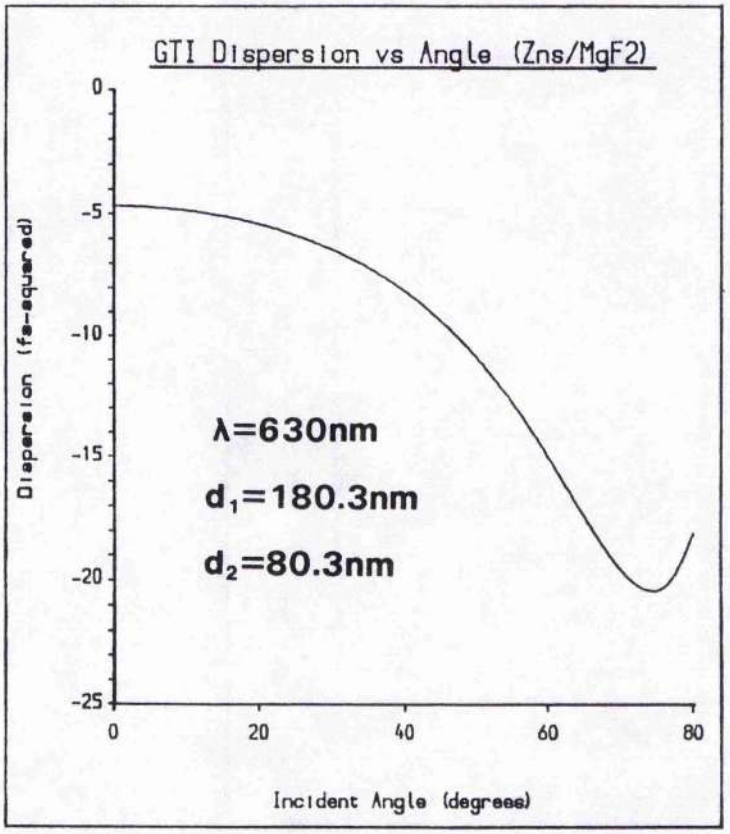

Figure 9.7 GVD contribution of GTI component

Insertion of the GTI's, between mirrors M_5 and M_6, proved problematical in that the silvered mirrors were lossy and hence laser thresholds were significantly increased from ~300 mW to 1.5 W with no saturable absorber present. DODCI was added in small amounts and it was immediately noticed that the laser would mode-lock at much lower concentrations compared to the case with the GTI's removed. The minimum duration achieved was 64fs (figure 9.8) for a DODCI concentration of 1.5×10^{-4} mol/litre. Unfortunately operation of the laser was difficult in that the high laser threshold and extra components made alignment very critical. This was exacerbated by the fact that the GTI mirrors were soft coated and hence could not be cleaned with lens tissue.

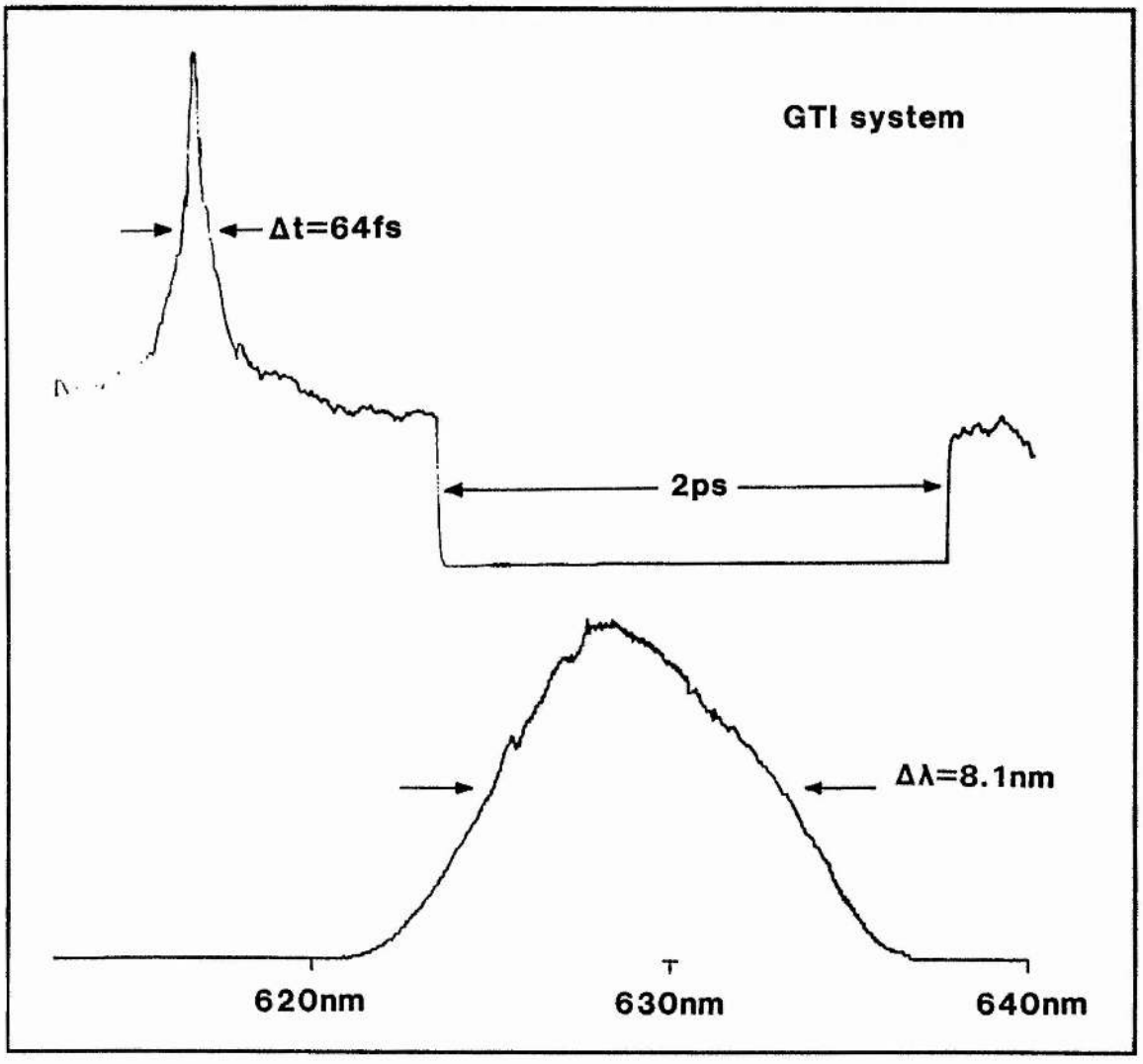

Figure 9.8 Autocorrelation and spectrum of optimum pulse obtained with GTI system

A second problem was that the interferometers could not be angle-tuned to incident angles larger than 25° as their reflectivity seemed to decrease and the lasing threshold became impracticably high (greater than 6 Watts). For this reason the data that could be obtained from these components were severely limited. The only useful conclusion that could be made was that addition of negative GVD to the cavity improved achievable pulse durations.

9.3.2 GVD COMPENSATION USING A FOUR-PRISM SEQUENCE

To allow for convenient adjustment of the intracavity GVD a sequence of four Brewster-angled prisms was incorporated in accordance with a scheme suggested by Fork and co-workers [12] and placed between mirrors M_6 and M_7 (see fig. 9.9). Since the dye jets had a horizontal orientation, to obtain Brewster angled incidence with *p* -polarisation at each prism the plane of the prism sequence was orthogonal to that of the rest of the cavity.

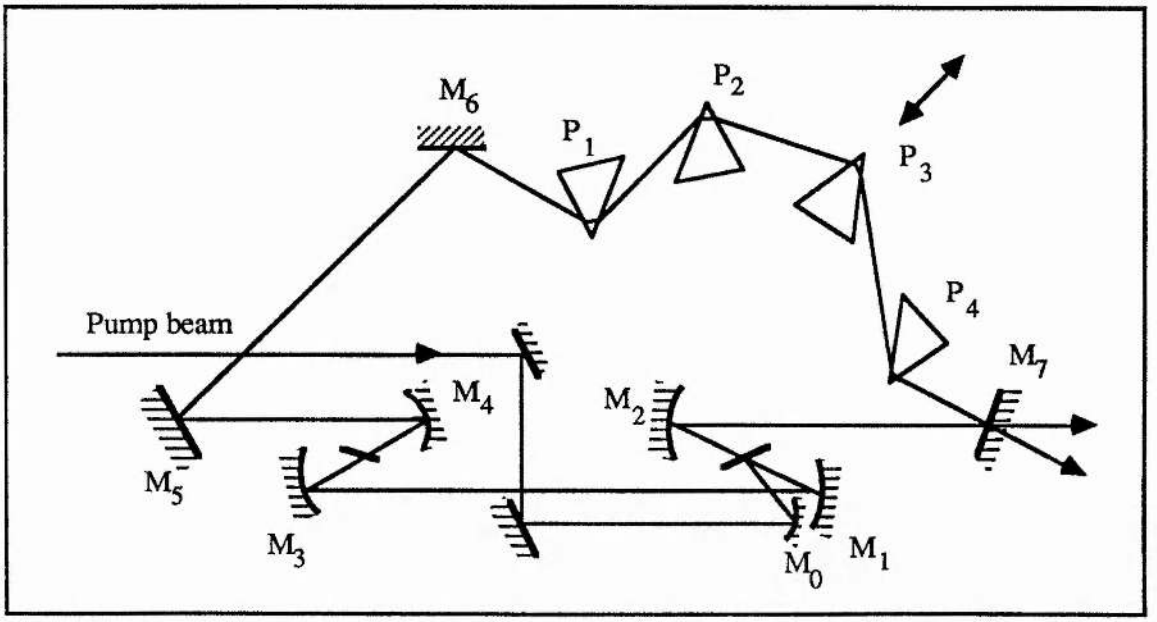

Figure 9.9 Schematic of CPM cavity with prism sequence

The prisms were manufactured in Suprasil I glass (Heraeus) with apex angles of 55.6°. All four were mounted on rotation and tilt mounts affixed to two optical rails on a vertical steel board (see frontispiece photograph). Prism P_3 was mounted on a translation stage so that the system's contribution to cavity dispersion could be varied from a negative value, through zero to positive. The separation between P_1 and P_2, P_3 and P_4 of 27 cm provided

a maximum negative GVD contribution of -436 fs^2 sufficient to compensate over 8mm of glass.

The prisms were of very high optical quality thus exhibiting minimal scattering and a very low insertion loss (the unmode-locked threshold increased from 300 to 400 mW). As a small amount of DODCI was added to the absorber jet mode-locked operation could be achieved very easily with pulses of a few hundred femtoseconds duration. Interestingly, by translation of the jet towards focus the laser could be made to operate stably around 590 nm in a switched mode producing square pulses with a period of 5ns as is shown by the oscillogram traces of Figure 9.10. This property has been predicted by Li et al [13] for partial mode-locking regimes.

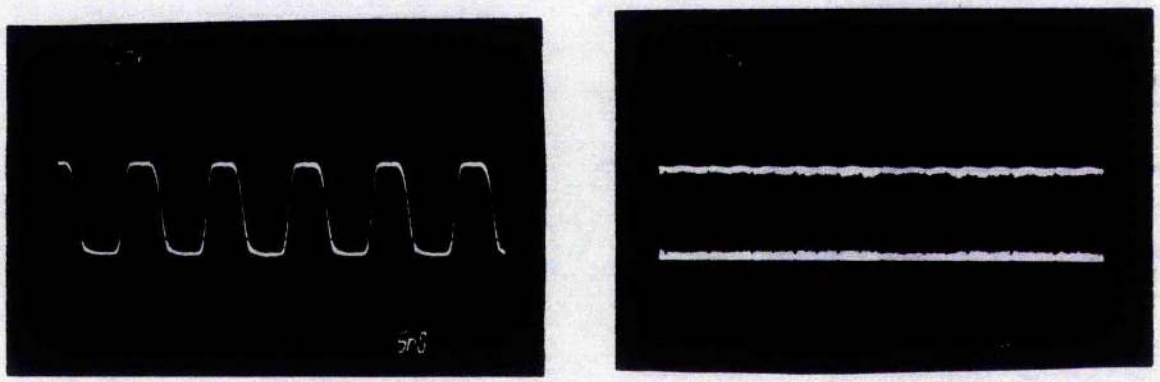

a) b)

Figure 9.10 Laser output exhibiting square pulse operation of CPM laser for low DODCI concentrations a) 5ns/div b) 5ms/div.

Once the DODCI concentration had been increased to more standard values (eg. 2.2 x 10^{-4} mol/l) the operating stability of the laser improved significantly. Output power fluctuations were confined to a few percent (and attributable to power-supply ripple at the 3-phase mains frequency which modulated the argon ion laser pump power) and pulse durations as short as 19 fs (figure 9.11) were obtained. The asymmetry of the slow scan intensity correlation is attributable to the finite response time of the chart recorder (this result was taken before the realtime pulsewidth measuring equipment was developed).

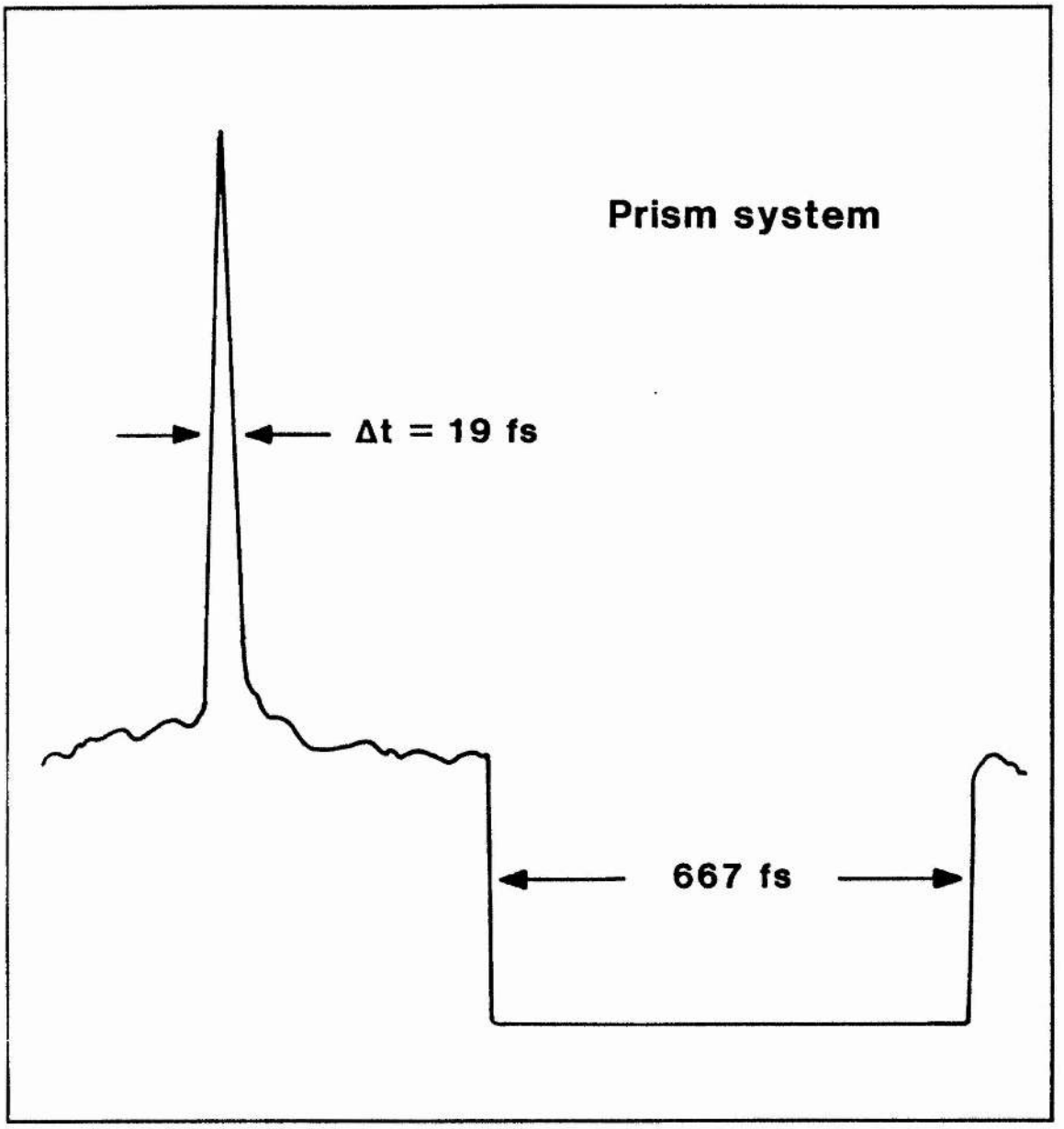

Figure 9.11 Autocorrelation trace for 19fs pulse

Clearly the prism sequence was proving a convenient means of controlling dispersion in the laser and thereby improving the laser stability and pulse duration characteristics. Nevertheless alignment seemed difficult and lasing mode quality was poor due to the large spot size of the beam in the main arms of the cavity. It was concluded that the laser was operating close to its unstable lasing regime and the gain section folding mirror separation was increased to improve mode quality giving a more confined beam in the cavity. Unfortunately pulse durations in this regime were restricted to around 40 fs although laser stability and ease of alignment were significantly enhanced.

9.4 CPM PERFORMANCE WITH GVD COMPENSATING PRISMS

9.4.1 LASER PERFORMANCE AS A FUNCTION OF INTRACAVITY GVD

Figure 9.12 shows the pulse duration as a function of prism position. Here we can see that stable operation is achievable over a wide range of pulse durations, from tens of femtoseconds upto 500 fs. This sensitive dependence on GVD is as predicted by Martinez and Fork [18] and resembles closely the behaviour of their laser as reported in reference 15.

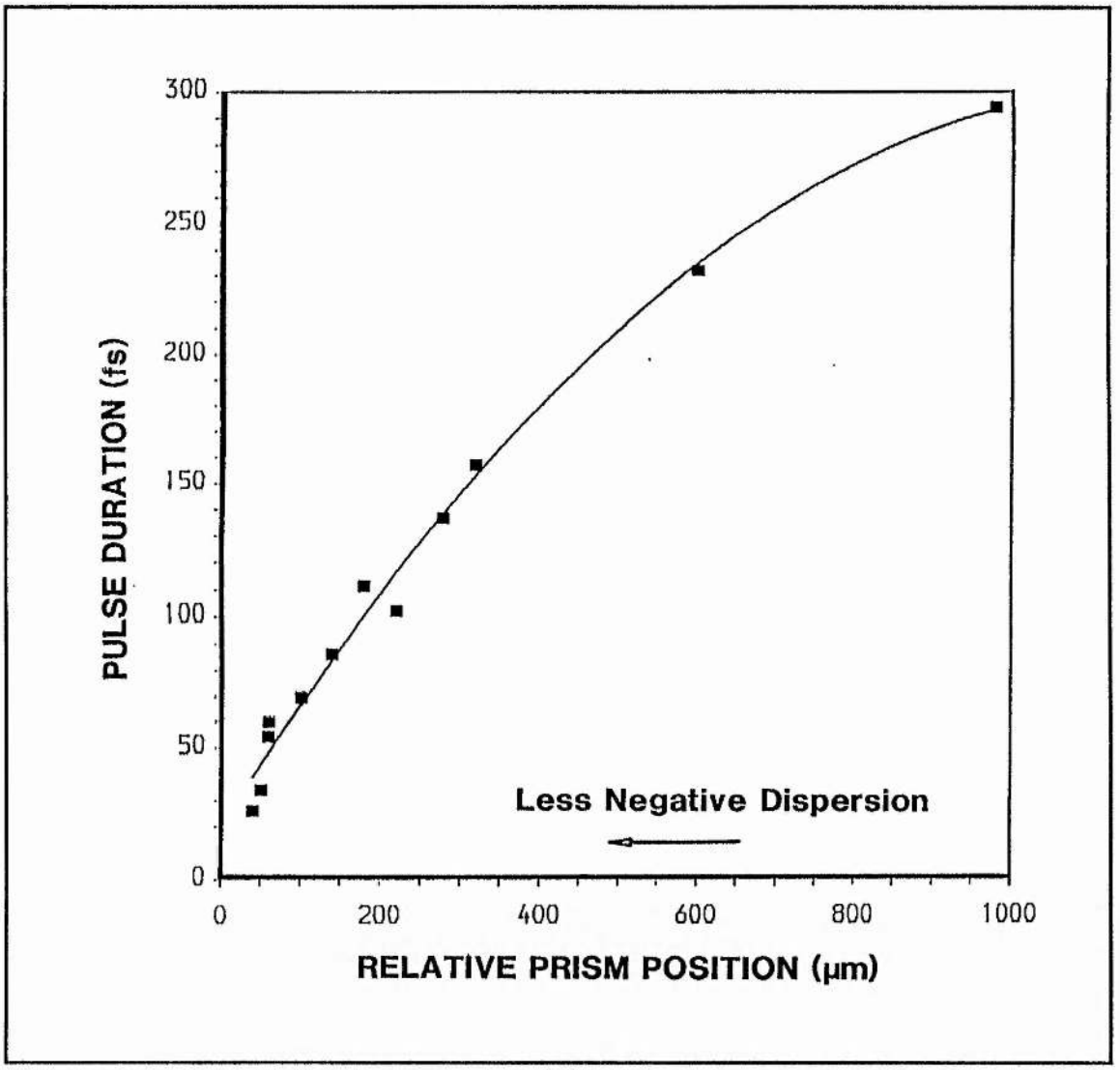

Figure 9.12 Pulse duration as a function of prism translation

The interferometric autocorrelation traces and spectral data taken from the laser for the prism P_3 in several different positions are illustrated in Figure 9.13. The upper figures (a-e) show the case for excess negative GVD within the cavity. The generated pulses are broad but very stable and the pulse spectrum has a characteristic asymmetry with a tail

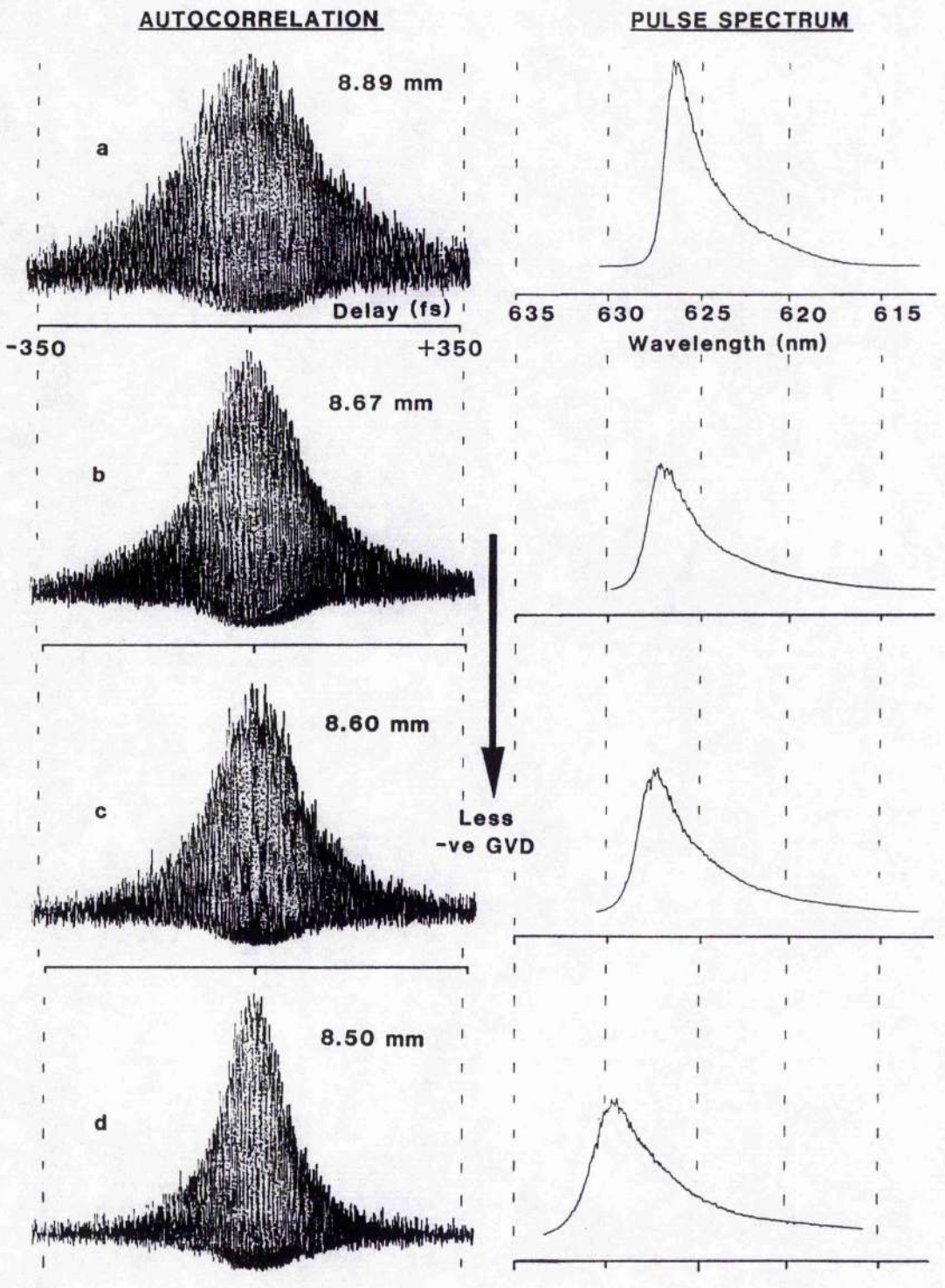
AUTOCORRELATION
PULSE SPECTRUM
8.89 mm
a
Delay (fs)
-350
+350
635
630
625
620
615
Wavelength (nm)
8.67 mm
b
8.60 mm
c
Less
-ve GVD
8.50 mm
d

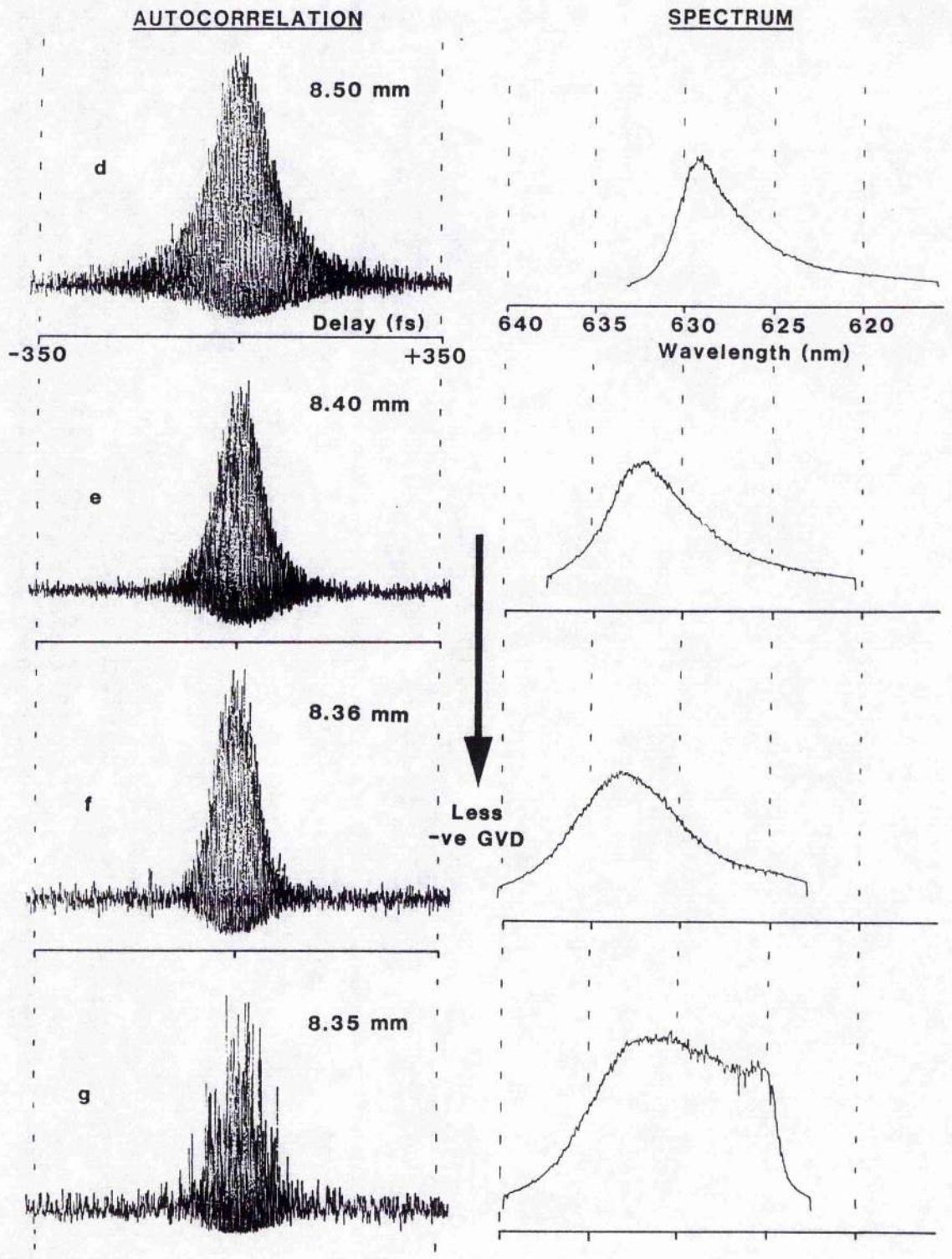

Figure 9.13 (and preceding page) Interferometric autocorrelation and spectral data showing CPM laser behaviour as a function of relative prism position

which extends towards shorter wavelengths. Translating the prism P_3 to decrease the negative GVD contribution by increasing the glass path length yields shorter pulses until an optimum pulse duration is reached which corresponds to the autocorrelation reproduced in figure 9.13f. It should be noted that the spectrum is more symmetrical and red-shifted with respect to that of the previous figures. Further translation of the prism by just 10 μm is sufficient to produce gross fluctuations in output power of the laser and pulse instability as illustrated by figure 9.13g. The asymmetry in the spectral intensity profile also reverses to exhibit an extended longer-wavelength tail which is characteristic of excess positive GVD in the cavity.

9.4.2 FREQUENCY–CHIRP PROCESSES INSIDE THE LASER CAVITY

As discussed in Chapter 1 there are several frequency chirp sources in the laser cavity namely, absorber saturation, gain saturation and SPM due to the Optical Kerr effect in ethylene glycol dye solvent. The source of frequency chirp which dominates is dependent upon the focussing conditions in the jet, the pulse energy and duration. Figure 9.14 shows the absorption profile of DODCI as a function of wavelength [14]. Also included on the diagram is a spectrum (and autocorrelation) of a 26fs pulse obtained from the CPM laser and its relative position to the absorbing species (ground state and photoisomer) in DODCI. It has been argued by Valdmanis et al [15] that for pulses in this spectral regime the Kerr nonlinearity and gain saturation will be the dominant sources of frequency chirp. The negative SPM contribution from the DODCI ground state molecule is small since it is only weakly absorbing at this operating wavelength. Conversely the photoisomer is so strongly absorbing it is saturated rapidly by the leading edge of the incoming pulse yielding a blue shift there, but for the remainder of the pulse propagation through the absorber jet offers only a small and constant negative SPM. Thus the central region of the pulse (where the pulse intensity changes most rapidly) acquires a large positive SPM or up-chirp due to the Kerr effect within the dye solvent and the trailing edge will see a further up-chirp due to gain saturation. Under these conditions one would expect to see stable operation for excess negative GVD within the cavity but unstable operation for excess positive GVD.

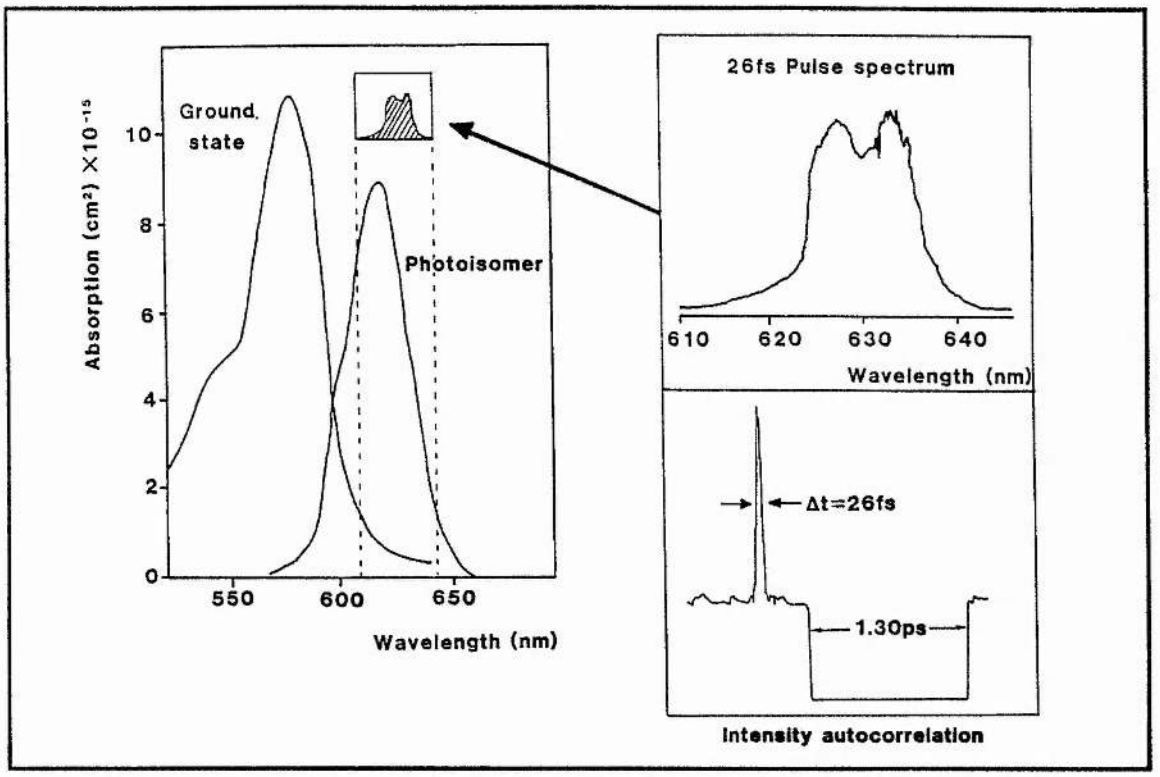

Figure 9.14 Absorption spectra of DODCI molecule shown in relation to a measured spectrum of a 26 fs pulse.

Several modelling exercises have been performed by Miranda et al [16] and later by Jiang et al [17] (who considered the colliding pulse effect and longer operating wavelengths >625 nm) to determine the dominant chirp source. The general conclusion was that for 100 fs duration, 10 nJ pulses or for a few nJ pulses <50fs the dominant chirp source is from the nonlinear refractive index of the dye solvent assuming typical focus spot sizes (~5 μm). Thus the central region of the pulse for these energies/durations will have an upchirp. Conversely for low energy (~1nJ) pulses of durations around 100fs the Kerr effect SPM contribution is negligible and the dominant chirp is negative due to absorber saturation.

The above analysis was repeated for the conditions existing in our CPM laser where in this case sech^2 pulses were considered (as opposed to gaussian in the above) and the wavelength was centred around 633 nm. Following the nomenclature in §7.5 the time dependent phase term within the pulse after passage through the absorber jet is given by:

$$\begin{aligned} \varnothing(t) &= \varnothing_k(E,t) + \varnothing_s(E,t) \\ &= -\frac{n_2 w l}{c} I(t) - \frac{\pi(w_c - w) w l}{2 w_c} \alpha(t)\, g(w) \end{aligned} \qquad \text{–eq(9.6)}$$

This can be rewritten to give the simplified expression:

$$\emptyset(t) = -\emptyset_{max}\, I(t) - \emptyset_{init} \exp\left(-\frac{a\int_{-\infty}^{t} I(t')dt'}{E_{sat}}\right) \qquad \text{–eq(9.7)}$$

Differentiaton of this expression with repect to time gives the instantaneous frequency shift, $\partial\nu$:

$$\partial\nu = \frac{1}{2\pi}\frac{d\emptyset}{dt}$$

$$= \frac{1}{2\pi}\left[-\emptyset_{max}\frac{dI(t)}{dt} + \frac{a\emptyset_{init}}{E_{sat}} I(t) \exp\left(-\frac{a\int_{-\infty}^{t} I(t')dt'}{E_{sat}}\right)\right] \qquad \text{–eq(9.8).}$$

Kerr effect — Absorber Saturation

Infact for the particular case of a $sech^2$ intensity profile the integral (ignoring pulsewidth scaling factors) reduces to:

$$\int_{-\infty}^{t} I(t')dt' = I_o \int_{-\infty}^{t} sech^2(t')dt' = I_o(1+\tanh(t)) \qquad \text{–eq(9.9).}$$

The parameters entered into the above equations are summarised in table 9.1. Note that no consideration has been made for the Kerr effect or saturation in the gain section as focussed spot sizes are much larger and consequently intensities much reduced. The saturation energy E_{sat} is calculated from the relation $E_{sat} = (h\nu \times \text{beam area})/\sigma(\lambda)$ [18] and then halved to allow for pulse collision processes [16] inside the absorber jet. The peak power of the pulse is related to the pulse energy , E_p by the equation $(aI_o) = E_p/(1.14\ \Delta t)$ for a $sech^2$ pulse. For the Kerr effect this value was then doubled again to allow for the effect of the counter-propagating pulses in the jet (this was shown to be a reasonable assumption in reference [17]). From the parameters in table 9.1 the relevant terms in eq(9.8) become:

Kerr effect: $\emptyset_{max} = 0.966\ E_p(nJ)/\Delta t(fs)$ rads

Absorber saturation: $\emptyset_{init} = 0.128$ rads (DODCI)

$\emptyset_{init} = 0.133$ rads (photoisomer).

The chirping effect of the photoisomer was ignored as its extremely low saturation energy implied that it is almost instantaneously saturated at the initial leading edge of the pulse and consequently self-phase-modulation will only appear in this region.

Table 9.1 CPM chirp parameters

Lasing centre wavelength	λ = 633 nm, w = 2.98 x 10^{15} rad s^{-1}
Jet thickness	ℓ = 130 μm
Beam area	a = 2.5 x $10^{-7}\pi$ cm^2 (radius = 5 μm)
Ethylene glycol nonlinear index	n_2 = 3.0 x 10^{-16} cm^2/Watt
Peak of DODCI absorption	λ_c = 588 nm, w_c = 3.20 x 10^{15} rad s^{-1}
FWHM of absorption line	Δw_c = 0.22 x 10^{15} rad s^{-1}
Unsaturated absorption at line centre	$\alpha_c \ell$ = 0.73
Saturation energy at 633 nm	0.25 nJ
Peak of photoisomer absorption	λ_c = 620 nm, w_c = 3.04 x 10^{15} rad s^{-1}
FWHM of absorption line	Δw_c = 0.18 x 10^{15} rad s^{-1}
Unsaturated absorption at line centre	$\alpha_c \ell$ = 0.59
Saturation energy at 633 nm	0.022 nJ

Two situations were considered in the CPM laser, pulse durations of 40 fs and 100 fs at energies of 2 and 4 nJ respectively. These are representative of the conditions inside the laser for optimum GVD compensation and with excess negative GVD. The calculated instantaneous frequency sweeps across the pulse are shown in figures 9.15.

The frequency chirp present differs somewhat from that predicted by Valdmanis in that for the 40 fs pulse both absorber saturation and Kerr effect frequency shifts are of comparable magnitude. For the longer duration pulse the Kerr effect is diminished but still present. The reason for this is that DODCI concentrations are lower in this particular CPM, the jet thickeness is longer (thereby reducing coherent collision processes) and the intracavity pulse energy lower than the CPM of reference [15].

How such chirped pulses would react to different signs of GVD in the cavity is open to argument. If the chirp process was purely dominated by Kerr effect then to enable stable pulse operation and compression the front red shifted region of the pulse would be required to be delayed slightly so that the rear blue shifted region could catch up. In other words optimum performance would occur if a net negative GVD was present in the cavity. If the chirp was purely due to the absorber saturation then the opposite criterion would apply and the cavity would require net positive GVD for stable operation. For the intermediate case the situation is much more complicated. However, for both pulse durations there is a

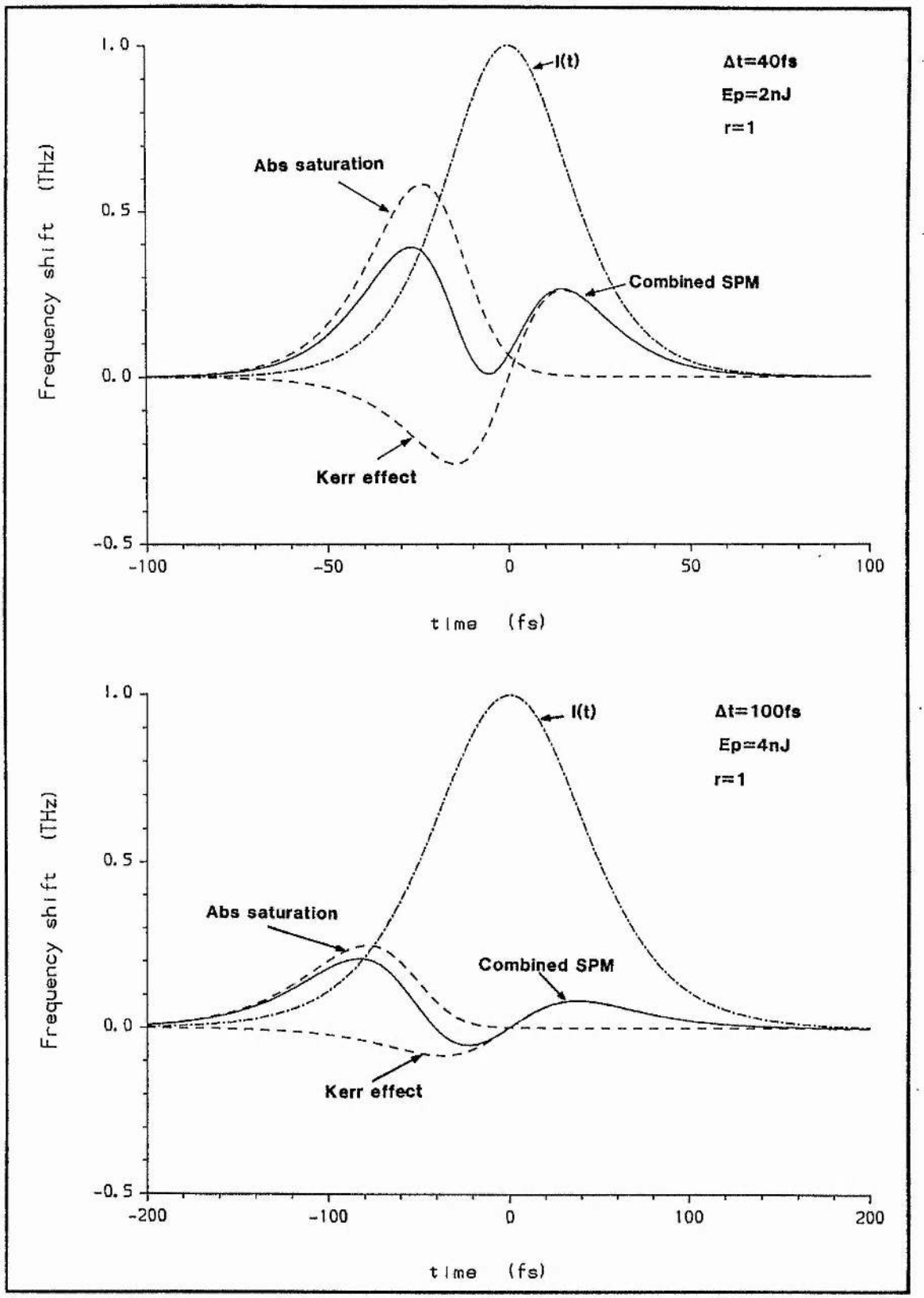

Figure 9.15 Instantaneous frequency shift arising from SPM effects in the absorber dye jet for pulses of differing energies and durations.

positive frequency sweep across the centre of the pulse which would allow some compensation by the prism sequence under the condition of excess negative GVD. Additionally such compensation would cause the central region of the pulse to be delayed with respect to the blue shifted components leading to the 'centre of gravity' of the pulse moving to its rear ie) the pulse would become asymmetric. The fact that no stable operation is possible for excess positive GVD inside the cavity seems to indicate that the optical Kerr effect is still the dominant chirping process. It should be emphasised that the chirping processes inside the laser are dynamically dependent on the pulseshape and duration and the above arguments can only be regarded in qualitative terms.

9.4.3 FOCUSSING CONSIDERATIONS

The attainment of different pulse durations as a function of folding section mirror separation can be understood in terms of focussing conditions inside the dye jet.

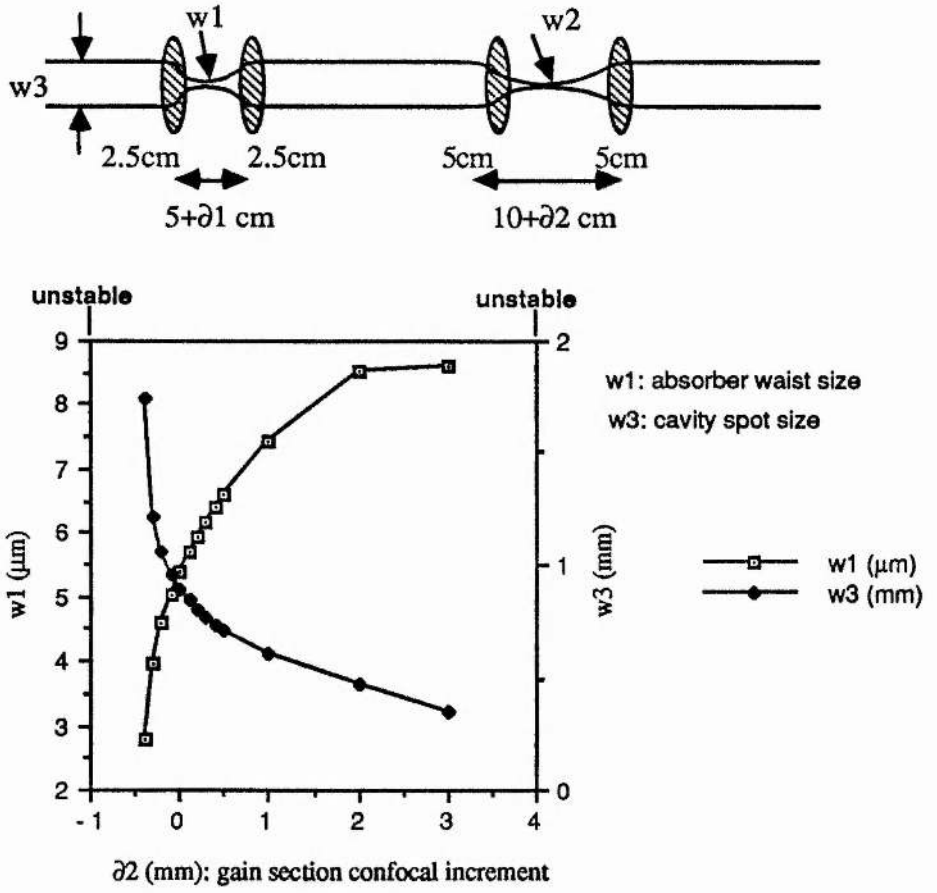

Figure 9.16 Spot sizes inside laser cavity as a function of folding section separation

Figure 9.16a shows a semi-quantitative model of the laser cavity where each mirror is treated as an equivalent lens.Figure 9.16b gives a plot of the calculated waist sizes inside the absorber jet as a function of confocal offset for the gain section, ∂_2 with the absorber section offset, ∂_1 kept constant. Also plotted are spot sizes in the main arms of the cavity. These values were calculated using a gaussian beams program [19] but no attempt was made to include the Brewster-angled dye jets and astigmatic effects.

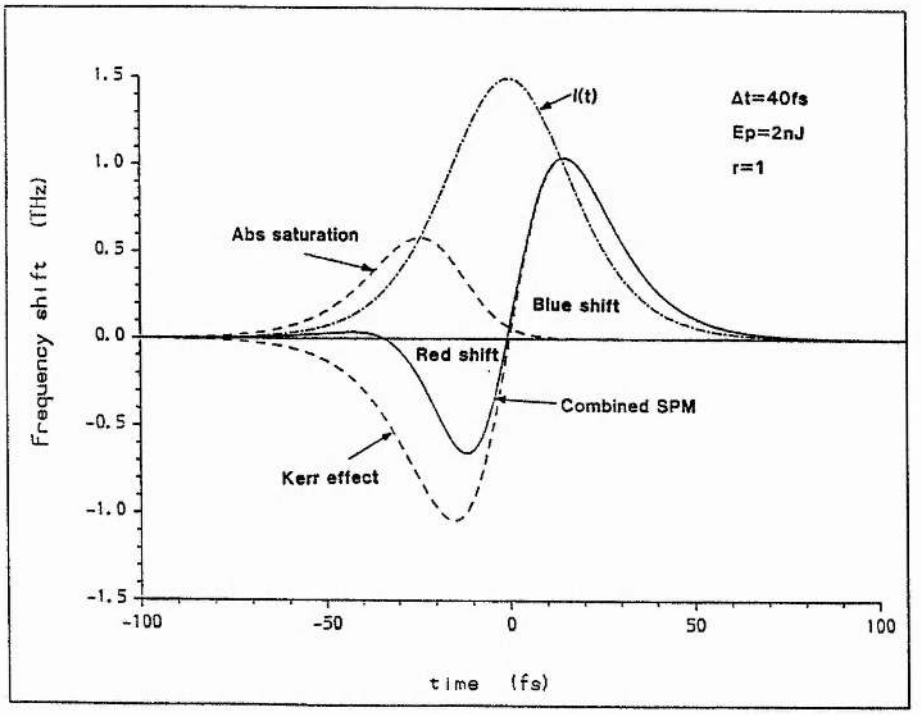

Figure 9.17 Instantaneous frequency chirp across pulse for tight focus condition

As was predicted in §9.3 the region of minimum waist size (maximum external beam size) lies close to the unstable regime of the cavity. In this region the power density at the jet will be very large. For a given pulse duration increasing the pulse energy density would have the effect of pushing the absorber saturation blue shift further to the front of the pulse and increasing the Kerr-related SPM contribution. Figure 9.17 shows the frequency chirp calculated assuming a halving of the waist size at the absorber jet. Kerr effect SPM is clearly dominating and the chirping effect is considerably enhanced which will lead to increased spectral splitting and after GVD compensation very short pulses. Conversely when folding section separations are moved to more stable regimes focussing is less tight,

and the Kerr effect is reduced giving longer pulses. This helps to explain why the shortest pulses in the CPM laser were obtained with cavity close to its unstable regime.

The above analysis results are consistent with the theory that under these operating conditions positive SPM is the dominant chirp in the pulse. The laser output pulse duration and power stability shows a strong sensitivity to jet position which further confirms the theory that in this short pulse regime SPM and GVD interaction are the main pulse shaping mechanisms. More evidence for this is provided at higher pump powers where the laser can show unidirectional operation and yet still maintain a short pulse output (~40fs). When this lasing action is deliberately interrupted, pulse evolution proceeds afresh with counter-propagation of intracavity flux and the laser can subsequently return to unidirectional behaviour. This indicates that in the short pulse regime the coherent interaction within the DODCI jet plays a rather minor role whenever the mode-locking becomes sufficiently well established.

9.5 EVIDENCE FOR PULSE ASYMMETRY

It was immediately apparent from our experimental spectral and autocorrelation data that for pulse durations less than ~ 100 fs the bandwidth-duration ($\Delta\nu\Delta t$) products were significantly less than the expected value of 0.315 which is expected for $sech^2$ intensity pulse profiles (see figure 9.18). Moreover, when $sech^2$ intensity profile fits were attempted on the measured data, the agreement between experimental and theoretical autocorrelations was poor as illustrated in figure 9.19a which corresponds to a 33 fs pulse. Figure 9.19b shows the corresponding fit assuming a single-sided exponential intensity profile ($\Delta\nu\Delta t$ = 0.110) where again a poor match is obvious. A likely inference was that the small value of $\Delta\nu\Delta t$ indicated some degree of asymmetry in the laser pulse although its functional form was not as severe as that of the single-sided exponential. To support this theory the general pulse function introduced in Chapter 7 was used for test fitting purposes. It is a function for which the asymmetry increases with the value of r. Choosing $r = 7$ and calculating the theoretical autocorrelation for a 33 fs pulse gives the fit shown in figure 9.19c where close agreement is obtained.

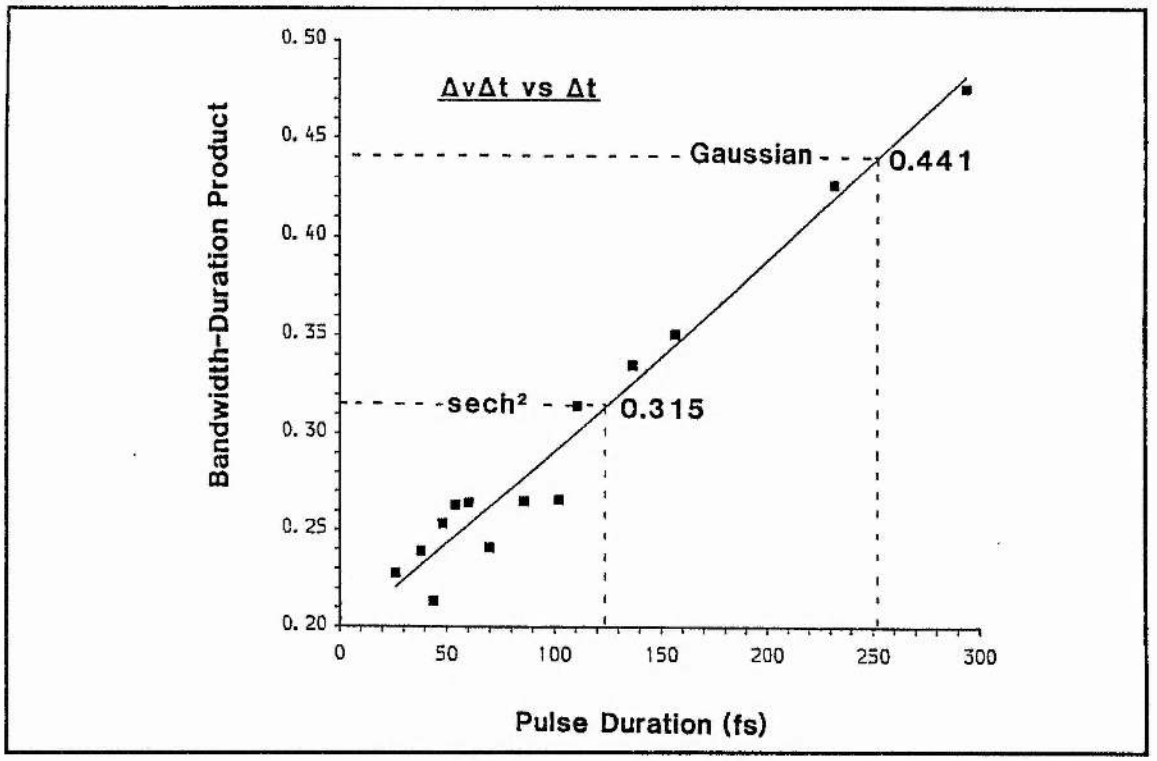

Figure 9.18 Measured bandwidth-duration product as a function of pulse duration

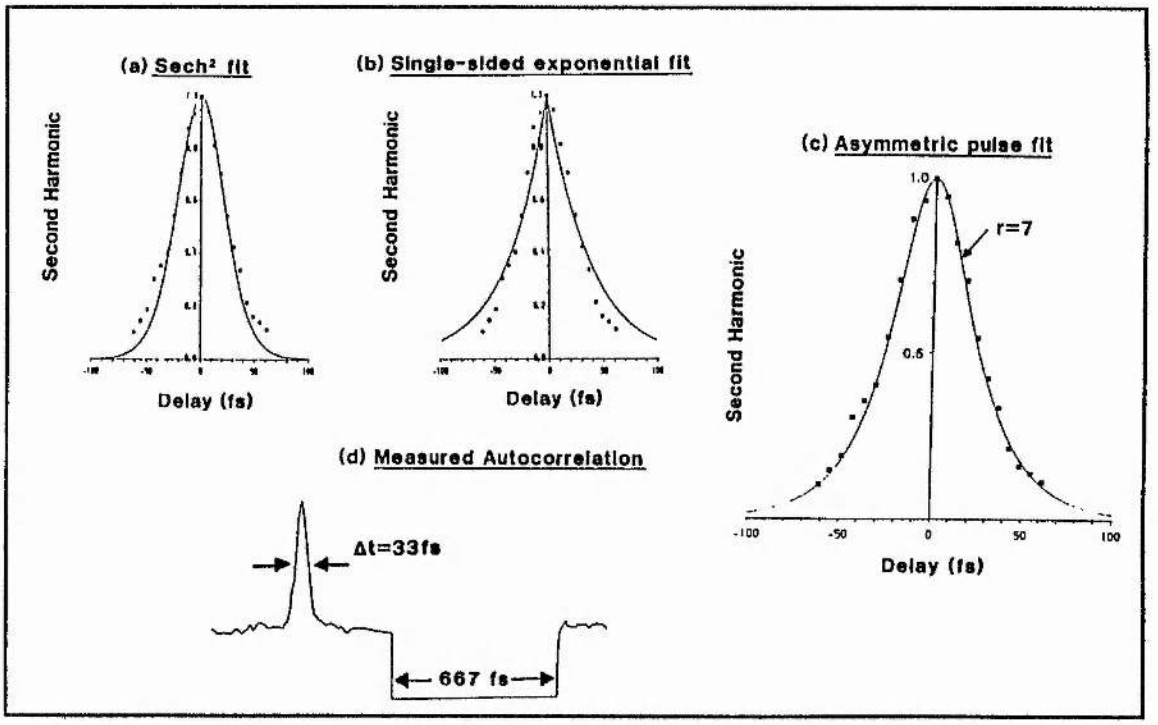

Figure 9.19 Theoretical autocorrelation fits to a measured intensity autocorrelation of a 33 fs pulse assuming various pulse shapes: (a) sech^2 fit. (b) single-sided exponential fit. (c) asymmetrical pulse shape (r=7) (d) Measured autocorrelation from which data points were obtained.

Figures 9.20a,b and 9.21a,b show the interferometric autocorrelations and spectra of 48 fs and 43 fs pulses respectively and the theoretical fits corresponding to r=4 and r=7 test pulses. Excellent agreement is again achieved and the measured bandwidth-duration products compares favourably with the predicted values. Evidence that these fits do not exactly correspond to the measured pulses is produced when a Fourier transform of the test pulses is taken and superimposed on the measured pulse spectra. This indicates that there is a small asymmetry in each pulse spectrum which implies the existence of a small frequency chirp in the pulse due to excess negative GVD compensation in the laser cavity or residual uncompensated nonlinear chirp. This will lead to the discrepancy between measured and theoretical $\Delta\nu\Delta t$ values. Following the computational analysis made in Chapter 7 the fact however that the measured spectrum is asymmetric is a sure indication of pulse asymmetry if linear chirp is present.

Figure 9.21a provides a clear illustration of the fringes in the interferometric autocorrelation. Remembering that the delay between two successive fringes corresponds to one optical cycle (2.1 fs in this case) this autocorrelation directly shows that there are only a small number of optical cycles within these short pulses. The sensitivity of interferometric autocorrelations to pulse shape and chirp and their inherent self-calibration make such measurements a powerful technique for pulse characterisation on the femtosecond scale. Indeed it could be contended that for pulse durations below 50 fs interferometric detail is vital if unambiguous results are to be obtained.

Thus strong evidence is provided which suggests that the output pulses from our laser have asymmetrical intensity profiles. Other workers [20] have seen similar effects and theoretical analyses made by Yoshizwa et al [21] and recently Petrov et al [22] have made predictions for pulse asymmetry. The explicit shape of the pulses in terms of whether the leading or trailing edges are steeper has yet to be determined. However the spectral shapes shown in figure 9.13 for the case of excess negative GVD are consistent with a steeper trailing pulse edge if the pulse is assumed to contain only negative linear chirp .

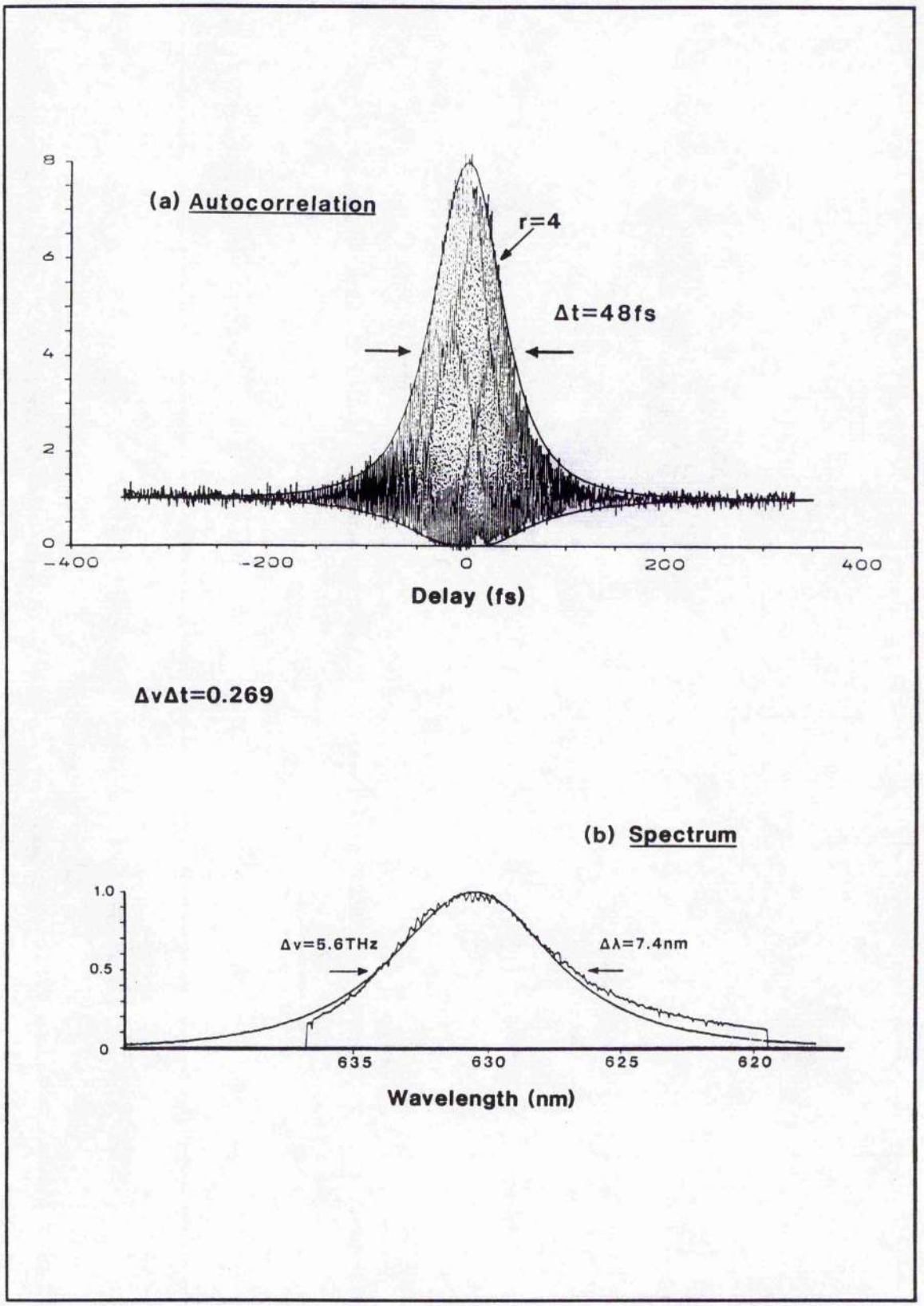

Figure 9.20 Theoretical fits to the a) interferometric autocorrelation and b) spectrum of a 48 fs laser pulse.

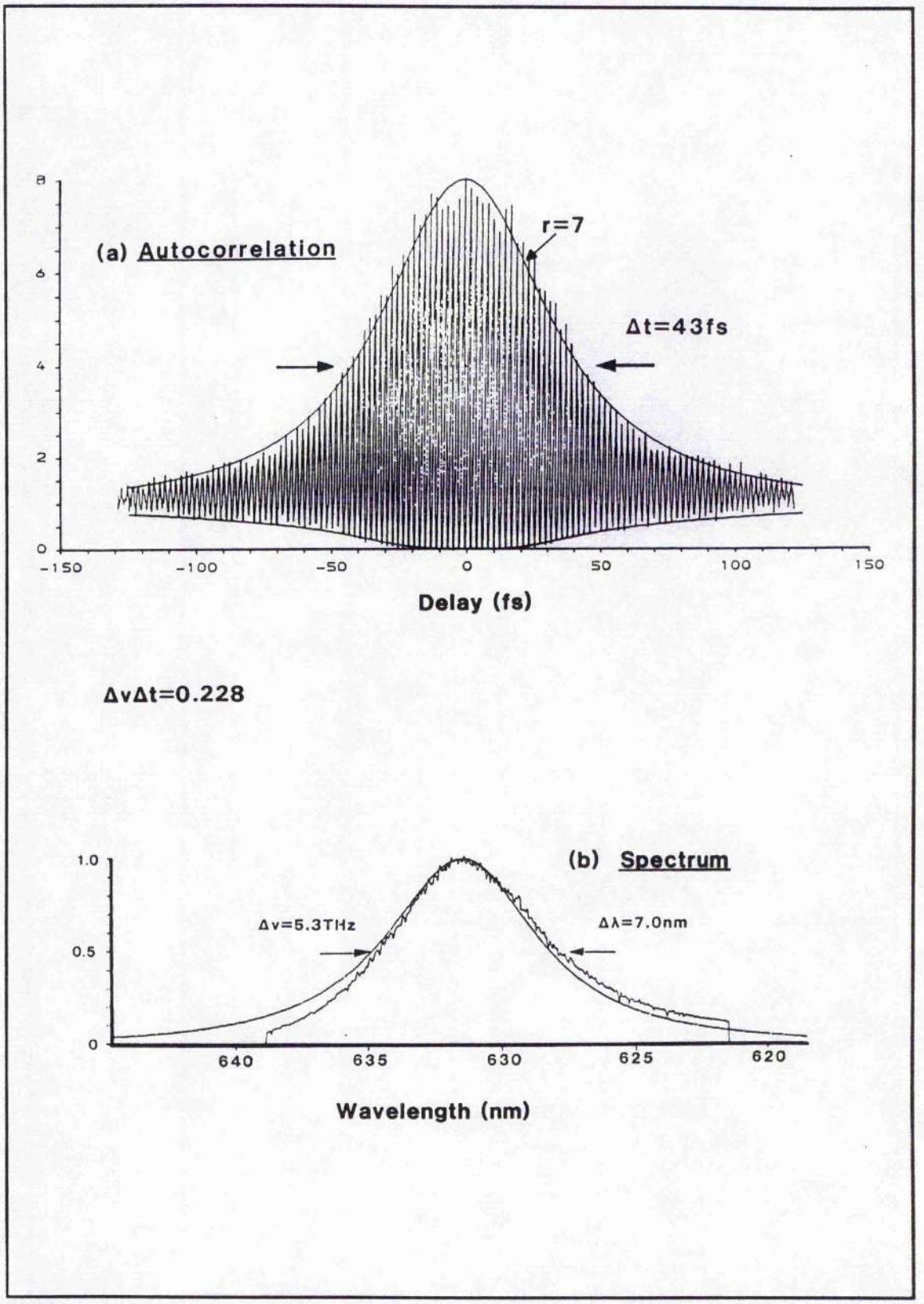

Figure 9.21 Theoretical fits to the a) interferometric autocorrelation and b) spectrum of a 43 fs laser pulse.

9.6 PROPAGATION OF LASER PULSES THROUGH GLASS

In the future it is hoped to adopt cross-correlation techniques as discussed in Chapter 8. As a preliminary experiment 60fs pulses from the CPM laser were passed through different lengths of high quality glass to observe the broadening effect. The input pulse correlation data and spectrum is shown in figure 9.22.

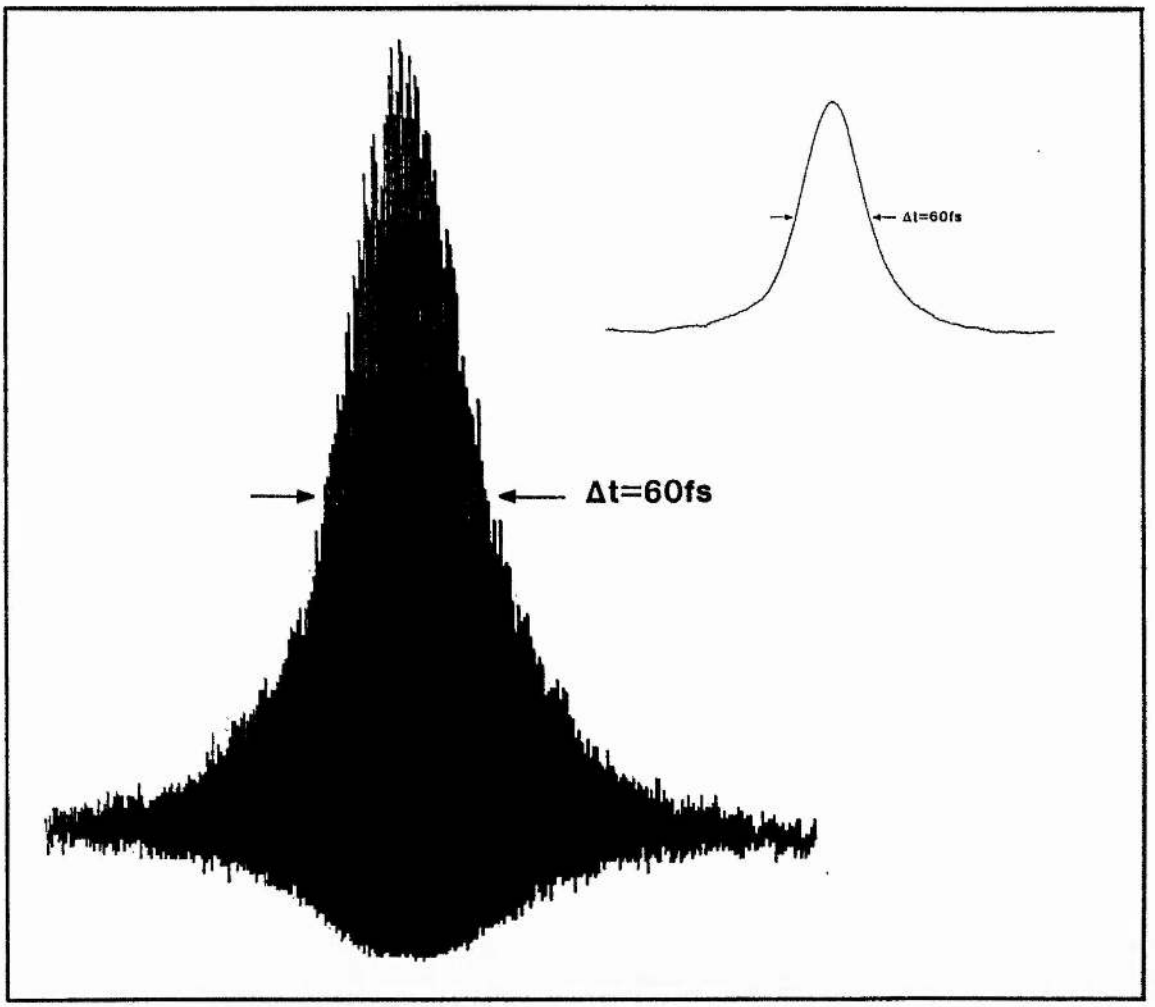

Figure 9.22 Interferometric and intensity autocorrelation of a 60fs pulse prior to passage through glass

The oscillogram traces of figure 9.23 show the interferometric correlations after passage through 5, 10 and 20 cm of Suprasil I glass. Note the broadening and increase in linear chirp as is evidenced by the slight rise in the wings of the correlation traces. From the above broadening it seems that 5cm length of glass placed in one arm of the correlator should be sufficent to give reasonable cross-correlation data.

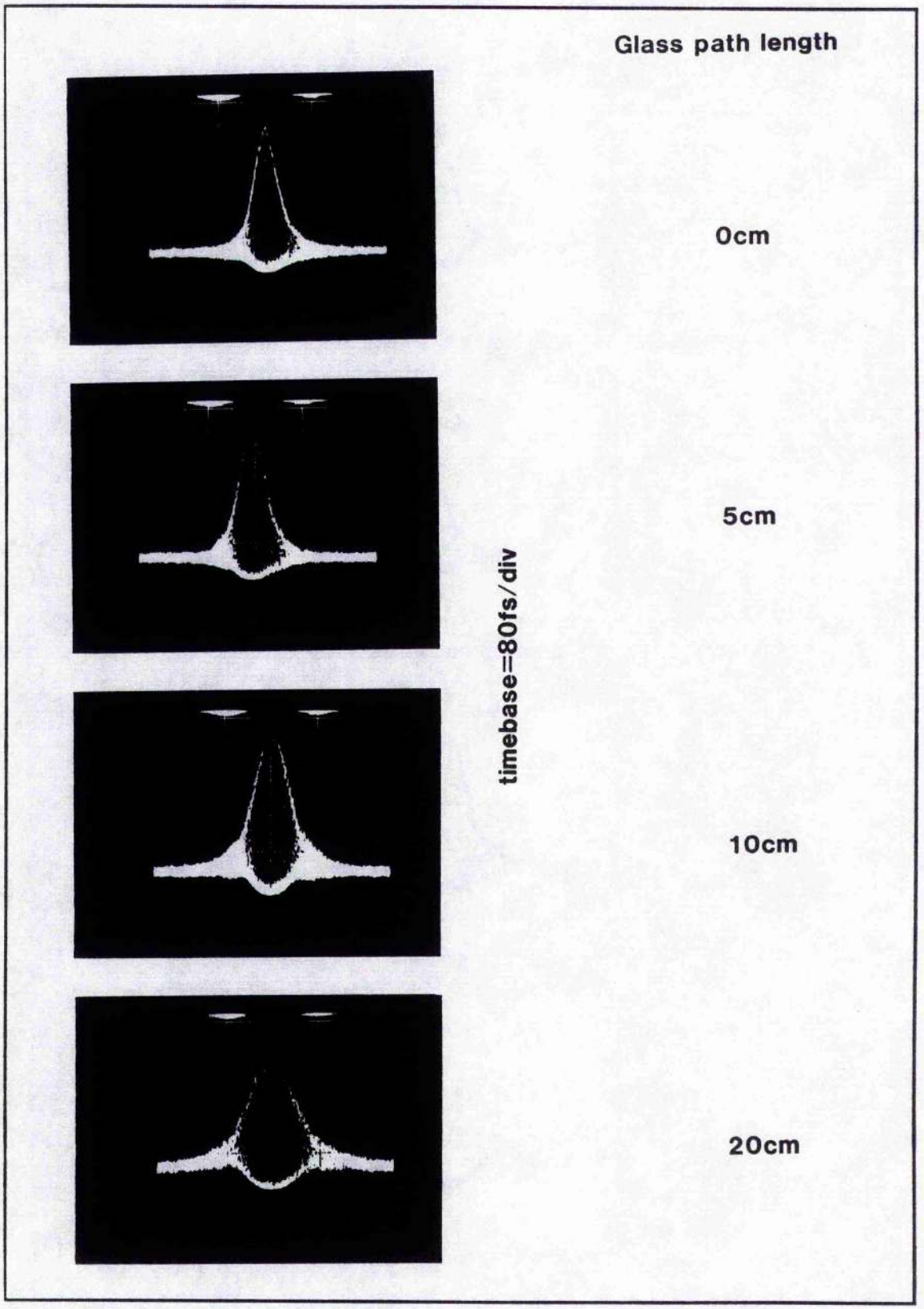

Figure 9.23 Interferometric autocorrelations of pulse after propagation through various lengths of glass rod.

By adopting these techniques it will be possible to determine most of the relevant information concerning the laser pulses. Such interrogations will enable the identification of the source of the observed pulse asymmetries and allow further optimisation of the CPM laser.

9.7 CONCLUSIONS

The inclusion of the four-prism GVD compensating sequence has proved a great success in the achievement of short pulses and the optimisation of laser stability. The latter property becomes apparent in the superior synchroscan temporal resolution achieved with the CPM laser as a test pulse source. Pulse durations of 40 fs are now readily attainable and if tight focussing conditions are adopted pulses as short as 19 fs have been achieved. Many questions have still to be answered, however, particularly with regard to the exact nature of the frequency chirp present in the pulse, its effect on pulse asymmetry and the source of the so-called soliton-mode of operation. Nevertheless it is safe to conclude that control of cavity GVD is vital for stable CPM laser operation and a prism-compensating system effectively transforms the laser into an extremely stable and reliable femtosecond pulse source.

REFERENCES

1 H.Kogelnik, E.P.Ippen, C.V.Shank and A.Dienes, IEEE J.Quant. Electron. **QE-8** 372 (1972).

2 O.E.Brigham, *The Fast Fourier Transform* : Publ. Prentice–Hall Inc. (1974).

3 F.Salin, P.Grangier, G.Roger, and A.Brun, Phys. Rev. Lett. **56** 1132 (1986).

4 H.Avramopoulos, P.M.W.French, J.A.R.Williams, G.H.C.New and J.R.Taylor, IEEE J.Quant. Electron. **QE-24** 1884 (1988).

5 V.E.Zakharov and A.B.Shabat, Sov. Phys. JETP **34** 62 (1972).

6 G.B.Whitham in *Linear and nonlinear waves* : Wiley - New York (1974).

7 L.F.Mollenauer and R.H.Stolen, Fiberoptic Technol. 193 (1982).

8 L.F.Mollenauer, R.H.Stolen and J.P.Gordon, Phys. Rev. Lett. **45** 1095 (1980).

[9] F.W.Wise, I.A.Walmsey and C.L.Tang, Opt. Lett. **13** 129 (1988).

[10] W.Dietel, J.J.Fontaine and J.C.Diels, Opt. Lett. **8** 4 (1983).

[11] O.E.Martinez, R.L.Fork and J.P.Gordon, J.Opt. Soc. Amer. B **2** 753 (1985).

[12] R.L.Fork, O.E.Martinez and J.P.Gordon, Opt. Lett. **9** 150 (1984).

[13] K.K.Li, G.Arjavalingham, A.Dienes and J.R.Whinnery, IEEE J. Quant. Electron. **QE-19** 539 (1983).

[14] D.N.Dempster, T.Morrow, R.Ranken and G.F.Thompson, J.Chem. Soc. Faraday II **68** 1479 (1972).

[15] J.A.Valdmanis and R.L.Fork IEEE J.Quant. Electron. **QE-22** 112 (1986).

[16] R.S.Miranda, G.R.Jacobovitz, C.H.Brito Cruz and A.F.Sarpara, Opt. Lett. **11** 224 (1986).

[17] W.B.Jiang, D.C.Sun and F.M.Li, Opt. Comm. **64** 449 (1987).

[18] O.E.Martinez, R.L.Fork and J.P.Gordon, J. Opt. Soc. Am. B **2** 753 (1985).

[19] A.Finch, MSc Thesis - St. Andrews (1985).

[20] J.C.Diels, W.Dietel, J.J.Fontaine, W.Rudolph and B.Wilhelmi, J.Opt.Soc. Am. B **2** 680 (1985)

[21] M.Yoshizawa and T.Kobayashi, IEEE J.Quant. Electron. **QE-20** 797 (1984).

[22] V.Petrov, W.Rudolph, U.Stamm and B.Wilhelmi, Phys. Rev. A (to be published).

CHAPTER 10: GENERAL CONCLUSIONS AND FUTURE WORK

The CPM laser has proved to be an excellent source for ultrashort pulses not only as an effective 'delta function' generator but also as a test-bed for mode-locking theories. The purpose of Chapter 9 was to present one particular CPM laser and show how, by suitable control of cavity group velocity dispersion, it could be stabilised and its performance enhanced significantly to yield pulses typically of 40 fs duration and, at the expense of mode quality, pulses as short as 19 fs. The relative importance of various chirping mechanisms within the absorber jet has been theoretically analysed and their dependence on focussing conditions discussed. It was found experimentally and theoretically that by tight focussing in the jet positive SPM from the solvent Kerr effect could be made to be the dominant chirping process. This effect could perhaps be enhanced by the addition to the dye solvent of substances with a high nonlinear refractive index eg) 2-methyl-4-nitroaniline (MNA). [1,2]

The 4-prism sequence was very successful in compensating linear dispersion inside the cavity and the active compression of the chirped pulses. However, it is limited in that only gross amounts of linear dispersion can be introduced, no provision is available for compensation of higher order cavity dispersive effects from cavity optics and nonlinear chirp in the pulses. It is these factors which limit the ultimate minimum pulse duration attainable [3]. With this in mind it may be possible to return to the Gires-Tournois interferometer compensation scheme discussed in Chapter 1 but used in tandem with and as a complement to the prism system. The GTI has the advantage in that its dispersive contribution can be easily and accurately modelled on a computer and consequently its cubic and higher order dispersion can be tailored to cancel that of the cavity mirrors and prism system. By these means it may be possible to accommodate the propagation of pulses with bandwidths as large as 30nm within the cavity. [4,5]

The evidence for asymmetry in the CPM laser pulses is almost certainly due to the intermediate nature of the chirp in the pulses (ie. absorber saturation processes competing

with the optical Kerr effect) and possibly the presence of residual uncompensated nonlinear chirp. This is due in part to the relatively low intracavity intensity. The asymmetry could possibly be removed by employing a thinner (50 μm) dye jet to enhance the coherent saturation of the absorber dye species by the colliding pulses. This would push the absorber blue shift further to the front of the pulse leaving the Kerr effect to dominate across the central region. Similar effects could be achieved by using a cavity configuration with smaller radii of curvature mirrors (thus increasihg the energy density inside the jet) and/or optimisation of output coupling.

Allied with the above research the remainder of Section II was concerned with femtosecond measurement techniques. The development of a realtime intensity–interferometric autocorrelator and a CCD spectral readout system enabled the day-to-day running and optimisation of the laser to become routine. These instruments also provided valuable information on pulseshape and frequency chirp characteristics. In the future, by suitable interfacing to a computer data processing system and adaptation of the correlator optics it will be possible to perform interferometric cross-correlation on the laser pulses which will allow the absolute pulse shape and chirp to be unambiguously determined. Such work will require an extension of the fitting procedures developed to generate the computer correlation simulations presented in Chapter 7.

In Section I various aspects of the linear picosecond pulse measurement technique employing streak cameras were detailed. In synchroscan mode the importance of laser stability and phase noise contributions from drive electronics was investigated. With the so-called active synchronisation operation, with an estimated integrated noise level 70 dB below the drive carrier signal, a synchroscan temporal resolution of 0.93 ps was demonstrated for the first time. From the theoretical model developed in this work it is estimated that if camera limited resolutions are to be achieved then the noise floor must be further reduced to atleast 80 dB below the carrier. This could possibly be achieved by using a crystal oscillator to phase-lock the laser system and then driving the streak camera deflection system with the low noise oscillator output. The further improvement of the computational model used in Chapter 4 could perhaps allow an alternative streak camera

based estimation of phase noise levels in mode-locked laser sources and detectors [6] which is currently of prime interest in high bit rate telecommunication research.

Although not reported within the body of this thesis, work has progressed on streak camera designs per se. In particular the computer modelling program discussed in Chapter 2 has been put to good use and new tube designs are emerging which should radically improve camera performance. Present designs being considered are meshless tubes (the high photocathode field being provided by redesigned electrode structures) and a miniature tube nearly one third the size of existing designs.

In collaboration with the Institute of Optics and Precision Mechanics in Xian, China preliminary testing of streak tubes with refined designs of the Photochron IV type have been performed. With one such tube having a specially tailored photocathode and travelling-wave deflection system a single-shot camera temporal resolution of ~ 300 fs has been demonstrated [7] (this work is summarised in a publication reprint at the rear of this thesis). New tube designs now exist which employ internal temporal dispersion compensation [8] and yield theoretical temporal resolutions of 50 fs. However the merits of such designs are dubious – the temporal scrambling of ~ 100fs by even the best engineered photocathodes can never be removed. The streak images that these designs will give will bear little linear relation to the intensity distribution of the light inputed at the photocathode. Indeed one must begin to consider the effect of the electron velocity distribution generated by the 6 THz bandwidth of the 50 fs optical pulse itself.

The CCD readout system developed within this research (Chapter 5) has been shown to work in principal but the problems of reduced sensitivity and RF interference must be addressed. Internal CCD readout structures within streak cameras are now feasible, preliminary experimentation (Chapter 6) shows that both CCD and photocathode can survive the presence of each other during streak tube manufacture.

In the longer term the techniques developed for ultrashort pulse generation in dye-based mode-locked lasers will be transferred to solid-state systems. In these miniaturised sources the gain medium will be a diode laser, the saturable absorber will be in the form of quantum well structure and the free space cavity will be replaced by a fibre loop with

directional couplers for output. For communication applications convenient operating wavelengths are 1.5 μm and in this case the intrinsic negative GVD of the fibre could be used to enable intracavity pulse compression. The use of such pulse sources will be widespread in the fields of optical communications and data processing, electro-optic probing of high speed integrated circuitry aswell as offering new areas of time-resolved spectroscopic research. Allied with this the miniaturisation of streak cameras coupled with dedicated compact, internal or external CCD readout systems will allow the development of bench-top "optical oscilloscopes" with sub-picosecond resolutions. The applications of such instruments extend far beyond that of laboratory research including, for example (as well as laser ranging), time-resolved spectroscopy of cancer specific dyes for the bioassay of human tissue [9] and industrial applications such as field testing of diode pulse sources in fibre communication networks.

REFERENCES

1 M.Yamashita, K.Torizuki and T.Sato, Opt. Lett. **13** 24 (1988).

2 N.Jamashi, J.C.Diels and L.Sarger, J.Mod. Opt. **35** 1891 (1988).

3 V.Petrov, W.Rudolph, U.Stamm and B.Wilhelmi, Phys. Rev. A (to be published).

4 A.Finch, E.Williams and W.Sibbett, Tech. Dig. XVI Int. conf. Quant. Electron. (IQEC'88) paper MP16 92 (1988).

5 Such a GTI design has been recently performed by E.Williams at St. Andrews.

6 U.Keller, K.D.Li, M.J.W.Rodwell, and D.M.Bloom, IEEE J.Quant. Electron. (to be published).

7 A.Finch, Y.Liu, H.Niu, W.Sibbett, W.E.Sleat, D.R.Walker, Q.L.Yang and H.Zhang in *Ultrafast Phenomena VI* :Springer Series in Chem. Phys. **48** 159 (1988).

8 H.Niu, V.P.Degtyareva, V.N.Platnov, A.M.Prokhorov and M.Ya.Schelev, Proc. XVIIIth ICHSPP paper T02-09 -to be published (1988).

9 This work has recently been initiated within the St. Andrews group.

APPENDICES

APPENDIX A: SPACEBORNE LASER RANGING

A.0 INTRODUCTION

The European Space Agency (ESA) are currently funding a research project to develop a spaceborne ranging system which would be used to monitor earth crustal movements along tectonic fault lines or at plate boundaries [1]. Such monitoring requires ultra-precise measurement of displacements in both vertical and horizontal planes between reference points spread over the entirety of an active zone. A suitable precision of measurement would be to within 1cm over a baseline length of 50 to 100km. It is necessary to access between 50 and 80 reference points in a time period short compared to the timescale of tectonic movements in order to observe interplate motion and the discontinuous movements associated with earthquakes.

Such stringent accuracy requirements precludes most landbased ranging systems simply on ecconomic grounds. Very long baseline interferometric (VLBI) systems and direct landbased laser ranging are ruled out due to the shear number of reference points required. Mobile laser ranging systems are excluded since they do not meet the necessary precision. Laser ranging from space, however, offers an ideal solution. A large number of passive ground based retroreflectors can easily be installed over the entire active zone and each can be accessed directly by a spaceborne laser ranger. The striking advantage of this approach is the possibility for global coverage at a very low cost. The following sections contain a description of the operating principles of the proposed laser ranger with a review of the system requirements.

A.1 OPERATING PRINCIPLES

The spaceborne laser ranging system will consist of a mode-locked laser, capable of producing high energy pulses of a few picoseconds duration, transmitting and receiving optics, and a time measuring system incorporating a circular scan streak tube (CSST). This

instrumentation is detailed in §A.2. The ranging system will determine relative vertical and horizontal displacements within tectonic faultline areas of approximately 100km extension. This will be achieved by measuring straight line distances from satellite to reference points of interest and referring them to a model orbital trajectory obtained by fitting data supplied from global tracking stations. The satellite's centre of mass will deviate to a certain extent from the model orbit and to reduce this to less than 5cm an orbital height of 1600km will be chosen. Such deviation will be sufficiently low to enable tectonic plate displacements to be resolved to a precision of 2cm or better. Orbital fit simulations have been reported [1] using short arc fitting procedures that incorporated data supplied from 5 tracking stations and were shown to provide a good orbital model. For the case of ESA project it is estimated that after an initial preparatory period of 10 days, during which the orbital data is amassed, straight-line distances between satellite and ground based retroreflectors will be accurate to better than 1.5cm. This corresponds to a determination of baseline lengths to an accuracy of better than 1cm.

Ranging will be determined by measuring the time of flight of a picosecond laser pulse to travel from the satelite to the ground based reference point and back again, ie) the measurement of the time interval between a "start" and "stop" pulse. Straightline distances are then obtained by converting the transit time into distance with suitable correction for the retardation of the pulse associated with atmospheric refraction. The correction formulae used in this case have been shown to be accurate to a model bias error of $\pm$ 0.5cm [2] using ray tracing methods through pressure profiles received from weather balloon radiosondes.

The main sources of range measurement error that will limit the overall system accuracy are: 1) Uncertainty in knowledge of atmospheric surface pressure, water vapour pressure and temperature at target site (these are important parameters to be inputed into the atmospheric correction formulae), 2) Turbulence and scattering effects in the atmosphere, 3) Eccentricities of optical centre of target with respect to target zone and optical centre of ranging instrument with centre of mass of the satellite (these effects should contribute an inaccuracy of less than $\pm$ 0.5cm), and 4) Instrumental error in transit time measurement associated with the time resolution of the streak camera.

Of the errors grouped in 1) the uncertainty in atmospheric pressure at the target is the most critical since the atmospheric refraction correction is extremely sensitive to pressure. To keep the ranging error to within an acceptable limit of order 1cm requires a knowledge of the target surface pressure to an accuracy of between 2.3 and 4.0 mbarr while limiting the maximum zenith angle to less than 50° [1]. Measurement of atmospheric pressure can be achieved by the laser ranger using two wavelengths in its firing pulse and recording the transit time difference between the differentially delayed return pulses [3]. This time difference, caused by atmospheric dispersion, is proportional to the surface pressure. Clearly this method of determining pressure obviates the problematical requirement of establishing weather station networks around the target retroreflectors. Such two-colour laser ranging has been airborne operated and was found to be accurate to less than 1mb [4].

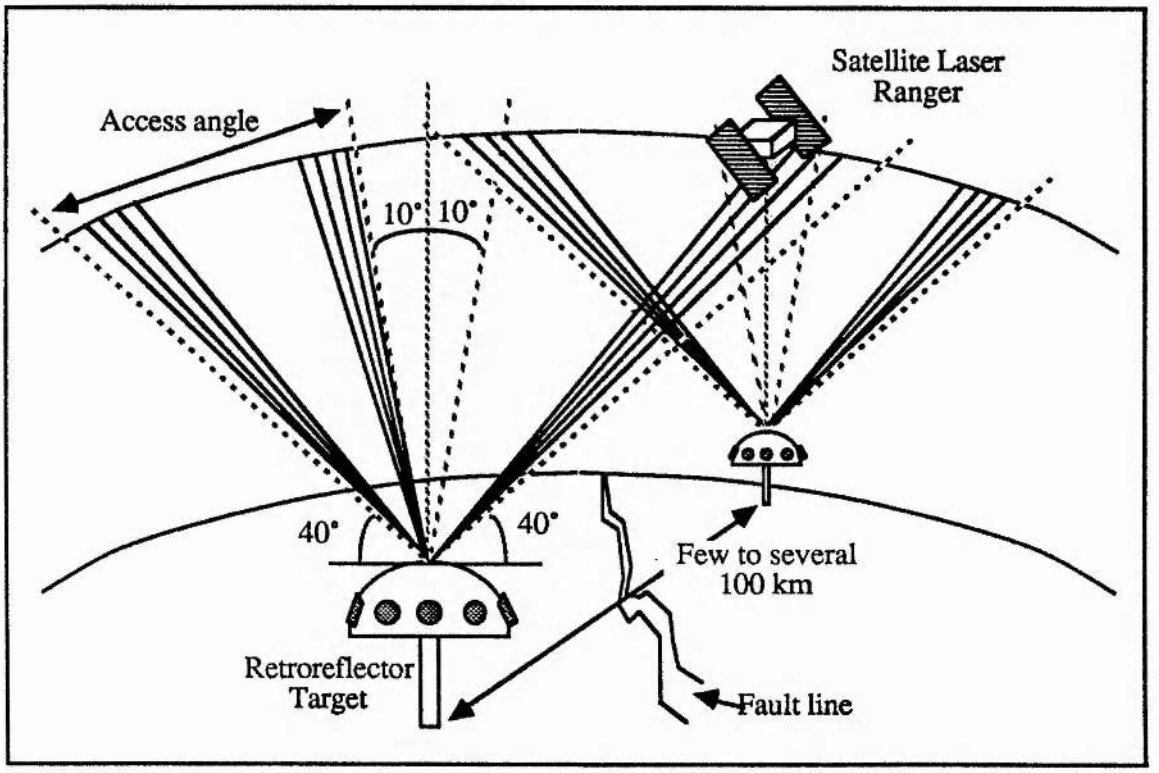

Figure A.1 Spaceborne ranging concept

The general method of targeting is illustrated in figure A.1. Measurements will be iniated immediately after the satellite has reached an elevation angle of ~40 degrees relative to the first retroreflector. After approximately 20 pulses, at a transmission rate of around 20Hz, the aiming mirror of the satellite will be directed towards the next retroreflector target. A

minimum of 3 measurement cycles will be performed for every pass over a test region, each cycle consisting of a complete scan of all targets in the area. Thus data is acquired from three different viewing angles - approach, near zenith and departure. Zenith angles greater than 50° are ruled out so as to reduce the error in the atmospheric refraction correction to an acceptable upper limit. Zenith angles less than 10° will most likely be avoided to prevent background noise associated with diffuse back scattering from the forward propagating pulse.

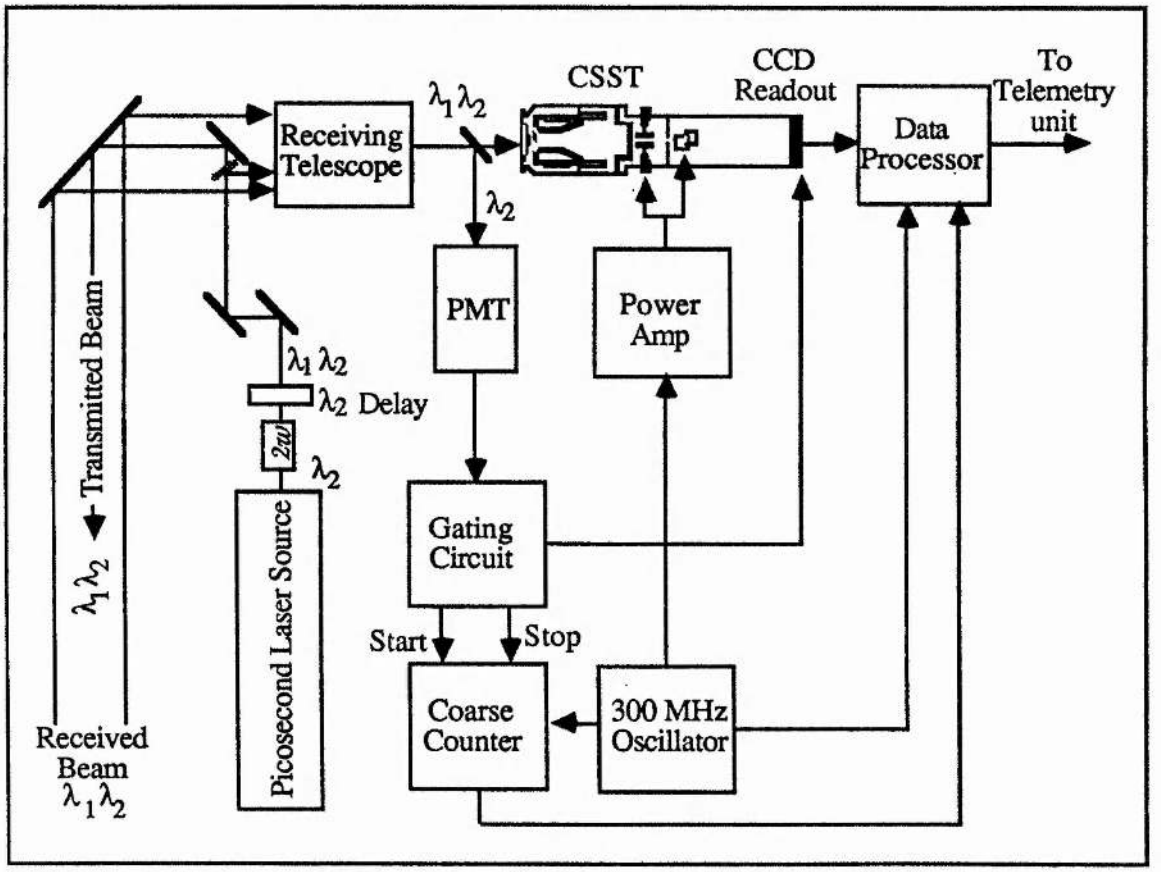

Figure A.2 Schematic of spaceborne laser ranging system

A.2 THE LASER-RANGING INSTRUMENT

The satellite ranging system is represented in figure A.2. The mode-locked laser will produce pulses of some picoseconds duration at a repetition rate of 10Hz. Measurement of roundtrip transit times to an accuracy of picoseconds necessitates the use of a streak camera and in particular for this project, one in circular scan mode [5]. The laser pulse will be frequency doubled and the two pulses of differing wavelengths, λ_2 for the fundamental, λ_1

for the second harmonic, fed into the transmitting optics. A small beam splitter will direct a fraction of the outgoing pulses into the CSST. A 300 MHz quartz frequency standard oscillator will drive the X-Y plates of the CSST causing the electron beam, derived from the input pulses at the tube photocathode, to be swept in a circle onto the readout system of the tube. One revolution on the camera output corresponds to 3.33 nanoseconds. One of the laser pulses will be retarded by calibrated delay and thus two "start" pulses will be registered on the CSST readout. A second beam splitter will route a fraction of the frequency doubled pulse to a photomultiplier which will trigger a coarse counter whose clock period will be in synchronisation to the 300 MHz standard oscillator.

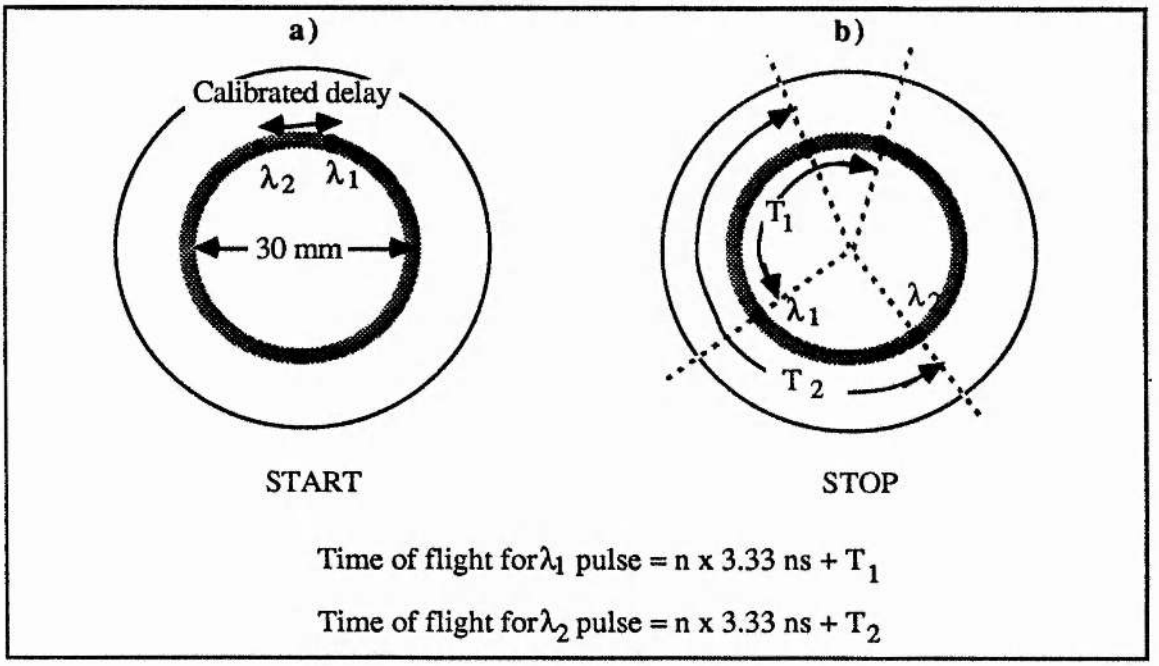

Figure A.3 Distribution of streak images at readout of CSST

The pulses leaving the satellite will travel down to the retroreflector, return, be received by the collecting optics and directed into the CSST. Once more a fraction of the λ_2 pulse will be split into the photomultiplier generating the "stop" for the coarse counter. The remaining light will form two more pulses to be registered on the camera readout. The distribution of the electron pulses on the camera readout are shown in figure A.3. Since the expected differential time delay between the λ_1 and λ_2 pulses due to atmospheric dispersion will be less than 3ns, both pulses will be recorded within one single scan of the

streak tube. Refering to figure A.3 we note that four electron pulses will be recorded; the outgoing pulses separated by a calibrated delay (figure A.3a), and the return pulses (figure A.3b). The fractional separation of the start and stop pulses with respect to the cicumference of the circular sweep gives a precise time measurement to be combined with the coarse count, n. Effectively the CSST is acting as a "vernier" to suppliment the coarse counter. At present CSST's are available with a time resolution of ± 6ps and hence the laser ranger will yield a straight line distance measurement with an accuracy of ± 1.5mm.

The system requirements on pulse energy, repetition rate and wavelength dictate the choice of laser. Ideally a firing rate of 20Hz is desired producing picosecond pulses close to the 350nm atmospheric window edge - this enhances the accuracy of measurement of the surface pressure. Compatibility with space satellite use provide further constraints, viz high efficiency, simplicity of laser services, compactness etc. The most likely candidate is the vibronic mode-locked alexandrite laser system. This laser oscillates near 750nm, is tunable and has sufficient gain bandwidth to form 8ps pulses or less [6]. 380nm can readily be produced by use of a nonlinear crystal.

Retroreflector ground targets will consist of 8 cube corners of aperture diameter 12.7 cm mounted on a mushroom shaped mechanical support. Such targets will be reasonably inexpensive to manufacture and hence a large quantity of reference points can be set up over the tectonic plate zone. Targeting and optical steering will be achieved by both a fixed reference system, which employs star tracking, and orbital prediction data.

A.3 SUMMARY

An brief description of the main design aspects of a spaceborne laser ranger has been given as a background for the development of a CSST with solid-state readout. The applications of such a device is not merely limited to tectonic plate monitoring; other applications that ESA would like to investigate include large object space ranging (eg for space construction) and coastal erosion.

REFERENCES

1 H.Lutz, W.Krause and G.Barthel, in *Space 2000* : Am. Inst. Aeronaut. & Astronaut., New York 236 (1983).

2 C.S.Gardner, Appl. Opt. **16** 22427 (1977).

3 J.B.Abshire, Appl. Opt. **19** 3436 (1980).

4 J.B.Abshire, NASA Tech. paper 1315 (1978).

5 W.Sibbett, W.E.Sleat, W.Krause and J.R.Taylor, Proc 16th SPLAT **SP-202** 171 (1984).

6 V.N.Liisitsyn, V.N.Matrosov, V.P.Orekhova, E.V.Pestryakov, B.K.Sevast'yanov, V.I.Trunov, V.N.Zenin aand Yu.L.Remigailo, Sov. J.Quant. Electron. **12** 368 (1982).

APPENDIX B: ELECTRON SENSITIVE CCD READOUT ARRAY FOR A CIRCULAR STREAK TUBE

(Conference reprint – *Solid state imagers and their applications* SPIE **591** 31 (1985))

ELECTRON-SENSITIVE CCD READOUT ARRAY FOR A CIRCULAR-SCAN STREAK TUBE

A. FINCH, W. SIBBETT, W.E. SLEAT

Department of Physics, University of St Andrews, St Andrews, Fife KY16 9SS, U.K.

C. CLAEYS, I. DEBUSSCHERE

Interuniversity Micro-Electronics Centre VZW, B-3030 Leuven, Belgium.

W. KRAUSE*

Department of Physics, University of Kaiserslautern, D-6750 Kaiserslautern, Federal Republic of Germany.

ABSTRACT

Design considerations and feasibility of a self-scanned circular electron-sensitive CCD readout array to be incorporated within a circular-scan streak tube are discussed. For a scan diameter of 30 mm the circular array will comprise 3500 detector elements. Estimates of the performance characteristics are presented with particular reference to detection sensitivity and signal-to-noise requirements. This streak tube with integral readout is designed to have a temporal resolution ≤5 ps and will form an essential part of a future spaceborne laser ranging system.

INTRODUCTION

A circular-scan streak tube (CSST) presently under development is to become an integral part of a high precision two colour spaceborne laser ranging system. Such a system can be used for monitoring, for example, the earth's tectonic plate movements to millimetre accuracy while simultaneously measuring atmospheric pressure to within mBar resolution[1]. This entails the measurement of the differential round-trip times of flight of laser pulse pairs, directed from a satellite to ground-based retroreflectors, to an accuracy of better than 5 picoseconds.

The general concepts of a modern two-colour spaceborne laser ranging system have been reviewed by Lutz and coworkers[1]. In the proposed system the time interval measurement unit incorporates a CSST operating in a 'vernier' mode whereby, in order to measure the round-trip transit time, the number of complete periods at the tube scan frequency between pulse emission and return is counted using a conventional counter and the fractional period recorded with high precision at the output screen of the streak tube. The signal registered on the circular scan trace of the tube will consist of three streak images arising from the propagated dual wavelength (fundamental and second harmonic) laser outputs. The most intense of these corresponds to signal obtained from the outgoing pulses and the two weaker image spots correspond to the return pulses. The separation of the pulses with respect to the circle circumference gives the fractional clock period and therefore provides an accurate measurement of the transit time.

An experimental 'Photochron IIC' CSST camera system recently developed[2] has been shown to satisfy the temporal resolution requirements[3]. This streak tube incorporates a microchannel plate (MCP) intensification stage and the streak images on the output phosphor screen are recorded either photographically or with an optical multichannel analyser. It is recognised, however, that a compatible charge coupled device (CCD) readout array, with its inherent ruggedness, small size and low power requirements, would be much better suited to spaceborne applications. This could also be conveniently interfaced with the appropriate data collection and communication links.

In this paper we discuss our consideration for a circular-format CCD and photodiode array designed specifically for use as a CSST readout system. The feasibility of incorporating an electron-sensitive version of the device within the vacuum envelope of the camera tube is given particular emphasis.

Image Tube Configuration

The basic electrode configuration of the Photochron IIC streak tube is illustrated schematically in figure 1. The two pairs of orthogonally oriented deflection plates are separately supplied with 300 MHz voltage sinusoids in phase-quadrature to give a circular sweep of diameter 30 mm at the phosphor screen using an acceptably modest power level of 10 W per channel.

The essential difference between the Photochron IIC camera described previously[2,3] and the system that we are now developing is in the method by which the electron signals are detected and analysed. Previous work has concentrated on the time resolution capabilities of this type of tube. Laboratory experiments, to date, have not been limited by available input signal intensity and so as yet the gain, signal-to-noise ratio and overall detection sensitivity have not been fully optimised. However, in a spaceborne application these parameters are of prime importance. One approach to improved signal detection

is to dispense with the MCP, phosphor and associated optics and incorporate a direct readout system in the form of an electron sensitive photodiode/CCD array mounted within the vacuum envelope of the tube.

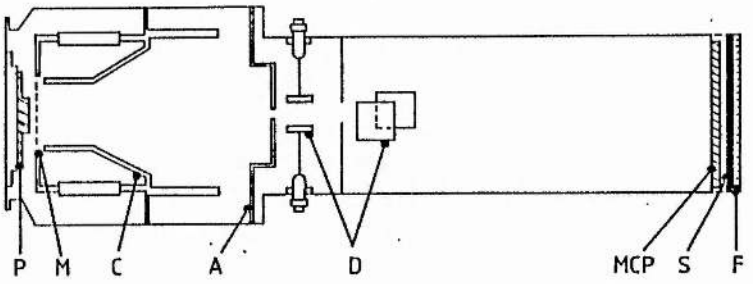

Figure 1. Photochron IIC streak tube. P is photocathode, M is mesh, C is cone, A is anode, D is deflection plates, MCP is microchannel plate, S is screen and F is the fibre optic face plate.

Readout Format

Several possible readout formats have been considered, each having relative advantages and disadvantages. Three of these, (i) a CCD circular array, (ii) a CCD/photodiode circular array, and (iii) an area CCD array are considered. The principal design features that must be taken into account include the following.

(a) The electron pulse will have a typical spatial extent of 150 μm (between 3σ points) and this is the minimum radial pixel dimension that could be accepted before losing signal electrons. Earlier evaluations[2] have indicated that small errors introduced by slight inaccuracies in the relative phase and amplitudes of the deflection drive waveforms, in addition to incorrect positioning of the circular scan, could result in significant registration and time measurement errors. Thus considerations relating to the alignment of the electron beam, the temperature dependent deflection variations, noise characteristics and device processing yield, results in a chosen pixel size of 500 μm in the radial direction.

(b) For a time resolution of 5 ps a suitable number of pixels would be 3500, which represents approximately 1 ps per resolution element in the scan direction. This is an acceptable number from the manufacturing viewpoint.

1. CCD circular array

Using MOS capacitors as sensing elements for electrons has the advantage that the readout of the signal can be effected by transfer of charge around the circular array to output structures.

Frontside electron sensing, however, is not practical due to the loss incurred at the electrodes and gate oxide of the MOS device. In addition there is the problem of radiation damage, where the electron energy absorbed in the gate oxide results in the creation of electron-hole pairs. These are separated under the influence of the local electric field and the holes are drawn towards the silicon/oxide interface which results in a build-up of positive charge and an increase in the interface state density. Both effects seriously degrade the characteristics of the sensor with respect to charge capacity and dark current.

To allow "backside" irradiation[4] the device must be thinned. In this mode of operation signal electrons from the tube are incident on the rear of the device generating electrons within the bulk silicon which diffuse to, and are collected in, the pixel potential wells. An array of too great a thickness would have a poor efficiency due to recombination losses during diffusion.

2. CCD/Photodiode array

This configuration, illustrated in figure 2, avoids the problems mentioned above. It uses a photodiode as the sensing element and a CCD as a shift register to read out the resulting charge. Photodiodes as sensors have the advantage over MOS capacitors in that they have a better detection efficiency and are less susceptible to electron damage. Each photodiode is covered with only a thin oxide layer, which serves no electrical function, and which absorbs only a small amount of the electron energy.

The separation of the sensing and transfer operations will also improve manufacturing yield since two output shift registers can be provided, one on each side of the sensor. By providing an additional register some redundancy can be introduced without the penalty of increased fabrication difficulties.

Increased yield can also be achieved by subdividing the circular array into small sections. This

results in a number of rather short shift registers along the circumference of the array where either the inner or the outer register can be used for reading out a number of sensors. The division of the circle has additional advantages in that it avoids some of the transfer loss. A buried channel CCD has a typical transfer inefficiency of 2×10^{-5} per transfer and therefore about 20% of the charge would be lost if it had to be transferred along the complete circle of 3500 elements.

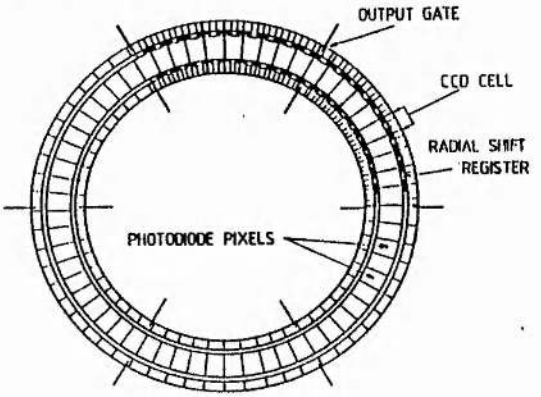

Figure 2. CCD/Photodiode circular array

3. CCD area array

The use of two dimensional CCD arrays offer several advantages. Ease of beam alignment and correction for non-circular scan, effected during signal processing, are two of particular relevance. However, as yet, area arrays of sufficient size and pixel number are difficult to obtain without incurring prohibitive expense and therefore this approach is not regarded as a viable option in the context of the present considerations.

Sensitivity of device

In a spaceborne application, where the intensity of the return signal to be detected is extremely weak, it is necessary for the camera system to have both an optimally high detection sensitivity and signal-to-noise ratio. It has been estimated that each return light pulse will, taking into account typical collecting optics and photocathode efficiencies, result in an emission of approximately 10 photoelectrons from the photocathode[1]. A realistic estimate for the loss within the tube, due to the mesh electrode and other focusing electrodes, would suggest that each charge packet arriving at the detector will comprise about 5 electrons. In the case of the Photochron 11C these will have energies of 11 keV.

The ability of the camera system to detect such low signal levels will therefore be limited by the intrinsic noise within the CCD/photodiode array, noise generated by the tube photocathode and electrodes (tube noise) and also by noise produced by any intervening electron amplification stages, such as a microchannel plate, if such amplification should be necessary. The addition of an MCP also has the disadvantage that, due to its 'open area ratio' some of the few signal electrons must inevitably be lost.

It is important to ascertain the significance of each of these sources of noise in order to determine the sensitivity of the overall system. For the purposes of this analysis it will be assumed that the configuration using a charge coupled photodiode array (Fig 2) has been adopted as the detector. The conclusions are however, directly applicable to other detector configurations.

Photocathode Noise

The cathode which will be processed in the streak tube will be of the S20 type which has an appropriate spectral sensitivity characteristic. An estimate of its noise contribution at 20°C, obtained from measurements of dark currents in photomultipliers[5], indicates that the photocathode dark current is of the order 5000 electrons sec^{-1} cm^{-2}. The 'gating period', which is the time during which the tube is switched on, is typically one millisecond, so the noise contribution expected from thermionic emission, assumed to be the major source of tube noise, is approximately 5 electron cm^{-2}. The scan deflection will present this 'noise image' around the circular detector and thus the photocathode noise is shared among all pixels. Allowing for magnification in the tube and the aperturing effect of the sensor radial dimension, the expected tube noise reduces to 10^{-1} electrons per gate period shared among all pixels. This is equivalent to 3×10^{-5} electrons per period per pixel. At this time the exact dimensions of the detector have not been determined. However, to illustrate the feasibility of the solid state readout device we will calculate noise contributions on the basis of a reasonable pixel dimension of 30 μm x 500 μm and a three phase CCD

element of 50 um x 100 um. Using these dimensions, the five signal electrons will therefore be distributed over 5 pixels and thus implies that the tube noise contribution will be negligible compared to signal, irrespective of any preamplification stages.

CCD noise

There are four main sources of noise associated with a CCD, viz, dark current noise, reset noise, amplifier noise and transfer noise. Each is discussed below in respect to its relevance to the linear CCD array and this particular application.

Dark Current Noise

The operation of the buried-channel CCD is based on the formation of potential energy wells which collect minority carriers injected from the photodiode. In these wells charge packets, Q_n, are formed and as long as this charge is smaller than the inversion charge, Q_{inv}, the structure is in thermal non-equilibrium. Equilibrium will be restored by collecting minority carriers resulting from thermally generated electron-hole pairs. This so-called dark current has the three components of thermal generation at the silicon/silicon dioxide interface, thermal generation in the depleted volume and thermal generation in the bulk within a diffusion length of the interface. The dark current is never completely uniform throughout the device and this causes a fixed pattern noise to be imposed upon the signal. Such noise, however, can be corrected for if one first makes a "dark scan" which is afterwards subtracted from the "signal scan".

Thermal generation is a random process so this noise has a temporal characteristic associated with it. The process obeys Poisson statistics and thus the noise is the square root of the mean dark current integrated over the gating period. Hence the dark current noise in electrons per CCD element is given by:

$$N_d = \left[\frac{A_e J_d t_g}{e} \right]^{\frac{1}{2}} \qquad (1)$$

where A_e is the area (cm^2) over which thermally generated charges are collected in the CCD, J_D is the dark current, typically 2.9×10^{-9} A/cm^2 at 20°C, t_g the integration period ~10^{-2} sec and, e the charge of the electron.

In this configuration we must also allow for the dark current noise arising from electron-hole generation in the photodiode. Assuming the thermal generation rates in the CCD silicon and the photodiode to be the same, the noise expression becomes:

$$N_d = \left[(A_e + A_p) \frac{J_d t_g}{e} \right]^{\frac{1}{2}} \qquad (2)$$

where A_p is the pixel area of the photodiode.

Substituting values and dimensions of CCD and photodiode gives an estimated N_d of 180 electrons at a temperature of 20°C. Of these noise electrons, 70 actually come from the CCD.

Reset Noise

A common technique for CCD readout involves the charging of a capacitance, C_o, through a switch. The Johnson noise in the on-resistance of the reset transistor appears as noise on the reset level which contributes directly to the output signal. The number of noise electrons introduced by this circuit is given by:

$$N_r = \frac{1}{e} (kTC_o)^{\frac{1}{2}} \qquad (3)$$

A typical value for the output capacitance is 0.3 pF and thus the reset noise is equal to 220 electrons per pixel.

Source-follower (amplifier) noise

Due to various noise sources in a MOS transistor, the output voltage is a random variable. These two sources of noise are thermal noise and 1/f noise. The former is due to the thermally induced motion of electrons and holes in the semiconductor and can be characterised by a constant frequency spectrum such that the noise voltage is given by[6] :

$$v_n^2 = \frac{4kT\gamma B}{g_m} \qquad (4)$$

where B is the bandwidth (Hz), g_m the transconductance (mho) and, γ a coefficient depending upon drain and source voltage and the oxide capacitance and substrate doping ($\gamma = 2/3 \rightarrow 10$). 1/f noise arises through recombination of electron-hole pairs and the presence of surface states and in this case it can be neglected.

The noise voltage, V_n, can be converted into a number of noise electrons, N_v, at the input source of the follower, such that

$$N_v = \frac{C_o}{e}\left[\frac{4kT\gamma B}{g_m}\right]^{\frac{1}{2}} \qquad (5)$$

Typical values for the source follower transistor are $B = 5MHz$, $g_m = 10^{-3}$ A/V. For the worst case situation ($\gamma = 10$) the number of noise electrons due to the source follower is equal to 54.

Transfer noise

The transfer of electrons from one site to another is a random process due to the presence of trapping and emission centres in the bulk of the silicon. The number of noise electrons due to interaction with these bulk trapping states is given by[7] :

$$N_b \sim \left[n\frac{N_t}{N_D}\tfrac{1}{2}(m+1)\right]^{\frac{1}{2}} \qquad (6)$$

where n is the number of signal electrons, N_t the density of bulk states, N_D the doping concentration in the buried layer and m is the total number of transfers.

This expression is valid only for high signal charge packets present in the CCD. A saturated CCD element of dimensions 30 μm x 30 μm will have, typically, $n = 6 \times 10^6$, $N_t = 2 \times 10^{11} cm^{-3}$ and $N_D = 3 \times 10^{-16} cm^{-3}$. A 500 element three phase CCD shift register having 1500 charge transfers will therefore generate a transfer noise of 200 electrons.

For low signals (charge packets of less than 2×10^4 electrons per element) the transfer noise becomes independent of signal and is of the order $0.3\sqrt{m}$ [7]. This is the worst case transfer noise level for low signals and corresponds to approximately 10 electrons per pixel.

Summary of noise values

The total noise expected N_t is calculated from the sum of the squares of the above noise levels and becomes at room temperature, for the low signal case, approximately 300 electrons per pixel. It can be seen from the above analysis that the two major sources of noise in the detector are dark current noise and reset noise. Since the dark current J_D is due to thermal generation it has the strong temperature dependence described by:

$$J_D \propto \exp(-E_g/2kT) \qquad (7)$$

Consequently a reduction in temperature, for example to -40°C would reduce J_D by a factor 300 and hence the dark current noise by a factor 17. Reset noise may be reduced in the detection circuit by noise cancellation. The most common method used is that known as "double correlated sampling" where the waveform is sampled twice, once after resetting and again after output. Another method of noise suppression proposed by Endo et al[10], if applied here could possibly enable a reset noise level as low as 10 electrons per pixel to be achieved. It follows that if we operate the array, as discussed, at a temperature of -40°C and use optimised noise cancellation charge detection circuits we find N_t = 60 electrons per pixel. In order to compare this noise level with the expected number of signal electrons obtained from the incident pulse it is necessary to determine the inherent gain and efficiency of the photodiode.

As the electrons penetrate the silicon and dissipate their energy in absorption or scattering processes they create electron-hole pairs. Raising an electron to the conduction band requires a minimum amount of energy equal to the forbidden energy gap, E_g. Excitation processes can also take place in which electrons are raised to intermediate levels, and thus, although the energy required to form one electron-hole pair is E_g, much of the energy deposited in the crystal is dissipated in parasitic excitation processes. The mean energy deposited per electron-hole pair formed, E, is needs to be much larger than E_g. In silicon E_g is 1.1 eV, and E is approximately 3.6 eV. Because of the statistical nature of the scattering process the distance penetrated varies from one electron to another. There is, however, a well defined mean range, R, and it is this parameter that proves to be most useful in the determination of the detection efficiency.

In order to realise a good efficiency, the entry window must be thin enough to allow transmission of the electrons with minimal energy loss but it is also necessary that the sensitive region must be thick enough to maximise the collection of generated electron-hole pairs. For a CCD with a photodiode sensor, the entry window is formed by the oxide layer which covers the photodiode. The sensitive region extends from the silicon surface to a depth of approximately one diffusion length (~50 μm) in excess of the depletion layer width. All the electrons generated in the depletion layer (width ~5 μm) will be collected, whereas some of those generated in the quasi-neutral substrate will recombine before they can reach the depletion layer. Thus for optimum efficiency, the mean electron range should not exceed the depletion layer width.

Figures 3,4 illustrate the range/energy relationship for electrons in silicon dioxide and silicon respectively. With the operating voltages of the Photochron IIC camera that has been evaluated, electrons with energies of 11 keV arrive at the MCP. If we take the case of a CCD array having a 100 nm oxide passivating layer, in place of the MCP, then the electrons will enter the silicon with a residual energy in the region of 9 keV. For this energy the mean range in the Si will be 0.6 μm and all of the 2500 generated electrons will be collected. An increase in photoelectron energy to 17 keV would result in a residual range of 2 μm which is still within the depletion layer and will give close to 100% detection efficiency. Approximately 4500 electrons will be generated, giving considerably increased gain and therefore leading to an improved signal-to-noise ratio. Under these conditions the tube should also have a slightly improved temporal resolution but at the expense of a higher electrical power requirement to maintain a scan diameter of 30 mm.

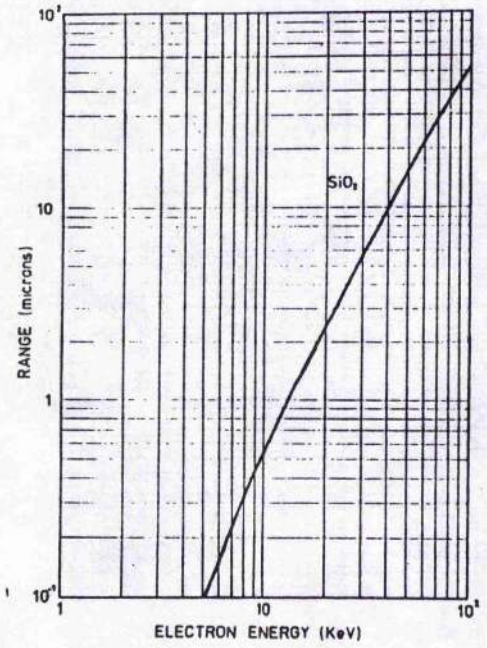

Figure 3.

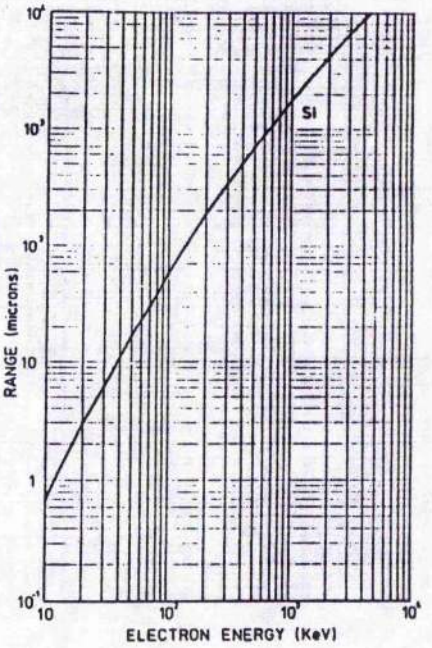

Figure 4.

It can be noted, however, that even at the lower energy of 11 keV it is evident that a solitary electron is all that should be required to overcome CCD and photocathode noise and give an adequate signal-to-noise ratio for the detection of the estimated signal level.

The dynamic range and linearity are not of primary relevance here because it is necessary to determine only whether a signal is present in a pixel of the CCD. For this reason, signal induced noise has also been discounted. A fully saturated pixel will, however, store approximately 10^7 electrons and hence for 11 keV electrons a dynamic range of greater than 5×10^3 should be achievable.

Photocathode (tube) noise will be responsible for one or two detectable events per scan but, as these will be weak signals of a random nature, repetitive signal recording and processing should allow them to be identified.

Construction

It is proposed that the tube will be of the metal and ceramic construction described previously[2,3] in order to benefit from the improved manufacturing tolerances and ruggedness that this technique has to offer. It is recognised, however, that some further optimisation of the tube processing procedures is still required. In particular slight impurity contamination can impair cathode sensitivity and lifetime. The sustained high bake-out temperatures that are normally necessary during tube processing could in turn exacerbate problems relating to fabrication with internally mounted CCD arrays. Some research has been reported[4] in this field, but it must be noted that the image tubes were processed at reduced temperature.

Conclusion

From these analyses we can conclude that sufficient gain is present in the photodiode, under electron excitation, to achieve an acceptable signal-to-noise ratio for the low signal intensities associated with a spaceborne laser ranging system. Thus any preamplification involving, for example, a microchannel plate (MCP) would both reduce the dynamic range, and perhaps more seriously, a MCP would have associated operating effects which are likely to lead to reduced signal-to-noise ratio. Amplification after the scanning process in any case, means that a large area of the amplifier will become a source of noise which is transferred directly into the input of the CCD. In addition, it may be noted that while it is essential to cool the detector to reduce its noise contribution, it would not appear necessary to use temperatures below -40°C and image tube photocathode cooling may not be required.

Acknowledgements

The support of this work by ESTEC/ESA on Contract No. 6223/85/NL/PR(SC) is gratefully acknowledged.

* Mailing address: W Krause
Space Systems Group,
Messerschmitt-Bölkow-Blohm Gmbh,
P.O. Box 801169, D-8000 Munich 80,
Fed Rep Germany

References

1. Lutz, H., Krause, W. and Barthel, G., "High-precision two-colour Spaceborne Laser Ranging System for Monitoring of Geodynamic Processes", Space 2000 (Edit: L. G. Napolitano) Amer. Inst. of Aeronautics and Astronautics, New York, pp236-254, 1983.

2. Sibbett, W., Sleat W.E. and Krause W., "Circular Scan Photochron Streak Camera for Spaceborne Laser Ranging Applications", Proc. E.S.A. Workshop on Space Laser Applications and Technology E.S.A. Sp-202, pp171-174, 1984.

3. Sibbett, W., Sleat, W.E., Krause, W. and Taylor, J.R., Photochron IIC Streak Tube for 300 Mhz Circular-Scan Operation", Proc. 16th Inter. Cong. on High Speed Photography and Photonics, (Strasbourg) Vol 491, pp76-81, 1984.

4. Lemonier, M., Richard, J.C., Piaget, C., Petit, M. and Villot, M., "Photon-in and Electron-in CCD Arrays for Image Readout in Tubes", IEE Conference on Photoelectronic Imaging, Conf. Pub. No. 253 pp74-77, London, 1985.

5. "Photomultiplier Tubes", EMI Brochure P001/TP70. Thorn-EMI Electron Division, Ruislip, Middx.

6. Carnes, J.E. and Kosonocky, W.F., "Noise Sources in Charge-Coupled Devices", RCA Review, Vol 33, pp327-343, June 1972.

7. Barbe, D.F., "Imaging Devices Using the Charge-Coupled Concept". PROC IEEE Vol 63, No 1, pp38-74, Jan 1975.

8. Kosonocky, W.F., "Charge-Coupled Devices - An Overview". Western Electron. Show and Conv. Tech. Papers, Vol 18, pp2/1-2/20, Sept 1974.

9. "CCD Imaging", ECV publication Tech. Notes Issue 1, June 1982, EEV, Chelmsford, Essex.

10. Endo, Y., Furukawa, A., Matsunaga, Y., Harada, N. and Yoshida, O. "A New Noise Reduction Method for CCD Image Sensors". IEE Conference on Photoelectronic Imaging, Suppl. to Pub. No 253, London, 1985.

ACKNOWLEDGEMENTS

During the course of this project I was extremely fortunate in working with many gifted people from a wide range of research fields and countries. I would first like to thank my research supervisor, Professor Wilson Sibbett for all his guidance, encouragement and for sending me to innumerable conferences in many exotic locations. I am particularly grateful to Dr. Bill Sleat for all his advice, electronics expertise and plain common sense, to Prof. Guofu Chen for introducing me to the CPM laser and to James Wade and Professor Ruduan Zhang for constructing most of the CCD electronics. On the computing side thanks must go Dr. Reg Killean and to Yuping Liu for use of their streak camera modelling programs and to Dr. Jim Lawrence for letting me "borrow" most of his computing equipment. In the development of the electron sensitive CCD I am grateful to Drs C.Claeys and Ingrid Debusschere from IMEC. I would like to thank Dave Walker and Edmund Williams and the other members of the "WS" research group for help when needed. I am indebted to Dave Crust for assistance in the graphical plotting of data, Dr. John Ball for help in the wordprocessing of this thesis and Jim Allan for his photographic expertise. I would also like to thank the technical staff of the department for all their assistance, the Science and Engineering Council for financial support and finally my friends and flatmates for their undying sense of humour .

PUBLICATIONS

1. A.Finch, W.Sibbett, W.E.Sleat, C.Claeys, I.Debusschere, and W.Krause, "Electron sensitive CCD readout array for a circular streak tube," *Solid state imagers and their applications* SPIE **591** 31 (1985).

2. A.Finch, G.Chen, W.Sleat and W.Sibbett, "Pulse asymmetry in the colliding-pulse mode-locked dye laser," J.Mod. Opt. **35** 345 (1988) – paper presented at QE8 (St. Andrews, Scotland 1987).

3. A.Finch, Y.Liu, H.Niu, W.Sibbett, W.E.Sleat, D.R.Walker, Q.L.Yang and H.Zhang, "Recent advances towards a 100 fs–resolution streak camera," in *Ultrafast Phenomena VI* :Springer Series in Chem. Phys. **48** 159 (1988) – paper presented at ICUP'88 (Kyoto, Japan 1988).

4. A.Finch, Y.Liu, W.E.Sleat and W.Sibbett, "Subpicosecond synchroscan operation of a Photochron IV streak camera," Rev. Sci. Instrum. (to be published May, 1989).

Papers presented at ICHSPP XIII (Xian, China 1988) and to be published by SPIE include:

5. A.Finch, Y.Liu, W.E.Sleat, W.Sibbett and G.Chen, "Phase noise limitations in synchroscan streak camera operation."

6. A.Finch, Y.Liu, H.Niu, W.Sibbett, W.E.Sleat, D.R.Walker, Q.L.Yang and H.Zhang, "Development and evaluation of a new femtosecond streak camera."

7. R.Zhang, A.Finch, W.Sibbett and W.E.Sleat, "Streak camera readout systems."

8. G.Chen, A.Finch, W.Sibbett and W.E.Sleat, "Generation and measurement of 19 fs light pulses."

Reprints of papers 2,3,5 are included in the rear and paper 1 in Appendix B.

JOURNAL OF MODERN OPTICS, 1988, VOL. 35, NO. 3, 345–354

Pulse asymmetry in the colliding-pulse mode-locked dye laser

A. FINCH, G. CHEN†, W. SLEAT and W. SIBBETT
Department of Physics, University of St Andrews,
St Andrews, Fife KY16 9SS, Scotland

Abstract. The design and performance characteristics of a group velocity dispersion-compensated colliding-pulse passively mode-locked ring dye laser are discussed. Pulses as short as 19 fs have been observed and analyses of experimental autocorrelations—both intensity and interferometric—together with spectral data that show evidence of pulse asymmetry are presented.

1. Introduction

Since its development in the early 1980s [1] the colliding-pulse passively mode-locked (CPM) dye laser has proved to be an excellent source of ultrashort pulses. Using this type of laser, pulses shorter than 100 fs are readily achieved [1, 2]; the normal pulse-shaping/compression mechanisms of absorber and gain saturation being enhanced by a coherent absorption grating in the passive dye jet which acts to increase laser stability and pulse compression velocities [3, 4]. It is now generally accepted, however, that in order to achieve pulse durations in the tens of femtosecond regime it is imperative to have some control on the net cavity group velocity dispersion (GVD) to actively provide compensation for self-phase modulation (SPM) contributions generated in the dye jets [5]. Adjustment of the SPM is achieved by altering the focal beam power density in the saturable jet, whereas adjustable GVD may be accomplished by means of a sequence of Brewster-angled prisms [6], Gires–Tournois interferometers [7, 8], or a combination of both [9]. Indeed pulses as short as 27 fs have been reported for a ring dye laser cavity that incorporated a four-prism arrangement [10].

In this paper we describe the characteristics of a CPM dye laser, similar in many respects to that reported in [10] and with which pulses as short as 19 fs (figure 1) have been generated. Our analyses of the femtosecond laser pulses indicate that their intensity profiles have distinct asymmetrical features.

2. Laser behaviour

The laser configuration is illustrated in figure 2. The active Rhodamine 6G dye and passive diethyloxadicarbocyanine (DODCI) dye dissolved in ethylene glycol are pumped through standard commercial 250 μm nozzles in a horizontal orientation. The gain and absorber folding sections of the resonator have focusing mirrors of 10 and 5 cm radii of curvature respectively. The pump argon-ion beam (Spectra-Physics 2030) is focused into the gain jet via a separate 7·5 cm radius of curvature mirror.

† Permanent address: Xian Institute of Optics and Precision Mechanics, Xian, P.R. China.

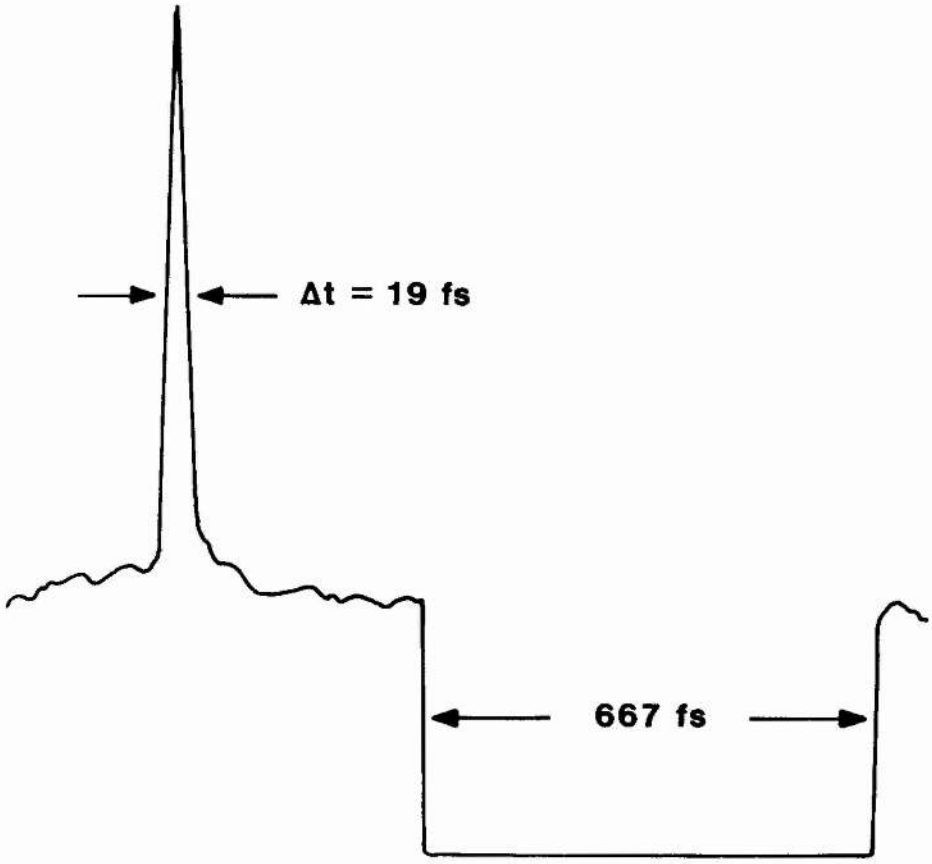

Figure 1. Intensity autocorrelation of a 19 fs pulse.

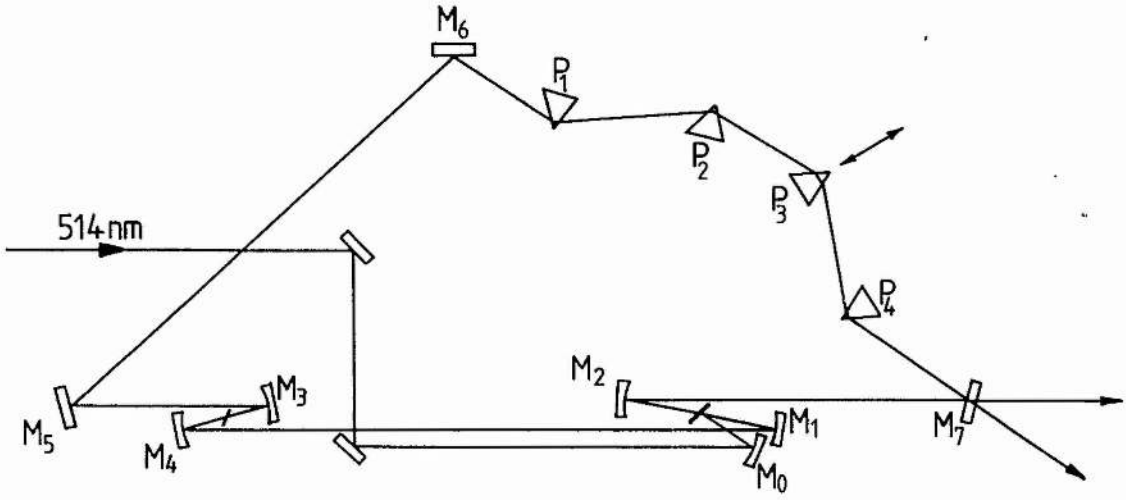

Figure 2. Laser cavity configuration.

With a 2% transmission output coupler M_7 and without any intracavity GVD compensation, typical pulse durations of 70–90 fs at a repetition frequency of 100 MHz and average powers ~ 5 mW per beam are obtained. Although pulses as short as 50 fs have been measured, the stability of the laser was relatively poor and the spectra of the pulses had characteristic longer-wavelength tails extending beyond the peak spectral intensity around 630 nm.

To allow for adjustment of the intracavity GVD, a sequence of four Brewster-angled prisms were incorporated in accordance with a scheme suggested by Fork and co-workers [6]. Since the dye jets had a horizontal orientation, the plane of the prism sequence was orthogonal to that of the rest of the cavity. Prism P_3 was mounted on a translation stage so that the prism-sequence contribution to cavity dispersion could be varied from a negative value, through zero to positive. The separation between P_1 and P_2, and P_3 and P_4 of 27 cm provided a maximum negative GVD contribution sufficient to compensate the positive GVD produced by the cavity optics.

Once the prism system had been inserted, the operating stability of the laser improved significantly. Output power fluctuations were confined to a few per cent (and are attributable to power-supply ripple at the three-phase mains frequency which modulated the argon-ion laser pump power) and pulse durations around 40 fs were reliably obtained.

Pulse durations were measured by both intensity and interferometric autocorrelation techniques [11, 12] using aluminium-coated retroreflectors and a $<100\,\mu$m KDP frequency-doubling crystal. Spectral data were recorded with a scanning monochrometer (1 m Monospek) with an S11 photomultiplier tube or in real-time using a Thomson CSF linear photodiode array.

Table 1 gives a summary of the dominant sources of SPM within the dye jets and the sign of the GVD that is required for compensation. The sign of the chirp which dominates within the pulse has a complex dependence on operating wavelength, energy density in the jet, pulse duration and pulse energy [10, 13]. Figure 3 shows the absorption profile of DODCI as a function of wavelength [14]. Also included on the diagram is a spectrum of a 26 fs pulse obtained from the laser and its position relative to the absorbing species (ground state and photoisomer) in DODCI. It has been argued by Valdmanis and Fork [10] that for pulses in this spectral regime, the Kerr effect and gain saturation will be the dominant sources of chirp. The negative SPM contribution from the DODCI ground-state molecule is small since it is only weakly absorbing at this operating wavelength. Conversely the photoisomer is so strongly absorbing it is saturated by the leading edge of the incoming pulse, yielding a down-

Table 1. Sources of self-phase modulation within CPM laser and corresponding cavity group velocity dispersion required for stable short-pulse operation.

Source	Sign of induced SPM	GVD compensation required
Off-resonant DODCI saturation (long-wavelength side)	Negative (down-chirp)	Positive GVD
Fast Kerr effect in dye solvent (ethylene glycol)	Positive (up-chirp)	Negative GVD
Off-resonant gain saturation (long-wavelength side)	Positive	Negative GVD

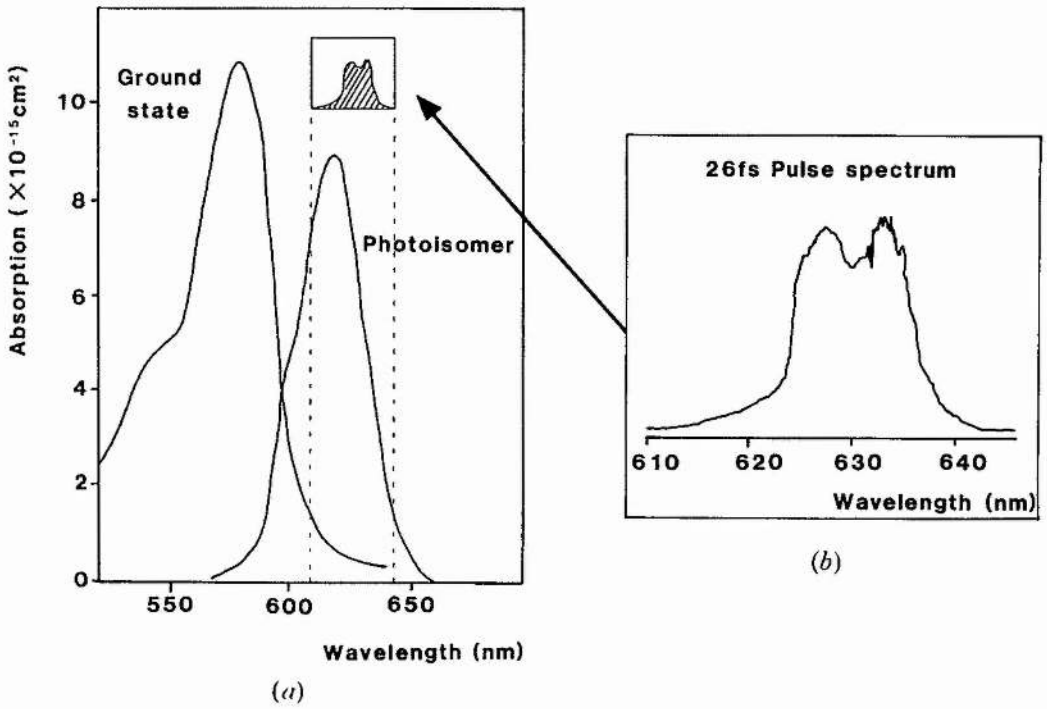

Figure 3. Absorption spectra of (*a*) DODCI molecule shown in relation to (*b*) a measured spectrum of a 26 fs pulse.

chirp there; but for the remainder of the pulse propagation through the absorber jet the photoisomer offers only a small and constant negative SPM. Thus the central region of the pulse (where the pulse intensity changes most rapidly) acquires a large positive SPM or up-chirp due to the Kerr effect within the dye solvent and the trailing edge will see a further up-chirp due to gain saturation. Under these conditions one would expect to see stable operation for excess negative GVD within the cavity but unstable operation for excess positive GVD.

Figure 4 shows interferometric autocorrelation and spectral data taken from the laser for the prism P_3 in three different positions. Figure 4 (*a*) shows the case for excess negative GVD within the cavity. The generated pulse is broad but very stable and the pulse spectrum has a characteristic asymmetry with an extended tail towards shorter wavelengths. Translating the prism P_3 to decrease the negative GVD contribution by increasing the glass path length yields shorter pulses until an optimum pulse duration is reached, which corresponds to the autocorrelation reproduced in figure 4 (*b*). It should be noted that the spectrum is more symmetrical and red-shifted with respect to that of figure 4 (*a*). Further translation of the prism by just 10 μm is sufficient to produce gross fluctuations in output power of the laser and pulse instability, as illustrated by figure 4 (*c*). The asymmetry in the spectral intensity profile also reverses to exhibit an extended longer-wavelength tail, which is characteristic of excess positive GVD in the cavity. This sensitive dependence on GVD is as predicted by Martinez and Fork [15] and closely resembles the behaviour of their laser reported in [10].

The results are consistent with the theory that under these operating conditions, positive SPM is the dominant chirp in the pulse. The laser output pulse duration and power stability shows a strong sensitivity to jet position which further confirms the

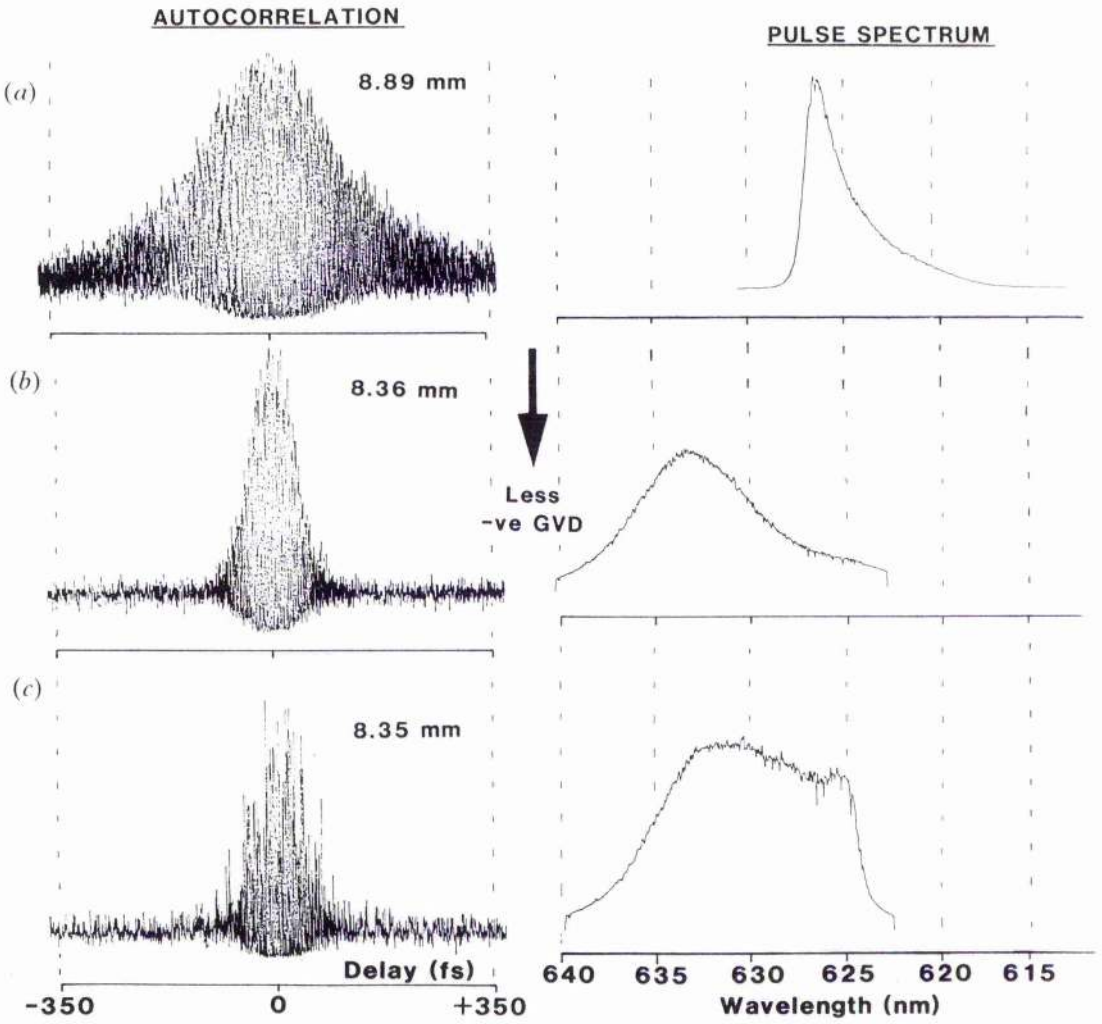

Figure 4. Interferometric autocorrelation and spectral data showing CPM laser behaviour as a function of relative prism position (indicated in mm on each figure): (*a*) condition of excess negative GVD in cavity; (*b*) optimum position yielding shortest pulse; (*c*) condition of excess positive GVD in cavity.

theory that in this short-pulse regime SPM and GVD interaction are the main pulse-shaping mechanisms. More evidence for this is provided at higher pump powers where the laser can show unidirectional operation and yet still maintain a short-pulse output (~ 40 fs). When this lasing action is deliberately interrupted, pulse evolution proceeds afresh with counter-propagation of intracavity flux and the laser will then return to unidirectional behaviour. This indicates that in the short-pulse regime the coherent interaction within the DODCI jet plays a rather minor role whenever the mode-locking becomes sufficiently well established.

3. Pulse-shape fitting

It was immediately apparent from our experimental spectral and autocorrelation data that for pulse durations less than ~ 100 fs the bandwidth–duration ($\Delta\nu\Delta t$) products were significantly less than the expected value of 0·315 which applies to sech^2 intensity pulse profiles. Moreover, when sech^2 intensity profile fits were

attempted on the measured data, the agreement between experimental and theoretical autocorrelations was poor, as illustrated in figure 5 (*a*), which corresponds to a 33 fs pulse. Figure 5 (*b*) shows the corresponding fit assuming a single-sided exponential intensity profile ($\Delta\nu\Delta t = 0{\cdot}110$) where again a poor match is obvious. A likely inference was that the small value of $\Delta\nu\Delta t$ indicated some degree of asymmetry in the laser pulse although its functional form was not as severe as that of the single-sided exponential. To support this theory the general pulse function displayed in table 2 was used for test fitting purposes. It is a function for which the

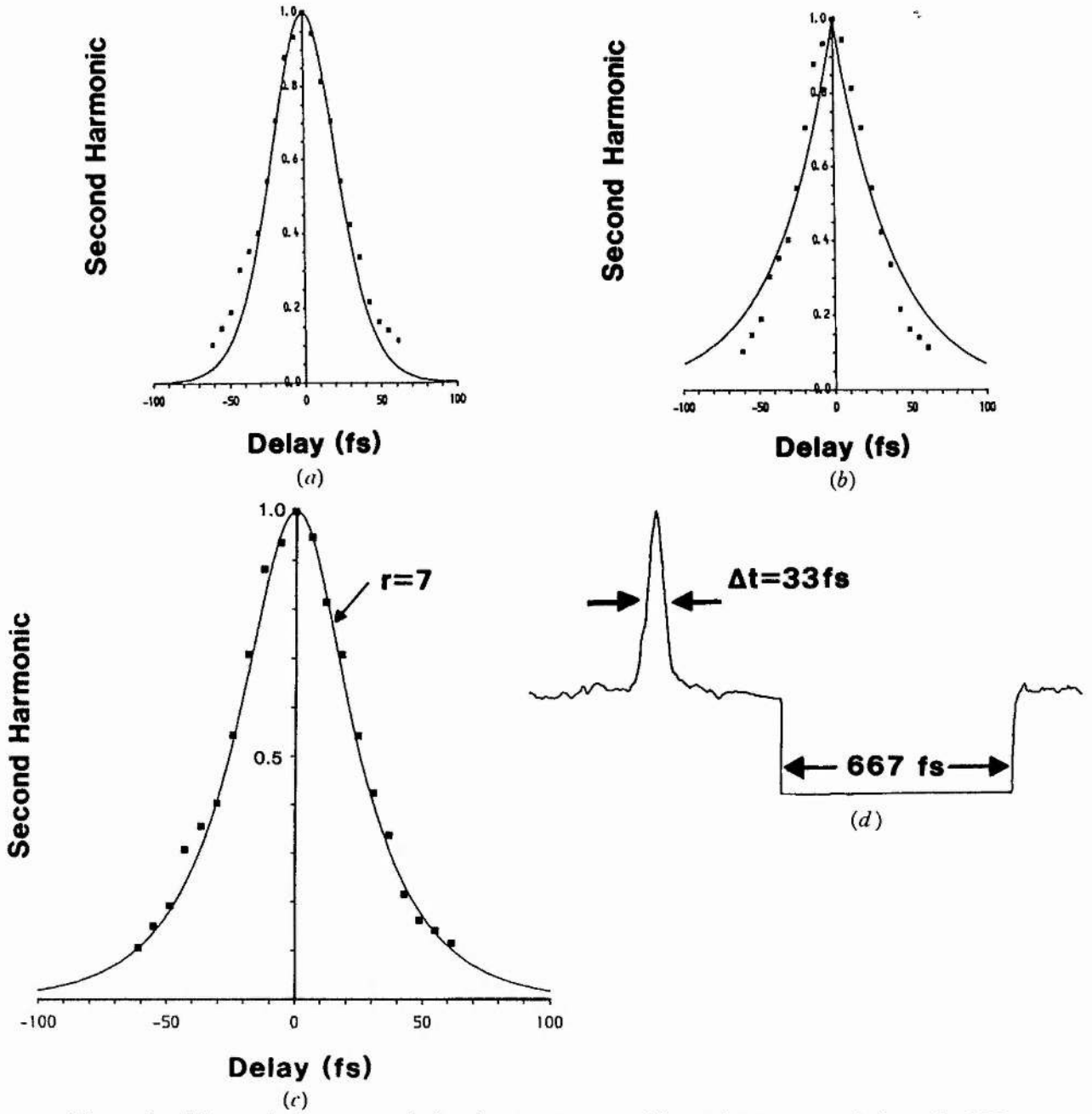

Figure 5. Theoretical autocorrelation fits to a measured intensity autocorrelation of a 33 fs pulse: (*a*) fit assuming sech^2 intensity profile; (*b*) fit assuming single-sided exponential intensity profile; (*c*) fit assuming asymmetrical pulse shape ($r = 7$); (*d*) measured autocorrelation from which data points were obtained.

Table 2. Asymmetric pulse function used in theoretical analyses of measured autocorrelation and spectral data. Bandwidth–duration products together with autocorrelation correction factors are also given.

Asymmetric pulse function: $E(t)=\dfrac{2}{[\exp(-t)+\exp(rt)]}$

r	$\Delta\nu\Delta t$	$\Delta\tau/\Delta t$ intensity	$\Delta\tau/\Delta t$ interferometric
1	0·315	1·543	1·897
4	0·260	1·554	1·920
7	0·221	1·571	1·954

asymmetry increases with the value of r. Some specific $\Delta\nu\Delta t$ values are shown for given values of r, together with the corresponding correction factors for the intensity and interferometric autocorrelation functions. Figures 6 (*a*)–(*c*) show the corresponding intensity profiles and it can be seen that as r increases, the intensity profile becomes more asymmetrical and the $\Delta\nu\Delta t$ product decreases. As r approaches infinity then $\Delta\nu\Delta t$ approaches the value 0·110, for the single-sided exponential.

Choosing $r=7$ and calculating the theoretical autocorrelation for a 33 fs pulse gives the fit shown in figure 5 (*c*) where close agreement is obtained. Figures 7 and 8 show the interferometric autocorrelations and spectra of 48 and 43 fs pulses, respectively, and the theoretical fits corresponding to $r=4$ and $r=7$ test pulses. Excellent agreement is again achieved and the measured bandwidth–duration products compare favourably with the predicted values. Evidence that these fits do not exactly correspond to the measured pulses is produced when a Fourier transform of the test pulses is taken and superimposed on the measured pulse spectra. This

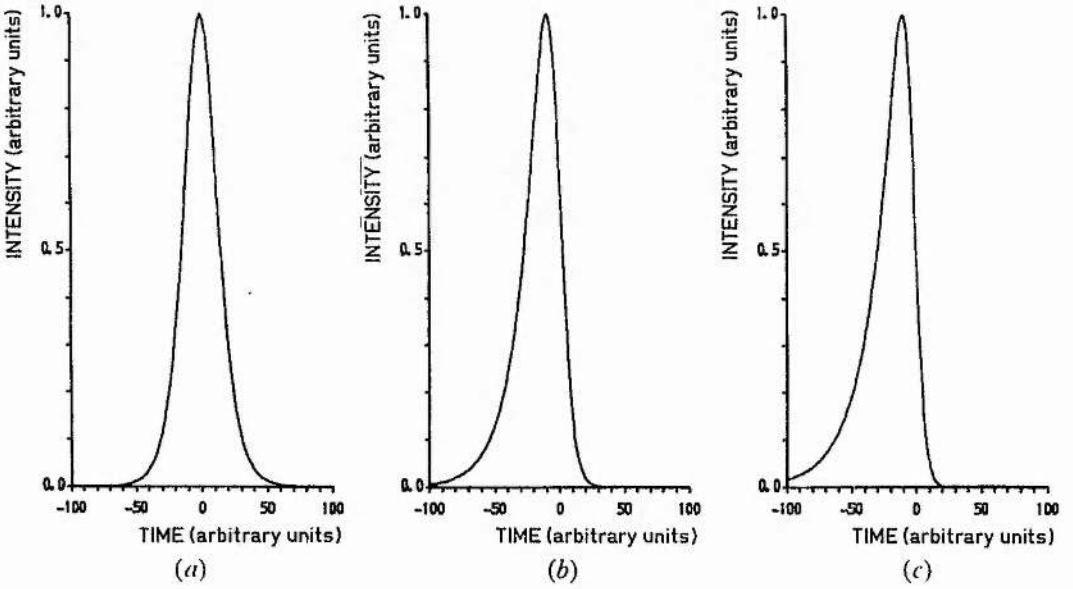

Figure 6. Intensity profiles for different values of r generated from asymmetrical pulse function displayed in table 2: (*a*) $r=1$; (*b*) $r=4$; (*c*) $r=7$.

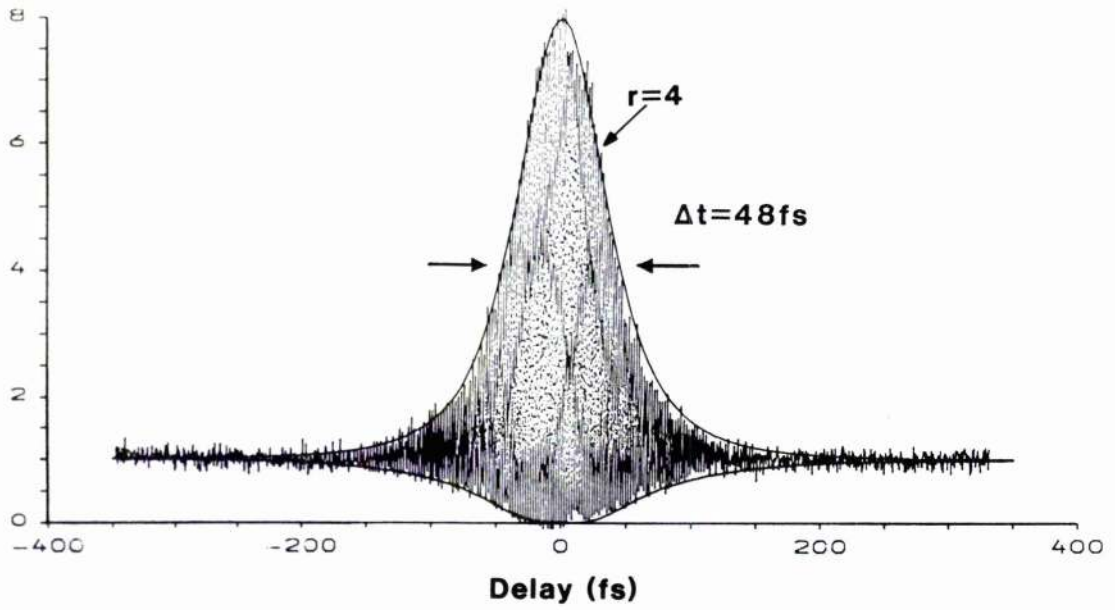

(*a*)

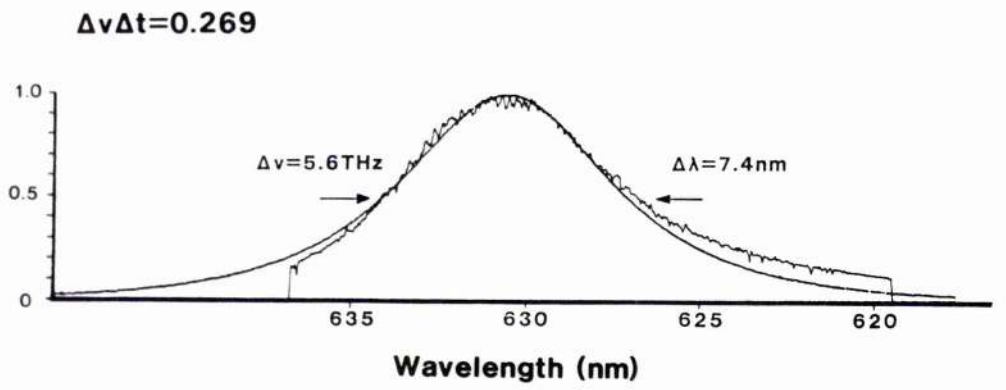

(*b*)

Figure 7. Measured interferometric autocorrelation (*a*) and spectral (*b*) data of a 48 fs pulse with the corresponding theoretical autocorrelation fit assuming an $r=4$ asymmetric pulse function.

indicates that there is a small asymmetry in each pulse spectrum, which implies the existence of a small frequency chirp in the pulse arising from excess negative GVD compensation in the laser cavity. This will lead to the discrepancy between measured and theoretical $\Delta\nu\Delta t$ values but will not significantly affect the autocorrelation fits.

Figure 7 (*a*) provides a clear illustration of the fringes in the interferometric autocorrelation. Remembering that the delay between two successive fringes corresponds to one optical cycle (2·1 fs in this case) this autocorrelation shows directly that there are only a small number of optical cycles within these short pulses. The sensitivity of interferometric autocorrelations to pulse shape and chirp and their inherent self-calibration make such measurements a powerful technique for pulse characterization on the femtosecond scale. Indeed we would contend that for pulse durations below 50 fs interferometric detail is vital if unambiguous results are to be obtained.

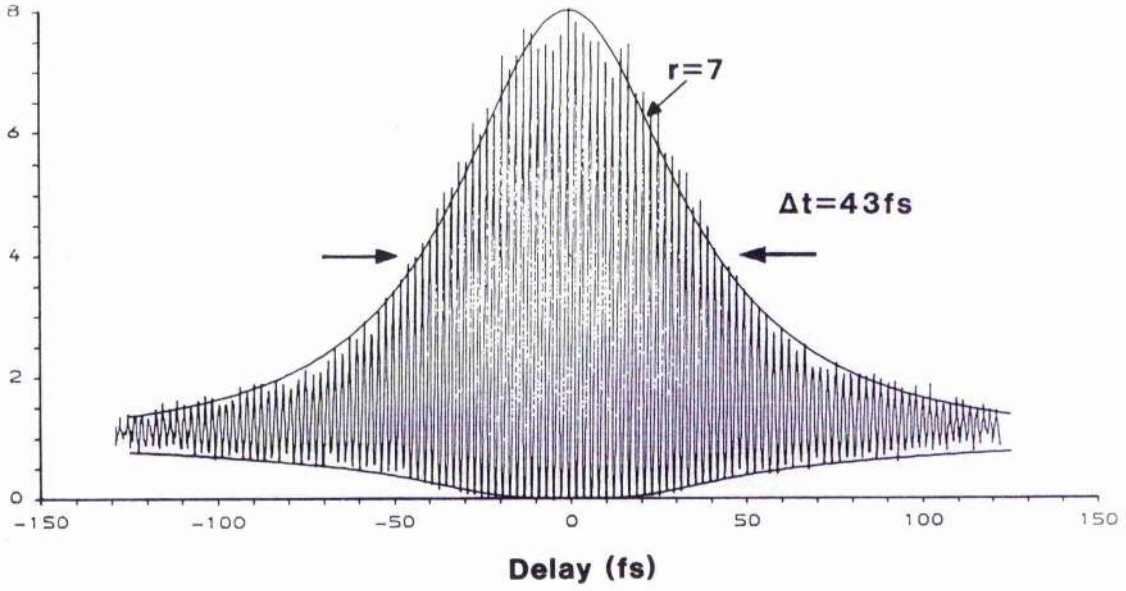

(*a*)

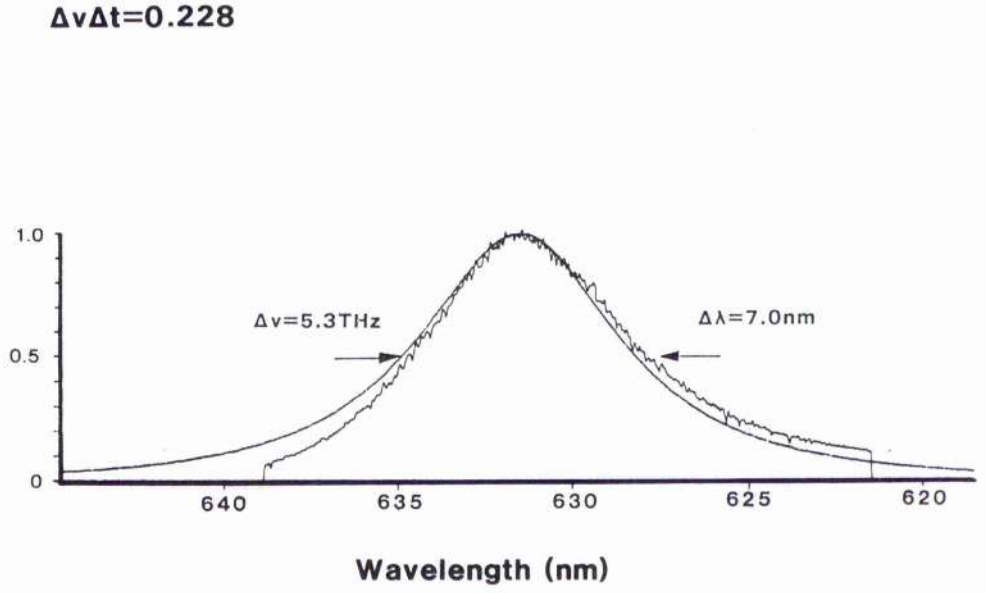

(*b*)

Figure 8. Measured interferometric autocorrelation (*a*) and spectral (*b*) data of a 43 fs pulse with the corresponding theoretical autocorrelation fit assuming an $r=7$ asymmetric pulse function.

4. Conclusion and discussion

The CPM dye laser has been shown to display the behaviour which is consistent with dominant frequency-chirp arising from positive SPM due to the Kerr effect in the dye solvent and gain saturation. Strong evidence is also provided to suggest that the output pulses from our laser have asymmetrical intensity profiles: whether the leading or trailing edge is steeper has yet to be determined. We plan to use extracavity chirp adjustment and to extend the pulse-fitting techniques to take full account of

frequency-chirp and thus deconvolve the measured autocorrelation data. Also, by adopting cross-correlation techniques similar to those developed by Diels *et al.* [11, 16] we will be able to determine most of the relevant information concerning the laser pulses. By means of such studies we should be better equipped to identify the source of the observed pulse asymmetries. Several theories are being examined at present including variable chirp sign across the pulse (as mentioned in § 1) and its interaction with GVD of a specific sign. The concept of extreme gain saturation leading to severe depletion of the pulse trailing edge is another possibility.

Such investigations should significantly advance the understanding of the CPM laser and ultrashort pulse generation *per se*.

Acknowledgments

The specialist assistance of Ruduan Zhang and his development of the photodiode-array imaging system is gratefully acknowledged. The overall funding for this project and a CASE studentship (A.F) was provided by the Science and Engineering Research Council and financial support by The Royal Society and Chinese Academy of Sciences for one of us (G.C.) is also acknowledged with thanks.

References

[1] Fork, R. L., Greene, B. I., and Shank, C. V., 1981, *Appl. Phys. Lett.*, **38**, 671.
[2] Fork, R. L., Shank, C. V., Yen, R., and Hirlimann, C. A., 1983, *IEEE Jl quant. Electron.*, **19**, 500.
[3] Dietel, W. E., Kuhlke, D., Rudolph, W., and Wilhelmi, B., 1982, *Picosecond Phenomena III*, Springer Series in Chemical Physics 23 (Berlin: Springer-Verlag), p. 45.
[4] Willson, J. P., Sibbett, W., and Sleat, W. E., 1982, *Optics Commun.*, **42**, 208.
[5] Diels, J. C., Dietel, W., Fontaine, J. J., Rudolph, W., and Willhelmi, D., 1985, *J. opt. Soc. Am.* B, **2**, 680.
[6] Fork, R. L., Martinez, O. E., and Gordon, J. P., 1984, *Optics Lett.*, **9**, 150.
[7] French, P. W., Chen, G. F., and Sibbett, W., 1986, *Optics Commun.*, **57**, 263.
[8] Heppner, J., and Kuhl, J., 1985, *Appl. Phys. Lett.*, **47**, 453.
[9] Kuhlke, D., Bonkhofer, T., and Von Der Linde, D., 1986, *Optics Commun.*, **59**, 208.
[10] Valdmanis, J. A., and Fork, R. L., 1986, *IEEE Jl quant. Electron.*, **22**, 112.
[11] Diels, J. C., Fontaine, J. J., McMichael, I. C., and Simoni, F., 1985, *Appl. Optics*, **24**, 1270.
[12] Mindl, T., Hefferle, P., Schneider, S., and Dorr, F., 1983, *Appl. Phys.* B, **31**, 201.
[13] Miranda, R. S., Jocobovitz, G. R., Brito-Cruz, C. H., and Scarparo, M. A. F., 1986, *Optics Lett.*, **11**, 224.
[14] Dempster, D. N., Morrow, T., Rankin, R., and Thompson, G. F., 1972, *J. chem. Soc. Faraday II*, **68**, 1479.
[15] Martinez, O. E., Fork, R. L., and Gordon, J. P., 1985, *J. opt. Soc. Am.* B, **2**, 753.
[16] Diels, J. C., Fontaine, J. J., Jamasbi, N., Ming Lau, and Mackey, J., 1987, *Proc. CLEO*, Baltimore, paper MD3, p. 14.

Recent Advances Towards a 100fs-Resolution Streak Camera

A. Finch [1], *Y. Liu* [2], *H. Niu* [2], *W. Sibbett* [1], *W.E. Sleat* [1], *D.R. Walker* [1], *Q.L. Yang* [2] and *H. Zhang*[2]

1 J.F. Allen Physics Research Laboratories, Department of Physics and Astronomy, University of St. Andrews, North Haugh, St. Andrews, Fife KY16 9SS, Scotland, U.K.
2 Xian Institute of Optics and Precision Mechanics, Xian, China.

1. Introduction

In view of the generation and application of laser pulses in the femtosecond regime it has become necessary to further improve the performance of linear-response streak cameras. The approach that we have taken involves several refinements to a previous design of electron-optical streak tube [1]. These include (i) a photocathode having reduced photoelectron energy distribution, (ii) optimised electron-optical lens configuration, (iii) ultrahigh-sensitivity travelling-wave deflection arrangement and (iv) high quantum-efficiency phosphor screen.

The purpose of this paper is to detail the pertinent design aspects of the tube and present experimental data to indicate that the camera, in its present state of development, has a limiting temporal resolution of approximately 300fs. Design modifications aimed to further improve this resolution to around 100fs will also be briefly discussed.

2. Tube Design and Construction

The new design of tube [2] is represented schematically in Fig. 1 and is based on the electrode configuration of the Photochron IV which has been demonstrated to have a single-shot temporal resolution of 800fs and a synchroscan resolution ~900fs [3,4]. Notable improvements in the new tube design relate to the structure of the photocathode and deflection system. The photocathode is especially thin to minimise any electron emission time distribution and its composition, with increased bandgap, gives rise to a calculated initial electron energy spread of ~100meV at 620nm.

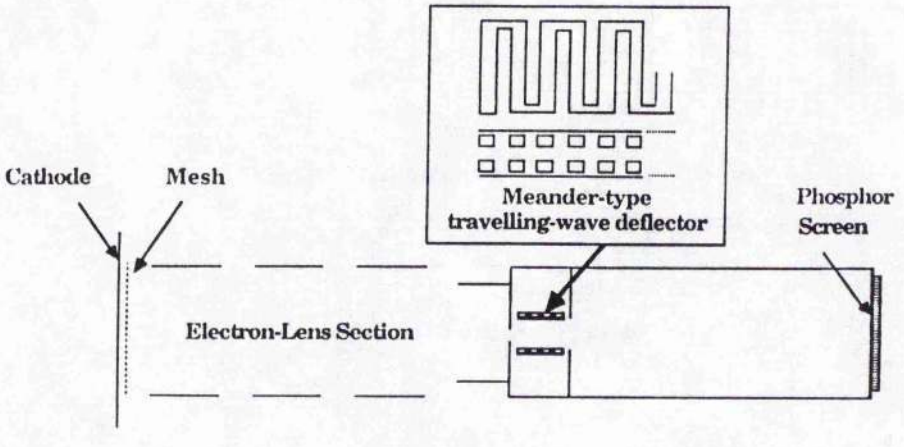

Fig. 1 Schematic of new streak tube

The redesign of the deflection system has proved very successful. By adopting a meander-type travelling-wave configuration which crosses the electron path a total of 23 times, the deflection sensitivity and hence achievable streak speeds have been significantly enhanced. The meander line, constructed from 1mm^2 copper bar has a total length of 4cm, with a 5mm spacing between the two deflector lines. The lines were impedance matched to the 50Ω drive cable via a tapered transmission line inside the image tube and a 50Ω termination was externally connected to the deflector system. For this arrangement the bandwidth of the deflector network exceeded 2.5GHz, yielding an experimentally measured static and dynamic deflection sensitivity of 8.5cm/kV, with streak speeds of 2×10^{10}cm/s.

The operating voltages of the tube photocathode and mesh were −8kV, −3kV respectively relative to the grounded anode. This gave, for a mesh to cathode spacing of 1.2mm, an electric field in the vicinity of the photocathode of ~40kV/cm and an electron-optical magnification of 2. A static limiting spatial resolution of 50 lp/mm was observed at the output phosphor screen. The enhanced quantum efficiency of the phosphor implied a reduced photoelectron current requirement and therefore minimised possible space charge effects.

3. Dynamic Operation

The experimental arrangement that has been employed in the assessment of the single-shot streak performance of the camera is shown in Fig. 2. The image from the streak tube output screen was fibre-optically coupled to a microchannel plate intensifier which provided a luminous gain of 10,000 and a spatial resolution of ~50 lp/mm at its photocathode. This was compatible with the dynamic performance of the streak tube. Ultrashort pulses from a colliding-pulse, passively mode-locked ring dye laser [5] were employed directly as test optical signals and the streak images were recorded using an optical multichannel analyser.

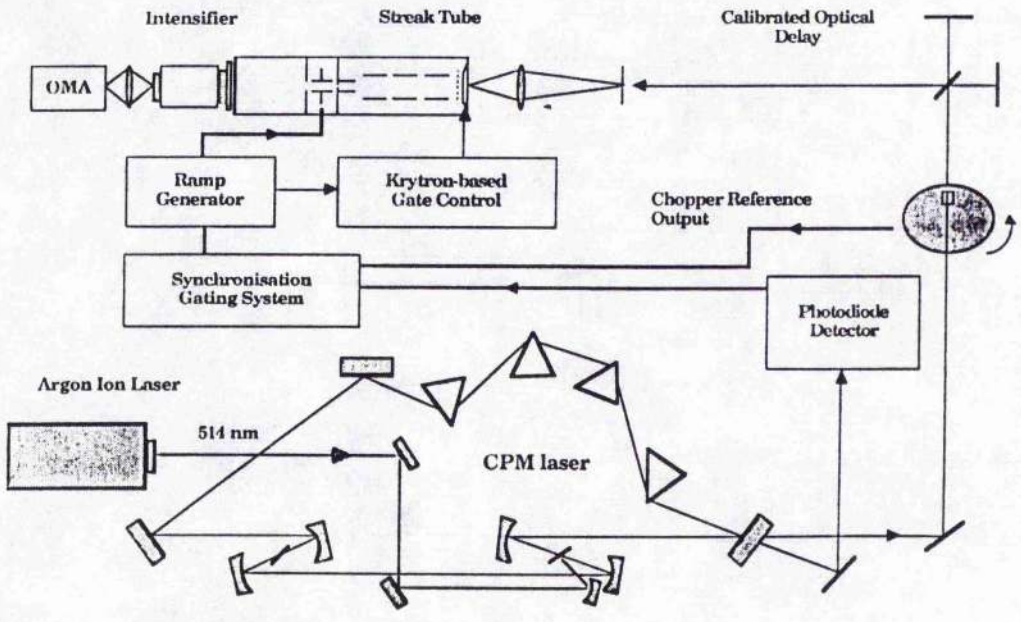

Fig. 2 Experimental arrangement

A double avalanche transistor chain generated a differential voltage ramp of 3kV in 1.5ns across the deflector. An initial problem encountered with this circuit was its slow recovery time (1/e point ~800μs) which tended to generate an intense "fly-back" on the streak camera output. This masked any streaked image, even when the input light signal was mechanically chopped. By applying an appropriate electronic gating signal to the photocathode it was possible to turn off the camera immediately after streaking. This method effectively provided single pulse selection and, as a result, no external Pöckels cell arrangement was required.

The CPM laser when operated deliberately with excess negative group velocity dispersion in the cavity produced pulses of ~150fs duration with a central wavelength of ~630nm and energies that were suitable for recording purposes. Typically, the pulse energies were ~20pJ per pulse at the input slit. In preliminary studies the measured temporal resolutions were around 500–600fs and were found to be limited by a dynamic defocusing effect from the deflector network. This was found to result from slight asynchronism in the switching characteristics of each transistor chain which gave rise to non-symmetric ramp generation. By optimising focus voltages during streaking this effect could be eliminated. Under these optimal operating conditions the temporal resolution was substantially improved to within the range of 300-400fs and the streak result reproduced in Fig. 3 shows intensity profiles which indicate a temporal resolution around 300fs. [The background noise is due to light transmitted through the photocathode which illuminated the back of the phosphor.]

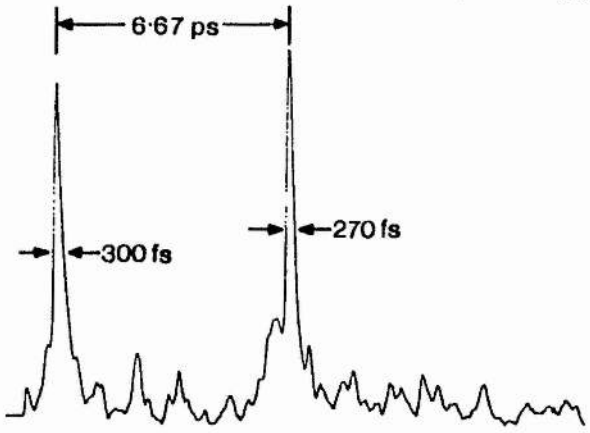

Fig. 3 Intensity profiles of recorded streak images for an input pulse separation of 6.67 ps.

4. Conclusions

The measured dynamic performance of this femtosecond streak tube compares well with the theoretical prediction of ~250fs for the applied operating voltages. With improved tube designs it is hoped to operate at higher cathode voltages and generate higher electric fields in the vicinity of the photocathode by transient voltage pulsation of the mesh. The significant advantages of travelling-wave deflection are obvious; high streak scan speeds have been achieved with comparatively small ramp voltages without the need to resort to laser pulse amplification and Auston-type switching elements. The single-shot/gating system reported here proved highly convenient giving repeatable streak results with a jitter of less than 50ps. It is our intention to use this camera system to directly study "solitonic" effects [6] in the CPM laser.

Acknowledgements

The support of this collaborative programme by The Royal Society and The Chinese Academy of Sciences is gratefully acknowledged. Acknowledgement is also made for personal support as a Chinese Royal Fellow (Y.L) and for visits (H.N, Q.L.Y) by The Royal Society and The Chinese Academy of Sciences. Two of us (A.F and D.W) express gratitude for CASE studentship support by the Science and Engineering Research Council.

References

1. W. Sibbett, H. Niu and M.R. Baggs: Rev. Sci. Instrum., 53, 758 (1982)
2. Y. Liu, H. Niu, Q.L. Yang and H. Zhang: Proc. 5th National Conf. on High Speed Photography and Photonics, China (1985)
3. M.R. Baggs, R.T. Eagles, W. Margulis, W. Sibbett and W.E. Sleat: Adv.Electron. and Electron Phys., 64B, 617 (1985)
4. A. Finch,W.E. Sleat and W. Sibbett: Rev. Sci. Instrum. (in press)
5. A. Finch, G.F. Chen, W.E. Sleat and W. Sibbett: J. Mod. Opt., 35, 345 (1988)
6. F. Salin, P. Grangier, G. Roger and A. Brun: Phys. Rev. Lett., 56, 1132 (1986)

Phase noise limitations in synchroscan streak camera operation

A. Finch, Y. Liu*, W.E. Sleat,W. Sibbett and G.Chen*

J.F.Allen Physics Research Laboratories, Department of Physics and Astronomy,
University of St. Andrews, North Haugh, St. Andrews, Fife, KY16 9SS, Scotland, U.K.
*Permanent address: Xian Institute of Optics and Precision Mechanics, Xian, China

ABSTRACT

A numerical assessment of the role of phase noise in the synchroscan deflection signal and its effect on achievable streak camera temporal resolution is detailed and tested experimentally. The circuitry employed in the synchroscan streak operation of the Photochron IV camera system is described. The experimental performance of two synchronisation systems, (i) a *passive* configuration whereby the deflection signal is derived directly from a mode-locked pulse source and, (ii) an *active* system incorporating a tunnel-diode oscillator phase-locked to the laser, have been experimentally compared. By taking phase noise into account the circuitry has been appropriately optimised and this has permitted the demonstration, in synchroscan mode, of a limiting temporal resolution of 930 fs for the Photochron IV synchroscan-camera. Techniques to further enhance this performance and extend synchroscan operation further into the sub-picosecond domain will be outlined.

1. INTRODUCTION

The generation and application of ultrashort optical pulses over a wide range of operating wavelengths has advanced significantly over recent years. With such developments there is the associated need to enhance monitoring devices such that these refined laser sources may be optimised and conveniently applied. To this end progress has been made in linear diagnostics with the existence of electron-optical streak image tube designs having theoretical temporal resolutions in the 100fs regime[1]. Experimental single-shot evaluation of cameras incorporating such tube structures[2] have demonstrated temporal resolutions of less than 300 fs, but in synchroscan operation the best reported results to date[3] imply a temporal resolution of 1.2 ps. The purpose of this paper is to examine the limiting factors on realtime streak operation and to discuss the methods that we have employed to significantly improve realtime synchroscan performance of the Photochron IV streak tube[4,5] (see Fig. 1) and thereby obtain instrumental functions of better than 1ps.

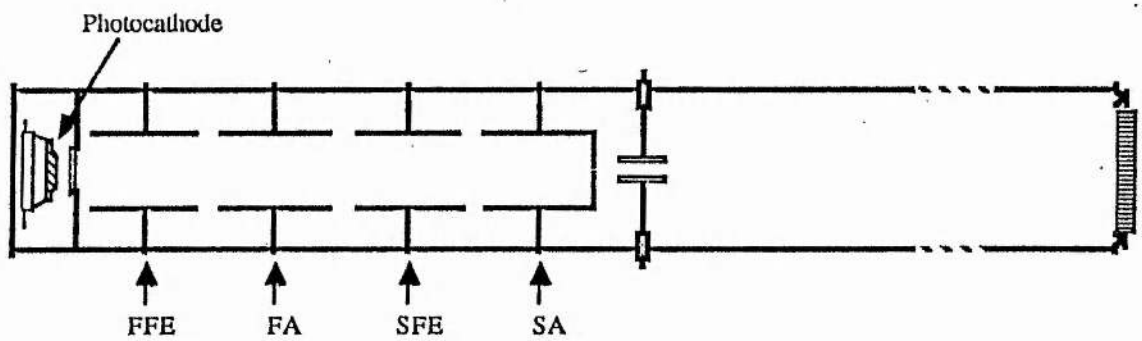

Figure 1. Schematic of Photochron IV streak tube. FFE=First Focus electrode, FA= First Anode, SFE=Second Focus Electrode and SA= Second Anode.

2. SYNCHROSCAN OPERATION

Continuous wave mode-locked lasers generate pulses at a constant repetition rate and are therefore ideally suited for monitoring with synchroscan streak methods. Application of a sinusoidal waveform to the deflector system which is in synchronism with the modelocked pulse train causes the streak pulse image to be constantly overwritten on the phosphor. The relatively long decay time of the phosphor yields integration of image signal and hence effectively provides gain. As a consequence it is possible to detect extremely weak, incoherent optical events eg. time-resolved monitoring of laser-induced fluorescent decay from various dye species[6]. Space charge effects within the tube are insignificant in this mode of operation and so large dynamic ranges are available.

To allow integration of the streak images on the phosphor screen without loss of temporal resolution, the precise synchronisation of the deflecting signal to the repetition frequency of the laser is vital. However, the synchronicity is influenced by the presence of any phase noise in the deflecting sinusoid and so all phase noise sources must be traced and their influence minimised. The problem of pulse-to-pulse jitter in the laser is another possible limiting factor, but we believe this to be negligible in the particular case of a properly passively mode-locked test laser source.

The synchroscan system that has been developed most recently has two operating configurations: either a passive synchronisation system whereby the deflection signal is generated directly from the output of a photodiode illuminated by the laser, or an active system whereby the photodiode output initially triggers a tunnel-diode oscillator. Each will be discussed in turn and the experimental performance data are then compared.

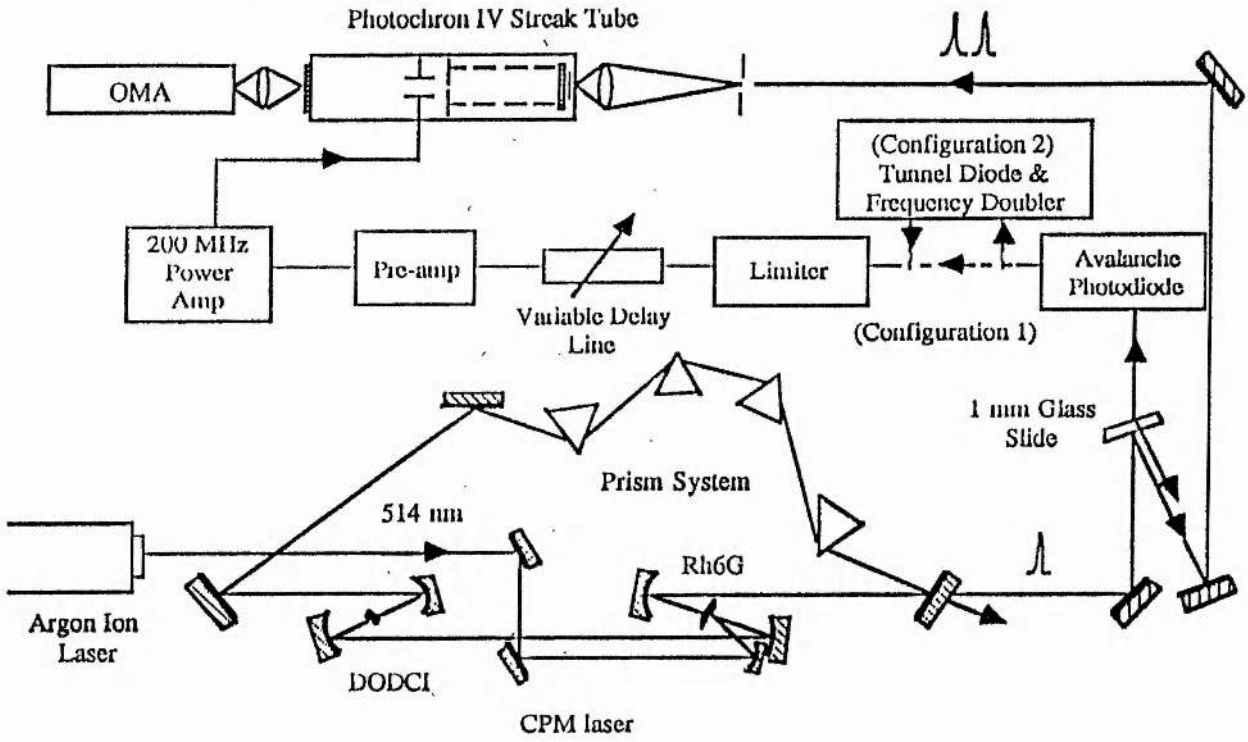

Figure 2. Experimental set-up.

The experimental set-up employed during our investigations is shown schematically in Fig. 2. The test laser source was a colliding-pulse, passively mode-locked (CPM) ring dye laser with the standard Rh6G and DODCI combination of gain/absorber dyes and a 4-prism sequence to control intracavity group velocity dispersion (GVD)[7,8]. Generally the operating wavelength was around 630 nm where the pulse durations were typically 30-40 fs. Synchronisation was initially achieved directly from the laser pulse train. For the passive synchronisation system the laser signal was directed onto a fast avalanche photodiode (risetime < 250ps) and the electrical output passed through a 200 MHz bandpass filter. In this case we are using the fact that a train of impulses separated by a constant time period, T (the round-trip time of the CPM laser) transforms into frequency space as a comb of Fourier components separated by $1/T$. There is an associated roll off in the higher frequency amplitudes and this is a function of the electrical pulse width and for the case of the photodiode employed the 3dB point occurred at ~2.5 GHz. Output signal from this filter was fed through an electronic limiter to amplify the synchronisation signal and to effectively remove any laser-related amplitude fluctuations. Subsequent to this the 200 MHz filtered signal was passed via a variable delay line and a broadband preamplifier to a tuned power amplifier and then to the deflectors of the Photochron IV streak tube. The deflectors were a constituent part of a resonant circuit (Q>50) which allowed optimum inductive coupling to be achieved for drive powers in excess of 15 W.

An alternative scheme employed for synchronisation involved only a slight modification of the above set-up and is also represented in Fig. 2. This so-called active synchronisation involved the replacement of the 200 MHz input filter by a tunnel diode oscillator. The tunnel diode, which has an intrinsic negative resistance, was biased just below its oscillation threshold and formed part of a resonant circuit designed to free run at around 100 MHz. The electrical pulse train from the photodiode, when applied to the bias line, was sufficient to drive the tunnel diode into oscillation such that it was precisely phase-locked to the laser pulse train. The signal from the oscillator was subsequently amplified and frequency-doubled prior to injection into the limiter stage as before.

Two calibration light pulses, separated by 10ps, were obtained as quasi-normal reflections from a 1mm thick glass slide placed in the beam path and these were directed onto the camera input slit as illustrated.

3. PHASE NOISE SOURCES AND EFFECTS

There are several possible sources of phase noise in the synchronisation circuitry; part is laser-related and part is generated internally in the electronics. Laser pulse train amplitude fluctuations are monitored as a modulation in the initial photodiode electrical signal. This will present only a minor limitation on achievable temporal resolution because the high degree of overscanning at the phosphor implies a large region of scan linearity and thus such modulation will have only a minimal effect on streak velocity. Any drive amplitude fluctuation is effectively removed by the action of the limiter but it is our belief that such limiting action actually introduces phase modulation. The FET amplifier outputs within the limiter are driven into varying degrees of saturation dependent upon input signal level and such saturation generates a varicap effect within the amplifier which has some relation to input amplitude. This will cause phase/frequency modulation to appear in the carrier and so although the laser source is inherently stable in terms of phase noise severe constraints are placed upon the constancy of its pulse train amplitude for the passive synchronisation technique.

The tunnel-diode system does not have this sensitivity because it acts as a narrow bandpass filter which effectively removes the amplitude modulation sidebands from the carrier signal. However, there will be an associated phase noise related to pulse train amplitude fluctuations due to the variable triggering point such fluctuations would induce, but this will be of a lesser effect than the passive impedance modulation effect described above. The active system also has the additional advantage over the passive counterpart that relatively high signal levels are maintained throughout and thus the system has a improved signal-to-noise ratio at the input. It will also be less susceptible to electromagnetic interference which can be a problem with the high gain and high deflection powers employed. Fundamental noise sources, eg. Johnson noise in the input stage, should also be less influential in the active system which has a lower source resistance, although it is difficult to quantify this figure for the two systems being evaluated.

To determine the effect of such noise sources on the achievable temporal resolution during synchroscan operation a detailed theoretical analysis has been performed. The input drive signal is treated as a single component of frequency f_0 which sits on a noise floor having an instantaneous amplitude $V_n(t)$ and random fluctuation (See Fig. 3a). The noise floor is assumed to originate from many sources but can be taken to have a uniform spectral distribution which will be tailored by the tuning characteristics of the circuit, T(f). (This is not necessarily true for a nonlinear limiting circuit but for the purposes of this preliminary analysis this will be ignored.) The instantaneous integrated deviating voltage is given by:

$$V_N(t) = \int_0^\infty V_n(t).T(f).\exp\{j[\varnothing(f,t)]\}df \qquad (1)$$

where $V_n(t)$ is the instantaneous amplitude of a noise sideband frequency component at frequency f and $\varnothing(f,t)$ is its instantaneous phase. T(f) is the tuning characteristic of the electronic circuit which will act to tailor the noise floor frequency distribution. Effectively $V_N(t)$ is the sum of a continuous set of uncorrelated oscillators weighted by the bandpass response of the system. Evaluation of the distribution of deviating voltages represented in equation 1 is extremely difficult using numerical techniques without knowledge of the noise floor distribution. Nonetheless, since noise content in a signal is often measured in terms of noise power within a given bandwidth it is instructive to represent V_N by a Gaussian distribution:

$$\mathcal{P}[V_N(t)] = \frac{1}{\Delta V_m\sqrt{2\pi}}\exp\left[-\frac{1}{2}\frac{(V_N - V_m)^2}{\Delta V_m{}^2}\right], \qquad (2)$$

where V_m is the root mean square voltage obtained from the noise power appearing at the deflector plates and its variance, $\Delta V_m{}^2$ taken as a fixed percentage of the mean. Hence the instantaneous drive signal applied to the deflector is given by the

sum of the carrier and the deviating noise contribution (as represented in Fig. 3b) such that:

$$V_S(t) = \mathrm{Im.}[V_c \exp\{j(2\pi f_o t)\} + V_N(t)\exp\{j\emptyset\}] \quad (3)$$

where Ø, the phase of the deviating integrated noise voltage, will be uniformly distributed between 0 and 2π. For a particular streak operation the deviating voltage is calculated by a Monte-Carlo method.

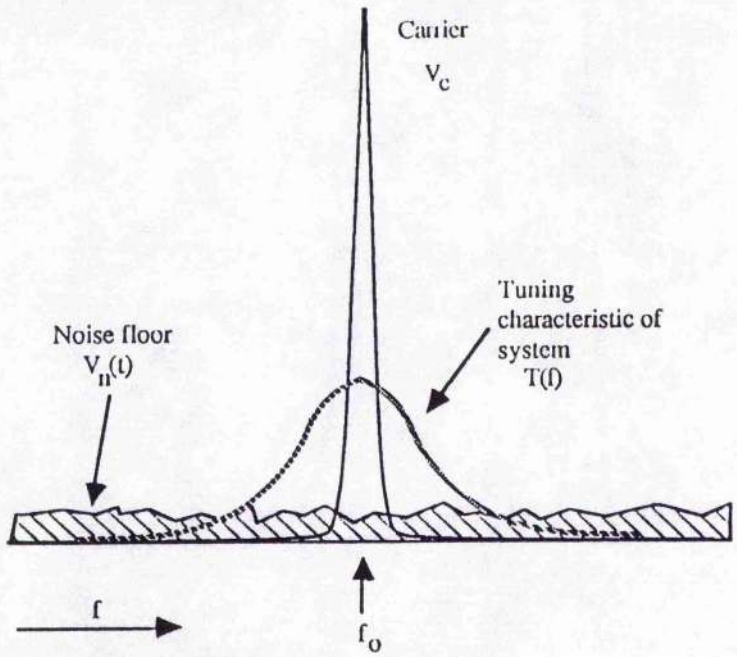

Figure 3a. Representation of phase noise and drive signal in synchroscan circuitry.

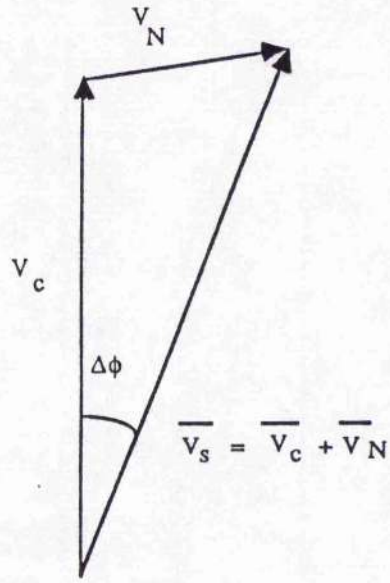

Figure 3b. Vector summation of carrier and deviating noise contribution.

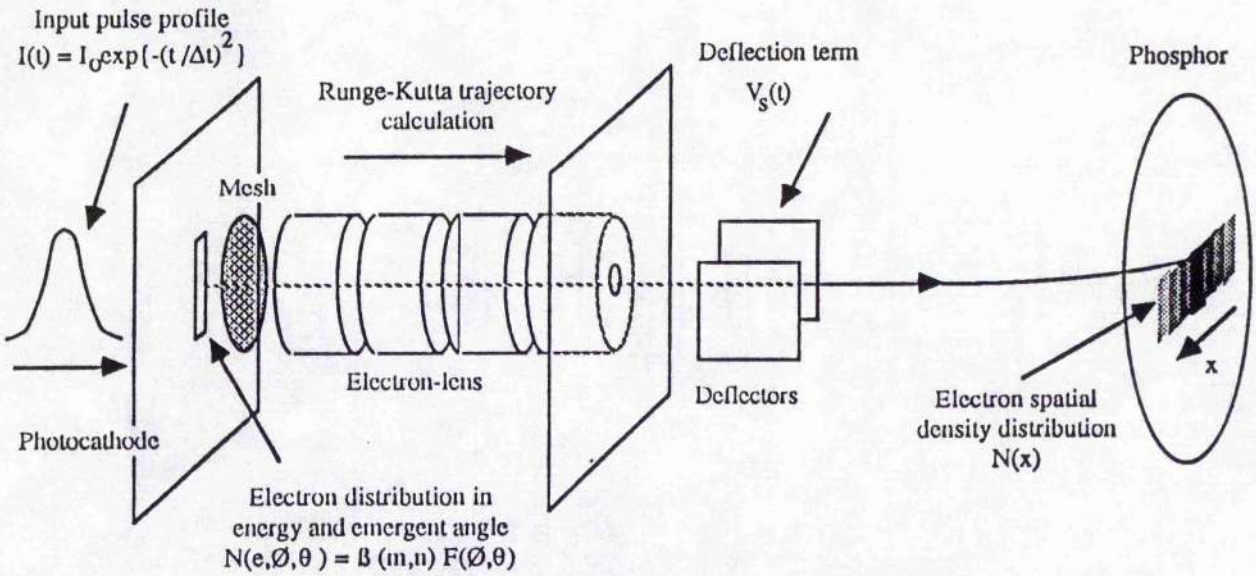

Figure 4. Schematic of calculation process used in computer model.

The electron trajectory within the streak tube was calculated by the Runge-Kutta technique where the potential distribution of the Photochron IV was determined by a finite difference solution of the Laplace equation. A Gaussian input optical pulse profile of duration 300 fs was assumed. The distribution of electron energies leaving the photocathode was modelled by a Beta function and the distribution in exit angles modelled by a uniform and cosine distribution for angles in the photocathode plane and normal respectively. Again a Monte-Carlo technique was used to generate the initial values. For each streak the electron density distribution appearing at the deflectors was computed and the above expression representing the total deflection voltage was then mapped onto this distribution to generate a spatially varying electron density profile at the phosphor screen. The magnitude and phase of the deviating noise voltage was assumed not to vary as the electron distribution was deflected on the basis that the bandwidth of the deflection system would limit fluctuations to a few megahertz and consequently during the transit time of the electrons through the plates (~0.5 ns) any additional variation of the deviated deflection voltage would be minimal. Provision was made for a second term in the input pulse profile to represent jitter between the laser and the deflection signals. These calculations were then performed over a total of 10^4 streaks and an integrated spatial electron density profile N(x) was generated. With a knowledge of the streak velocity, N(x) was transformed into a temporal spread distribution from which the temporal resolution was deduced. This process was repeated for a range of noise powers. The computational process and the various distribution functions used are summarised schematically in Fig.4.

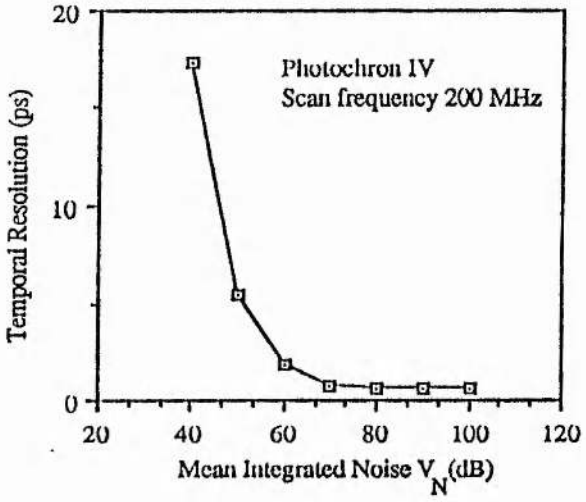

Figure 5. Achievable temporal resolution as a function of integrated noise level with respect to carrier signal.

Figure 5 shows the expected temporal resolution as a function of integrated noise level with respect to the carrier signal ($20\log_{10}(V_C/V_N)$). Note that for noise levels below 80 dB with respect to the drive signal the achievable resolution is almost equal to the tube limiting temporal resolution. Between 80dB and 70dB temporal response is degraded until at 60dB the available resolution is nearly 2.0ps which exceeds the limiting temporal resolution by more than x3.

A further calculation was carried out to represent the direct phase modulation of the carrier signal. In the case of phase modulation, with an index $\Delta\emptyset$ and modulation frequency f_m, the deflection voltage was represented as:

$$Vsum(t) = Im.[V_C \exp[j(2\pi f_0 t + \Delta\emptyset.\cos(2\pi f_m t))]] \quad (4)$$

The results of this calculation are discussed in the next section.

4. EXPERIMENTAL RESULTS

To test the effect of saturation effects in the limiter we took advantage of a interesting property of the CPM laser. When operated with large amounts of excess positive GVD inside its cavity, adjustment of the absorber jet can cause stable production of relatively long (0.5 – 1.0ps) duration pulses and the gross periodic amplitude modulation evident in the mode-locked pulse train (Fig. 6a) leads to a large sideband content in the synchroscan carrier signal (Fig. 6b). Such laser

phenomena have also been reported by other workers and have been ascribed to the propagation of a higher order soliton around the cavity with a characteristic frequency related to the sideband separation[9]. Other workers[10] have suggested that such behaviour is semi-solitonic but cannot be explained by simple nonlinear wave equations. In any case this property provided a convenient means of introducing amplitude modulation of the laser output.

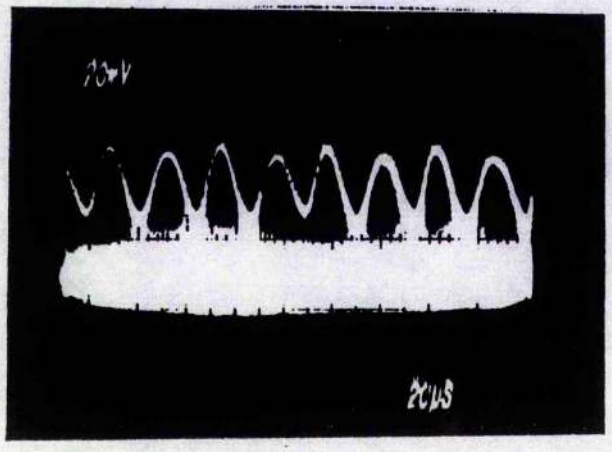

Figure 6a. Gross amplitude modulation of pulse train due to the "soliton effect" in CPM laser.

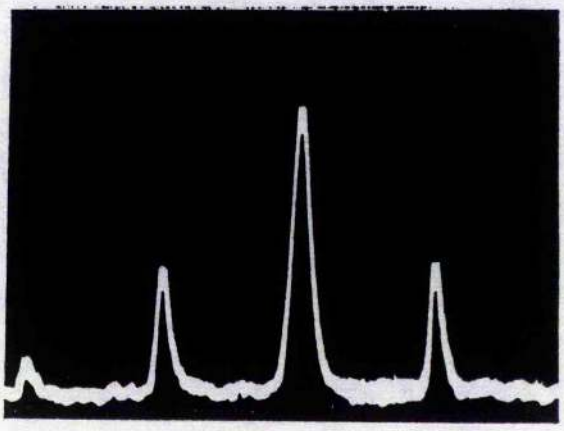

Figure 6b. Associated amplitude modulation sidebands around the 200 MHz component in frequency spectrum (20kHz/div).

By varying the rail voltages of the limiter the level of sideband content applied to the streak camera could be adjusted. Since no amplitude modulation was present after the limiter stage it was assumed that the sidebands represented frequency modulation. This would manifest itself as a sinusoidal phase term in the carrier signal of index $\Delta\emptyset$ and frequency f_m the sideband separation (as represented in equation 5) and the appearance of frequency modulation sidebands either side of the carrier. The relative amplitudes of these sidebands are defined by a Bessel function, J_n of the phase modulation index thus: $V_c = J_0(\Delta\emptyset)$, $V_1 = J_1(\Delta\emptyset)$, $V_2 = J_2(\Delta\emptyset)$ etc. Hence by examining the relative sideband content it is possible to determine an effective modulation index for different limiter rail voltages.

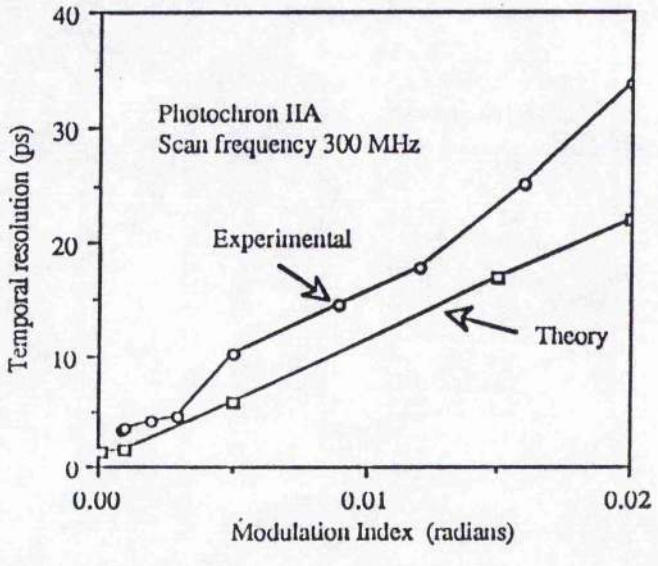

Figure 7. Measured and theoretically predicted temporal resolution as a function of phase modulation index in the carrier signal (frequency of modulation = 90kHz).

Figure 7 shows the measured temporal resolution as a function of effective modulation index, $\Delta\emptyset$ for our Photochron IIA camera when operated at a streak frequency of 300 MHz and sideband separation frequency 90kHz. Plotted on the same figure are the expected values of temporal resolution as calculated using the computer model based on equation 4 where V_N = 60dB below the carrier. Reasonable agreement has been obtained which indicates that the analysis holds and the assumption of saturation induced phase modulation in the limiter is valid. The fact that the model consistently gives lower values of temporal resolution implies that during the experimentation other noise sources and deliterious factors were present.

The passive and active synchronisation systems were then employed on the Photochron IV streak tube and the optimum results are shown in Fig. 8a-c. With passive synchronisation and a mean noise floor ~65 dB below the carrier the best realtime temporal resolution was 1.3 ps and employing a 1ms mechanical shutter this value reduced to 1.1 ps (Fig. 8a). When the tunnel-diode system was used the noise floor was reduced to 70 dB below the carrier and synchroscan temporal resolutions of 1.3 realtime and 0.93 ps shuttered were obtained (Fig. 8b,c). The measured performance for each associated noise level agrees well with the computer model and shows the importance of maintaining a good signal-to-noise ratio in the synchronisation system if limiting temporal resolutions are to be achieved. The actual results should be compared to the realtime and shuttered values of ~2.5 and 1.2 ps reported in reference 3. Moreover, when the active synchronisation system result is compared to the 0.8 ps resolution demonstrated for the Photochron IV operated in single-shot mode[6] it becomes apparent that the active synchroscan technique is now only marginally limiting the overall expected instrumental function of this particular streak tube.

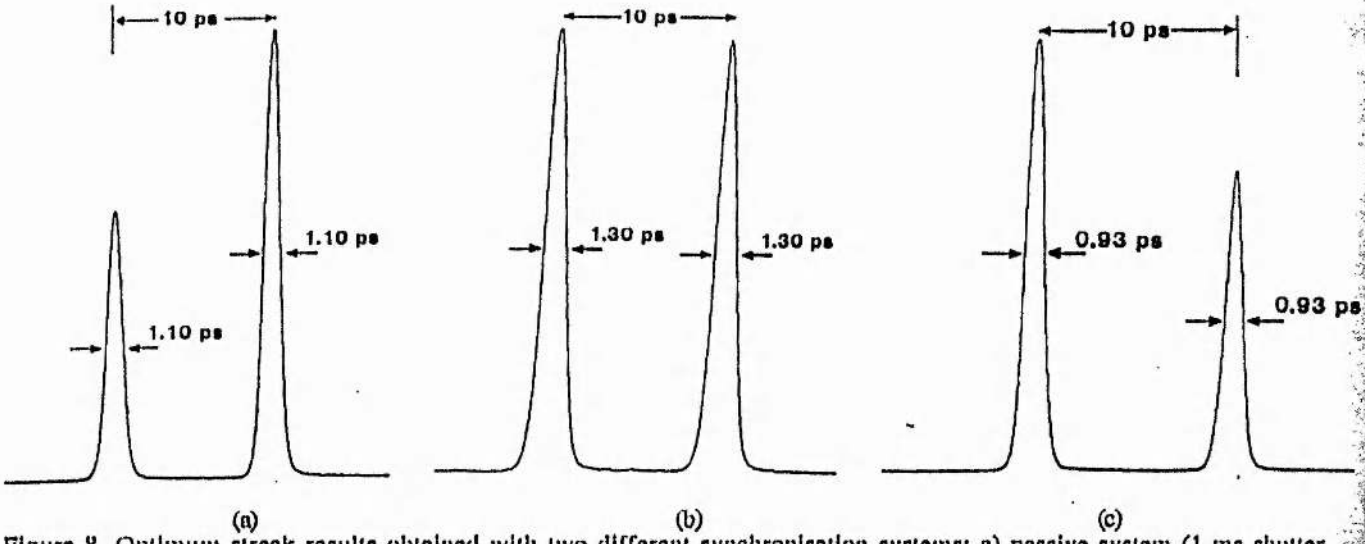

Figure 8. Optimum streak results obtained with two different synchronisation systems: a) passive system (1 ms shutter employed), b) active tunnel-diode system realtime result, and c) active system employing a 1ms shutter.

5. CONCLUSIONS

We have semi-quantitatively investigated the limitations generated by phase noise on synchroscan streaking operation and have made some investigations into methods by which this problem might be reduced. As result of this analysis it has become apparent that to achieve sub-picosecond synchroscan performance it is necessary to minimise integrated phase noise sources to at least 70 dB below the carrier signal. It is our intention to extend this development by implementing other forms of phase control and also to further optimise the various components of the synchronisation circuitry. Refinements to the electron-optics and deflection configurations of the streak image tube are currently being assessed so that cameras may be operated with enhanced time resolution and deflection sensitivity. Consequently we believe that it may be possible to extend the operation of synchroscan streak cameras further towards the femtosecond regime.

7. ACKNOWLEDGEMENTS

The experimental assistance of G. Chen is gratefully acknowledged. The overall funding for this project and a CASE studentship for one of us (A.F) was provided by the Science and Engineering Research Council.

8. REFERENCES

1. Y. Liu, H. Niu, Q.L. Yang and H. Zhang, "A new subpicosecond streak tube with travelling-wave deflector," Proc. 5th National Conf. on High Speed Photography and Photonics, China (1985).

2. A. Finch, Y. Liu, H. Niu, W. Sibbett, W.E. Sleat, D.R. Walker, H. Yang and R. Zhang, "Recent advances towards a 100fs-resolution streak camera," in Ultrafast Phenomena VI, Springer Series in Chem. Phys., Springer-Verlag 1988 (to be published).

3. J.P. Willson, W. Sibbett and W.E. Sleat, "Pulsewidth and interpulse jitter measurements of a passively mode-locked ring CW dye laser," Opt. Commun. **42**, 208-210 (1982).

4. W. Sibbett, H. Niu and M.R. Baggs, "Photochron IV subpicosecond streak image tube," Rev. Sci. Instrum. **53**, 758-761 (1982).

5. M.R. Baggs, R.T. Eagles, W. Margulis, W. Sibbett and W.E. Sleat, "Subpicosecond chronoscopy using a Photochron IV streak tube," *Adv. in Electronics and Electron Phys.* **64B**, 617-625 (1985).

6. W. Sibbett, "Synchroscan streak camera systems," Proc. **15th** Inter. Cong. on High Speed Photography and Photonics, SPIE **348**, 15-26 (1982).

7. J.A. Valdmanis, R.L. Fork and J.P. Gordon, "Generation of optical pulses as short as 27 femtoseconds directly from a laser balancing self-phase modulation, group velocity dispersion, saturable absorption, and saturable gain," Opt. Lett. **10**, 131-133 (1985).

8. A. Finch, G. Chen, W.E. Sleat and W. Sibbett, "Pulse asymmetry in the colliding-pulse mode-locked dye laser," Jour. of Mod. Opt. **35**, 345-354 (1988).

9. F. Salin, P. Grangier, G. Roger and A. Brun, "Observation of high-order solitons directly produced by a femtosecond ring laser," Phys. Rev. Lett. **56**, 1132-1135 (1986).

10. H. Avramopoulos, P.M.W. French, J.A.R. Williams, G.H.C. New and J.R. Taylor, "Experimental and theoretical studies of pulse evolutions in a femtosecond dye laser," CLEO'88 Tech. Dig.7, TUM58, 116 (1988).